Title
Hemodynamics and Transport in Patient-specific Abdominal Aortic Aneurysms

Author
Arzani, Amirhossein

Publication Date
2016

Peer reviewed|Thesis/dissertation

Hemodynamics and Transport in Patient-specific Abdominal Aortic Aneurysms

by

Amirhossein Arzani

A dissertation submitted in partial satisfaction of the
requirements for the degree of
Doctor of Philosophy

in

Engineering – Mechanical Engineering

in the

Graduate Division

of the

University of California, Berkeley

Committee in charge:

Professor Shawn C. Shadden, Chair
Professor Mohammad R. K. Mofrad
Professor Per-Olof Persson

Fall 2016

Hemodynamics and Transport in Patient-specific Abdominal Aortic Aneurysms

Abstract

Hemodynamics and Transport in Patient-specific Abdominal Aortic Aneurysms

by

Amirhossein Arzani

Doctor of Philosophy in Engineering – Mechanical Engineering

University of California, Berkeley

Professor Shawn C. Shadden, Chair

Abdominal aortic aneurysm (AAA) is a permanent local enlargement of the abdominal aorta. Complex anatomies, presence of side branches, and pulsatility of blood flow creates a complex chaotic flow field in AAAs. The progression of AAA can lead to rupture, which is one of the leading causes of death in the elderly. In this study, the flow topology in AAAs, role of hemodynamics in AAA progression, complex vectorial wall shear stress (WSS) patterns, and near-wall transport in AAAs were investigated.

Patient-specific computational fluid dynamics (CFD) was used to obtain blood flow information. Lagrangian coherent structures (LCS) were computed to study the flow physics. The utility of these structures in studying chaotic mixing and transport, flow separation, and vortex wall interaction was demonstrated in different patients. The effect of exercise on flow topology and quantitative mixing was evaluated. The evolution of a systolic vortex formed in the proximal region, strongly influenced the flow topology in the aneurysms. Intraluminal thrombus (ILT) deposition and lumen progression were quantified in several patients using magnetic resonance imaging over a 2–3 year followup. Point-wise spatial correlation of hemodynamic parameters to ILT deposition, revealed a negative correlation between oscillatory shear stress and ILT deposition. This was attributed to persistence recirculation, which can lead to unidirectional backward WSS.

Complex vectorial variations in WSS was studied. Namely, variations in WSS magnitude, direction, and vector in space and time were quantified and compared. Several new WSS measures were introduced to better quantify WSS vectorial variations. The concept of Lagrangian wall shear stress structures (WSS LCS) was introduced. WSS was scaled to obtain a first order representation of near-wall velocity. Tracers representing biochemicals in thin concentration boundary layers were tracked on the aneurysm surface based on the WSS vector field. Formation of coherent structures from WSS tracers were shown. The WSS LCS organize near-wall transport in high Schmidt number flows and could be used to predict regions of high near-wall stagnation and concentration. A wall shear stress exposure time (WSSET) measure was introduced to quantify near-wall stagnation and concentration. Excellent agreement between WSSET and surface concentration obtained from 3D contin-

uum mass transport was obtained. Finally, the important roles that WSS fixed points play in cardiovascular flows was discussed.

To the best wife and parents in the world.

Contents

Acknowledgments

I have been blessed to have amazing people in my life. I owe much of my success to them, and I certainly can not thank them enough. My journey into graduate school started in Fall 2010 when I started my Masters degree at Illinois Institute of Technology (IIT). I was lucky to have a young enthusiastic advisor, Shawn Shadden, who continued to be my advisor at Berkeley. Shawn was everything a student could ask for. He contributed a lot to my professional developments. I have learned a lot from him, which will be a treasure for my future career. During the early years, with his remarkable patience, Shawn spent a lot of time with me, helping me with my research. Whenever I had a question or a problem, I knew I had Shawn next door who was always ready to help. I still remember how much time he spent with me during the early years to improve my presentation skills. After my Masters thesis won the Midwestern Association of Graduate Schools Distinguished Thesis Award, I was invited to give a talk at the meeting. After my presentation, I was asked by a senior faculty how I possessed such presentation skills. My answer was very clear, my advisor, Shawn Shadden. I would also like to thank him for believing in me. When I first told him about the ideas I had to study wall shear stress (WSS), which constitutes the second half of my thesis, he was skeptical at first. However, his trust led to what I believe is the highlight of my thesis.

I have also always treasured the excellent instructors I have had in my education. I am grateful to Dr. Hasan Nagib and Dr. Kevin Cassel at IIT. Dr. Nagib taught me how to think of fluid mechanics in terms of vorticity, and Dr. Cassel showed me how to deliver crystal clear lectures. I would also like to thank Dr. Panos Papadopoulos at Berkeley, for his inspirational style of teaching finite element methods. I would also like to thank my qualifying exam committee, Dr. Mohammad Mofrad, Dr. Panos Papadopoulos, Dr. Tony Keaveny, and Dr. Per-Olof Persson.

I am also very thankful to my very friendly lab-mates. Sahar Hendabadi at IIT who helped me a lot during my first days, when I was not familiar with many things. Kirk Hansen for his critical, thought provoking comments that led to some improvements in my research. Adam Updegrove for helping us with the new features in SimVascular and also for always answering my technical programming questions. I am also thankful to all the other members of the Shadden lab who created a friendly environment that I will always remember. I would like to particularly mention our lab soccer team (known as the Carotid Kids) for the fun moments, and for winning the Etcheverry cup every single time! I would also like to thank my very good friend Reza Kamyar, whom I learned a lot from. Reza taught me a lot about what it means to be a graduate student.

This thesis could not have been done, without my collaborators. I am thankful to Dr. Ronald Dalman and Dr. Ga-Young Suh from Stanford for providing the imaging data, which was used to build the patient-specific models. Also, for providing the longitudinal aneurysm progression data. I would like to thank Dr. Charles Taylor and Dr. Andrea Les from Stanford for providing the velocity data for our first studies. I am also thankful to Dr. Alberto Gambaruto from University of Bristol, whom I met in the 2014 World Congress of

Biomechanics. This led to a collaboration on the Lagrangian WSS study. I am extremely thankful to Dr. Guoning Chen from University of Houston. Guoning provided me with his code for surface vector field calculations, which I extended to use for the Lagrangian WSS and WSS fixed points studies. I perhaps could not have successfully extended his code, if it was not for his quick and thorough responses. Guoning was always responsive and helpful with emails, and I am very thankful to him.

Finally, but most importantly, I would like to thank my lovely family. My beloved beautiful wife, Samaneh, who I have always felt next to me in the passed years, even during the hard times when we were thousands of miles apart. Her presence has changed my life in so many beautiful ways, and she sometimes makes me wonder if there is anything else that I want for myself in this life. My sister, Vida, who is currently a postgraduate student of oral and maxillofacial radiology. I am also truly grateful to my parents, whom I have always felt their support. There is no way that I can imagine myself in my current position, if it was not for all the unconditional love and support that I have received from my mother and father through all stages of my life. My father, Ahmad, who is a Professor at Isfahan University of Technology, was my first role model. I was lucky to live in an academic environment from my early childhood days, where my father's success in his career was one of my biggest motives to move in this path.

My research was supported by NIH Grant No. 5R21HL108272 and an NSF CAREER AWARD, Grant No. 1354541.

Chapter 1

Introduction

1.1 Patient-specific computational fluid dynamics (CFD)

Patient-specific computational fluid dynamics (CFD) is a promising non-invasive tool to investigate blood flow in diseased arteries [256]. The advances made in medical imaging and computational techniques over the passed couple of decades has led to application of these tools in the study of various cardiovascular diseases. The procedure consists of constructing computer models of the 3D geometry in the region of interest from medical images. The boundary conditions are obtained from the patient's pressure and flow rate measurements. The Navier-Stokes equations are subsequently solved, typically using the finite element, finite volume, or spectral element method.

A distinction needs to be made between image-based CFD and patient-specific CFD, although these words are sometimes used in the literature interchangeably. In image-based CFD, only the patient's anatomy is derived from imaging techniques, while general boundary conditions, often based on averaged population data are prescribed. In patient-specific CFD, the boundary conditions are also patient-specific to reproduce the patient's exact flow rate and blood pressure. However, in order to claim that fully patient-specific conditions are being simulated, patient-specific rheological and material parameters are also needed. The blood viscosity and non-Newtonian characteristics are almost always assumed without prior knowledge. While changes in viscosity can be fairly small, in some diseases such as diabetes mellitus significant patient-specific variations in viscosity can occur [60]. Moreover, in fluid-structure interaction (FSI) problems the exact patient-specific material property of the arterial wall is almost never available. Nevertheless, the geometry and boundary conditions are the most important factors that mostly influence patient-specific simulations [242].

Patient-specific boundary conditions are often not available in CFD simulations. Most studies simply rely on a population averaged volumetric flow rate waveform for the inlet boundary conditions, and the outlet boundary conditions are tuned to match a population-averaged flow distribution. In patient-specific simulations, measured flow waveforms are

available, improving the simulation reliability. However, even the measured flow rates only represent the flow rate of the patient at one time point. Considerable variations in heart rate and flow rates can happen throughout the day and night, therefore even patient-specific flow rates can not reproduce all the flow conditions.

Early patient-specific simulations focused on developing the necessary computational tools to carry out these simulations. Taylor and colleges made significant contribution to developing these methods [257]. The goal of most of these simulations were to study the flow patterns and hemodynamics, which had been hypothesized to be important in regulating various cardiovascular diseases. These studies often quantified wall shear stress (WSS) and pressure fields, and depicted flow patterns using velocity streamlines and vector fields. More recent studies have proposed various WSS measures based on WSS vector field to quantify different potential pathways that WSS can affect cardiovascular disease (see Chapter 6). Different indices based on flow patterns and velocity field have also been proposed to quantitatively evaluate relevant flow conditions. Helicity is used to characterize the helical nature of flow, typically observed in large arteries [95, 157]. Aneurysm number has been proposed as an indicator of vortical flow patterns in idealized aneurysms [142]. An impingement index has been proposed to characterize flow impingement in aneurysms [126]. Due to the inherent unsteady nature of blood flow in large arteries, Lagrangian methods have been developed to study transport and evaluate complex flow patterns [227].

Early CFD studies of cardiovascular flows were based on idealized geometries. Significant advances have been made since the previous decade in image-based/patient-specific CFD modeling, which have improved our understanding of many cardiovascular diseases, including abdominal aortic aneurysms [151], cerebral aneurysms [48], coronary aneurysms [222], thoracic aneurysms [251], coronary stenosis [298, 218], carotid stenosis [143], aortic dissection [3, 54], and aortic coarctation [139, 7].

While in early studies the proposed parameters were used to improve our understanding of the flow conditions in diseased and healthy arteries, in more recent studies attempts have been made to correlate these parameters to clinically available data. These correlation studies are carried out in different manners. In most studies, baseline data is not available, and CFD-derived parameters are correlated to the clinically available data at the same time point that the CFD simulation is done. In some studies, followup data is available and CFD parameters are derived from the baseline and correlated to the data available at followup. Spatially point-wise correlation should be done to correlate local hemodynamics to the locally quantified clinical data. However, most studies perform average-based correlations where the hemodynamic parameters are averaged in some region.

Verification and validation is another important topic in patient-specific CFD simulations. In their 2005 review, Steinman and Taylor recommended more study in this area [243]. Since then, many studies have focused on in-vitro [117, 138, 208, 137] and in-vivo validation [35, 7, 121, 26], using phage contrast magnetic resonance imaging (PCMRI) and particle image velocimetry (PIV). Uncertainty quantification is another important topic, which has gained more attention recently [217, 81, 216].

Defining new metrics and new concepts relevant to cardiovascular disease based on CFD

data is another important topic. This will be the focus of a few Chapters in this thesis. Most studies simply rely on computing traditional measures derived from CFD data, without enough biological motivation for the problem under study.

Another area of great interest in recent years is multiphysics blood flow simulations. Coupling solid mechanics with CFD in FSI simulations of blood flow is a fairly mature topic, although significant progress is still being made [34]. Coupling chemical transport processes with CFD simulations is another growing area. The biochemical reactions are usually solved using continuum advection-diffusion-reaction equations where the velocity is obtained from CFD. The coagulation cascade of several biochemicals in thrombosis [145] and the transport of atherogenic biochemicals in atherosclerosis [64, 272] represent important applications. While many studies do a one way coupling of CFD velocity to biochemical transport and reaction, two way coupling studies have also been done where the product of the reactions either change the CFD boundaries [64], or add extra resistance to the flow [192, 176].

Multiscale modeling is another important area of recent interest [299, 199]. Patient-specific CFD simulations are carried out on the organ scale. However, the biological events that control cardiovascular disease happen at the cellular and sub-cellular scale. The cells, smallest units of life, are active units that constantly control many cardiovascular functions and diseases. Cells are able to probe their extracellular environment and sense and response to mechanical and chemical stimuli in their environment. Mechanical forces or biochemical stimuli can induce a series of reactions (signaling events) inside the cell that can propagate to the cell nucleus, affecting gene expression and major cell functionalities. While cell scale is micro-meters, the sub-cellular events occur on a nano-scale. There have been progress in coupling CFD simulations with cell level information in endothelial cells [291], platelets [239, 286, 204], and red blood cells [154, 127, 87]. However, coupling CFD data with sub-cellular molecular events is an important topic that has not yet been developed.

Future patient-specific studies should attempt to include relevant biological events in their simulations, with multiphysics and multiscale modeling. This is anticipated to improve the capabilities of patient-specific CFD simulations in studying cardiovascular disease.

1.2 Abdominal aortic aneurysm (AAA)

Abdominal aortic aneurysm (AAA) is a localized irreversible expansion of the abdominal aorta and is a compelling application area for patient-specific CFD analysis and the related topics mentioned above. Current surgical planning relies on maximum diameter, although this is not always a reliable decision, as many factors play a role in AAA expansion and rupture. Monitoring of the AAA expansion rate is also recommended for smaller aneurysms in surgical decision making.

Male gender, age, smoking, genetic factors, hypertension, and high cholesterol are among known risk factors [30], and diabetes is a negative risk factor [279]. Degradation of the aortic wall, inflammation with immune responses, and biochemical wall stress, are mechanisms that promote AAA initiation, influenced by molecular genetics [1]. After the irreversible

process of aneurysm formation, the dilated vessel creates an environment with complex blood flow and wall shear stress distribution [73, 151, 246, 247, 10, 9], which is thought to perpetuate aneurysm progression. AAA expansion is associated with wall weakening and inflammation where continuous progression and weakening of the arterial wall can lead to rupture if the tissue can not support the mechanical forces exerted by the blood at any location, irrespective of the global strength [205]. Aneurysm rupture prediction is highly complex, although different geometric factors, and biomechanical parameters have been used to assess the probability of rupture [274, 169, 209].

AAA disease currently does not have an effective medical treatment. Exercise has been proposed for smaller AAAs in order to control their growth. Initial findings from the Stanford AAA SCCOR study [182] demonstrated that exercise training is sustainable in patients with small AAA over a 1 year period. There is thus motivation to understand the hemodynamic changes of the flow topology in AAA due to lower limb exercise (see Chapter 4).

Due to complex anatomy and the high flow rates in the aorta, AAAs accommodate a complex mechanical environment. Computational modeling can be used to obtain useful data, not otherwise available clinically. Solid mechanics can quantify the wall stress in the AAA wall, which is a risk factor for AAA rupture. Fluid mechanics can be used to quantify the complex flow and transport patterns inside the aneurysm and the frictional fluid force on the AAA wall. Early computational studies of AAAs used idealized geometries [260, 91, 93]. Les et al. performed the first comprehensive patient-specific CFD simulation in several AAAs [151].

Early focus in AAA CFD studies was on studying the flow patterns and quantifying hemodynamics parameters like WSS and pressure. More recent studies have studied fluid-structure coupling [220, 153], graft design [221], chemical transport [29], residence time [246, 247], monocyte deposition [111], platelet activation potential [108], and global stability [102, 101]. Geometrical indices have also been proposed as potential indicators of rupture risk [237].

The presence of intraluminal thrombus (ILT) in most AAAs plays an important role in AAA biomechanics [282, 264]. Controversy exists regarding the role of ILT in AAA fate. Biomechanical studies have shown that ILT can reduce wall stress, therefore have a shielding mechanism [76, 287]. Moreover, the presence of ILT reduces the lumen diameter, therefore contributing to a potentially simpler flow field with less stagnation. However, it is known that ILT creates an inflammatory environment in the AAA wall that leads to wall weakening [45]. It may be hypothesized that ILT deposition is a defensive mechanism, however at the same time excessive ILT deposition is also a sign of deleterious events and an indicator for the severity of the AAA disease.

The current main focus in AAA CFD studies is to predict the aneurysm growth. Hemodynamics have been used as predictors of AAA and ILT progression [12, 295] (see Chapter 5). However, AAA progression is a multiscale process where several inflammatory biochemicals such as leukocytes and matrix metalloproteinases (MMP) play a role [100]. Growth and remodeling simulations are a promising method to study AAA progression [235, 104, 284]. However, these methods rely on very simple phenomenological models to relate hemodynamics to growth laws. The process of growth and remodeling is mediated by the smooth muscle

cells and fibroblasts in the aneurysm wall. Biochemical events controlled at the cellular level play a key role in the growth and remodeling. An accurate model should account for the transport of inflammatory biochemicals and the communication between the cells. To this end, recently a chemo-mechano-biological model has been developed to study growth and remodeling [5].

The role of endothelial cells (EC) in AAA pathology is another controversial topic. Current growth and remodeling models incorporate WSS with the motivation that ECs are able to sense and response to these forces [90]. However, it is very likely that ECs in AAAs are damaged, although currently no definite evidence exists on their mechanotransduction capabilities in AAAs. Di Achille *et al.* [74] have introduced an endothelial cell activation potential measure based on WSS for AAAs. However, it is likely that such measures are biologically more relevant to the initiation phase of the disease where the ECs play a more crucial role. In Chapter 7 we introduce a novel concept on how WSS controls near-wall transport. It may be perceived that the near-wall transport of inflammatory biochemicals is a more relevant mechanism in AAA pathology, compared to the shear force on ECs.

Recent advances in medical imaging have enabled quantification of inflammatory cellular activity inside the vessel wall. ^{18}F-fluorodeoxyglucose positron emission tomography (FDG-PET) combined with computed tomography (FDG-PET-CT) represents a promising technique to detect inflammation by measuring metabolic activity [46, 269]. FDG uptake has been observed in AAAs with ILT [183], and has been correlated to inflammation and wall instability [212]. FDG uptake has been correlated with increased wall thickness [213] and increased wall stress [163] in AAAs. However, contradictory results have been observed in correlating FDG uptake to AAA pathology [122]. Increased FDG uptake has been reported to be rare in AAAs with large diameters [193]. FDG uptake has been negatively correlated to AAA expansion [134], and no difference has been observed between FDG uptake in aneurysms of different size and controls [21].

Aneurysms have been reviewed in several review papers [141, 274, 119, 209, 63]. Future studies on AAA biomechanics should incorporate relevant biological events that have been shown to contribute to AAA expansion. Modeling these biological events and coupling them to AAA hemodynamics and growth and remodeling models can improve current computational tools.

1.3 Thesis outline and objective

The goal of this thesis was to improve our understanding of the complex flow environment in AAAs and use hemodynamics to predict AAA progression. In Chapter 2 the patient-specific CFD methods used are described. The resulting velocity and WSS data are used in the subsequent chapters of this thesis. The first step was to understand the complex flow topology in AAAs. In Chapter 3, Lagrangian methods are used to rigorously study the flow features is AAAs. The effect of exercise as a proposed therapy on AAA flow topology and mixing is evaluated in Chapter 4. After this thorough study of flow topology in AAAs, in Chapter 5

hemodynamics are correlated to ILT deposition and AAA expansion. The surprising result obtained in this Chapter where low oscillatory shear index was correlated to ILT deposition, motivated exploration of WSS vector fields in the AAAs. In Chapter 6 different aspects of WSS vector field variation was investigated and several WSS measures were introduced to study the spatial and temporal variations in WSS vector field. In Chapter 7 and 8 the novel concept of Lagrangian WSS structures in the study of near-wall transport was introduced. Finally, in Chapter 9 the different roles that WSS fixed points can have in cardiovascular flows is discussed.

Chapter 2

Patient-specific computational fluid dynamics (CFD)

2.1 Introduction

The CFD simulations in our study are patient-specific where the boundary conditions are tuned to represent patient-specific measured flow rate and pressure data. However, we can not claim a fully patient-specific simulation, since a patient-specific rheology is lacking, and our boundary conditions are perhaps better classified as quasi-patient-specific. It should be mentioned that patient-specific models are always built based on the accuracy of available data. Noise and poor resolution in the image acquisition, and also errors in flow rate and pressure measurements always exist, which limit the accuracy of patient-specific CFD simulations.

In the following we discuss the patient-specific CFD simulation done for the AAA patients in this research. The data obtained from these simulations are used in the next chapters.

2.2 Patient-specific CFD simulation of abdominal aortic aneurysms

Two set of patient-specific CFD data were obtained for the AAA patients used in this research. The first set of data was obtained from a previous study where complete details of the simulation procedure is documented in [151]. The second set of data was obtained using similar procedures, but with minor differences mentioned below. The data presented in Chapters 3 and 4 are based on the first data set, Chapters 5, 6, 7, and 9 are based on the second data set, and the data in Chapter 8 is from both data sets.

Imaging studies were conducted under a protocol approved by the institutional review board at Stanford University and informed consent was obtained from all participants. The patient-specific models were constructed and simulated using the open-source software pack-

age *SimVascular* (www.simvascular.org). Contrast-enhanced magnetic resonance angiography (MRA) was used to obtain image stacks of the abdominopelivic cavity, creating a bright-blood image of the aorta and surrounding vessels. Paths were created along each vessel of interest, and segments of the vessels were obtained along each path. The segments were subsequently lofted into a unified geometric model. The models were blended at the location of bifurcations. Each model included the aorta starting from the level of the diaphragm, and included the celiac trunk (with hepatic and splenic arteries), superior mesenteric artery, the renal arteries, and continued through the internal and external iliac arteries. The model geometry represents the fluid domain; i.e. in some regions the model boundary could be due to intraluminal thrombus rather than the native vessel wall. Contrast-enhanced MRA images provided a clear representation of the lumen, making the exclusion of thrombus possible.

Each geometric model was discretized into a linear tetrahedral mesh that was used for CFD simulation of the blood flow. Blood was modeled as an incompressible, Newtonian fluid by the Navier-Stokes equations,

$$\rho\frac{\partial \mathbf{v}}{\partial t} + \rho\mathbf{v}\cdot\nabla\mathbf{v} = -\nabla p + \mu\nabla\cdot\nabla\mathbf{v} \tag{2.1a}$$

$$\nabla\cdot\mathbf{v} = \mathbf{0}\ , \tag{2.1b}$$

where the velocity $\mathbf{v}$ and pressure p are functions of space and time $(\mathbf{x}, t)$ and the density ρ and viscosity μ were assumed constant with values of 1.06 g/cm^3 and 0.04 P respectively. Rigid wall assumption was made. Vessel wall motion was assumed negligible since the abdominal aorta becomes stiffer with AAA progression due to an increase in collagen and decrease in elastin [75], and often an increase of mural thrombus. To solve Eq. (2.1), initial and boundary conditions were specified. The velocity was specified at the inflow face $\mathbf{v}(\mathbf{x}, t) = \mathbf{g}(x, t)$ using PCMRI data, as described below. Zero velocity (no-slip and no-penetration) was specified along the walls. At the outlets, a Neumann-type boundary condition was imposed by coupling lower order models as described below using the coupled-multidomain formulation [271]. An initial value for velocity $\mathbf{v}(\mathbf{x}, t) = \mathbf{v}^0(\mathbf{x})$ was assumed known, which was obtained either from a steady simulation, or was set to zero. The simulations were run until the flow became periodic with small cycle-to-cycle variations. The simulations continued an additional five (four) cardiac cycle for the first (second) set of data to produce data that were used for post-processing. The time step was chosen to divide the cardiac cycle into 1000 time steps.

The Navier-Stokes equations were discretized using a streamline-upwind Petrov-Galerkin finite element formulation [36] with same order interpolation for velocity and pressure. The equal order interpolation results in continuous linear velocity and pressures on each element. Stabilization was used to overcome instabilities in velocity due to presence of advection terms, and instabilities in pressure due to the equal order pressure and velocity formulation used. A preconditioner suitable for cardiovascular applications was used to improve the linear solver performance [85].

The discretization was semidiscrete, i.e. the spatial domain was discretized by finite elements (tetrahedra), leaving a system of ordinary differential equations to be integrated in time using an implicit, second-order accurate generalized-α method [123]. The finite-element formulation and integration method are described in more detail in [281, 89]. The solver has been extensively used and validated for image-based blood flow modeling, including validation in aortic flow studies [138, 7]. Direct numerical simulation was used since the flow conditions were observed to be predominantly laminar or transitional, and turbulence was transient due to the pulsatile nature of the flow. Turbulence models are difficult to apply in cardiovascular flows since most models assume developed turbulence, however when turbulence becomes present in cardiovascular flows it is mostly transitional i.e it fluctuates between laminar and transitional states. Moreover the flow remains laminar in large portions of the domain. The unsteady effects of pulsatile flow also influence the turbulence. It has been shown with hot film anemometer measurements [184] that at higher frequencies the flow happens to be more protected from turbulence because the chaotic velocity fluctuations associated with turbulent flow require a certain amount of time to become fully developed.

Planar PCMRI was used to obtain through-plane blood flow velocities under resting condition at a cross-section of the supraceliac aorta over time. The expected error in the PCMRI measurement ($\approx$5%) is less than typical variation of cardiac output for a given patient over a day. The inlet of each model was chosen to correspond to the PCMRI measurement plane. The PCMRI velocity was integrated over the cross-section to provide a time-dependent supraceliac volumetric flow for each patient. The resulting waveform was used to prescribe a time-dependent Womersley velocity profile at the model inlet [283]. While the in vivo profile at the supraceliac aorta likely deviates from a Womerseley profile, imposing the profile at the supraceliac level ensures sufficient length for the flow to develop so that flow features at the infrarenal segment are not sensitive to the profile at the supraceliac level.

Three-element (RCR) Windkessel models were used to impose outflow boundary conditions at each outlet of the model. These lower order models of the downstream vascular beds were coupled to the computational domain using methods described in [271]. The Windkessel parameters were set to replicate measured flow rate and pressures. To configure the flow rate to each vessel outlet, suprarenal and infrarenal PCMRI data was used to compute expected flow rates to branch vessels. Supraceliac minus infrarenal flow was distributed as 33.0% to the celiac trunk and 67% evenly to the SMA and renal arteries [180]. Infrarenal flow was split equally between iliac arteries, and subsequently 70% of common iliac flow was distributed to the external iliac and 30% to the internal iliac arteries. The total resistance at each outlet (R_{tot}) was set to the patient's mean brachial pressure divided by the expected flow rate of the outlet. The resistance ratio R_p/R_{tot} was set to be 5.6% (28% for the renal arteries to avoid retrograde diastolic flow) [151], which enabled the calculation of the proximal (R_p) and distal (R_d) resistances, where $R_{tot} = R_p + R_d$. For determining compliance values, the total arterial compliance was obtained by the pulse pressure method [245], and distributed to the outlets proportional to the anticipated flow rate. The pulse pressure method was chosen, because it does not require information about the complete pressure waveform. An optimization algorithm that takes the pulse pressure and mean flow rate as inputs was developed to find

the total arterial compliance that best matched the given pressure pulse.

The presence of flow reversal in cardiovascular flows lead to numerical instability due to backflow at the outlet boundaries. Backflow divergence is a common numerical issue in cardiovascular simulations, and there are different methods to solve this problem [177]. At the present study two different approaches were used for resolving this issue. The augmented Lagrangian method [132], which exerts a velocity profile shape at the outlets without affecting the amount of outflow rate was used. This method can be considered as an artificial force required to keep a prescribed velocity profile. This method uses Lagrangian multipliers to enforce a velocity profile at each outlet. The other method used, overcomes backflow divergence by modifying the weak form at the outlet boundaries [177].

In the first data set, mesh independence tests were performed for one patient by comparing results from ≈2 million, ≈8 million and ≈32 million element meshes. The 8M and 32M element meshes showed relative agreement in the flow field and the nominal tetrahedral edge size (500 μm) for the 8M element mesh was used for all patients. In the second data set, the maximum edge size of 0.075 cm in the interior was used. In addition, five layers of boundary layer meshing, with a next to wall edge size of 0.025 cm, was performed along all walls. Qualitative comparison of wall shear stress patterns to a mesh with maximum edge size of 0.05 cm in the interior and a next to wall edge size of 0.01 cm in the boundary layers was performed to ensure mesh convergence. Figure 2.1 shows the computer model and a schematic of the boundary conditions in one of the patients.

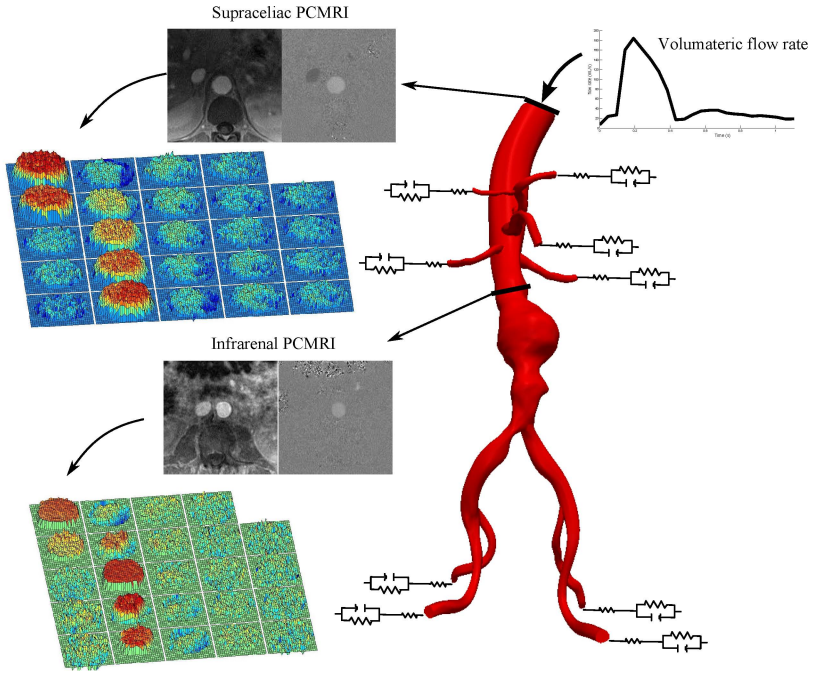

Figure 2.1: A schematic of a AAA computer model and boundary conditions.

Chapter 3

Flow topology in patient-specific abdominal aortic aneurysms using Lagrangian coherent structures

3.1 Introduction

Abdominal aortic aneurysm (AAA) is characterized by disturbed flow patterns, including low and oscillatory wall shear stress with high gradients [214], increased particle residence time [246], mild turbulence [151], and a decrease in wall strength [274]. Moreover, most AAAs are accompanied by mural thrombus [275], due in part to flow recirculation in the aneurysm [32]. Aneurysm rupture kills thousands annually, and a reliable predictor for aneurysm progression remains unknown, though maximum AAA diameter, AAA expansion rate, and peak AAA wall stress have been used with varying success [274].

Studies into AAA hemodynamics have helped reveal possible biomechanical mechanisms underlying AAA pathogenesis and progression, and these mechanisms have been reviewed by [141, 274, 119]. Early studies started from idealized models, e.g. to track the formation and propagation of vortices, and to determine regions of high shear stresses at the proximal and distal ends of an aneurysm [260]. Finol, *et al.* [93] and Deplano, *et al.* [73] studied common asymmetry in AAA, reporting the appearance of asymmetric vortices, and a relative higher shearing of the posterior wall of the aneurysm, which is the most prevalent location of rupture [141]. Peattie, *et al.* [196] and Salsac *et al.* [215] demonstrated changes to the flow patterns based on bulge diameter, and Egelhoff *et al.* [82] considered the effects of exercise.

In vivo flow conditions can be far more complex than flow in simplified aneurysm models. Patient-specific computational models have been used to predict possible in vivo flow patterns and wall shear stress in AAA [92]. Patient-specific AAA models have also been used in studies of fluid structure interaction [194], particle image velocimetry [241], intraluminal thrombus formation [27, 22], and validation of image-based flow modeling [138]. Vessel morphology has wide variability in AAA and the geometry of the aneurysm and surrounding vasculature is

critical in determining the hemodynamics. Les, *et al.* [151] compared different Eulerian-based flow measures in multiple patient-specific computational models, and Suh, *et al.* [246, 247] investigated AAA flow using a Lagrangian-based particle residence time (PRT) measure.

The purpose of the study herein is to provide a more detailed description of blood flow inside AAA. Specifically, this is the first study to compare the transport topology inside different patient-specific AAA models. Previous studies investigating AAA hemodynamics have reported on Eulerian measures, or generic transport characteristics (e.g. PRT), that are unable to convey the complete flow topology. Instantaneous Eulerian measures place inherent limits on interpretation due to flow unsteadiness. While it may be reasonable to infer the bulk fluid motion from velocity data, inferences into transport mechanisms can easily result in misinterpretations. This is noteworthy because transport processes, and disruption of such processes, have significant physiologic relevance. Furthermore the transport mechanics can be tightly and synergistically coupled to the fluid forces that may influence cellular function. Our objective is to provide more precise characterization of the unsteady transport topology observed over different patient-specific abdominal aortic aneurysms under physiological conditions. We utilize the computation of Lagrangian coherent structure (LCS) from finite-time Lyapunov exponent (FTLE) fields. This method has been applied previously to cardiovascular applications [233], including flow near clots [289], in the carotid arteries [270, 233], and flow through the aortic valve [228, 13].

3.2 Methods

Six patients with small AAA (maximal diameter <5 cm) were considered for this study. These aneurysms demonstrated wide variability, which enabled comparison of flow topologies resulting from a range of morphology. The computed velocity data (see Chapter 2) was used for FTLE/LCS computations.

The computational models are displayed in Fig. 3.1, and Figure 3.2 shows the volumetric flow rate used as inlet boundary condition for each patient .

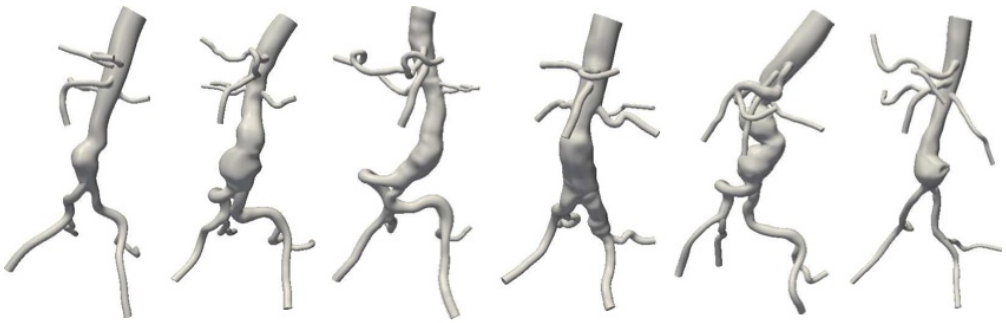

Patient 1 Patient 2 Patient 3 Patient 4 Patient 5 Patient 6

Figure 3.1: AAA computer models derived from magnetic resonance angiography (MRA).

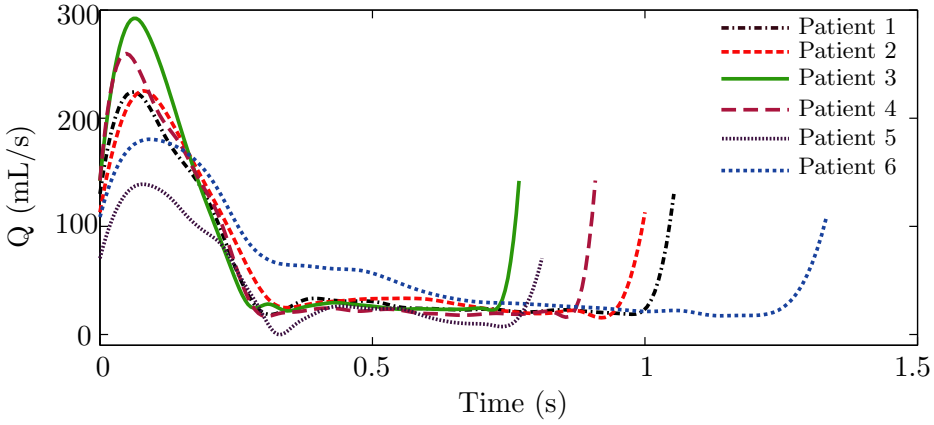

Figure 3.2: Volumetric flow rates prescribed at the inlet of the models.

The peak Reynolds number and the Womersley number based on the infrarenal artery were computed as:

$$Re_{max} = \frac{4\rho Q_{max}}{\pi D \mu} , \tag{3.1}$$

$$\alpha = \frac{D}{2}\sqrt{\frac{\omega\rho}{\mu}} , \tag{3.2}$$

where D is the mean diameter at the infrarenal section, Q_{max} is the peak systolic flow rate at the infrarenal section, μ is the dynamic viscosity , ρ is the density, and ω is the heartbeat frequency. Note, that the Womersley number is more commonly written in terms of the angular frequency, therefore adding a $\sqrt{2\pi}$ factor to the above definition.

Table 3.1 compares these nondimensional parameters, the maximum diameter of the aneurysm, the ratio of the maximum diameter to the infrarenal diameter, and the fraction of the supraceliac flow to the infrarenal level, between the patient models.

Table 3.1: Fluid dynamic and geometric parameters of computer models.

Patient #	$Re_{\max}$	α	$D_{\max}(cm)$	$\frac{D_{\max}}{D_{\text{infra}}}$	$\frac{Q_{\text{infra}}}{Q_{\text{supra}}}$
Patient 1	2002	4.92	3.36	1.71	0.48
Patient 2	2241	5.20	3.72	1.84	0.66
Patient 3	2256	6.22	3.16	1.49	0.59
Patient 4	1667	5.86	3.24	1.49	0.47
Patient 5	1791	4.86	3.00	1.76	0.69
Patient 6	1419	3.63	3.89	2.39	0.31

3.2.1 FTLE/LCS Computations

Lagrangian coherent structures are material surfaces in the flow that have distinguished attracting or repelling properties [107]. While the computation of LCS originated to understand chaotic transport, LCS have been shown to organize both laminar and turbulent fluid motion. This method is compelling for unsteady flow conditions where fluid transport can be difficult to impossible to understand using traditional Eulerian techniques. Numerous applications have demonstrated the utility of LCS for understanding unsteady flow, including the ability to delineate boundaries of unsteady and interacting vortices, flow attachment or separation profiles, and the mechanisms underlying mixing, see [226, 106] for a review. Computationally, LCS can be identified as hypersurfaces that locally maximize a finite time Lyapunov exponent measure [232, 148]. This method is relatively straightforward and robust, and hence has become widely used.

The computation of the FTLE field requires the advection of a dense grid of fluid tracers over the domain of interest. Velocity data, $\mathbf{v}(\mathbf{x},t)$ were used to solve the Lagrangian advection equation

$$\begin{array}{rcl} \dot{\mathbf{x}}(t) & = & \mathbf{v}(\mathbf{x},t) \\ \mathbf{x}(t_0) & = & \mathbf{x}_0 \ , \end{array} \tag{3.3}$$

over a grid of initial conditions $\mathbf{x}_0$ to provide final locations $\mathbf{x}(t_0+T)$ after an integration time T. This equation was solved using the fourth order Runge-kutta method with a sufficiently small time step.

The FTLE was computed at each initial location $\mathbf{x}_0$ as

$$\mathbf{\Lambda}(\mathbf{x}_0,t_0;T) = \frac{1}{|T|}\ln\left\|\nabla_{\mathbf{x}_0}\mathbf{x}(t_0+T)\right\|_2 \ , \tag{3.4}$$

where $\|.\|_2$ is the induced 2-norm. Advection of the particles forward in time ($T>0$) revealed *repelling* LCS in the FTLE field, whereas advection backward in time ($T<0$) revealed *attracting* LCS in the FTLE field. As the notation in Eq. (3.4) indicates, the FTLE field corresponds to time t_0 and likewise the values are plotted at the initial locations $\mathbf{x}_0$, and the integration time T is considered a parameter. Thus, while computed from a Lagrangian frame, the FTLE values are mapped back to the initial locations, and plotted as an Eulerian measure. Locally high values of FTLE appear along hypersufaces that are identified with LCS. This procedure is repeated for a range of initial times t_0 to obtain the time evolution of the LCS.

The identification of LCS is relatively robust to changes in the integration length $|T|$ used to compute FTLE. Nonetheless, the signature of any particular LCS in the FTLE field is dependent on the Lagrangian time scales of the dynamics. In general, since we seek to understand inherently transient phenomena, the integration time should be chosen long enough for dominant features to be revealed, but short enough for the FTLE to be representative of the transient dynamics. Herein the integration time for each patient was set to the respective cardiac cycle length, which is suitable for cardiovascular applications [233]. Specifically, the dominant structures become well-defined in less than one cycle and the

field does not change much by further increase in integration time length since most of the tracers used to compute the FTLE leave the computational domain. The FTLE field was sampled every $t_0 = 1/25$th of the cardiac cycle. This sampling frequency was sufficient to observe the temporal evolution of flow structures. In our computations we dropped the $1/T$ multiplication factor in the definition of FTLE (Eq. 3.4). This helps prevent particles that leave the computational domain in a short time from misleadingly increasing the FTLE value [226].

To increase efficiency of the computations, 3D FTLE caclulations were done only for thin slices positioned at the desired location, unless the full 3D FTLE field was desired. To do this, A thin planar slice with a small lateral dimension was constructed. Initial condition of particles was evenly distributed (≈ 0.01 cm spacing) in this slice. These particles were subsequently integrated in the entire 3D computational domain. This method allows for 3D FTLE calculation in any desired planar location, with much less computational effort. The FTLE calculations were done in *FlowVC*, an in-house discrete transport code [225]. The results were written in the Visualization Toolkit (VTK) format and visualized in ParaView [14].

Effect of Aperiodicity on LCS

The presence of transitional flow or mild turbulence observed in the aneurysms leads to cycle to cycle variation of the flow field, and the relevance of LCS derived from a single cardiac cycle may not be clear. Therefore three additional methods for evaluating FTLE/LCS were explored. We defined an ensemble FTLE from a cycle-based temporal average of the FTLE field, i.e.

$$\langle \mathbf{\Lambda} \rangle_{\text{ens}}(\mathbf{x}, t; T) = \frac{1}{n} \sum_{k=0}^{n-1} \mathbf{\Lambda}(\mathbf{x}, t + kT; T) \ , \tag{3.5}$$

where $t \in [0, T)$, and n is the number of cardiac cycles considered. Second, we defined a max-ensemble FTLE as the maximum FTLE among the corresponding ensembles of the FTLE data, i.e.

$$\mathbf{\Lambda}_{\text{max-ens}}(\mathbf{x}, t, T) = \max_{0 \le k \le n-1} \{\mathbf{\Lambda}(\mathbf{x}, t + kT, T)\} \ . \tag{3.6}$$

Finally, we defined a velocity-ensemble FTLE, $\mathbf{\Lambda}_{\text{vel-ens}}$, as the FTLE obtained from the ensembled average velocity field

$$\langle \mathbf{v} \rangle_{\text{ens}}(\mathbf{x}, t) = \frac{1}{n} \sum_{k=0}^{n-1} \mathbf{v}(\mathbf{x}, t + kT) \ . \tag{3.7}$$

We used five cardiac cycles of FTLE data for ensemble FTLE and max-ensemble FTLE, and five cardiac cycles of velocity data for velocity-ensemble FTLE computations.

3.3 Results

Sections of the 3D FTLE field are shown in the results. Curves of high FTLE correspond to cross-sectional slices of embedded LCS hypersurfaces. Nominally, two planes are shown for each patient. A sagittal plane approximately bisects the left and right hemispheres of the aneurysm, and a transverse plane was chosen slightly distal to the location of maximal bulge, see Fig. 3.3. For Patient 4, a cross-sectional view of the flow in an iliac aneurysm was added, and for Patient 5, additional sections of the AAA were chosen due to the complexity of the aneurysm shape. Sections of the backward and forward FTLE fields are presented in Fig. 3.4–3.11 for the six patients. The Eulerian velocity field is also included for comparison. The colorbars are scaled based on the specific maximum range of each case.

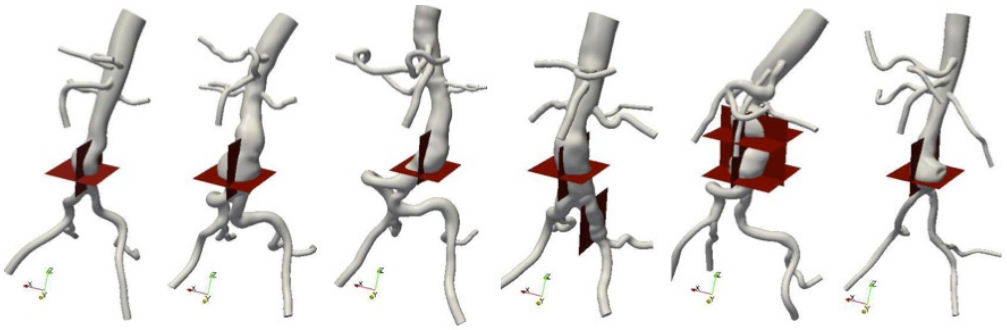

Patient 1 Patient 2 Patient 3 Patient 4 Patient 5 Patient 6

Figure 3.3: Cross-sections used for displaying results.

Patient 1. Figure 3.4 shows the FTLE and velocity fields for Patient 1. During peak systole (top row) there is a region of low backward FTLE in the proximal segment. This region indicates a penetrating inflow jet into the aneurysm. The low backward FTLE values indicate low sensitivity to initial conditions when particles in this region are integrated backward in time. This implies that the inflow jet is coherent. The indicated aLCS1 marks the boundary of the jet. The jet penetrates deep into the aneurysm and as it enters the expansion region it rolls up into a large vortex ring. The cores of this vortex ring on the sagittal cross-section are clear in the backward FTLE during mid-deceleration. The jet impinges on the anterior wall just distal to the region of maximal bulge as indicated by the arrow in the forward FTLE field during mid-deceleration. Specifically, in the forward FTLE field there is an accumulation of repelling LCS orthogonal to the anterior wall, indicating the flow is directly impinging and rolling up on either side of this location.

As the jet penetrates into the abdominal aorta, it separates from the anterior aortic wall, as indicated by the separation profile marked by aLCS2. This separation induces vortical motion along the proximal anterior aspect of the bulge and along with the vortical motion induced from the roll up of the inflow jet, contributes to a persistent region of recirculation in the proximal anterior bulge. The aLCS3 and aLCS4 are separation surfaces from the

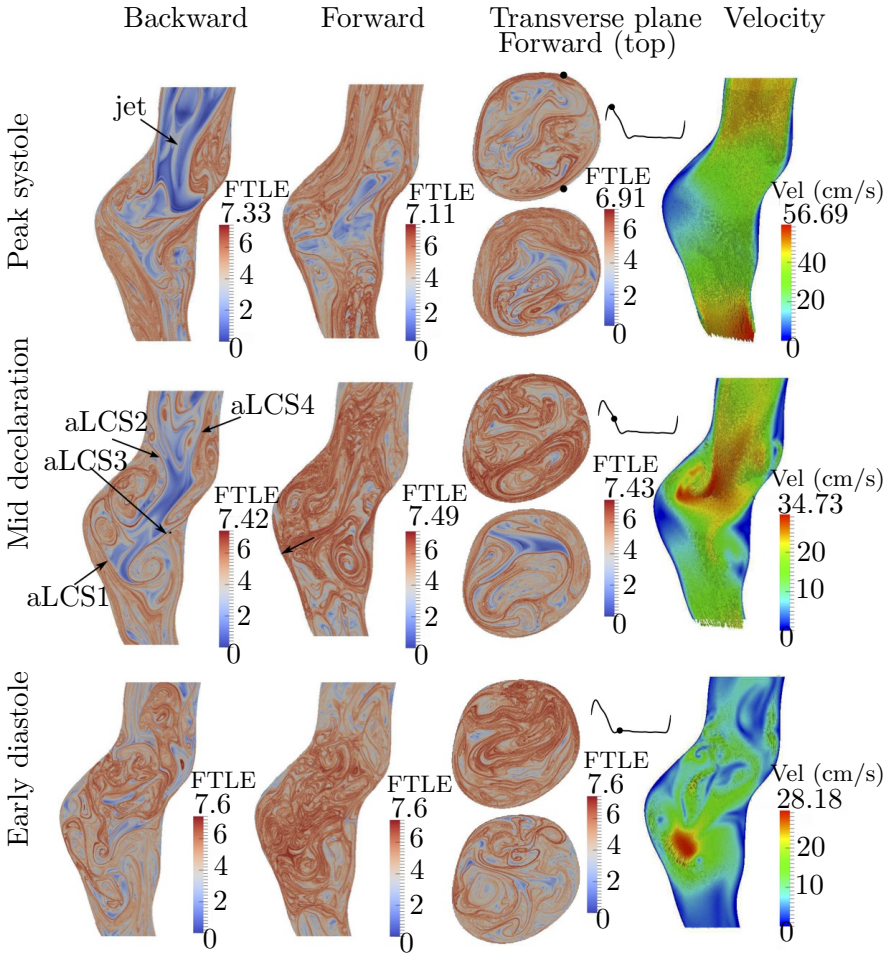

Figure 3.4: Sagittal and transverse sections of the forward and backward FTLE fields, and sagittal section of velocity field for Patient 1 at different times of the cardiac cycle. The two points in the top transverse plane show where the sagittal plane intersects.

posterior wall that are formed by the jet and roll-up. The distal separation from the posterior wall persists during much of the cardiac cycle. In both anterior and posterior regions of separation, there are dense sets of LCS, indicating well mixed separation regions, as opposed to stagnant. During the diastolic phase, both the forward and backward FTLE indicate several coherent vortices spanning the entire aneurysm, which indicate strong stirring/mixing during diastole from mechanisms described in [231].

Patient 2. The results for Patient 2 are shown in Fig. 3.5. For this patient the inflow jet does not coherently penetrate into the main aneurysm bulge. While a vortex ring can be seen in the proximal abdominal aorta in the backward FTLE field during systole (top left), the vortex breaks up, and results in mixing and dissipation in the proximal segment,

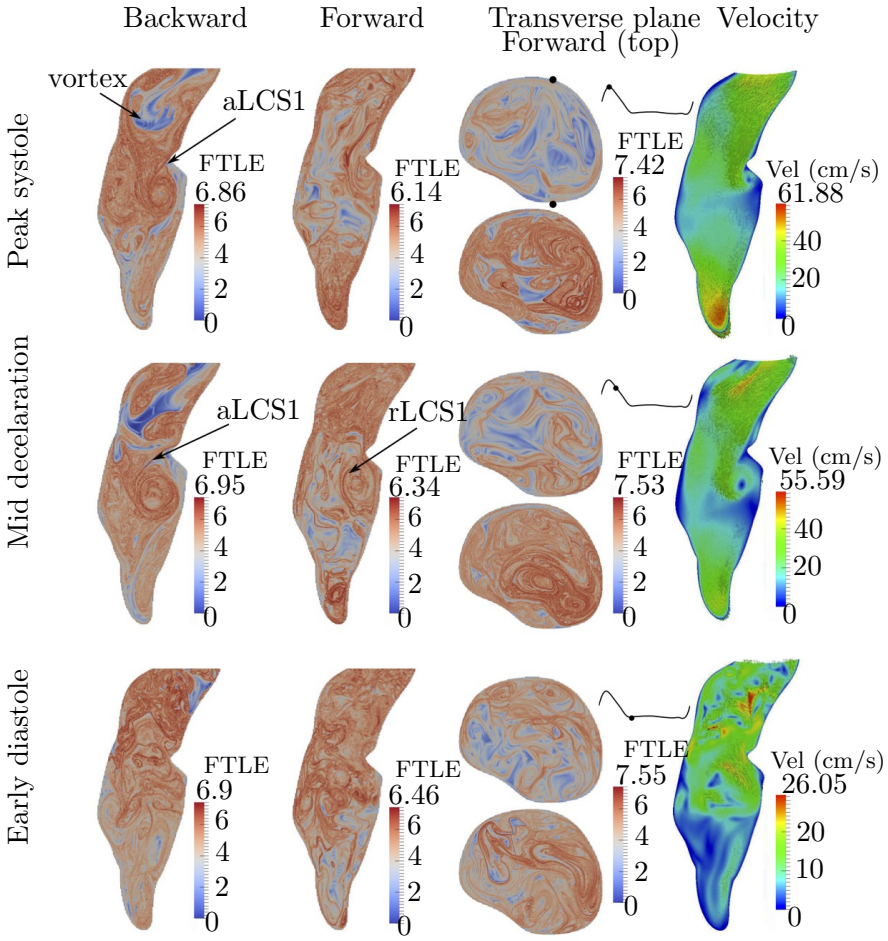

Figure 3.5: Sagittal and transverse sections of the forward and backward FTLE fields, and sagittal section of velocity field for Patient 2 at different times of the cardiac cycle. The two points in the top transverse plane show where the sagittal plane intersects.

and relatively low flow in the main bulge. This appears to be a self-sustaining process; the break up of the vortex and subsequent dissipation during diastole leads to dense LCS in the proximal region that cause the early break-up of the subsequent systolic inflow jet/vortex. This leads to stronger mixing proximal to the aneurysm than in the aneurysm. Large flow separation is observed from the posterior wall (aLCS1). The indicated attracting and repelling LCS (aLCS1 and rLCS1) together form a boundary to a large vortex formed in the separation region, cf. [229] for a discussion on the relationship of LCS to vortex rings. However, this separated region is well-mixed, as indicated by high FTLE inside the vortex. It is the shedding of this posterior wall vortex during diastole that leads to the majority of the mixing observed in the main bulge, i.e. the mixing appears less due to the break up of the inflow jet, and more due to the distal vortex formation and dissipation.

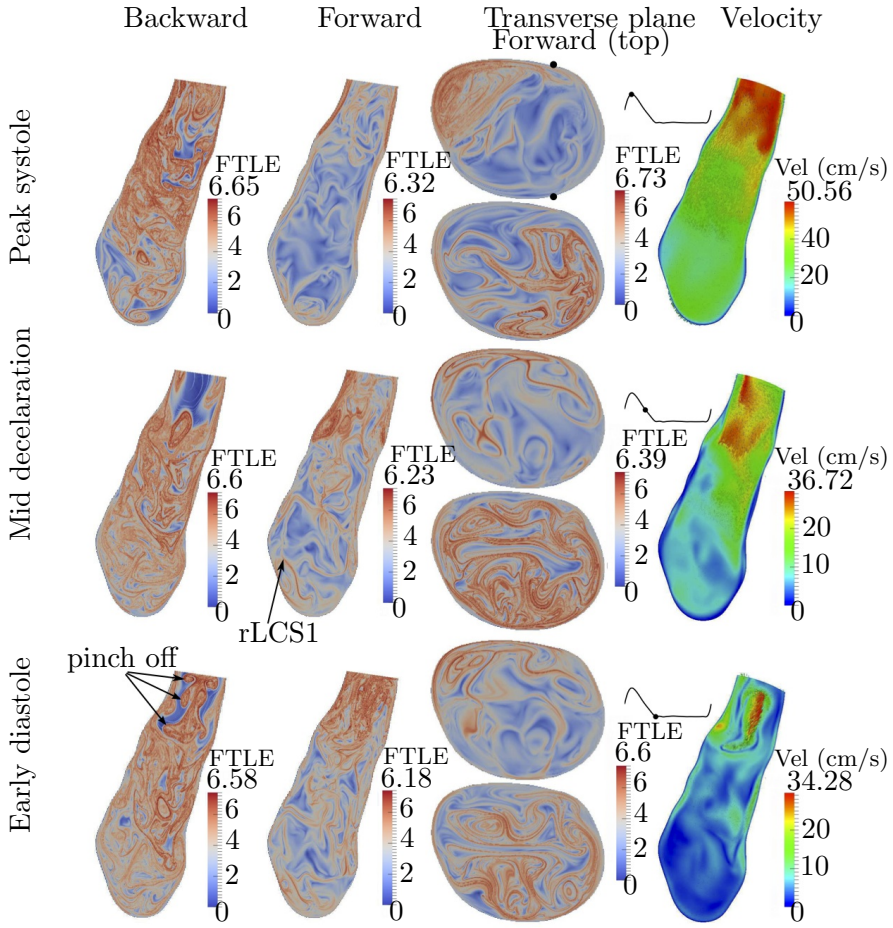

Figure 3.6: Sagittal and transverse sections of the forward and backward FTLE fields, and sagittal section of velocity field for Patient 3 at different times of the cardiac cycle. The two points in the top transverse plane show where the sagittal plane intersects.

Patient 3. Figure 3.6 shows the results for Patient 3. There is a lack of coherent structures in the forward FTLE field during most of systole, whereas there are several LCS indicated in the backward FTLE. This indicates relatively low mixing in the aneurysm itself but high mixing proximal to the aneurysm. Indeed, at the end of systole, there is significant retrograde flow in the abdominal aorta for this patient and a vortex forms at the proximal segment and propagates *upstream* resulting in vortex pinch off. The vortex pinch off phenomenon could be observed from the termination of an LCS and generation of a new LCS at the trailing edge of the previous LCS [186]. This vortex pinch off event and subsequent dissipation into several vortices during the diastolic phase contributes to the subsequent high backward FTLE values and prevalent coherent structures observed during systole in the backward FTLE plots. Specifically, the vortices formed in the proximal segment due to the retrograde flow get pushed into the aneurysm during systole. There are few and sparse LCS in the

forward FTLE field, which indicates that the vortices originating from the proximal segment rapidly dissipate as they are advected into the main bulge. Therefore, relatively low mixing occurs in the distal segment. For example, the indicated rLCS1, which partitions fluid flushed from the aneurysm, showed very slow rate of change in its structure or movement.

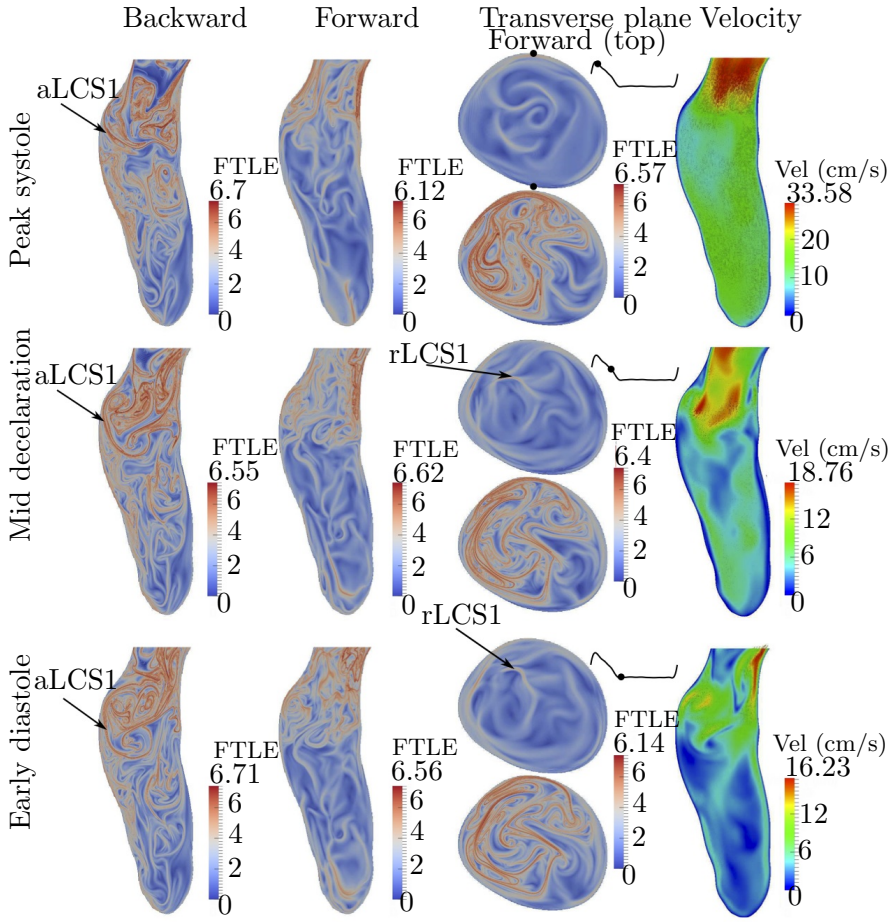

Figure 3.7: Sagittal and transverse sections of the forward and backward FTLE fields, and sagittal section of velocity field for Patient 4 at different times of the cardiac cycle. The two points in the top transverse plane show where the sagittal plane intersects.

Patient 4. Figure 3.7 shows the results for Patient 4. The aLCS1 is the boundary of a proximal inflow jet to the aneurysm, which forms a well-defined vortex ring. The vortex ring impinges on the proximal anterior wall of the aneurysm at the end of systole. The vortex subsequently breaks up and dissipates during diastole, but maintains a relatively coherent large scale vortical structure over much of the cardiac cycle. As with Patient 3, because of the strong dissipation in the proximal segment, and relatively smooth aneurysm geometry, there is a lack of coherent structures in the forward time FTLE field in the majority of the

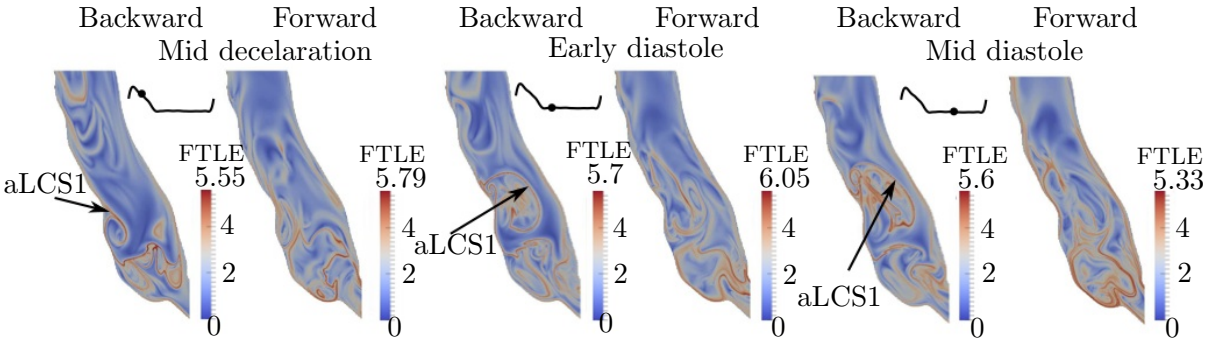

Figure 3.8: Section of the forward and backward FTLE fields in Patient 4's iliac aneurysm at different times of the cardiac cycle.

distal segment, leading to low mixing. This patient demonstrated very little change in the FTLE field with time in both planes (cf. rLCS1); in fact, the forward FTLE in the transverse plane changed very little over the cycle even though there was more evident change to the velocity field.

Patient 4 had a mild aneurysm in the right iliac artery. Figure 3.8 shows the FTLE fields in the right iliac. The aLCS1 captures flow separation that occurs at the proximal aspect of the aneurysm. Similar to the posterior wall separation described for Patient 2, the separation surface moves proximal and expands during diastole, extending the recirculating region, however flow here is more laminar and less mixing occurs in the separated region.

Patient 5. The results for Patient 5 are provided in Figs. 3.9 and 3.10. This patient had a significantly bi-lobed aneurysm. There is transitional/mild turbulence in both lobes during most of the cardiac cycle. This is indicated by high FTLE throughout both lobes. More specifically, the flow topology contains fine scale LCS throughout the aneurysm, which when viewed as shown, appear as regions of high FTLE, but when viewed closer are tightly spaced individual structures. This indicates small scale vortices dominating the flow topology throughout. These small scale LCS are apparent in the other patients, but to lesser extent. Due to the randomness this imparts to the flow field, the incoming jet during systole quickly destabilizes. During the acceleration phase of systole, an inflow jet can be distinguished in the backward FTLE field forming a vortex ring. This jet can be distinguished in both sagittal and coronal views in Fig. 3.9. Following peak systole it is difficult to identify any large scale Lagrangian structure from this vortex (even though it appears well-defined in the Eulerian field). The rLCS1 in the forward FTLE plot of Fig. 3.9 divides the flow in the second bulge into two regions at the beginning of systole. This LCS marks the boundary of particles that are flushed from the distal bulge on the posterior side from a region on the anterior side that recirculates. Figure 3.10 shows the FTLE field for two transverse planes, one section for each lobe. The regions of low backward FTLE show the inflow into the first

bulge.

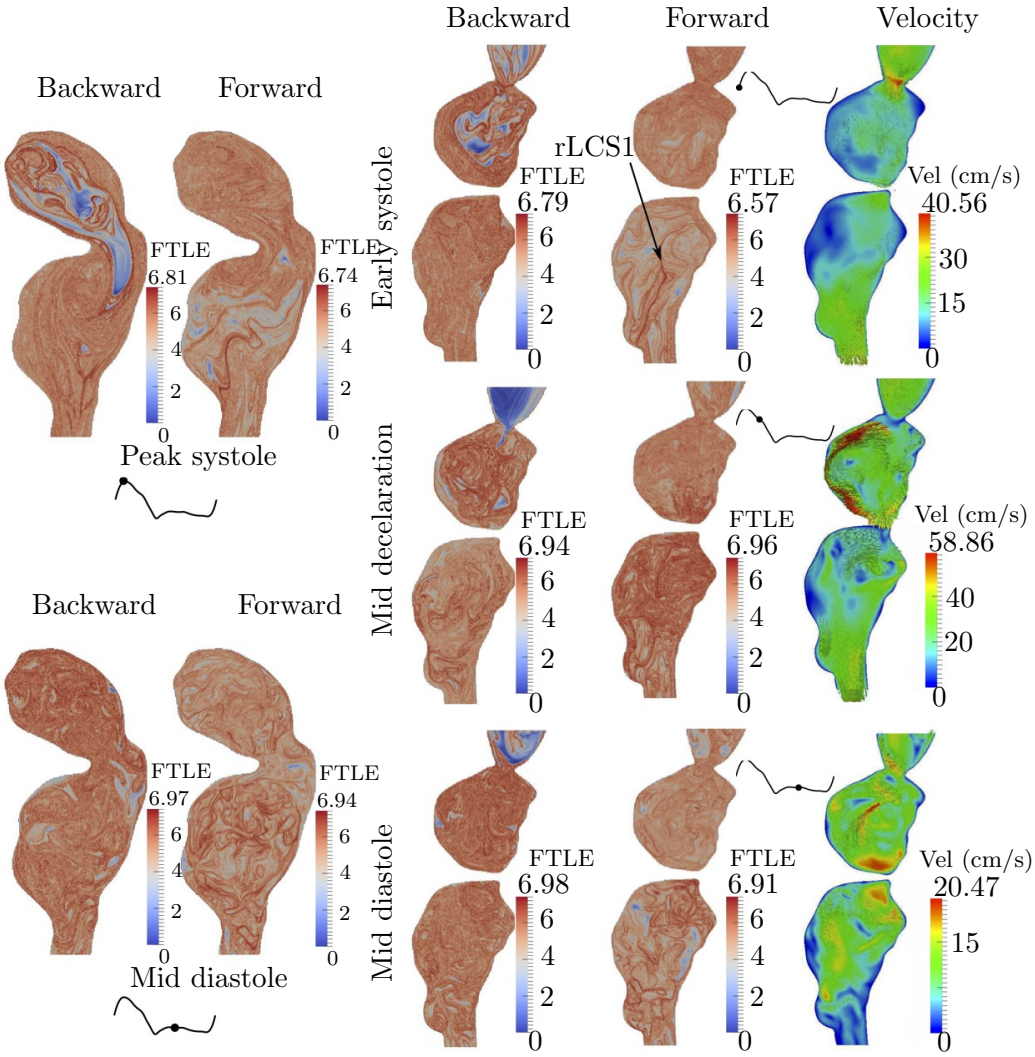

Figure 3.9: Coronal (left) and sagittal (right) sections of the forward and backward FTLE fields, and velocity field for Patient 5 at different times of the cardiac cycle.

Patient 6. Figure 3.11 shows the results for Patient 6. The flow topology is similar to that observed in Patient 1. There is a large jet that penetrates far into the aneurysm during systole, with boundary marked by aLCS1. Since the backward FTLE in the jet is low, the inflow jet is highly coherent. Flow separates (aLCS2) from the posterior wall before the aneurysm bulge, which forces the inflow jet to the anterior side, shearing the anterior wall. The jet rolls up into a large vortex ring that spans nearly the entire aneurysm and impinges on the distal anterior wall. The dissipation of the vortex leads to relatively large scale mixing by smaller scale vortical structures throughout the aneurysm during diastole as observed in

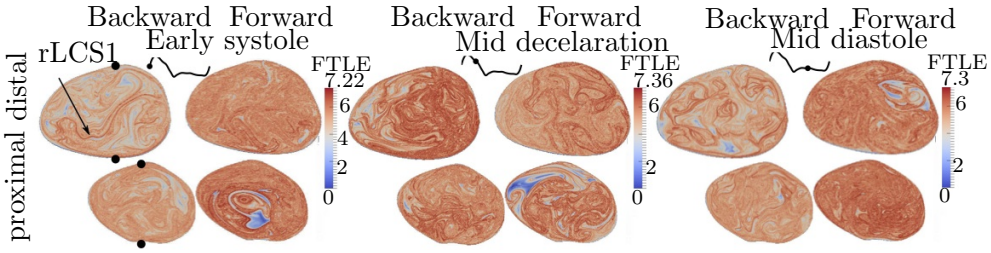

Figure 3.10: Transverse sections of FTLE in the proximal and distal lobes for Patient 5. The points show where the sagittal plane intersects.

both the forward and backward FTLE fields. The rLCS1 partitions the particles that are advected out of the aneurysm from the posterior side.

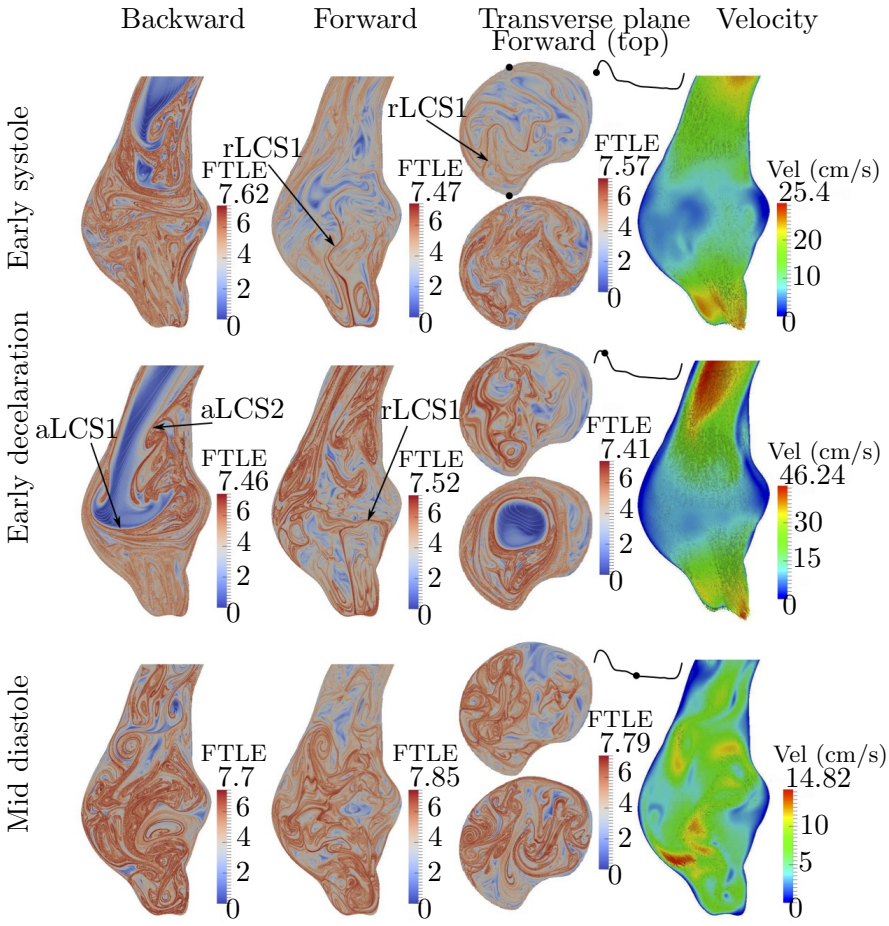

Figure 3.11: Sagittal and transverse sections of the forward and backward FTLE fields, and sagittal section of velocity field for Patient 6 at different times of the cardiac cycle. The two points in the top transverse plane show where the sagittal plane intersects.

3D LCS. Figure 3.12 shows 3D attracting LCS that show the vortex-wall interaction arising from impingement. The Patient shown in this figure is Patient 10 in Chapter 5. The penetrating jet is seen to form a vortex ring. The subsequent interaction of this coherent vortex ring with the vessel wall creates very complex flow structures with high mixing throughout the aneurysm.

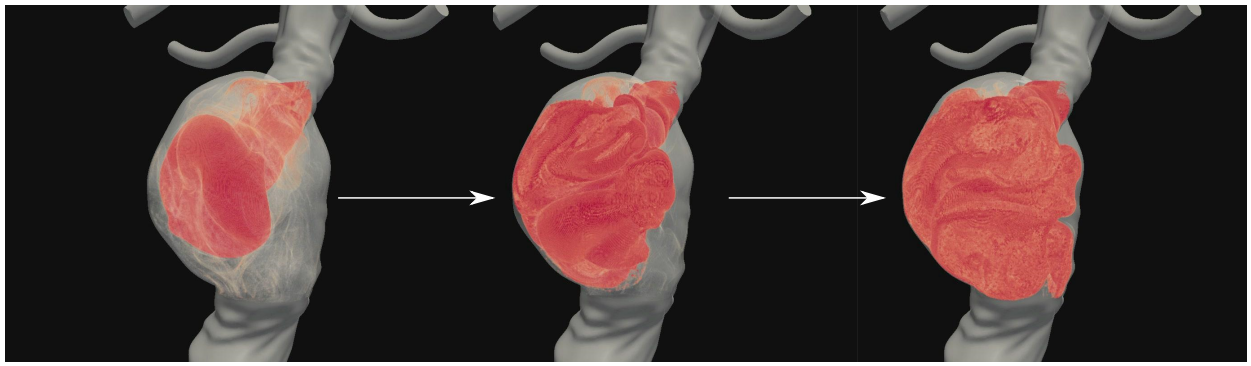

Figure 3.12: 3D attracting LCS showing the vortex-wall interaction.

Aperiodicity. Figure 3.13 shows the different representations of FTLE discussed in §3.2.1. Results are only shown for Patient 4, but similar observations were made from data of the other patients. The max-ensemble FTLE presents more structures due to cycle to cycle variations of the flow and a combining of the maximum FTLE from each cycle. This was even more pronounced in other patients. The ensemble FTLE dissipates the flow structures and only the most persistent structures remain. The velocity-ensemble FTLE represents the structures based on the average behavior of the flow, which most closely resembled the FTLE based on a single realization of the flow. For all patients, the dominant LCS and flow features discussed above persist in all representations, which motivated the use of one realization for presentation of the results.

3.4 Discussion

The results demonstrate dramatic difference in the AAA flow patterns between patients. One persistent trait of all aneurysms studied was the formation of a proximal vortex during systole. High flow enters the expansion region during systole, and an adverse pressure gradient causes separation and subsequent roll-up. The implication of this vortex formation must be considered on a patient-to-patient basis. Whether this vortex penetrated into the main bulge seemed to depend on the initial orientation of the inflow jet, or perhaps more importantly the complexity of the flow in the proximal aneurysm during diastole. The initial orientation of the inflow jet itself depended on the orientation of the proximal artery and

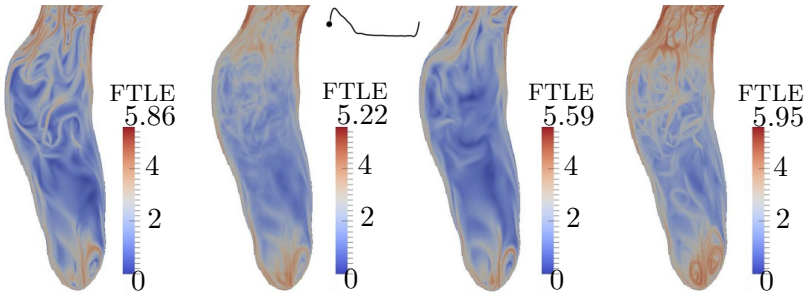

(a) FTLE (b) Ensemble FTLE (c) Vel-Ensemble FTLE (d) Max-Ensemble FTLE

Figure 3.13: Comparison of different representations of FTLE for Patient 4. The figure is based on forward FTLE.

the disturbances induced from the renal arteries. The dynamics of the flow topology during diastole, which is roughly 2/3 of the cardiac cycle, and the systolic vortex propagation appeared tightly coupled. Specifically, the dynamics of the vortex depended strongly on the diastolic flow topology, and the diastolic flow topology depended strongly on the inflow vortex. Another general trait was that even though flow separation was prevalent in several of the aneurysms, flow in the separated regions was well-mixed. This is likely due to the unsteadiness and transitional nature of the flow. Indeed, even small levels of unsteadiness are known to induce significant entrainment and detrainment [229] in cases where the steady background flow would result in a closed vortex or recirculation bubble.

In some situations, the Eulerian velocity field could also be used to identify the flow features revealed by the LCS. For example the velocity field during mid-deceleration in Fig. 3.5 shows a recirculation region near the posterior wall. This is the same vortex described by aLCS1 and rLCS1. The attracting LCS gives however, clearer indication to the exact location of separation. The attracting and repelling LCS together give a more precise boundary to the vortex. In most other cases, the LCS provided delineation of vortex boundaries or other flow features that were much more difficult, or impossible, to distinguish from snapshots of the velocity data.

Flow impingement, an important parameter in the rupture of intracranial aneurysms [126], was observed in some of the AAA models, e.g. Patients 1, 4 and 6. Impingement may cause degradation of the vessel wall, thereby affecting AAA progression and subsequently rupture potential. This may be especially relevant for patients with a coherent inflow jet, since greater momentum transfer to the wall may occur. Moreover, impingement significantly affects the wall shear stress patterns. In other patients, complexity of the flow in the proximal segment may have prevented such impingement on the aneurysm wall, however this led to relatively lower mixing in the aneurysm. The results in Figs. 3.6 and 3.7 show less repelling LCS and mixing in the distal segments of the aneurysms of Patient 3 and 4. These aneurysms had relatively long lengths and our results are similar to previous findings that demonstrated increased length of the aneurysm diminishes the strength of the vortices and disturbances to the flows [214]. In most patients, separation occurred on the posterior wall, which shielded

the posterior side of the aneurysm from the inflow jet. This result was contrary to previous reports of aneurysm asymmetry resulting a higher shearing of posterior wall compared to the anterior wall of the aneurysm. LCS results were primarily presented beginning at peak systole since most structures observed were formed in the acceleration phase and further developed until peak systole.

The non-Newtonian nature of blood may change the vortex structures in a AAA, e.g. by increasing dissipation [28, 131]. Similarly, the flow topology could also change by fluid structure interaction between the blood flow and vessel motion. These effects were neglected in the present study. However, the flow topology changes from cycle to cycle and it is unclear that non-Newtonian rheology or vessel motion would dominate these changes to the flow. Furthermore, other physiologic considerations that manifest in changes to the inflow or outlet boundary conditions may have greater influence.

Regions of transitional or mildly turbulent flow resulted in small scale LCS that appeared as regions of high FTLE when viewed from the scale of the aneurysm. It was verified that in these regions it is possible to extract well-defined coherent structures on smaller scales by locally refining the FTLE mesh. This brings up an important point that Lagrangian flow features can be revealed at scales smaller than the Eulerian flow data/features. This is because trajectory data incorporates spatiotemporally interpolated data, not solely instantaneous data. Therefore, it is typically prudent to make the FTLE mesh more resolved than the velocity mesh for LCS identification. This is often even necessary in order to be able to extract flow structures at a reasonably well resolution.

Previous AAA studies have used instantaneous Eulerian fields to identify disturbed flow patterns. Most of these studies focused on tracking vortices [196], with the consequences of vortex interaction or mixing remaining unclear. For example, the λ_2-method has been used for detecting the vortical structures in AAA [28], however these Eulerian measures break down for unsteady flow, or vortex interaction, and do not provide any indication of the mechanisms of transport. Moreover, these methods are sensitive to the specification of a threshold.

It has been hypothesized that vortices may trap platelets in a region that is separated from the rest of the flow inside AAA [28] leading to the progression of intraluminal thrombus. However, our results indicated that the vortices typical to AAA show strong entrainment, detrainment and interaction, leading to well mixed flow even in separated regions. The results herein begin to address the complexity of transport in AAA but more in-depth studies are needed to clarify the extent and effects of mixing on thrombus formation in aneurysms (see Chapter 5).

Maximal AAA diameter has been the standard parameter for AAA intervention. Indeed, there are correlations between AAA size and rupture. However, there are numerous cases of small to medium aneurysms unexpectedly rupturing, and numerous cases of aneurysms growing to copious size without rupturing. While acute rupture is due to mechanical wall failure, the progression of the AAA over time is likely influenced strongly by fluid mechanical processes. The flow topology is difficult to predict from AAA morphology alone, much less from maximal diameter. Therefore a closer look into the flow topology of AAA along with

relevant hemodynamic parameters may enable better understanding, and perhaps predictions, of aneurysm progression. This will ultimately require close comparisons of AAA flow topologies to actual progression data (see Chapter 5).

Chapter 4

Effect of exercise on flow topology and mixing

4.1 Introduction

There is currently no pharmaceutical treatment of AAA, and lower extremity exercise is a proposed therapy that may favorably affect the mechanisms behind the initiation and progression of AAA [71, 79]. Higher risk of AAA has been demonstrated in persons that suffer from reduced infrarenal abdominal aortic blood flow, including persons with spinal cord injury [292], and persons with above-knee amputation [273]. Increased flow rates in the abdominal aorta associated with lower limb exercise appears to protect against atherosclerosis formation [255], which is one of the risk factors for AAA development [119]. In addition, reduced retrograde flow, higher mean wall shear stress, lower oscillatory shear index (OSI), and a decreased diastolic length resulting from exercise [53, 252] may be beneficial in preventing or slowing AAA.

Different studies have investigated the effect of exercise on AAA flow and stress fields. Idealized models have been used to compare rest and exercise conditions in AAA, including the transition to turbulence and vortex formation [82], the effect of wall compliance [73], and pressure and wall shear stress (WSS) changes [130]. More recently patient specific modeling has been used to provide closer representations of *in vivo* conditions. Les et al. [151] compared WSS, OSI, and turbulent kinetic energy between different patient specific AAA models during rest and exercise. Suh et al. [247] compared the particle residence time (PRT) between different patients at mild and moderate exercise intensities. Exercise has also been studied in other cardiovascular applications, such as abdominal aorta [259, 252], carotid bifrucation [293], total cavopulmonary connection [167], pulmonary artery [253], coronary artery [288], and aortic valve [17].

The present study seeks to compare the topology of blood transport and mixing in patient specific AAAs during rest and exercise. For the purpose of studying blood flow topology, the computation of finite-time Lyapunov exponent (FTLE) fields and Lagrangian coherent

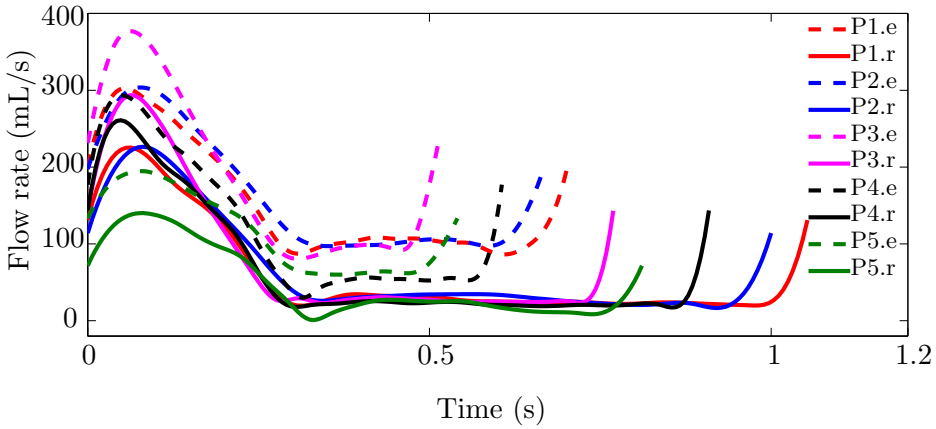

Figure 4.1: Volumetric flow rates for rest and exercise used as inlet boundary condition.

structures (LCS) has been used [233, 10]. This approach uncovers various features of unsteady chaotic flows that are not obtained from traditional Eulerian characterizations of blood flow. For a quantitative comparison of mixing we propose a method with mix-norm and mix-variance measures [170].

4.2 Methods

Five patients with small AAA (diameter <5 cm) having distinct morphologies were chosen for this study. Velocity data was obtained by image-based computational fluid dynamics (CFD), with magnetic resonance imaging (MRI) providing the computational domain and data for boundary conditions (as described in Chapter 2). The resulting velocity data was used in FTLE/LCS, and mixing quantification, calculations.

4.2.1 Computational fluid dynamics simulation of exercise

Moderate lower limb exercise waveforms were derived from the resting waveforms by methods described in [151]. A roughly 5-fold increase in infrarenal flow and 20% decrease in flow to the abdominal branches was imposed, resulting in roughly a 2.5-fold increase in supraceliac flow depending on the patient. Diastole was shortened so that the resting heart rate was increased by 50%, and the resulting waveform was shifted to match the new supraceliac mean. This waveform was mapped to a Womerseley profile and imposed at the inlet. Figure 4.1 displays the rest and exercise waveforms. The exercise waveforms, and pressures derived from data in [179], were used to compute new values for total resistance and arterial compliance, which were distributed similarly as done for rest, except the proximal resistance (R_p) was kept the same as rest, and the distal resistance (R_d) was adjusted accordingly. All the other simulation parameters were similar to the rest condition (see Chapter 2). Five patients were considered in the exercise study.

Table 4.1 shows the Reynolds number at the infrarenal level for each patient at peak systole during rest and exercise.

Table 4.1: Peak Reynolds number during rest and exercise

Patient #	Patient 1	Patient 2	Patient 3	Patient 4	Patient 5
Rest	2002	2241	2256	1667	1791
Exercise	4254	4552	4935	3125	3570

4.2.2 FTLE/LCS computations

FTLE and LCS calculations were done similar to the methods described in Chapter 3.

4.2.3 Quantification of mixing

LCS help to reveal the mechanisms of advective transport. However, to quantify mixing via a single measure a metric is needed. In order to quantify mixing we follow the definitions of mix-norm and mix-variance in [170], and propose a suitable scalar field to be used for these measures. The key idea of mix-norm is to integrate the square of the averaged values of the given field over a set of sub-domains, instead of the whole space, so that mixing over all scales can be assessed.

To understand mixing, we evaluate how new blood penetrating into the aneurysm occupies the aneurysm as compared to the blood that is initially inside the aneurysm. That is, two sets of dense tracers that follow the fluid are introduced. First, tracers are seeded to initially occupy the entire aneurysm uniformly at $t = 0$ (*initial tracers*). These tracers are released only once. Second, tracers are constantly released based on the flow rate at the inlet of the aneurysm (*inlet tracers*). These tracers are released at all times. A scalar function c is defined as the percentage of inlet tracers on a volumetric basis, Eq. (4.1).

Let Γ be the domain of interest (the aneurysm in this case). The aneurysm is divided into distinct equally-spaced subdomains $\Gamma_i(s_j)$, such that

$$\Gamma = \bigcup_{i=1}^{N_{s_j}} \Gamma_i(s_j),$$

where N_{s_j} is the total number of subdomains, and s_j is the particular length scale used to form the subdomains. The function $c_i(s_j, t)$ in domain $\Gamma_i(s_j)$, and at time t is obtained by

$$c_i(s_j, t) = \frac{\sum\limits_{\mathbf{x}(t)\in\Gamma_i(s_j)} \text{inlet tracers}}{\left(\sum\limits_{\mathbf{x}(t)\in\Gamma_i(s_j)} \text{initial tracers}\right) + \left(\sum\limits_{\mathbf{x}(t)\in\Gamma_i(s_j)} \text{inlet tracers}\right)}, \tag{4.1}$$

where $\mathbf{x}(t)$ is the tracer position given by Eq. (3.3). Therefore, c_i is the percentage of inlet tracers in subdomain Γ_i, which is a function of time and the size s_j of Γ_i. A metric is developed to measure c over the domain

$$\varphi(c, s_j, t) = \left(\frac{1}{N_{s_j}} \sum_{i=1}^{N_{s_j}} c_i(s_j, t)^2 \right)^{\frac{1}{2}} . \tag{4.2}$$

Subsequently the mix-norm is defined by further developing a metric to measure c over all choices of length scales s_j

$$\Phi(c, t) = \left(\frac{1}{N_t} \sum_{j=1}^{N_t} \varphi(c, s_j, t)^2 \right)^{\frac{1}{2}} , \tag{4.3}$$

where N_t is the total number of length scales used ($s_j,\ j = 1, \ldots, N_t$). The mix-norm quantifies the ratio of "new blood" to "old blood" in a way that is invariant of location or scale. Our goal is to observe how Φ changes over time in each AAA between rest and exercise.

In order to quantify variations of the amount of mixing throughout the domain we compute the mix-variance. To define mix-variance, the mixing in the entire domain is evaluated by replacing $\Gamma_i(s_j)$ in Eq. (4.1) with Γ. Denoting the resulting function as $\overline{c}(t)$, the mix-variance is

$$\Phi^2(c - \overline{c}, t) = \frac{1}{N_t} \sum_{j=1}^{N_t} \varphi(c - \overline{c}, s_j, t)^2 . \tag{4.4}$$

The above procedure was repeated for each 1/25th of the cardiac cycle, and for a total of five cardiac cycles. The tracer initial positions were seeded with a uniform spacing of 1 mm in each direction. A total of five different length scales ($N_t = 5$) were used in mix-norm calculations. These scales divided the aneurysm to 2^3, 4^3, 6^3, 8^3, 10^3 number of subdomains in each case. The smallest length scale has the dominant influence in mix norm calculations.

Residence time was also computed to evaluate stasis. The PRT is calculated as the minimum time needed for a tracer at position $\mathbf{x}_0$ at time t to leave the domain Γ, i.e.,

$$PRT(\mathbf{x}_0, t; \Gamma) = \min(t') \in (0, \infty) \ \text{ s.t. } \ \mathbf{x}(\mathbf{x}_0, t + t') \notin \Gamma . \tag{4.5}$$

The PRT was calculated for five cardiac cycles, with the same spatial resolution of the tracer seeding used for mix-norm calculations. Regions of high residence time are thought to play an important role in the formation of thrombus due to low particle clearance that can lead to platelet aggregation [115]. To quantify the overall level of PRT for each case, a mix-norm for particle residence time was calculated ($\Phi(PRT(\mathbf{x}_0, t; \Gamma))$), based on the method described above.

In performing Lagrangian post processing, tracers may cross no-slip boundaries (vessel wall) due to the discrete nature of integration. This can lead to errors in Lagrangian based

measures if not properly handled. As discussed in prior studies [228, 80], an efficient, yet accurate, method to solve this problem is to impose a very small inward velocity at the no-slip nodes along the vessel walls that effectively negates or reverses a particle's outward normal velocity component (as may be expected for when a cell or other particle collides with the vessel wall). The imposed inward velocity is typically set such that the local CFL condition is at least 3 orders of magnitude less than 1; i. e., a very small but finite inward velocity is needed to prevent leakage due to truncation errors. Using this method helped ensure, in an accurate manner, that particles only leave the fluid domain through model outlets, as expected. To impose the normal velocity, the normal vectors were computed on the surface mesh using the VTK Generate Surface Normals filter.

Based on the presented method, we propose a thrombosis ratio (TR) to quantify the likelihood of thrombus formation. A higher mixing is thought to be beneficial regarding thrombosis, since regions that are protected from penetration of fresh blood due to low mixing can lead to thrombus formation. These observations could be used to propose the thrombosis ratio as a function of time:

$$TR(t) = \frac{\Phi(PRT(\mathbf{x}_0, t; \Gamma))}{\Phi(c, t)} \,, \tag{4.6}$$

where the mix-norm calculation procedure is repeated for PRT to ensure the contribution of all the subdomains. Higher TR values represent a higher chance of thrombosis, based on two of the advective transport properties.

4.3 Results

Figure 4.2 displays the computational models, and the sagittal cross-sections used for displaying the FTLE results. The following figures show the backward and forward FTLE fields at different phases of the cardiac cycle for the five patients. The colorbars are scaled to the maximum range of each case accordingly.

4.3.1 Changes to Flow Topology from Rest to Exercise

Patient 1. Figure 4.3 displays the FTLE fields for Patient 1. The prominent region of low *backward* FTLE in the left two columns indicates a coherent penetrating jet during both rest and exercise. Flow separation and vortical structures along the posterior wall during rest are mostly reduced or removed by the penetrating jet in exercise. However, exercise appears to contribute to furthering flow separation on the anterior wall. Specifically, under resting conditions there is a prominent separation bubble that forms in the upper anterior aspect of the aneurysm during systole due to the sudden expansion of the anterior wall. Furthermore, the penetrating systolic jet rolls up into a large laminar vortex ring, which is fully developed and most clearly observed during mid-deceleration (1st column, middle row). Therefore, two sources of recirculation are present in the anterior bulge; one is from the core of the vortex

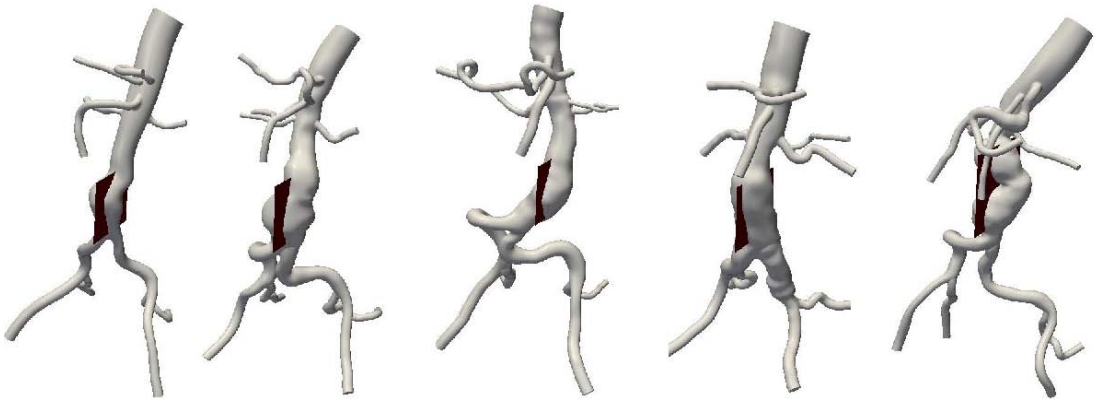

Figure 4.2: AAA computer models, and the cross sections used for showing results.

ring, and the other from the separation bubble. Both regions are bound by prominent LCS during mid-deceleration. Under exercise conditions, the jet does not appear to roll up into a vortex ring but instead the increased flow results in relatively unidirectional flow through the innermost region of the aneurysm. However, flow separation at the proximal, anterior wall of the aneurysm clearly persists, and roll-up associated with this separation is observed during peak systole (2nd column, top row). Under resting conditions, the impingement and break up of the large systolic vortex ring leads to mixing due to large scale vortices throughout the aneurysm during diastole (1st column, bottom row). However, this is not the case under exercise. The unidirectional flow through the innermost regions results in the anterior bulge remaining relatively cut off from the penetrating inflow throughout the cardiac cycle. The fluid in this separated region does eventually mix with the blood pumping through the aneurysm, but this occurs through entrainment and detrainment mechanisms into and out of the recirculation regions, not a complete washout of the recirculation zone. For this patient, exercise never removes, or even reduces, separated recirculating flow in the anterior bulge.

Patient 2. Figure 4.4 displays the FTLE fields for Patient 2. Under resting conditions flow into the aneurysm rolls up into a vortex ring, which is indicated by the low FTLE values in the proximal segment during peak systole (1st column, top row). Immediately distal to this vortex is highly chaotic flow, as indicated by the region of high backward FTLE. This disorganization to the flow appears to quickly destabilize the vortex, which leads to break up in the proximal segment during deceleration. Under exercise conditions, the systolic jet is able to penetrate slightly farther into the main aneurysm bulge. The jet appears to lack the strength or coherence to penetrate through the aneurysm, which is contrary to what was observed for Patient 1. During rest the proximal breakdown of the jet creates highly chaotic flow in the *proximal* aneurysm during diastole (1st column, bottom

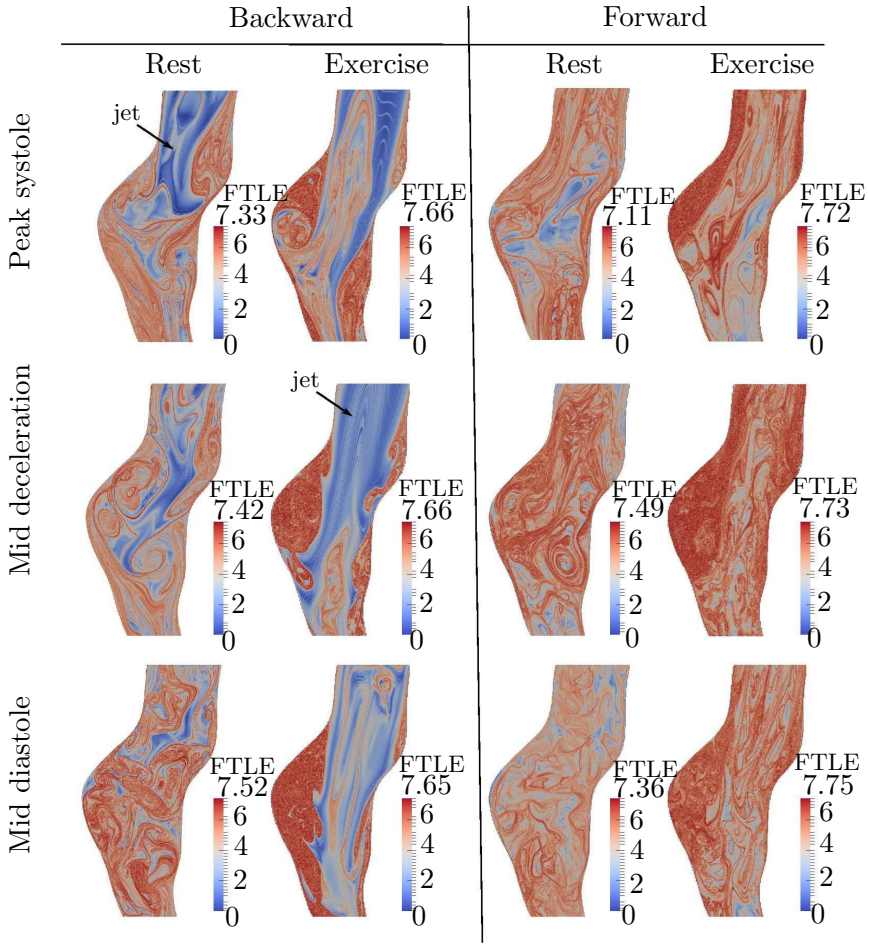

Figure 4.3: Cross section view of FTLE (sagittal plane), at rest and exercise for Patient 1 at different phases of the cardiac cycle.

row). However, the deeper penetration of the jet prior to breakdown during exercise leads to significantly higher chaotic mixing in the *distal* segment (2nd column, bottom row) under increased flow conditions. Unlike Patient 1, the highly recirculatory flow was not confined to a specific region, but instead occupied most of the aneurysm. The prominent flow separation (aLCS1) and subsequent recirculation region formed on the posterior wall of the main bulge during rest conditions appeared to be removed by the highly chaotic mixing during exercise. Differences in the forward FTLE fields are also dramatic. Under resting conditions, larger scale, laminar vortical structures dominate the flow topology in the aneurysm. Under exercise conditions, there is lack of coherent flow features and small scale mixing is observed over the entire aneurysm in the forward FTLE field. This indicates that as blood passes through the aneurysm it becomes well mixed before reaching the iliac bifurcation.

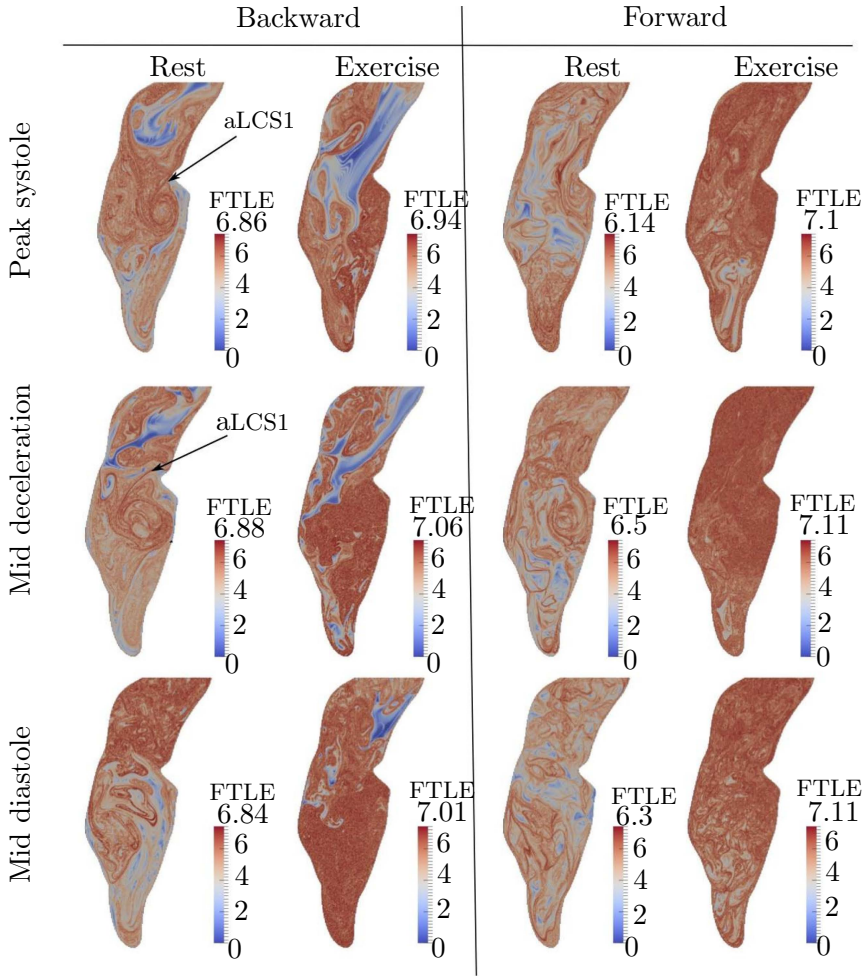

Figure 4.4: Cross section view of FTLE (sagittal plane), at rest and exercise for Patient 2 at different phases of the cardiac cycle.

Patient 3. Figure 4.5 displays the FTLE fields for Patient 3. This patient had noticeable left-to-right curvature of the abdominal aorta. Under resting conditions, the systolic jet forms a weak and shortly lived vortex ring, and the flow topology during rest appears mainly dominated by large scale vortices and laminar flow conditions. During exercise, the backward FTLE fields indicate that the flow into the aneurysm is coherent. However, under exercise the inflow does break up in the distal portion of the aneurysm, leading to highly chaotic flow in the distal segment (2nd column, bottom row). The influence of this mixing in the distal segment to the flow through the aneurysm is apparent in the forward FTLE fields. Under rest, the forward FTLE fields indicate mild mixing as blood passes through the aneurysm. During exercise, the forward FTLE shows vigorous and small scale mixing as blood passes through the aneurysm, and this occurs throughout the entire aneurysm domain.

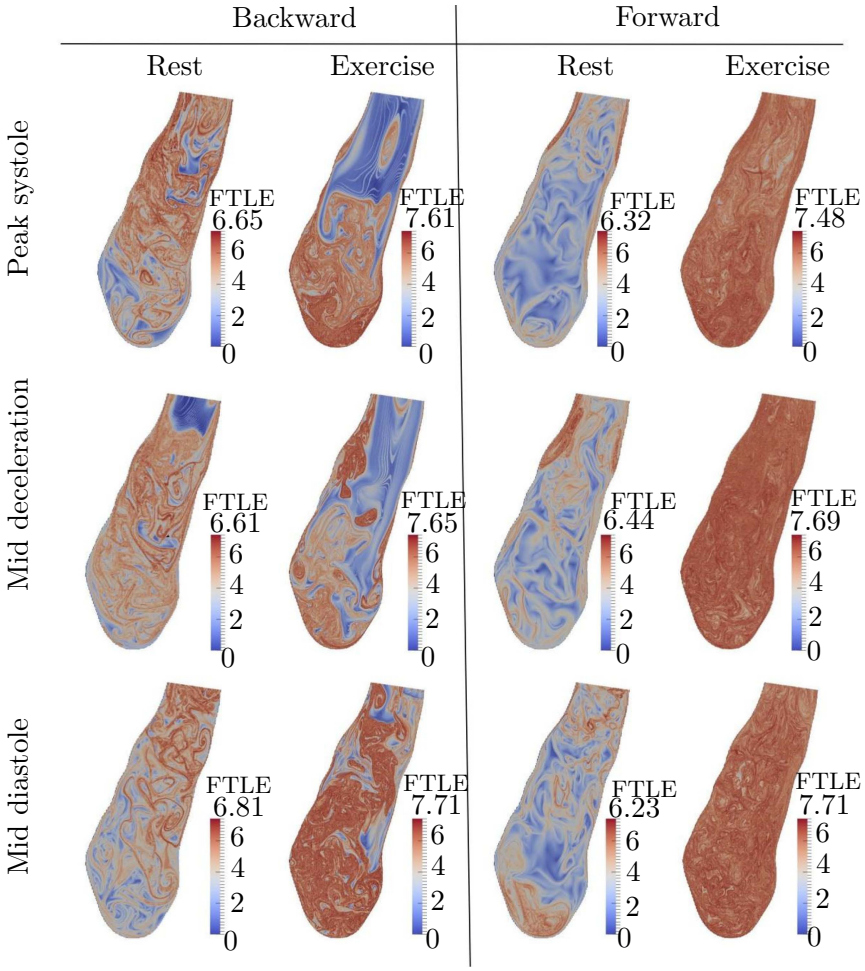

Figure 4.5: Cross section view of FTLE (sagittal plane), at rest and exercise for Patient 3 at different phases of the cardiac cycle.

Patient 4. Figure 4.6 displays the FTLE fields for Patient 4. Under resting conditions, a systolic vortex ring is formed from the penetration of a flow jet into the aneurysm during systole. Similar to Patient 2, the vortex breaks up in the proximal segment, however for this patient the break up of the vortex appears to result from impingement of leading edge of the vortex (aLCS1) on the anterior wall (1st column, middle row). This leads to more highly disturbed flow conditions in the proximal than distal segment of the aneurysm. Indeed, the forward FTLE fields during rest showed very little change in the distal segment of the aneurysm as well. Similar to previous patients, the inflow into the aneurysm under exercise conditions does not lead to a coherent vortex ring. Also similar to Patient 2, the flow here penetrates deeper into the aneurysm during exercise, but eventually breaks up leading to disturbed flow conditions in the distal segment during exercise, instead of the proximal segment as for rest. The backward FTLE reveals the appearance of extended separation

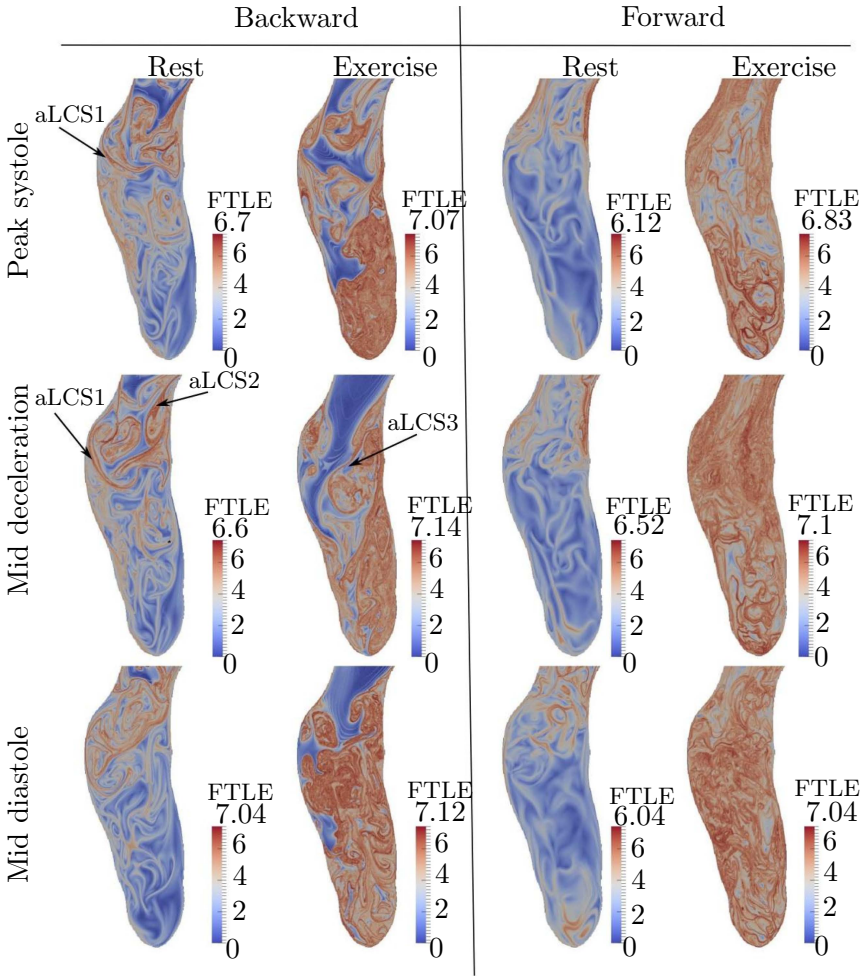

Figure 4.6: Cross section view of FTLE (sagittal plane), at rest and exercise for Patient 4 at different phases of the cardiac cycle.

lines in exercise, that is the separation lines in rest (aLCS2) are not removed by the jet in exercise, but instead the separation boundary (aLCS3) appears to have become extended. This separation on the posterior wall appears to contribute to the systolic vortex during rest, and systolic jet during exercise, being directed to the anterior wall, which prevents inflow from coherently penetrating into the aneurysm, even though the abdominal aorta is relatively straight and the aneurysm is diffuse. Similarly to Patient 3, blood moving through the aneurysm is not well mixed during rest, but becomes more highly mixed during exercise. Nonetheless, comparing the spacing and density of the structures in the forward and backward FTLE fields under exercise conditions with those from other patients, it is clear that less small scale mixing may be observed for this patient during exercise.

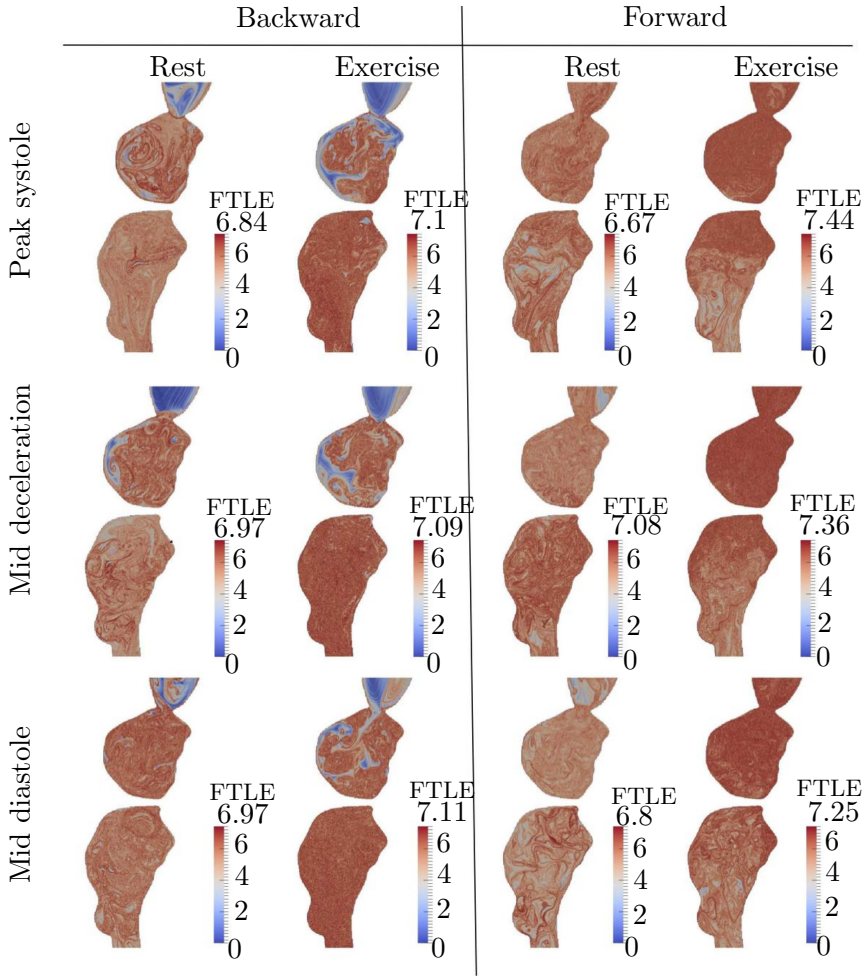

Figure 4.7: Cross section view of FTLE (sagittal plane), at rest and exercise for Patient 5 at different phases of the cardiac cycle.

Patient 5. Figure 4.7 displays the FTLE fields for Patient 5. This patient has a highly tortuous abdominal aorta and complex bi-lobed aneurysm shape. This led to a lack of coherent flow features and mostly chaotic flow topology throughout much of the abdominal aorta under resting conditions. While exercise led to slight stabilization of the inflow jet, the overall flow topology did not change significantly for this patient. That is, mild turbulence dominated the flow in this aneurysm under both rest and exercise.

Integration Time. To observe the effect of integration time τ in the computation of the FTLE fields, different choices of τ are plotted for the first patient in Fig. 4.8. Many of the prominent LCS are revealed even for short integration times. Comparing the FTLE fields in the forth and fifth column demonstrates that there is little change to the actual structures revealed. Hence, increasing the integration time beyond the cardiac length typically does

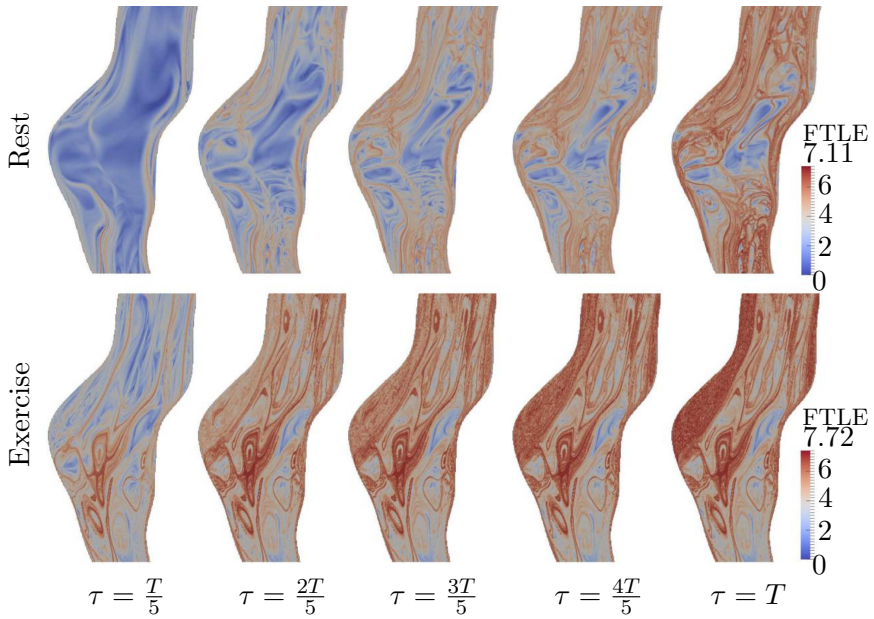

Figure 4.8: Effect of integration time on forward FTLE for different choices of τ in terms of the cardiac length T, during peak systole.

not introduce new LCS or significant changes to description of the flow topology. This is also in large part because after one cardiac cycle, most tracers have been flushed from the computational domain and hence are no longer being tracked and therefore will not contribute to changing the FTLE.

Mixing. Figures 4.9 and 4.10 show the mix-norm and mix-variance results, respectively, for all patients. The domain Γ in these computations was the aneurysm bulge. That is, quantification of mixing was made over the aneurysm itself, not the entire model. Based on the definition of the scalar function in Eq.(4.1), the rate that the mix-norm approaches unity can be considered a metric for comparison of mixing rates among the patients. Exercise led to improvement of mixing in the aneurysm for all patients. As expected from the FTLE/LCS results, Patient 4 had the lowest mixing. The mix-variance results show the amount of variation that mixing has in the subdomains of an aneurysm as compared to the overall mixing in the entire aneurysm quantified by the mixed norm. It can be seen from Fig. 4.10 that mix-variance is reduced during exercise, i.e., a more uniform mixing occurs throughout the aneurysm. Figure 4.11 shows the mix-norm residence time results. The residence time reduces noticeably during exercise. Patient 4, and Patient 5 had the highest and lowest residence time respectively, during both rest and exercise.

PCMRI Comparison. Velocity fields obtained from CFD were compared with velocity fields obtained by PCMRI at the mid-aneurysm level. Results of this comparison for Patient

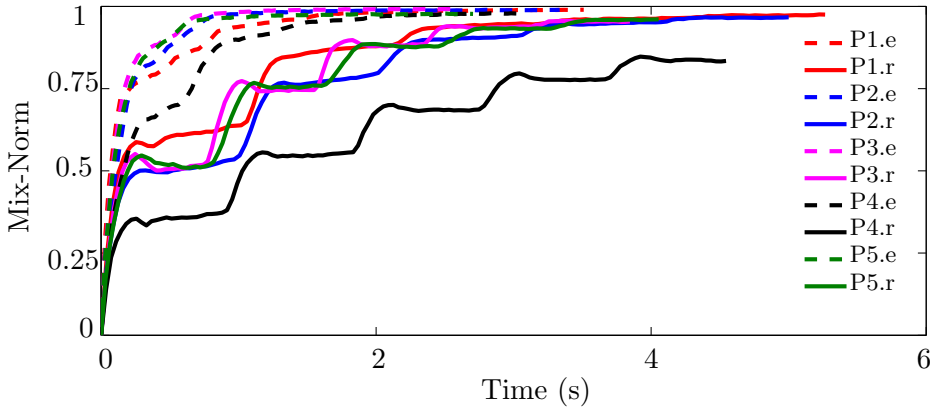

Figure 4.9: Mix-norm plots for the patients during rest (r) and exercise (e). Computations are done for 5 cardiac cycles.

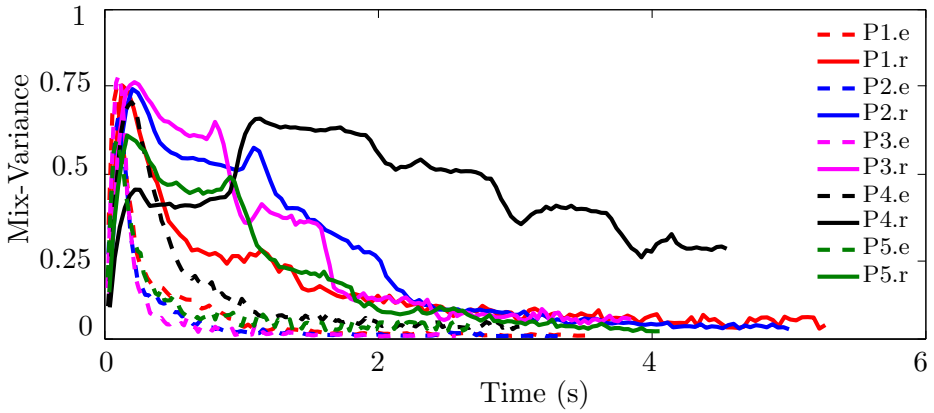

Figure 4.10: Mix-variance plots for the patients during rest (r) and exercise (e). Computations are done for 5 cardiac cycles.

2 are shown in Fig. 4.12. The PCMRI data was obtained from a previous study [150]. Both the computational results and PCMRI measurements show significant swirling/vortices at the mid-aneurysm level with qualitatively similar spatial features and velocity magnitudes. This indicates that the flow features at the mid-aneurysm level seem largely induced by the geometry modeled, rather than the inlet boundary profile, as long as the inlet boundary is sufficiently far from the region of interest. The differences between the PCMRI and CFD velocity fields are multifactorial including modeling assumptions used in generating CFD flow data, and cycle to cycle averaging and various filtering required in generating PCMRI flow data. Reproducibility studies of PCMRI measurements show differences similar to differences between the PCMRI and CFD results obtained herein, therefore the CFD results are expected to reasonably reproduce in vivo flow conditions inside the AAA.

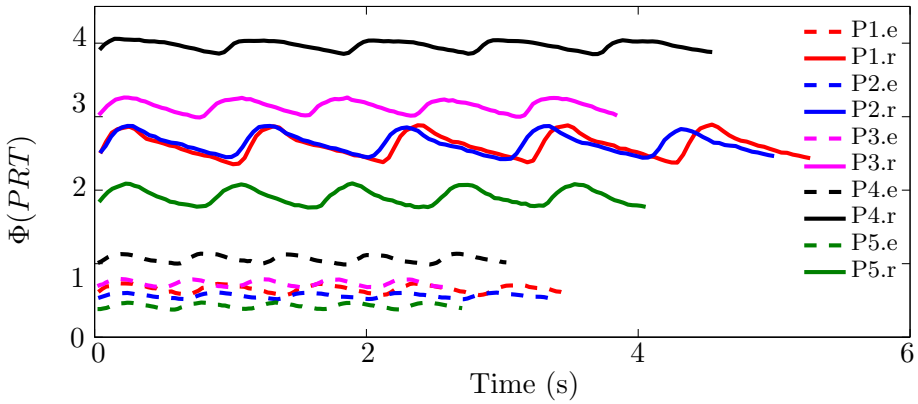

Figure 4.11: Residence time mix-norm plots for the patients during rest (r) and exercise (e). Computations are done for 5 cardiac cycles.

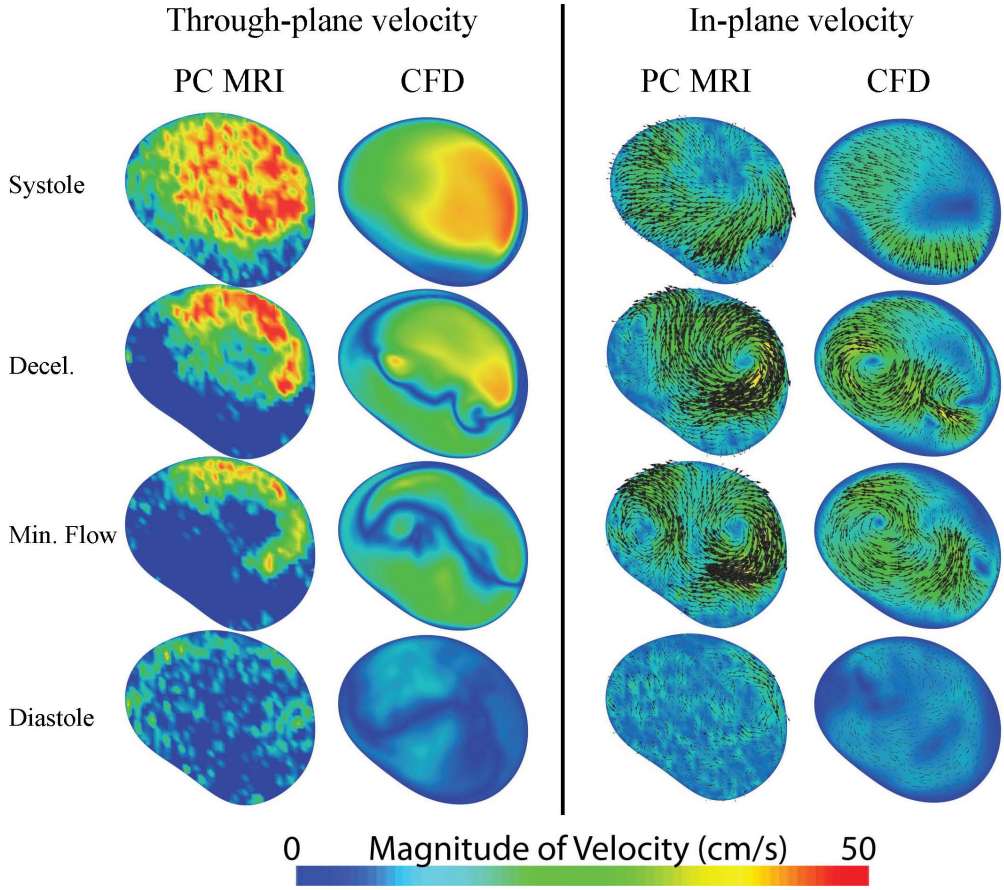

Figure 4.12: Comparison of measured PCMRI velocity fields versus computed velocity fields in the mid-aneurysm of Patient 2. The figure is acquired from [150].

4.4 Discussion

Changes to flow topology from rest to exercise in patient specific AAAs has been studied. Our results demonstrate that prominent large scale flow features generally observed during rest are removed in most, but not all, cases during exercise.

The main factor that determined the changes to the flow topology in exercise was the behavior of the penetrating jet in systole. It was previously observed that the evolution of the systolic vortex determined the flow topology in AAA under resting conditions (Chapter 3 [10]), and in a similar way the dynamics of the penetrating jet during exercise strongly influences the flow topology in AAA under exercise conditions. The jet either washed away recirculating regions that occurred under resting conditions, leaving regions of high local mixing near the walls, or the breakdown of the jet replaced recirculation regions with regions of chaotic mixing connected throughout the entire aneurysm. Finally, the penetrating flow could in some cases add to the extent of the separated flow regions.

The regions of high forward and backward FTLE observed throughout much of the aneurysms in exercise, and during rest in some cases, represent regions of closely spaced LCS that cause enhanced mixing of the flow. These regions are referred to as chaotic due to this implied topology. While defining when a flow is chaotic is a delicate task [37], chaotic flows are generally governed by homoclinic and heteroclinic tangles of invariant manifolds between hyperbolic sets [190]. These tangles gives rise to complex phase space transport typically described as chaos. LCS can reveal analogous invariant manifolds, and indeed the regions observed as having high FTLE were regions of dense heteroclinic tangles of LCS. The dynamics of these structures lead to complex mixing and high sensitivity to initial conditions, which are referred to as chaotic. It should be noted that these regions contain in fact high and low FTLE values, but appear as regions of high FTLE when viewed macroscopically.

Regions of dense LCS can be associated with small scale vortices from the presence of mild turbulence [171], thus we often consider regions of dense LCS as both chaotic and transiently turbulent. However, one must take care in considering the finite-time nature of the FTLE computation to properly interpret such regions. An example is the creation of a localized region of high FTLE such as confined to the anterior wall of the aneurysm in Patient 1 during exercise. While mild levels of turbulent kinetic energy exists in much of the aneurysm during exercise, the blood inside this anterior "pocket" is mostly cut off from the systolic jet passing through the aneurysm and the blood outside this region is flushed from the domain relatively quickly. The blood inside the high FTLE region is not necessarily confined to this region and it eventually mixes with the rest of the domain during diastole, but in doing so the blood spreads over time throughout the domain resulting in further stretching and hence higher FTLE (i.e., further resolved structures) as the integration time increases. This is apparent in Fig. 4.8, especially during exercise conditions (bottom row). The FTLE field along the proximal anterior wall corresponds to blood in, or entrained to, a region of separated, recirculating flow. The FTLE field continues to progress in this region as the integration time is increased, however the FTLE in the rest of the domain remains relatively unchanged since blood originating in this region has been flushed.

The increased flow rates associated with exercise increases the Reynolds number, and subsequently the levels of turbulence intensity. The transitional behavior of the flow might question the usefulness of LCS in interpretation of transport. More specifically, the relative importance of advective mixing versus diffusive mixing is usually considered to answer this question. The domination of diffusion in quasi-turbulent flows usually does not eliminate the advective patterns, and the LCS remain in the flow for considerable time [146]. In the present study a method was presented for direct quantification of mixing based on the fresh blood that occupies the aneurysm. The results based on this method are consistent with the interpretation of mixing from the LCS results. However, both of these methods are based on advection, and the interaction between advective and diffusive mixing contribute to the overall mixing in the aneurysm.

Several prior image-based computational studies of AAA hemodynamics have placed the inlet boundary condition in the abdominal aorta, and in doing so often neglected the major abdominal branch arteries. Under this scenario the flow in the aneurysm becomes sensitive to the chosen inlet velocity profile [112]. Moreover, disturbances due to flow separation from the celiac, superior mesenteric and renal ostia, as well as induced retrograde flow in the infrarenal aorta from the presence of these branch arteries, is not properly modeled. In this study the inlet boundary condition was imposed at the descending thoracic aorta. This, along with direct modeling of the major branch arteries proximal to the aneurysm, helped to ensure that idealization of the inlet profile would have minimal influence to flow topology in the aneurysm. As shown in Fig. 4.12, even though the computational results used an axisymmetric Womersley inlet profile, the vortical and swirling motions at the mid-aneurysm level were consistent with PCMRI measurement, indicating that flow topology was largely induced by the geometry, rather than the inlet boundary profile. This finding is consistent with prior results of Tang, et al., [252] who found little difference in abdominal aortic WSS patterns when prescribing either a Womersley inlet profile, or a measured inlet profile obtained by PCMRI at the supraceliac level.

The flow topology may be influenced by the idealized rigid wall, and Newtonian rheology assumptions. The effect of the rigid wall assumption has been shown to have relatively minor influence to Lagrangian measures of blood flow through a total cavopulmonary connection application [80]. Since typical deformation of AAA are of similar magnitude, we expect that fluid-structure interactions will not significantly alter the main flow features observed in this study. The effect of blood rheology on vortex formation inside AAA has been studied previously [28]. While some change to the flow topology was demonstrated, it remains unclear whether changes due to expected variations in blood rheology are significant in comparison to cycle to cycle variations in the flow and potential inaccuracies in boundary conditions (including errors in lumen reconstruction) [242].

We have proposed a method to compare the overall particle residence time inside aneurysms quantitatively. Residence time is hypothesized to be correlated with thrombosis. Furthermore, higher mixing inside AAA is thought to be beneficial. However, it is not clear that poor mixing is adverse. Indeed, unidirectional flow leads to poor mixing and this is the preferred physiologic state. Patient 3, followed by Patient 4, exhibited the most significant

increase in chaotic mixing from rest to exercise. Although the backward FTLE shows that exercise is washing away some of the disturbed regions in rest, the sparse LCS in the forward FTLE during rest shows that the bulk of the flow is unidirectional. This questions whether the high mixing observed in exercise is beneficial for these patients. Nonetheless, in locations of recirculating flow, increased mixing is likely beneficial. Therefore, TR may be considered as a parameter to correlate these advective properties of the flow to the likelihood of thrombosis. However, there are many factors that can lead to the formation of thrombus, and these parameters are only based on transport mechanisms.

There are several hemodynamic parameters in AAA that are affected by lower extremity exercise [151, 247]. Most of these parameters come from instantaneous information of the flow. However, each cardiac cycle is a continuous contribution of different phases, and ten minutes of exercise is comprised of hundreds of cycles. It is difficult to evaluate the combined effect with hemodynamic parameters. Moreover, most AAAs are accompanied by mural thrombus formation that inhibits the direct contact of flow with the vessel wall, questioning the role of shear endothelium-mediated process in aneurysm progression. Lagrangian analysis of flow field can use the continuous information of the flow from multiple cycles, and the LCS are tightly related to fluid forces [230]. However, it is still not clearly understood how all of these information precisely affect the progression of the disease.

Chapter 5

Abdominal aortic aneurysm progression and intraluminal thrombus deposition

5.1 Introduction

The presence of intraluminal thrombus (ILT) complicates AAA growth. ILT is fibrin structure compound of platelets, blood cells, blood proteins and cellular debris [113]. ILT is more frequent in larger AAA since most patients develop thrombus as the aneurysm progresses. It has been proposed that platelets activate in regions of high shear and are subsequently advected towards the aneurysm wall where they accumulate in regions of low shear and form thrombus [27], with a possible role played by the vortical structures formed inside the aneurysm [28]. It has also been shown that the flow field inside AAA may promote ILT formation by increasing residence time and trapping blood particles [22, 246, 247].

The effect of ILT on AAA progression and rupture remains controversial [282]. ILT may deprive the aneurysm wall of oxygen, which may exacerbate wall inflammation and weakening [275]. The rupture of ILT can lead to the rupture of the arterial wall [169], mature ILT can reduce the wall compliance [84] and increase dissection risk [263], and ILT growth rate can increase the likelihood of aneurysm rupture [244]. However, it has been reported that ILT can reduce the stresses acting on the wall of the aneurysm [276, 31].

Patient specific AAA blood flow modeling is a promising tool that may provide important information for understanding hemodynamic factors involved in AAA progression, and potentially data for clinical decision making. The goal of the present work is to investigate potential hemodynamic factors that may lead to progression of thrombus inside AAA. In this study, quantifications of time-averaged wall shear stress (TAWSS), oscillatory shear index (OSI) and mean exposure time (MET) at the luminal surface are compared to thrombus accumulation from longitudinal in vivo mid-aneurysm magnetic resonance wall content data in patients with small AAA.

5.2 Methods

5.2.1 Imaging

Ten patients with small AAAs (diameter < 5 cm) were recruited under a protocol approved by the institutional review board, and each patient consented to participate in imaging at baseline and followup visits. Patient information, including their followup interval, are shown in Table 5.1. The geometric characteristics of the patients are shown in Table 5.2.

During the baseline visit, aortic lumen, blood flow, and wall content data were collected. Patients were scanned with contrast-enhanced magnetic resonance angiography (MRA) in the supine position with a 1.5 T Signa MR scanner (GE Healthcare, Waukesha, WI). A 3D fast gradient echo MRA sequence was used to image the aortic lumen. The scan parameters for MRA included: 3.0–3.3 ms repetition time, 0.7–0.8 ms echo time, 25° flip angle, 3 mm thickness with 1.5 mm overlap, and 40 $\times$ 40 cm^2 field of view with 512 $\times$192 acquisition matrix per slice (reconstructed to 512 $\times$ 512). A single component phase contrast MR sequence (PCMRI) was used to acquire blood flow velocity at the cross-sections of supraceliac and infrarenal aorta. The scan parameters included: 11.9–12.7 ms repetition time, 4.5–5.3 ms echo time, 20° flip angle, 256 $\times$ 192 acquisition matrix per slice (reconstructed to 256 $\times$ 256), and 150 cm/s through-plane encoding velocity with 24 time point reconstruction. Subsequently, a T1-weighted, double-inversion recovery fast spin echo sequence (black blood MR) was used to image the aortic wall contents on the oblique axial plane at the level of maximal aortic dilatation. The single slice acquisition reduced the acquisition time while patients held their breaths. The scan parameters included: 42 ms echo time, 6 mm slice thickness, 34 $\times$ 34 cm^2 field of view with 320 $\times$ 320 acquisition matrix per slice. All images were acquired during inspiratory breath-hold to minimize the motion artifact. Brachial systolic and diastolic blood pressures were measured using an automatic pressure cuff (Omron Healthcare Inc., Bannockburn, Illinois). During the followup visit, aortic lumen angiography and black blood MR scans were collected using consistent imaging sequences.

5.2.2 Hemodynamics analysis

Wall shear stress was quantified using two standard parameters, the time average wall shear stress (defined as the magnitude of the vectorial average here), and oscillatory shear index (OSI). Four cardiac cycles were used in these computations, which was sufficient for convergence of results. Specifically, the TAWSS was calculated as

$$\mathrm{TAWSS} = \left\| \frac{1}{4T} \int_0^{4T} \overrightarrow{\tau}_{wall} \, \mathrm{d}t \right\| \, . \tag{5.1}$$

The OSI was calculated to measure oscillation of the wall shear stress vector from its mean direction as

$$\mathrm{OSI} = \frac{1}{2} \left(1 - \frac{\left\| \frac{1}{4T} \int_0^{4T} \overrightarrow{\tau}_{wall} \, \mathrm{d}t \right\|}{\frac{1}{4T} \int_0^{4T} |\overrightarrow{\tau}_{wall}| \, \mathrm{d}t} \right) \, . \tag{5.2}$$

Table 5.1: Patient information. Abbreviations: Type 2 diabetes mellitus (DM), Hypertension (HTN), Body mass index (BMI).

Patient #	Gender	Age at baseline (yrs)	Followup interval (months)	BMI	Smoked (yrs)	Quit smoking (yrs ago)	HTN	DM
1	M	73	36	30.10	5	48	Y	–
2	M	60	44	29.45	48	7	Y	–
3	M	66	24	26.39	30	20	Y	–
4	M	73	24	30.48	6	48	Y	–
5	M	62	38	29.16	15	31	–	–
6	M	61	36	30.38	18	23	Y	–
7	M	73	31	27.67	0	–	–	–
8	M	69	30	27.97	52	4	Y	–
9	F	78	16	26.63	8	30	Y	–
10	M	72	22	30.72	45	15	Y	Y

Table 5.2: Geometric characteristics of aneurysms. Lumen diameter is based on equivalent area diameter. Centerline length starts and ends when the aneurysm diameter is 10 % larger than the native aorta. All units are based on cm.

	P1	P2	P3	P4	P5	P6	P7	P8	P9	P10
max lumen dia	3.26	2.61	3.07	3.62	3.08	3.00	2.97	2.29	3.42	4.08
centerline length	8.82	4.49	8.76	5.85	7.79	5.92	6.43	7.25	4.47	9.12
lumen volume	45.3	18.9	39.8	34.1	46.2	26.1	25.9	26.1	24.5	60.5

Flow stagnation was quantified using the mean exposure time (MET) [160]. The MET of each element in the flow solver mesh was measured as the accumulated amount of time that Lagrangian fluid particles entering the model spent inside model elements

$$\mathrm{MET}(e) = \frac{1}{N_e \sqrt[3]{V_e}} \sum_{p=1}^{N_p} \int_0^\infty H_e(p,t)\, \mathrm{d}t\ , \qquad H_e = \begin{cases} 1 \text{ if } x_p(t) \in e \\ 0 \text{ if } x_p(t) \notin e \end{cases} \tag{5.3}$$

where N_p is the total number of particles released, N_e is the number of encounters of a particle into the element e, V_e is the volume of the element, $x_p(t)$ is the position of the particle, and H_e is the indicator function of the element e. MET by definition, measures both stagnation and recirculation, while weighing recirculation lower. To compute MET, particles were uniformly seeded (200 μm spacing) and released proximal to the aneurysm continuously over time. Namely, the particles were released in a way to maintain a uniform influx density by releasing based on local space-time flow rate for a total of four cardiac cycles. This created approximately 10 million released particles. The particles were integrated for an additional eight cardiac cycles so that nearly all particles were flushed, and hence the

indefinite integral in Eq. (5.3) could be truncated. The velocity data was assumed to be periodic after the sixth computed cardiac cycle to enable integration beyond the available data.

5.2.3 Wall content and thrombus quantification

Thrombus thickness was quantified from the black blood MR images. Segmentations were performed using ITK-Snap [294]. The black blood MR is prone to reduced signal to noise ratio in the region of low blood flow, which could lead to artifacts that were difficult to distinguish from thrombus. Therefore, the MRA for model construction was used to confirm lumen boundary from the black blood MR images. An axial plane of the MRA was chosen that matched as close as possible by visual inspection the axial plane of the black blood MR data. This allowed the lumen to be more readily identified or confirmed, and any intraluminal artifact in the black blood MR data discounted. Fig. 5.1 displays both MRA and black blood MR data at baseline and followup for each patient. Patients 1, 3, 5, 6 and 10 did not have noticeable thrombus at the baseline or followup scan. Patients 4 and 7 did not have significant thrombus during the baseline scan, Patient 8 had minimal thrombus progression from baseline to followup, and Patients 2 and 9 had significant thrombus in both scans with notable progression.

In order to quantify thrombus progression, a reference point on the spine was chosen from the baseline and followup image data. An angle θ was measured from the line connecting the center of the lumen to this reference point (Fig. 5.2). Thrombus thickness was measured as the distance between the lumen and the outer wall as a function of θ in the lumen-centered coordinate frame. Then the change in thrombus thickness was obtained as the difference between thrombus thickness at followup and baseline at the same θ locations. A similar procedure was used to quantify the different hemodynamic parameters described above as a function of θ. For the hemodynamic parameters, values were locally averaged from a 1.4 cm thick annular luminal section, which was nominally centered on the axial slice of the black blood MR scan. Once thrombus thickness and the respective hemodynamic parameters were obtained as a function of θ, the θ variable was eliminated between the two functions to enable the hemodynamic parameters to be plotted against the quantified thrombus growth. A Gaussian filter was used to remove the high frequency changes introduced due to this elimination, which did not affect the overall trend of the results.

5.2.4 Lumen expansion

The MRA scans at baseline and followup were used to quantify the lumen progression. The distance from centerline was computed to quantify the lumen size. The Vascular Modeling Toolkit (VMTK) [4] was used to compute the distance from centerline. Centerlines are created for the aneurysm bulge by fitting the largest inscribed sphere inside the lumen for each location in the superior-inferior direction, and connecting the centers of the spheres.

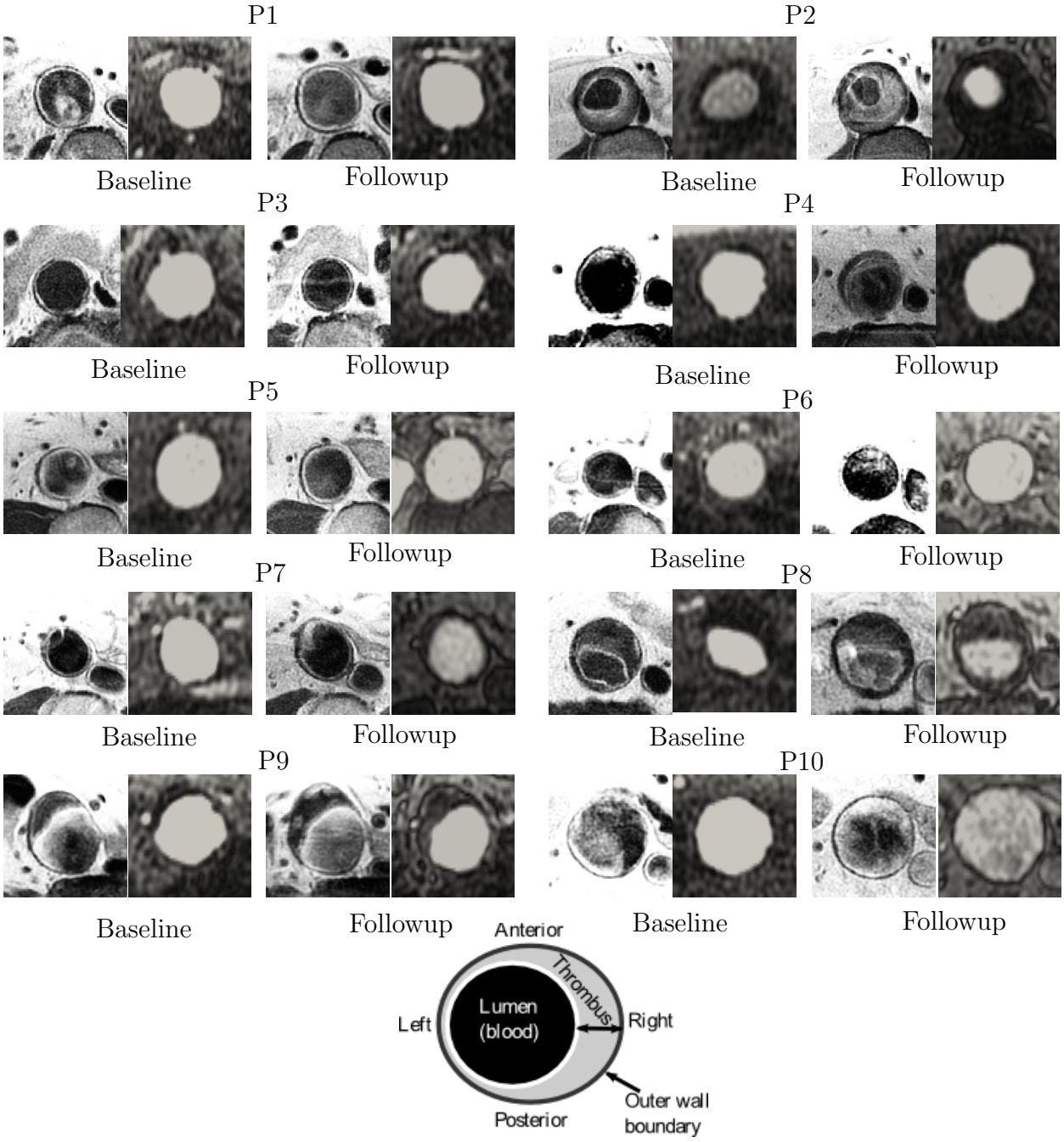

Figure 5.1: Axial view of black (left) and bright (right) blood MR at location of maximum aneurysm diameter for each patient. The black blood MR enables better visualization of soft tissue and thrombus burden, and the bright blood MRA enables better visualization the aortic lumen.

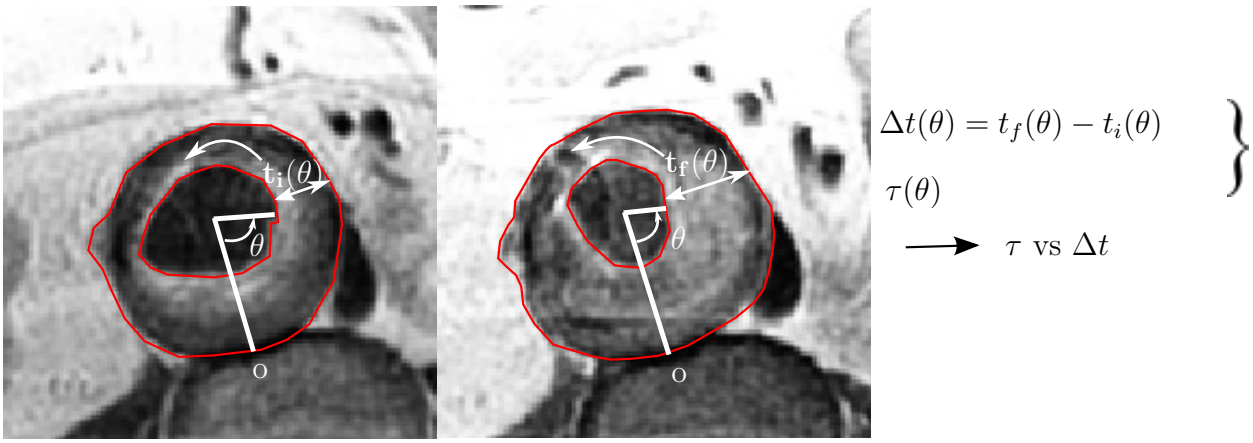

Figure 5.2: The procedure for quantifying thrombus thickness growth Δt as a function of θ. The hemodynamic parameters are also quantified similarly (TAWSS, OSI, MET).

Distance from centerline is calculated for each point on the lumen surface of the aneurysm as the minimum distance to the centerline. Figure 5.3 shows the procedure.

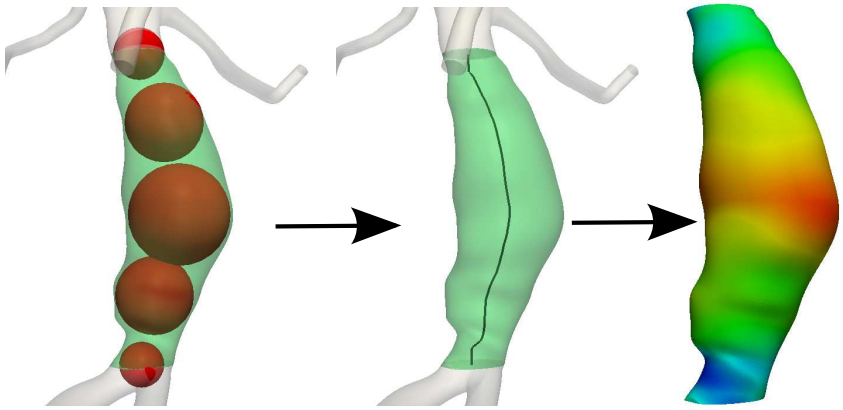

Figure 5.3: The procedure used in calculation of distance from centerline.

5.3 Results

5.3.1 ILT deposition

The fields used to quantify the hemodynamics are shown in Figs. 5.4–5.6. The approximate location of the plane where the planar black blood MR imaging was performed is indicated

by the arrows. Figure 5.4 displays the TAWSS results. The full 3D computer models are displayed in Fig. 5.4, whereas closer views of the aneurysmal segments are provided in Figs. 5.5 and 5.6 . Most of the patients that did not develop thrombus have notable regions of very low (< 1 dynes/cm^2) TAWSS at the aneurysm bulge. Fig. 5.5 displays the OSI fields. Most patients that demonstrated no thrombus deposition had significant regions of higher OSI. The MET results are displayed in Fig. 5.6. While MET was computed for all elements, this figure displays MET for the boundary elements only.

Quantification of thrombus growth versus the hemodynamic parameters, for patients that had thrombus progression from baseline to followup, is plotted in Fig. 5.7. Note, Gaussian filtering preserves boundary information more than the other parts, resulting in less removal of high frequency variations near the ends of each plot. Thrombus growth was mostly observed in regions with TAWSS between 2–3 dynes/cm^2. OSI had a significant negative correlation with thrombus deposition, i.e. there is an increase in thrombus thickness in regions of lower OSI. No obvious correlation was found for MET of the boundary elements. Table 5.3 shows the Pearson's correlation coefficient calculated from the hemodynamic parameters versus change in thrombus thickness. The correlation for TAWSS did not have acceptable p-value due to the negative correlation for one of the patients, and MET had no consistent correlation.

Figure 5.8 displays the distance from centerline during baseline and followup scans. This figure enables the visualization of the aneurysm growth.

Table 5.3: Pearson's correlation coefficient obtained from correlating different hemodynamic parameters with thrombus growth.

Parameter	Patient 2	Patient 4	Patient 7	Patient 8	Patient 9	p-value
OSI	-0.96	-0.98	-0.94	-0.80	-0.72	6.8e-5
TAWSS	0.96	0.99	0.80	0.82	-0.74	0.16
MET	0.20	-0.70	0.91	-0.88	0.30	0.93

5.3.2 Lumen expansion

Figures 5.9– 5.13 compare TAWSS, OSI, MET, particle residence time (see Chapter 4), and finite-time Lyapunov exponent (FTLE) to lumen expansion. Two new Patients are included in these figures (P11 and P12). Patient 2 and Patient 9 demonstrated diminished lumen size, due to thrombus deposition, and therefore were excluded. No definite conclusion can be made, however it can be observed that expansion typically happens in regions of low TAWSS, high OSI, high MET, and low mixing (low FTLE), with some exceptions. Clinically, the expansion of the outer wall of a AAA is of interest. Quantification of AAA expansion using the lumen is a serious limitation, if thrombus deposition occurs. The MRI data used in this study did not enable identification of the outer wall.

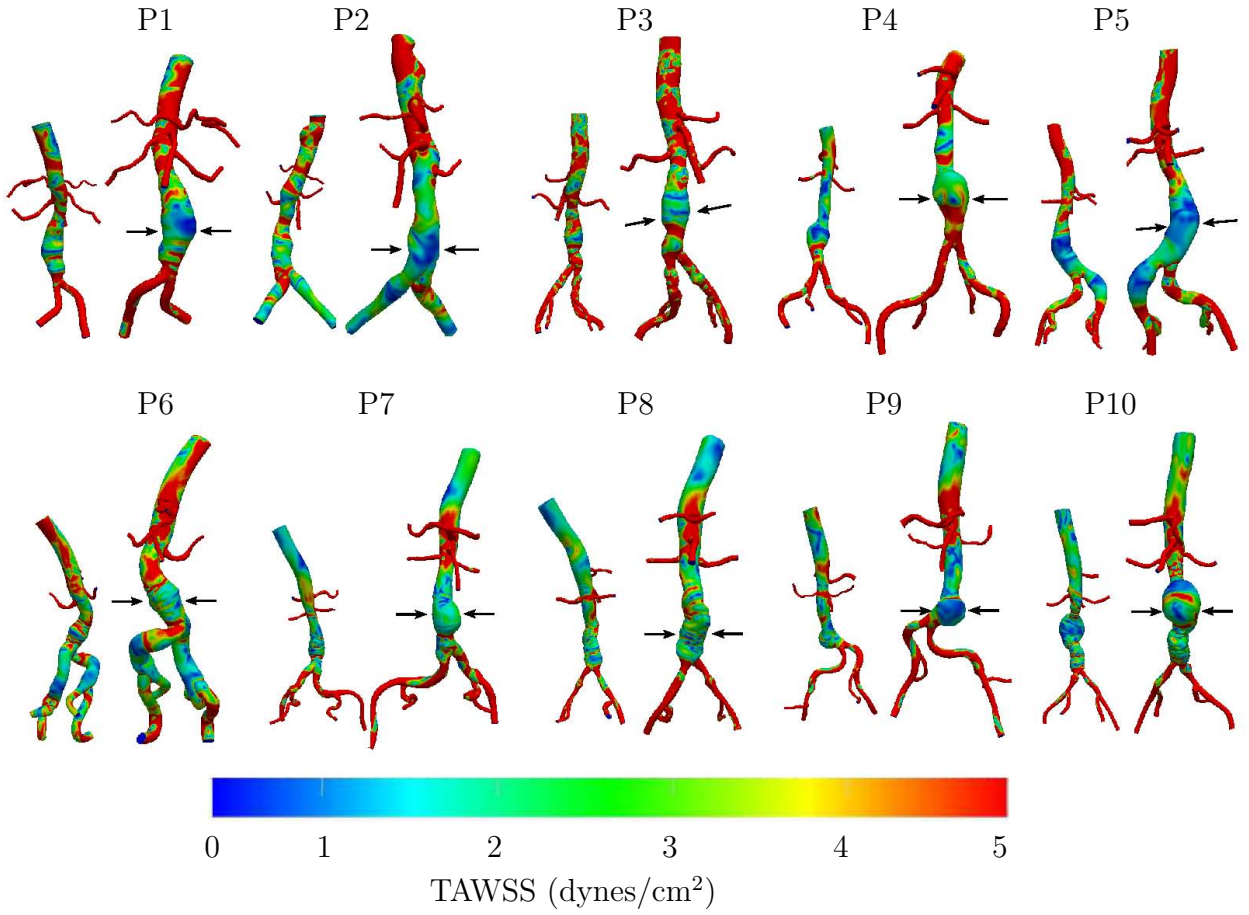

Figure 5.4: Time averaged wall shear stress (TAWSS) for the ten patients. The anterior (right) and posterior (left) views are shown. The arrows in the anterior view indicate the approximate plane where the black blood MR image data was acquired.

5.4 Discussion

Thrombosis is a highly complex process involving various biochemical, biomechanical and biophysical factors. This study investigated hemodynamic features in small AAA to explore possible relations to the development of intraluminal thrombus and lumen expansion. Our finding was that OSI appeared to be a significant factor influencing thrombus deposition among the factors studied. Thrombus deposition occurred in regions where OSI was low compared to the surrounding, and generally patients who had noticeable regions of relatively high OSI did not have thrombus deposition. These regions of high OSI often, but not always, coincided with regions of low TAWSS (<1 dynes/cm^2). While OSI is normalized to have value ranging from 0 to 0.5, values of TAWSS are more ambiguous. The range chosen for

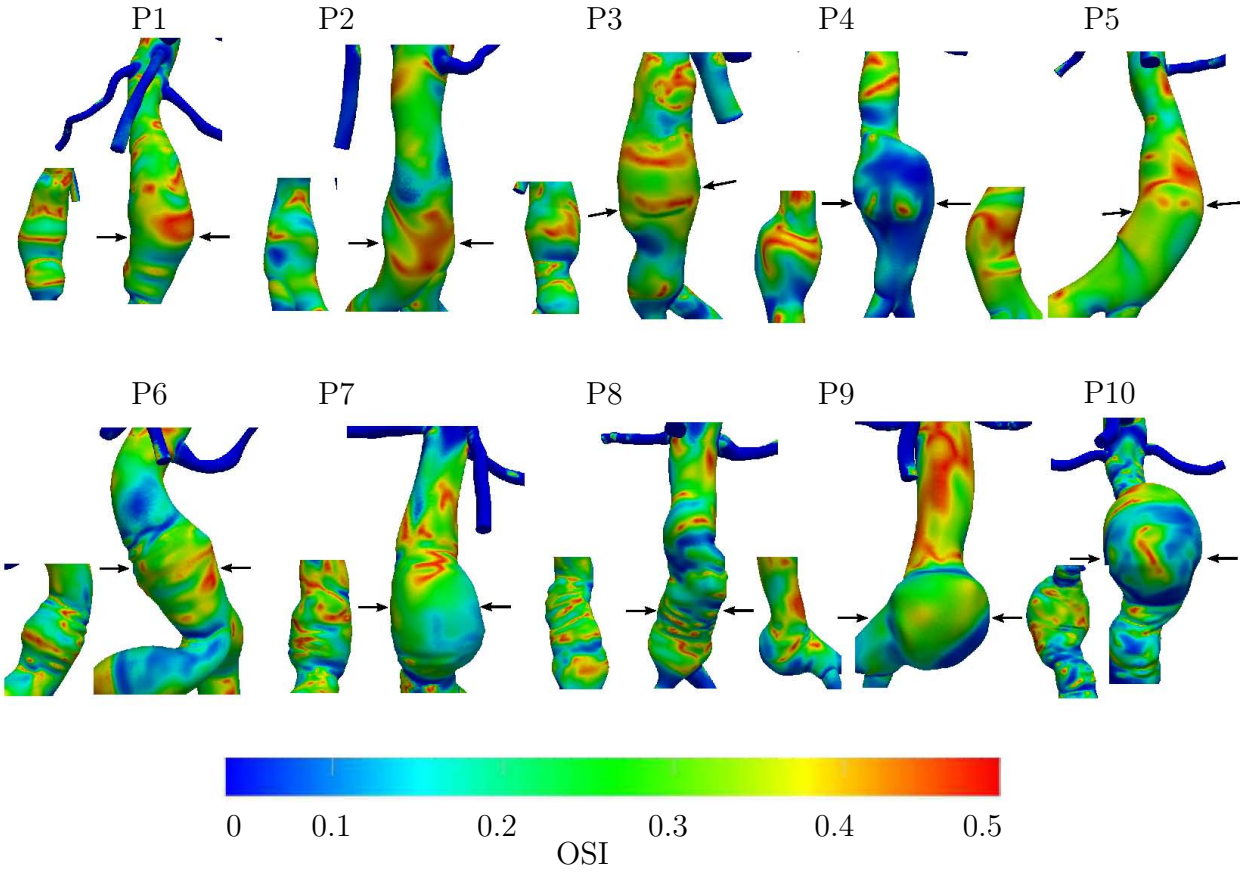

Figure 5.5: Oscillatory shear index (OSI) for the ten patients. The anterior (right) and posterior (left) views are shown. The arrows in the anterior view indicate the approximate plane where the black blood MR image data was acquired.

TAWSS here was set to 5 dynes/cm^2 to better stratify values. This enabled us to distinguish between regions of relatively low TAWSS (2–3 dynes/cm^2) where deposition occurred, and regions of lowest TAWSS (<1 dynes/cm^2) where thrombus progression was mostly absent, perhaps due to higher OSI in such regions.

Thrombosis is governed by proteins originating locally at the wall and from platelets and proteins originating upstream. Our near-wall MET computation was geared toward measuring how long particles (platelets) *entering the aneurysm from upstream* were trapped near the wall (lumen surface). This was based on the hypothesis that thrombus in AAA is due (at least in part) to upstream platelets entering the aneurysm, becoming mechanically activated, and subsequently becoming trapped in regions of high stagnation [27]. However, our MET results do not support this hypothesis. This is further confirmed by our study where the levels of mechanical platelet activation in AAAs were shown to be insignificant

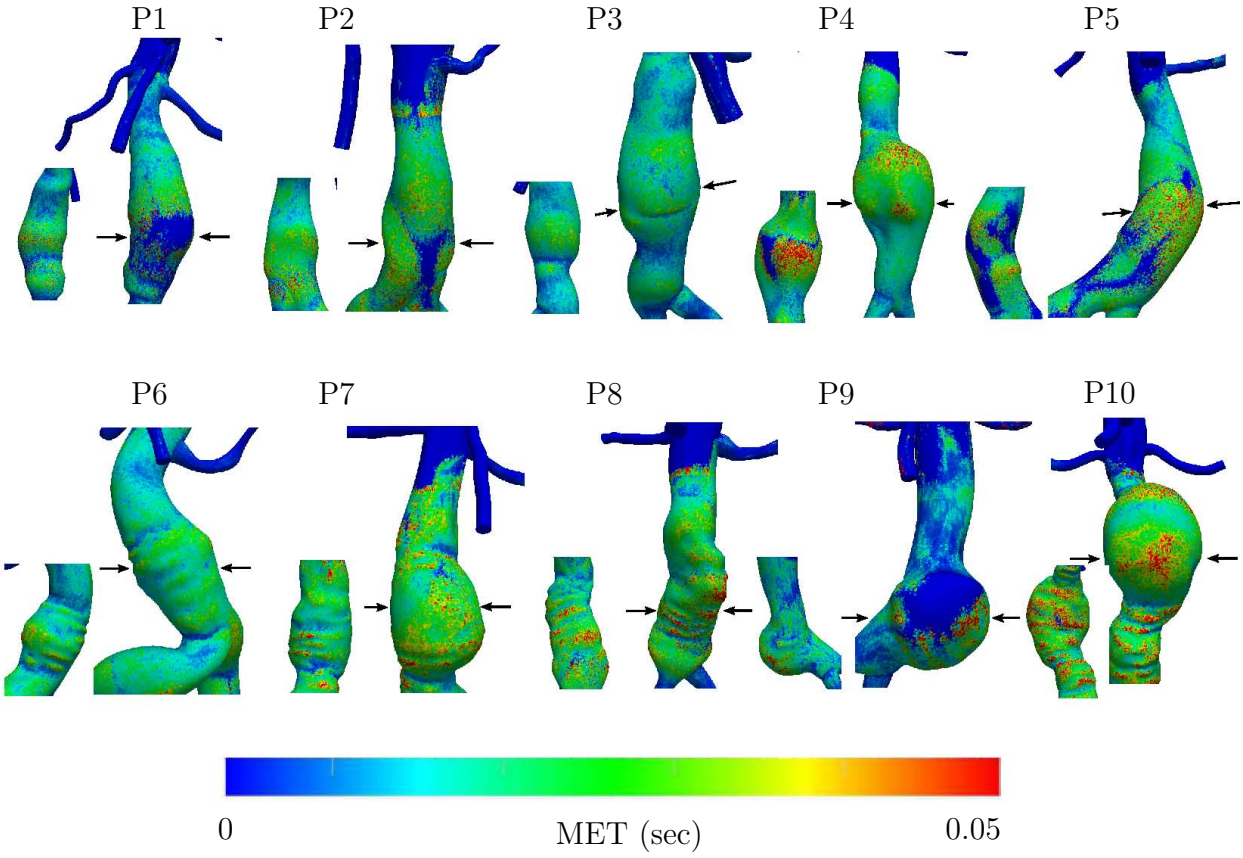

Figure 5.6: Mean exposure time (MET) for the ten patients for the elements on the boundary. The anterior (right) and posterior (left) views are shown. The arrows in the anterior view indicate the approximate plane where the black blood MR image data was acquired.

for mechanically induced platelet activation [108]. Alternatively, biochemical activation may be more important, as well as the transport of chemicals and proteins from the wall. These species depend strongly on local concentrations and reaction rates and care must be taken in how such species are introduced into the model. Therefore, considerations of stagnation, such as measured using MET, are likely most relevant in conjunction with models coupling biochemical reaction with transport.

The conclusion that OSI was negatively correlated with thrombus deposition may be considered contrary to prevailing theory. High OSI, which indicates flow with no preferred direction, is commonly thought to be an adverse hemodynamic condition likely playing a role in atherosclerosis [258]. While flow through a healthy aorta (during systole) may be generally considered attached and unidirectional, flow in AAA is generally separated [214, 233, 151, 246, 10]. Under such conditions, low OSI typically correspond to regions of persistent reverse

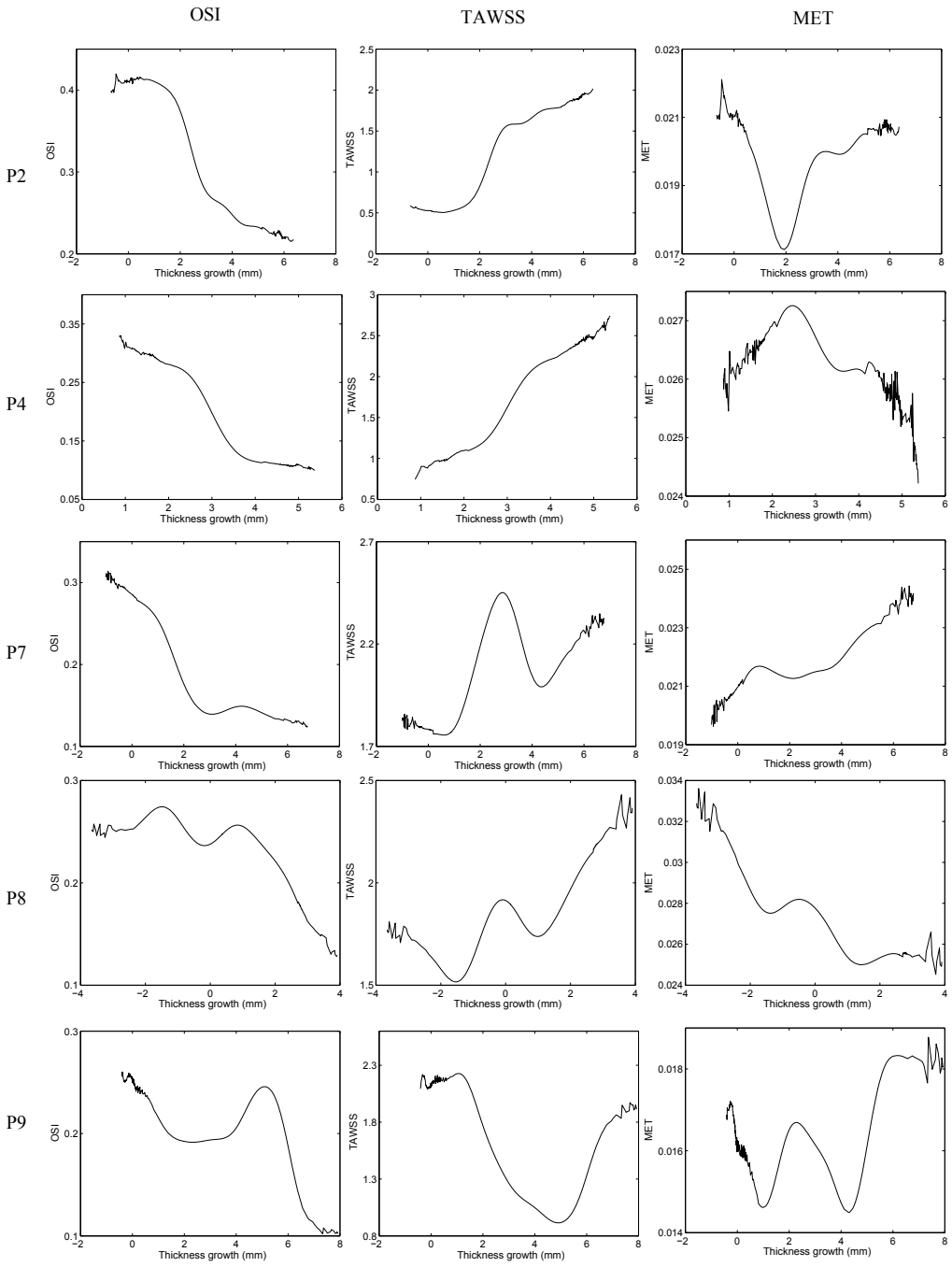

Figure 5.7: Quantification of OSI, TAWSS (dynes/cm^2), and MET (sec) vs thrombus thickness growth (mm) for the patients that had thrombus deposition between baseline to followup. Note that the abscissa (change in thickness) changes between patients.

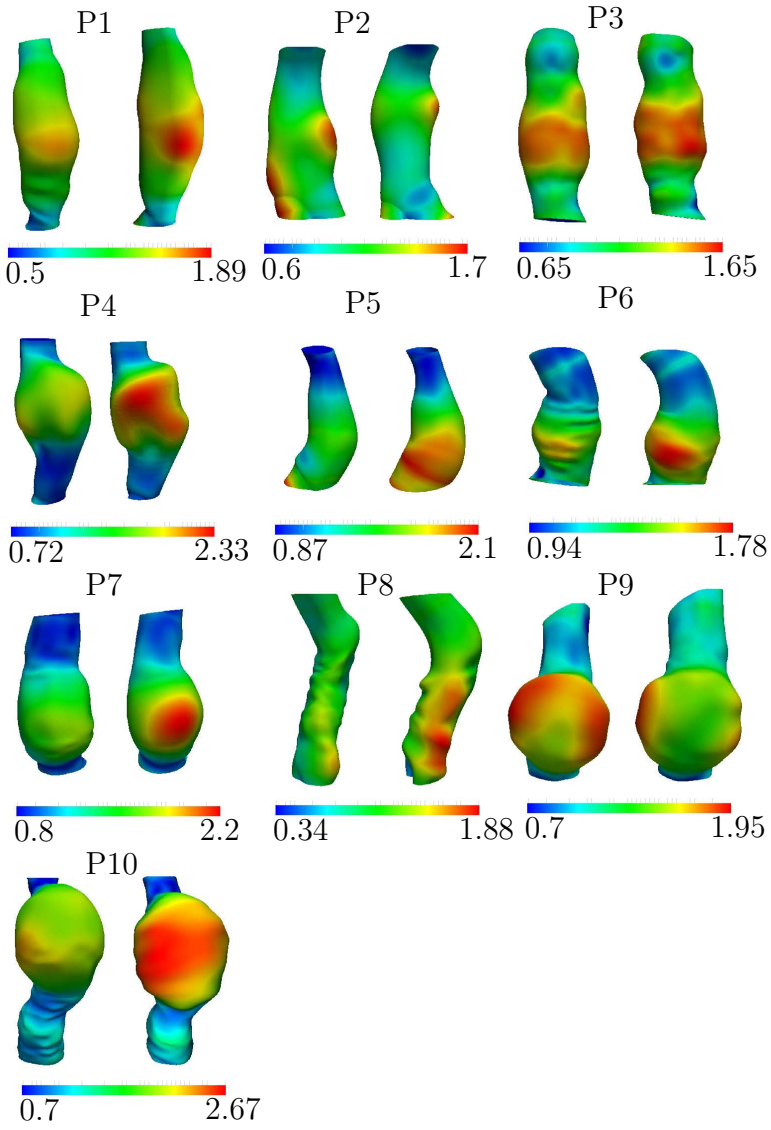

Figure 5.8: Distance (cm) between centerline and lumen surface at baseline scan (left) and followup scan (right) for each patient.

or recirculating flow, which may be prothrombotic. Figure 5.14 shows an example where low OSI corresponds to a recirculating region, which induces a persistent unidirectional *backward* WSS vector. The backward WSS can be due to a persistence recirculation region or a coherent vortex interacting with the vessel wall.

In prior comparisons of wall shear with thrombosis, Turitto and Baumgartner [267] observed an increase in platelet adhesion and thrombus formation with wall shear rate in vitro. Badimon *et al.* [15] studied the exposure of collagen, as well as deendothelialized aorta, to different wall shear rates. In both applications, an increase in wall shear rate caused an

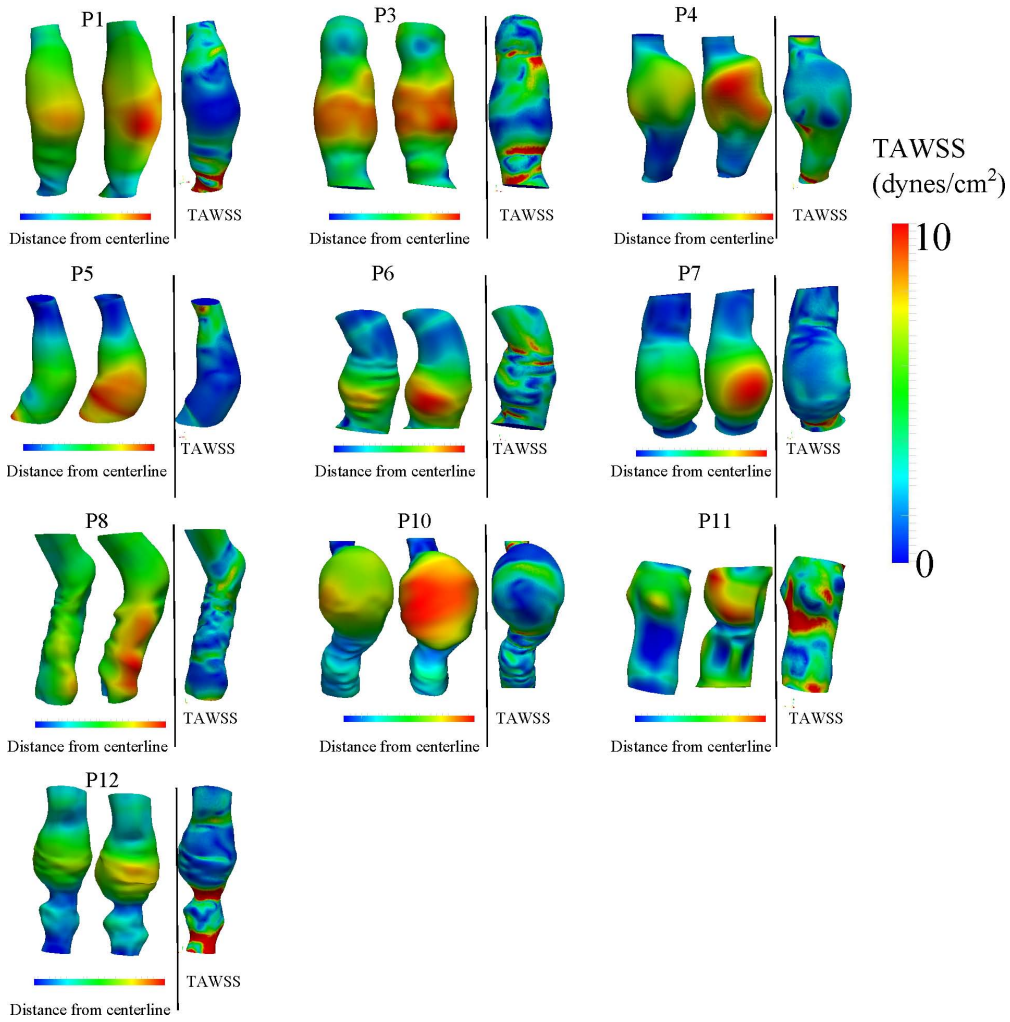

Figure 5.9: Comparison of lumen progression quantified by distance from centerline and time-average WSS (TAWSS). The left panel shows distance from centerline during baseline and followup, from left to right.

increase in platelet deposition. In the deendothelialized vessel, platelet deposition increased initially with an increase in exposure time but remained relatively unchanged for longer exposure times. The vessel wall conditions in their study represent an injured vessel wall, which may be considered relevant to AAA. These studies support the positive correlation of wall shear stress and thrombus formation found herein, although this finding was only modestly significant ($p = 0.16$). This correlation is potentially due to the higher rate of delivery of platelets at locations of (relatively) higher wall shear. This mechanism can promote thrombus formation through an increase in adhesion and aggregation of platelets flowing on the injured wall [2]. These platelets are likely chemically activated upon interaction with

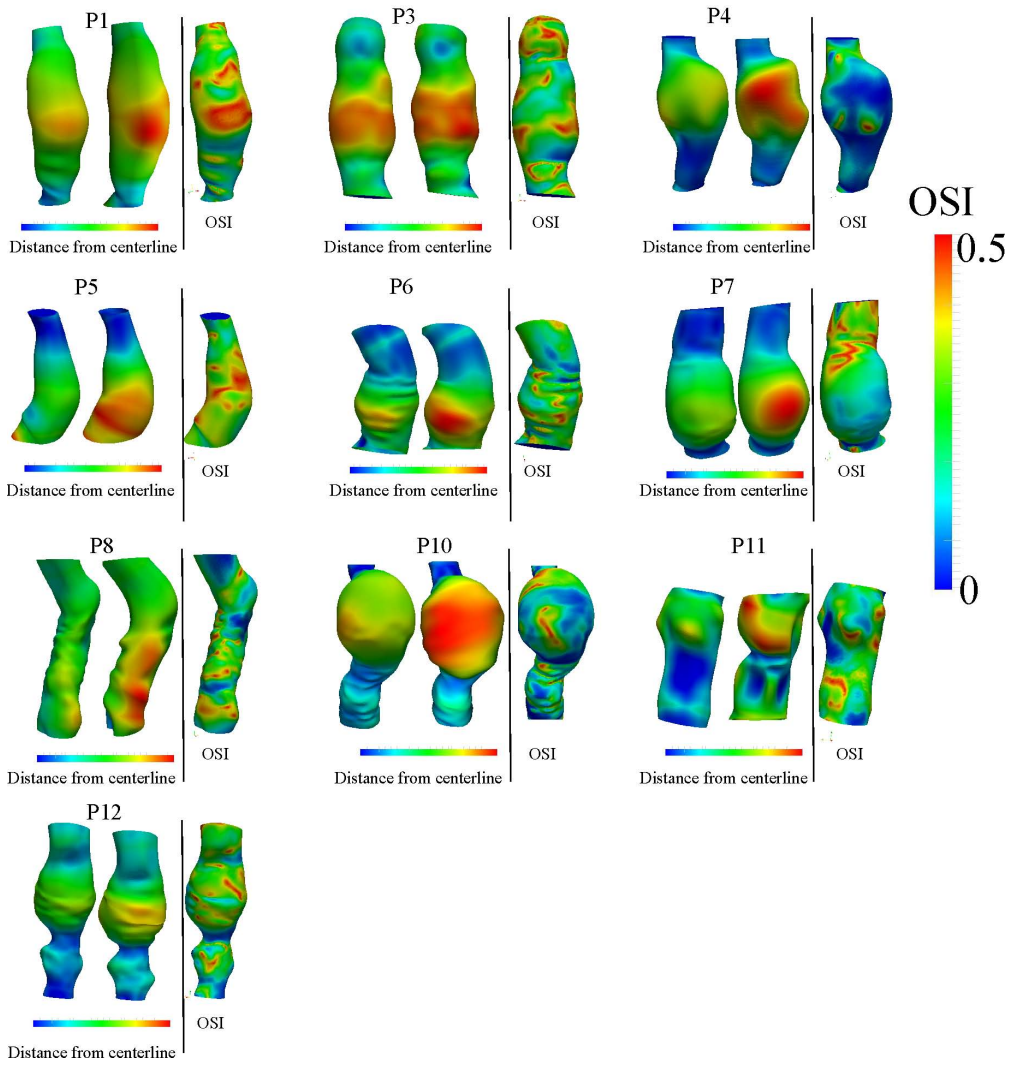

Figure 5.10: Comparison of lumen progression quantified by distance from centerline and oscillatory shear index (OSI). The left panel shows distance from centerline during baseline and followup, from left to right.

the injured vessel wall. As will be argued in Chapter 8, the near-wall concentration of biochemicals originating from the core flow (such as platelets) is higher in regions of high WSS. It should be noted that shear stress levels throughout AAA are generally lower than in the healthy abdominal aorta. Hence, it is the relative difference in shear rather than absolute values that are of relevance here. We note that temporal and spatial gradients of WSS could potentially be correlated with thrombus deposition. However, we have observed that these measures have high positive correlation with WSS magnitude (see Chapter 6), which prevents useful independent information from these measures.

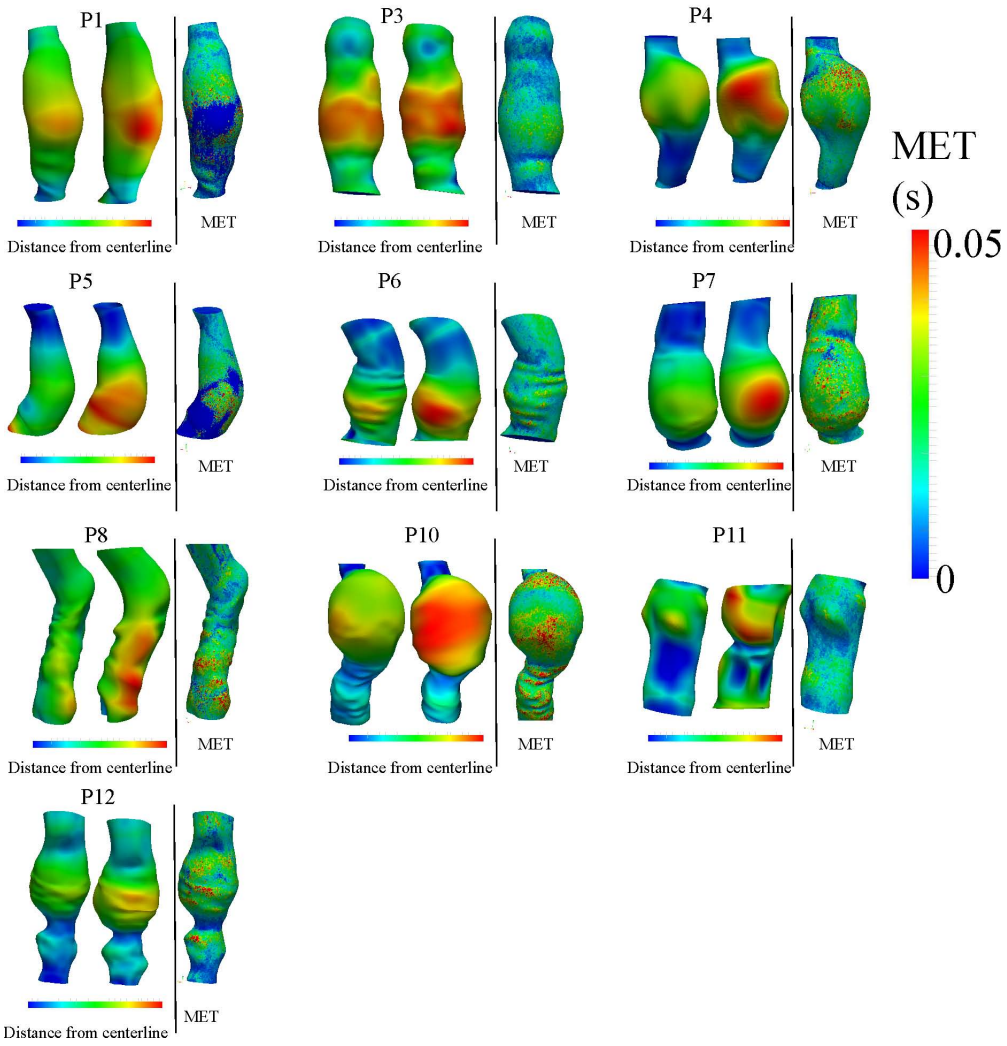

Figure 5.11: Comparison of lumen progression quantified by distance from centerline and mean exposure time (MET). The left panel shows distance from centerline during baseline and followup, from left to right.

Prior investigations have shown flow reversal at the wall may increase monocyte adhesion [67], and flow recirculation is positively correlated with thrombosis biomarkers [168]. Consistently, we observed that persistent regions of recirculation contribute to low OSI and enhanced thrombus deposition. In a recent computational study of AAA [188], OSI was found to be negatively correlated to thrombus deposition. We also note that the theory linking low, and oscillatory, WSS with atherosclerosis has recently been challenged [198], with the authors pointing out that such correlations have not been found in studies performing point-wise comparisons.

Previous studies have investigated thrombus deposition in intracranial aneurysms. Re-

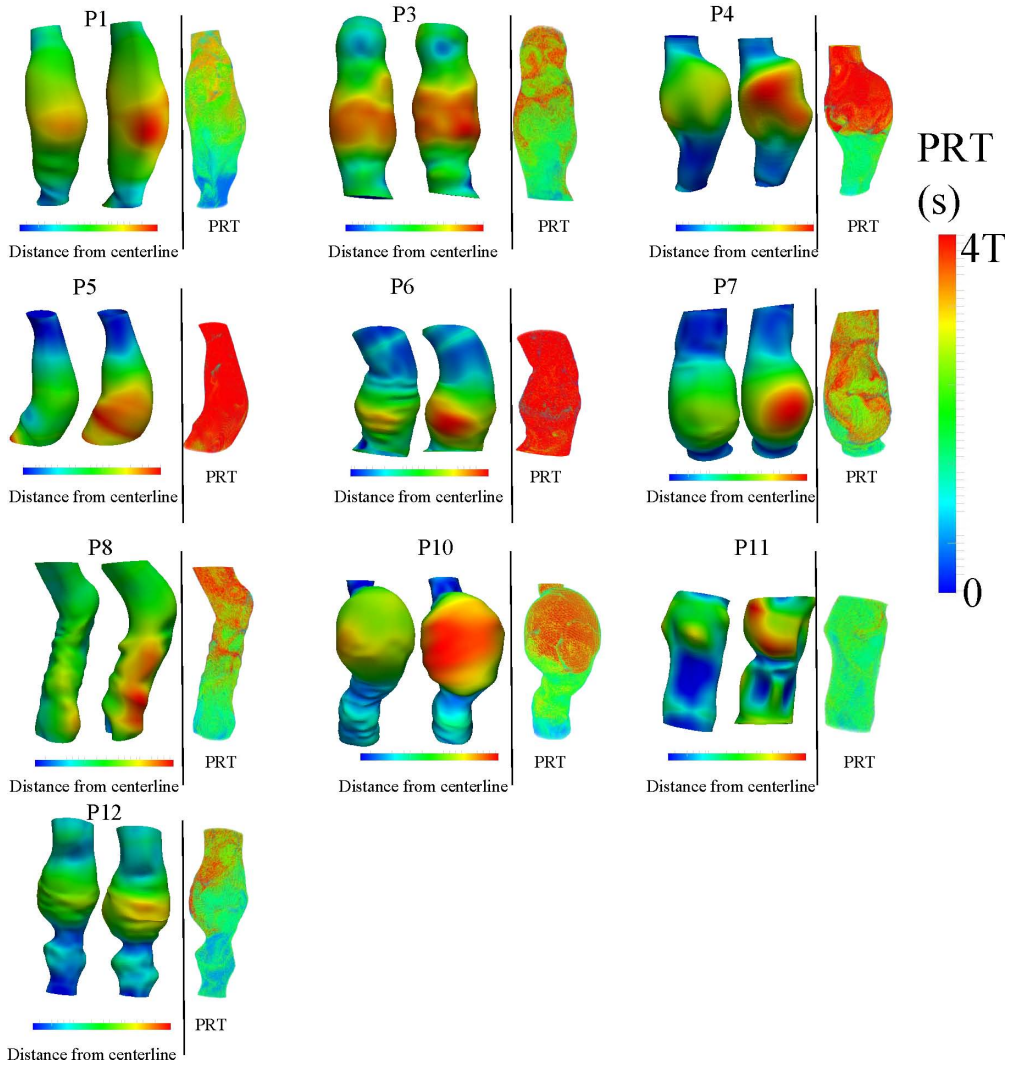

Figure 5.12: Comparison of lumen progression quantified by distance from centerline and particle residence time (PRT). The left panel shows distance from centerline during baseline and followup, from left to right. T is the cardiac cycle of each patient.

gions of slowly recirculating flow, and therefore low mixing have been shown to be related to thrombus deposition [211]. Low WSS and high stagnation have also been shown to be correlated with thrombus deposition in intracranial aneurysms with a better correlation when both WSS and stasis are considered together [210].

Identification of prothrombotic hemodynamic conditions is desirable since thrombus growth rate may be a predictor of rupture [244]. This study supports the possibility that thrombus deposition could be potentially predicted with a patient specific framework. However, due to the complexities involved in thrombosis, the identification of a single hemody-

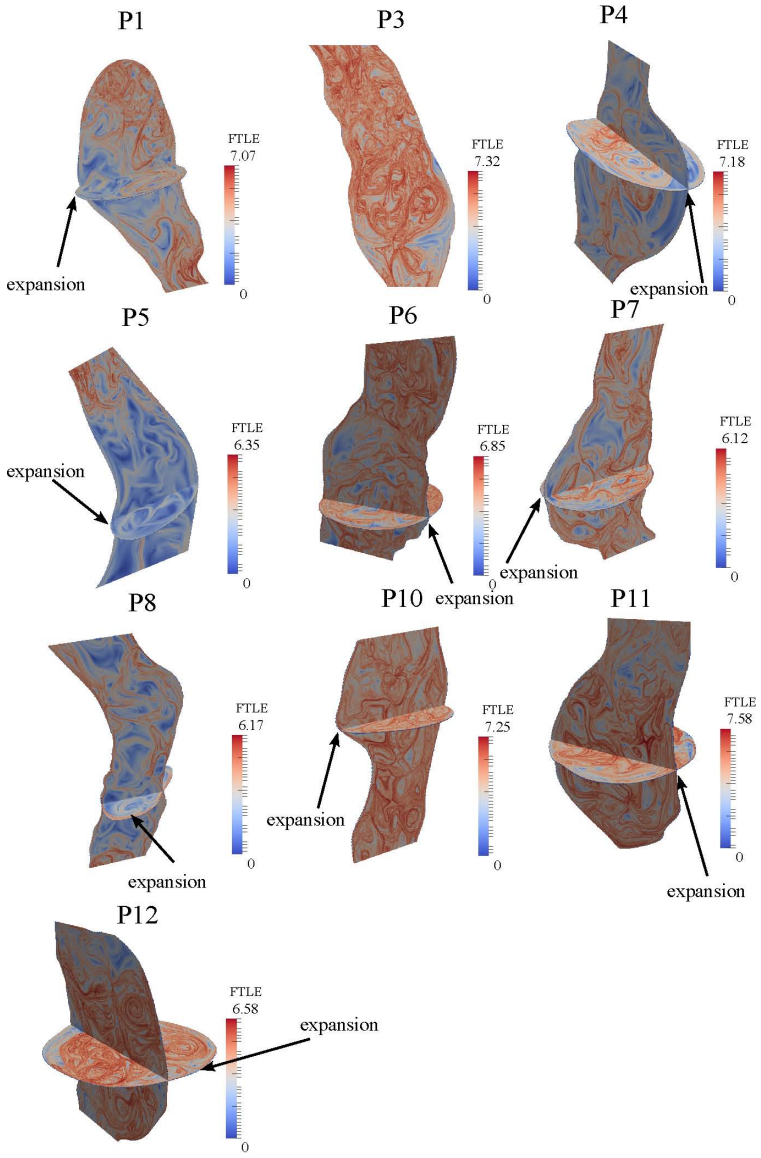

Figure 5.13: The finite-time Lyapunov exponent (FTLE) field. The location of lumen expansion is indicated with an arrow.

namic surrogate to predict thrombus accumulation is tenuous. Previous studies [27] have mentioned that low WSS cannot be the only hemodynamic parameter related to thrombus deposition due to the lower WSS observed in saccular aneurysms, which are more frequently thrombus free. Our investigations have shown that the regions of very low TAWSS (<1 dynes/cm^2) are generally accompanied by high OSI and do not favor thrombus deposition.

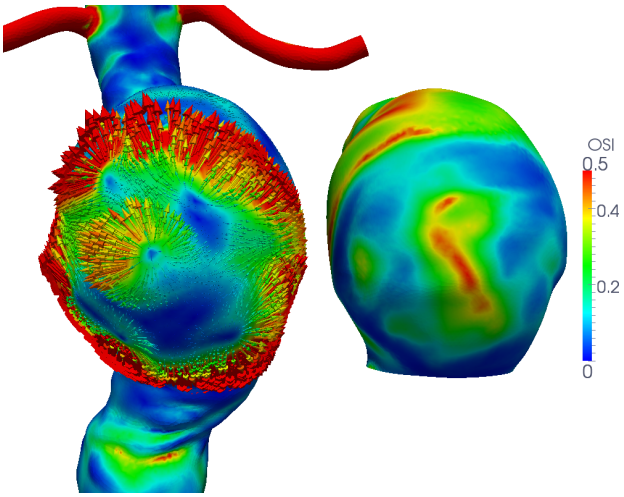

Figure 5.14: Persistence regions of backward WSS lead to low OSI. The left panel is the WSS vector and the right panel is the OSI.

5.4.1 Limitations

The main modeling assumptions used in this work were that macroscopic blood flow dynamics could be effectively recovered using a Newtonian fluid model and a no slip (zero velocity) condition on the lumen. Employing more sophisticated models for the blood rheology, or wall mechanics, is in theory possible, but without proper patient-specific data such models may not provide more accurate modeling of in vivo blood flow conditions [242]. Nevertheless, the flow field inside complex vascular geometries such as AAA is generally dominated by the local lumen morphology and inflow/outflow boundary conditions, with blood rheology and fluid-structure interactions having a relatively smaller effect on macroscopic flow conditions [242]. Changes in AAA hemodynamics between a Newtonian and a non-Newtonian model have been investigated [28], but differences in WSS did not appear compelling. Difference in hemodynamics due to wall motion have also been investigated [80] and found to be negligible when radial strains were less than $\approx$8%. Radial strains were observed to be $<$5% from the PCMRI data for the AAAs considered.

The presence of ILT in computational modeling of AAA wall has been shown to be an important factor altering wall stress distributions [276, 164]. From the fluid mechanics point of view, the presence of ILT can alter the flow field in different ways. ILT alters lumen morphology. This is expected to be the most significant effect and has been accounted for in this study. ILT can also alter the mechanical properties of fluid structure interaction, however such interactions were not considered for reasons stated above. The porous nature of ILT may question the no-slip (no-penetration) boundary condition used on the wall. Recent investigations have shown that this effect depends on the amount of compactness of ILT structure [207].

Our measurement of thrombus growth was limited by challenges that arose from co-

registration of baseline and followup image data. The lumen-centered coordinate choice used herein for quantifying thrombus thickness and hemodynamics data on the mid-aneurysm plane is not expected to provide precise registration, and there is uncertainty in axial slice location between the three scans used in our analysis (i.e. the hemodynamics data based on baseline MRA image coordinates, thrombus thicknesses based on baseline black blood MR coordinates, and thrombus thickness based on followup black blood MR coordinates). The induced errors are difficult to quantify. The former problem manifests in, among other things, potentially different θ's between baseline thickness, baseline hemodynamic parameter and followup thickness. To help reduce these errors a Gaussian filter was applied once θ was eliminated. However, the unfiltered data still produced Pearson correlations consistently negative for OSI (between -0.6 to -0.8 for most patients), and maintained statistical significance. To help alleviate potential differences in axial plane locations, we performed averaging of the hemodynamics data over a thin annular band, and confirmed that our results were insensitive to the chosen thickness (1.4 cm). Moreover, an inter-observer study was performed on two of the patients (4 and 8) to examine the sensitivity of the calculated correlation coefficients due to variability of segmentations between blinded operators. This comparison yielded all correlation coefficients changing less than 3%. In this study the full three-dimensional progression of thrombus was not known, and the approach presented here could benefit by being extended to multiple slices in studies where such data is available. Moreover, the small number of patients that developed thrombus in this study is another limitation, and a larger number of patients would be desirable for more definite conclusions.

Chapter 6

Vectorial characterization of WSS patterns in aneurysms

6.1 Introduction

Wall shear stress (WSS) is one of the most extensively studied parameters used to correlate hemodynamics to various aspects of cardiovascular disease. It affects the near-wall transport of chemicals and proteins, and regulates the mechanobiology of endothelial cell (EC) function [19, 161, 59]. In the large arteries, WSS can vary considerably in space and time at any particular location. This is especially true in diseased arteries that harbor complex flow conditions. Moreover, WSS is a vector, whose direction and magnitude are important in biomechanical processes. Each of these aspects is difficult to confront, and combined make quantification and interpretation of WSS onerous. This has resulted in development of various WSS parameters that each try to quantify different characteristics [6, 94].

Various WSS parameters have been linked with cardiovascular complications. Differences in WSS magnitude can trigger different EC alignment patterns [189]. Low and high WSS magnitude have each been linked to a different pathway for cerebral aneurysm progression [173, 278]. Oscillatory shear index (OSI) has been correlated with plaque formation [135, 133]. High spatial WSS gradients increase wall permeability [41], and initiate intracranial aneurysm formation [77]. WSS angle gradient has been associated with monocyte deposition [40]. EC proliferation has been shown to depend on temporal WSS gradients [280], and the sign of WSS spatial gradient [78]. Peak temporal WSS gradient has been proposed as an indicator of atherosclerosis [268], and has been correlated to EC proliferation [38]. Oscillation in WSS spatial gradient (gradient oscillatory number) has been correlated with cerebral aneurysm formation [236, 52]. More recently the multi-directionality of WSS has gained attention in WSS characterizations. Directional OSI has been proposed as a parameter that affects EC response [49, 50], transverse WSS (transWSS) has been proposed as a predictor of atherosclerosis [197, 178], and axial/secondary WSS have been proposed for quantifying multi-directionality of WSS [181]. Most of these WSS parameters have been used

extensively as indicators of disturbed flow. However, the relationship among these parameters has received less attention. Toward this goal, Lee *et al.* [144] performed a correlation study among different WSS parameters providing data on the dependency among some of these parameters for flow in the carotid arteries.

Despite the numerous WSS parameters that have been used, a number of issues have not received much attention, including the computation of WSS on a non-Euclidean surface, accounting for the vectorial nature of WSS, and obtaining proper references for measuring WSS variations. For example, most of the measures that quantify directionality of WSS rely on the time average WSS direction as the reference direction. This is motivated by the tendency of ECs to align in the time average direction, at least in simple flows. How ECs align in more complex flows is not well known. Complex flow is identified by measuring WSS variation from the time-averaged direction, but this reference vector itself is biased by the complexity of the flow, and moreover can have complex spatial variation. Alternatively, most studies rely on measures based on WSS magnitude, and the relation between the vectorial behavior of WSS and its magnitude or angle has received little attention. Likewise, WSS as a vector conveys information about near wall flow transport [96, 97, 83, 109], which is often not considered in WSS characterizations. This is particularly important in aneurysmal flows where transport of biochemicals/platelets to and from the wall are of great importance and could be potentially regulated by complex WSS behaviors. Even from the perspective of EC, the WSS has further influence than mechanical forcing. Near wall transport affects EC response to flow via an indirect mechanism [19]. This is manifested in transport of nitric oxide (NO), low density lipoproteins (LDL), monocytes, and adenine nucleotides ATP and ADP. The transport of these chemicals near the wall significantly affects ECs and atherosclerosis [66, 125].

The goal of the present study is to provide more comprehensive comparison of WSS magnitude, angle and vector changes in space and time in complex arterial flow. For this purpose, flow in abdominal aortic aneurysms (AAA) was chosen due to its complex temporal and spatial flow features [10, 9]. A framework is proposed to remove the dependency on the time average direction, as well as to compute WSS measures intrinsically on the local tangent plane. We propose new metrics to quantify different aspects of WSS behavior. Relative WSS gradients are proposed, which are less biased by WSS magnitude than prior measures. The correlation among all the parameters is investigated, and a measure is proposed to unify both temporal and spatial changes of WSS direction and magnitude into a single parameter.

6.2 WSS characterization

The total stress tensor is defined as

$$\boldsymbol{\sigma} = -pI + 2\mu\mathbf{S} = -pI + \mu(\nabla\mathbf{v} + (\nabla\mathbf{v})^T) \,, \tag{6.1}$$

where p is the pressure, $\mathbf{S}$ is the strain rate tensor, and $\mathbf{v}$ is the fluid velocity. The traction at the wall can be computed as $\mathbf{t} = \boldsymbol{\sigma} \cdot \mathbf{e}_n$ where the stress tensor $\boldsymbol{\sigma}$ and the unit normal vector

$\mathbf{e}_n$ are evaluated on the wall. The wall shear stress vector is then defined as the tangential component of traction on the wall

$$\boldsymbol{\tau} = \mathbf{t} - (\mathbf{t} \cdot \mathbf{e}_n)\mathbf{e}_n \ . \tag{6.2}$$

WSS lies on the local tangent plane at each point on the wall surface. In an intrinsic orthonormal frame, one can compute the normal vector $\mathbf{e}_n$ at each point, and choose an arbitrary unit tangent vector $\mathbf{e}_t$. Consequently, by computing the unit binormal vector $\mathbf{e}_b = \mathbf{e}_t \times \mathbf{e}_n$, an intrinsic coordinate frame $(\mathbf{e}_t, \mathbf{e}_b, \mathbf{e}_n)$ is constructed that varies along the surface. While the magnitude of WSS is independent of the choice of coordinate system, it is important to use an intrinsic frame in characterization of vectorial behavior of WSS. We propose to define $\mathbf{e}_t$ at each point as the tangent direction that is mostly aligned with the centerline path, parameterized by $\mathbf{c}(s)$. Namely,

$$\mathbf{e}_t = \frac{\mathbf{c}' - (\mathbf{c}' \cdot \mathbf{e}_n)\mathbf{e}_n}{\|\mathbf{c}' - (\mathbf{c}' \cdot \mathbf{e}_n)\mathbf{e}_n\|} \ , \tag{6.3}$$

where $\mathbf{c}' = d\mathbf{c}/ds$ is the centerline tangent in the proximal to distal direction, evaluated at the closest point on the centerline. Often disturbed flow is characterized by variations in WSS from the time-averaged vector. However, the TAWSS vector is itself dependent on disturbed flow conditions, and might not be a well defined direction in complex transitional flows. The motivation for the above definition is that $\mathbf{e}_t$ is independent of disturbed flow features, and it is (nominally) in the preferred direction of bulk flow. Figure 6.1 shows the resulting tangent and binormal vectors for a representative application to an aneurysm. The WSS vector can be decomposed as

$$\boldsymbol{\tau} = \tau_t \mathbf{e}_t + \tau_b \mathbf{e}_b \ , \tag{6.4}$$

where $\tau_t = \boldsymbol{\tau} \cdot \mathbf{e}_t$, and $\tau_b = \boldsymbol{\tau} \cdot \mathbf{e}_b$ are the components of the WSS vector in tangent and binormal directions, respectively. In this paper, the WSS angle, θ, is defined as the angle between the WSS vector and the tangent direction

$$\theta = \arccos \frac{\boldsymbol{\tau} \cdot \mathbf{e}_t}{\|\boldsymbol{\tau}\|} \ . \tag{6.5}$$

6.2.1 WSS parameters

We begin by defining the standard WSS parameters used in literature. $\|\overline{\boldsymbol{\tau}}\|$ is defined as the magnitude of the time average of wall shear stress vector, where the averaging time is typically one cardiac cycle T assuming the flow is periodic,

$$\|\overline{\boldsymbol{\tau}}\| = \left\| \frac{1}{T} \int_0^T \boldsymbol{\tau} \ \mathrm{d}t \right\| \ . \tag{6.6}$$

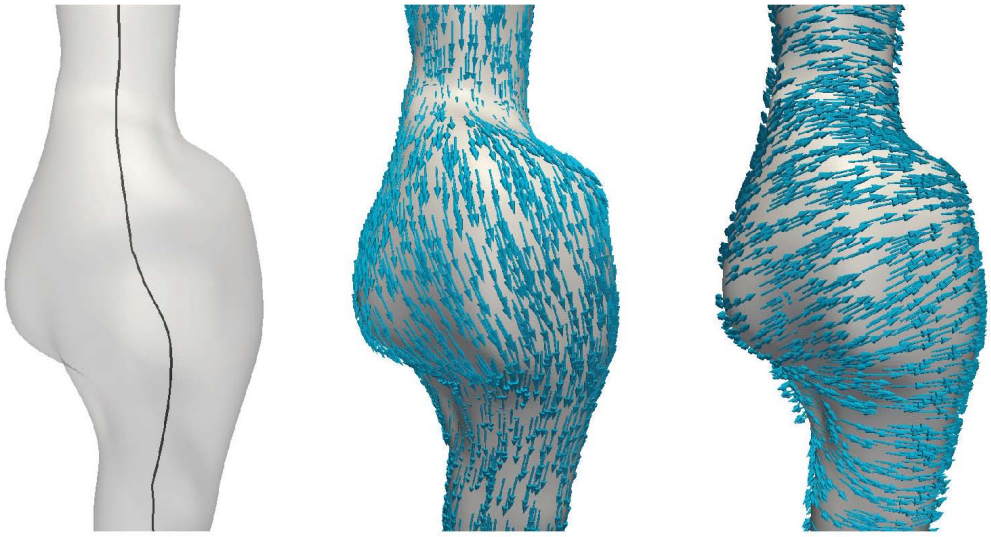

Centerline Tangent ($\mathbf{e}_t$) vectors Binormal ($\mathbf{e}_b$) vectors

Figure 6.1: Unit vector field $\mathbf{e}_t$ is defined as the unit tangent vector that is most aligned with the centerline direction. The binormal vector $\mathbf{e}_b$ is computed as the cross product of this unit tangent vector and the unit normal vector.

The standard time average of wall shear stress (magnitude) is defined as

$$\text{TAWSS} = \frac{1}{T}\int_0^T \|\boldsymbol{\tau}\| \ \mathrm{d}t \ . \tag{6.7}$$

The oscillatory shear index is defined as

$$\text{OSI} = \frac{1}{2}\left(1 - \frac{\|\overline{\boldsymbol{\tau}}\|}{\text{TAWSS}}\right) \ . \tag{6.8}$$

OSI becomes 0 for unidirectional WSS (steady direction) and 0.5 for WSS with no preferred time-averaged direction ($\|\overline{\boldsymbol{\tau}}\| = 0$). The values in between are not easily interpreted. We propose an additional measure to quantify WSS direction changes. Δ_{90} is defined as the number of instances that WSS angle θ changes more than 90^o (or any desired threshold could be used), which can be computed as follows:

$t_0 = 0$, $\Delta_{90} = 0$
for $t = 0$ to T **do**
  if $\max\limits_{t_0<t'<t} |\theta(t) - \theta(t')| > \frac{\pi}{2}$ **then**
    $\Delta_{90} \leftarrow \Delta_{90} + 1$
    $t_0 \leftarrow t$
  end if
end for

This measure inspects consecutive time steps to check when the WSS vector turns 90°, and then resets the reference direction for capturing the next 90° turn. Similar to Morbiducci *et al.* [181], we define $\overline{|\tau_t|}$, and $\overline{|\tau_b|}$ as the integrated amount of WSS in tangent and binormal directions respectively,

$$\begin{aligned} \overline{|\tau_t|} &= \frac{1}{T}\int_0^T |\tau_t| \ \mathrm{d}t \\ \overline{|\tau_b|} &= \frac{1}{T}\int_0^T |\tau_b| \ \mathrm{d}t \ . \end{aligned} \tag{6.9}$$

These measures can quantify the persistent alignment of WSS to the centerline, or perpendicular to centerline, direction, respectively. WSS vector fields can be scaled to obtain a first order approximation of near wall velocity vectors [96]. If sign is taken into account in above equations, then one can distinguish between persistent regions of forward and backward near wall flow, as well as clockwise and counterclockwise near wall flow, providing some insight on near wall transport. Specifically, backward WSS ($\overline{|\tau_{t^-}|}$) could be defined as the amount of near wall backflow

$$\begin{cases} \overline{|\tau_{t^-}|} = \frac{1}{T}\int_0^T |H(t)\tau_t| \ \mathrm{d}t \\ H(t) = \begin{cases} 1 \text{ if } \tau_t < 0 \\ 0 \text{ if } \tau_t \geq 0 \end{cases} \end{cases} . \tag{6.10}$$

This measure could be used in quantification of recirculating flow, which has been shown to promote thrombotic and atherosclerosis expressions [168]. Table 6.1 lists various forms of spatial and temporal gradient that could be defined. The WSS angle and magnitude provide scalar fields that could be used to compute spatial/temporal gradients. The spatial/temporal gradient of the WSS vector can also be computed, which inherently incorporates both direction and magnitude changes. See Sec. 6.3 for details on angle gradient and vector gradient computations. A relative measure of WSS gradient can be defined by dividing the vector gradient by the WSS magnitude. All of the measures defined in Table 6.1 are integrated and divided in time similar to previous parameters.

As will be shown in the Results, the spatial (temporal) WSS vector gradient has very high positive correlation with spatial (temporal) WSS magnitude gradient. This motivated the definition of new measures that can incorporate magnitude and angle changes more equitably. We define a mix spatial gradient as a linear weighting of WSS angle and magnitude gradients, such that the new measure is equally correlated with angle and magnitude gradients as follows

$$\begin{aligned} \nabla_{mix}\boldsymbol{\tau} &= w_s \frac{\|\nabla\theta\|}{\text{mean}\left(\|\nabla\theta\|\right)} + (1-w_s)\,\frac{\|\nabla\,\|\boldsymbol{\tau}\|\|}{\text{mean}\left(\|\nabla\,\|\boldsymbol{\tau}\|\|\right)} \\ w_s :\ & corr\left(\nabla_{mix}\boldsymbol{\tau}, \|\nabla\theta\|\right) = corr\left(\nabla_{mix}\boldsymbol{\tau}, \|\nabla\,\|\boldsymbol{\tau}\|\|\right) \ , \end{aligned} \tag{6.11}$$

where the mean operator computes the spatial average of the parameter in the region of interest. The normalization by the mean provides a dimensionless parameter with mean

Table 6.1: Scalar measures quantifying spatial and temporal changes of WSS derived from WSS angle, magnitude and vector. Relative measures are defined by dividing the variation by WSS magnitude. All of the measures would be averaged temporally. Prime denotes temporal gradient ($' = d/dt$). For $\|\nabla \boldsymbol{\tau}\|$ the induced L_2 (spectral) norm was used.

	Space	Time
Angle	$\|\nabla \theta\|$	θ'
Magnitude	$\|\nabla \|\boldsymbol{\tau}\|\|$	$\|\boldsymbol{\tau}\|'$
Vector	$\|\nabla \boldsymbol{\tau}\|$	$\|\boldsymbol{\tau}'\|$
Relative	$\frac{\|\nabla \boldsymbol{\tau}\|}{\|\boldsymbol{\tau}\|}$	$\frac{\|\boldsymbol{\tau}'\|}{\|\boldsymbol{\tau}\|}$

value equal to one. The weighting coefficient w_s is chosen to provide equal correlation coefficients. A similar approach could be taken for WSS temporal gradient to define a mix temporal gradient,

$$\begin{aligned} \boldsymbol{\tau}'_{mix} &= w_t \frac{\theta'}{\text{mean}\,(\theta')} + (1 - w_t)\, \frac{\|\boldsymbol{\tau}\|'}{\text{mean}\left(\|\boldsymbol{\tau}\|'\right)} \\ w_t &: \; corr\,(\boldsymbol{\tau}'_{mix}, \theta') = corr\left(\boldsymbol{\tau}'_{mix}, \|\boldsymbol{\tau}\|'\right) \;, \end{aligned} \tag{6.12}$$

where the weighting coefficient w_t provides equal correlation between the new measure and magnitude/angle temporal gradients. The spatial and temporal mix gradients could be combined to define a new measure $\boldsymbol{\tau}_{mix}$ that incorporates spatial and temporal changes of magnitude and angle of WSS as follows

$$\begin{aligned} \boldsymbol{\tau}_{mix} &= w_{st} \nabla_{mix} \boldsymbol{\tau} + (1 - w_{st})\, \boldsymbol{\tau}'_{mix} \\ w_{st} &: \; corr\,(\boldsymbol{\tau}_{mix}, \nabla_{mix} \boldsymbol{\tau}) = corr\,(\boldsymbol{\tau}_{mix}, \boldsymbol{\tau}'_{mix}) \;, \end{aligned} \tag{6.13}$$

where the weighting coefficient w_{st} results equal correlation of $\boldsymbol{\tau}_{mix}$ with spatial and temporal mix gradient.

6.3 WSS gradient calculations

6.3.1 Angle gradients

When computing the difference between two angles, one must take care to account for the discontinuity in quantifying angle (e.g., passing between $-\pi$ and π or 0 and 2π). For example, in Fig. 6.2 (a) if $\alpha_1 \approx \epsilon$ and $2\pi - \alpha_2 \approx \epsilon$ are small angles, the computed change in angle

will be $\approx 2\pi$, while the actual change is very small (2ϵ). To overcome this issue, another reference direction $-\mathbf{e}_t$ is introduced and a new angle θ_2 is measured with respect to this direction in the clockwise direction, as shown in Fig. 6.2 (b). The change in WSS angle is equal to the minimum of the two angle changes

$$\Delta\theta = \min\{|\theta_1(b) - \theta_1(a)|, |\theta_2(b) - \theta_2(a)|\} , \tag{6.14}$$

where a and b could be two points in space or time, and Δ can be the spatial/temporal gradients or any other measure that quantifies changes in angle. This definition is equivalent to

$$\Delta\theta = \min\{|\theta_1(b) - \theta_1(a)|, |2\pi - \theta_1(b) + \theta_1(a)|\} . \tag{6.15}$$

Figure 6.2: (a) Changes in WSS angle can be computed wrong in regions near the transition of the coordinate (between 0 to 2π using the convention shown). (b) Quantification of changes in WSS angle can be achieved by computation of WSS angle with respect to two reference directions and taking the minimum of the two differences.

6.3.2 WSS vector gradient

In the Cartesian coordinates WSS can be written as $\boldsymbol{\tau} = \tau_x\hat{\mathbf{i}} + \tau_y\hat{\mathbf{j}} + \tau_z\hat{\mathbf{k}}$. The WSS gradient becomes

$$\nabla_{\text{xyz}}\boldsymbol{\tau} = \begin{bmatrix} \frac{\partial\tau_x}{\partial x} & \frac{\partial\tau_x}{\partial y} & \frac{\partial\tau_x}{\partial z} \\ \frac{\partial\tau_y}{\partial x} & \frac{\partial\tau_y}{\partial y} & \frac{\partial\tau_y}{\partial z} \\ \frac{\partial\tau_z}{\partial x} & \frac{\partial\tau_z}{\partial y} & \frac{\partial\tau_z}{\partial z} \end{bmatrix} . \tag{6.16}$$

It is necessary to transform the gradient to the local intrinsic frame $(\mathbf{e}_t, \mathbf{e}_b, \mathbf{e}_n)$, and remove the normal contributions to the gradient, this will result in :

$$\nabla\boldsymbol{\tau} = \begin{bmatrix} \mathbf{e}_t^\intercal \cdot \left[\nabla_{\text{xyz}}\boldsymbol{\tau}\right] \cdot \mathbf{e}_t & \mathbf{e}_t^\intercal \cdot \left[\nabla_{\text{xyz}}\boldsymbol{\tau}\right] \cdot \mathbf{e}_b \\ \mathbf{e}_b^\intercal \cdot \left[\nabla_{\text{xyz}}\boldsymbol{\tau}\right] \cdot \mathbf{e}_t & \mathbf{e}_b^\intercal \cdot \left[\nabla_{\text{xyz}}\boldsymbol{\tau}\right] \cdot \mathbf{e}_b \end{bmatrix} . \tag{6.17}$$

The induced L_2 norm of this matrix has been used in the Results.

The fact that the gradient is acting on a surface manifold, requires incorporation of curvature effects into the gradient. This can be done by computing the Ricci rotation coefficients [55]:

$$\gamma_{abc} = \hat{\mathbf{e}}_a^\intercal \cdot \left[\nabla_{\text{xyz}}\hat{\mathbf{e}}_b\right] \cdot \hat{\mathbf{e}}_c , \tag{6.18}$$

where $(\hat{\mathbf{e}}_1, \hat{\mathbf{e}}_2, \hat{\mathbf{e}}_3) = (\mathbf{e}_t, \mathbf{e}_b, \mathbf{e}_n)$ are the basis used. The final form of WSS gradient can be written as:

$$\nabla_S \boldsymbol{\tau} = \nabla \boldsymbol{\tau} - \begin{bmatrix} \gamma_{111}\tau_t + \gamma_{211}\tau_b & \gamma_{112}\tau_t + \gamma_{212}\tau_b \\ \gamma_{121}\tau_t + \gamma_{221}\tau_b & \gamma_{122}\tau_t + \gamma_{222}\tau_b \end{bmatrix} , \tag{6.19}$$

where τ_t and τ_b are the components of WSS vector in the $\mathbf{e}_t$ and $\mathbf{e}_b$ directions, respectively. Note that the normal component of WSS is zero by definition and does not appear in Eq. (6.19.)

6.4 Results

The computational models used in this study are shown in Fig. 6.3. WSS correlations were performed in the shaded aneurysmal regions. Figure 6.4 shows some of the complex instantaneous vectorial WSS patterns observed in the AAA models.

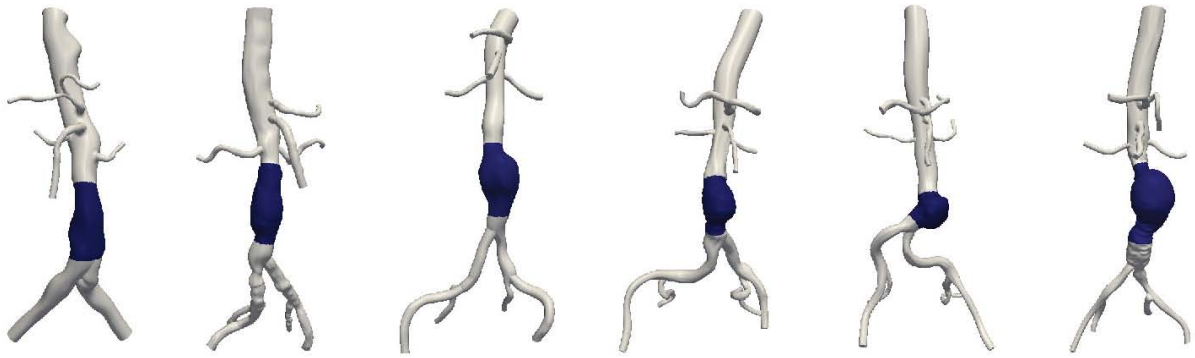

Patient 1 Patient 2 Patient 3 Patient 4 Patient 5 Patient 6

Figure 6.3: Patient-specific models used in this study. The shaded region shows the aneurysmal region, where the WSS correlations were performed.

Figure 6.5 and 6.6 show all the defined WSS parameters of a representative case for anterior and posterior views, respectively. A pointwise correlation study was performed among all the WSS parameters for each anatomic model, using the Pearson correlation coefficient. These coefficients were computed from point-wise correlation of all the surface points for each patient separately, resulting in six coefficients . The mean Pearson correlation coefficient resulting from all the patients is listed in Table 6.2, with the statistically significant correlations among the six patients indicated. A one-sample t-test analysis was performed to compute the p-values based on the Pearson correlation coefficients obtained for each patient, therefore the correlations that are not marked significant had notable inter-patient variability.

Several observations are made from this table:

1. TAWSS is highly correlated with $\|\overline{\boldsymbol{\tau}}\|$.

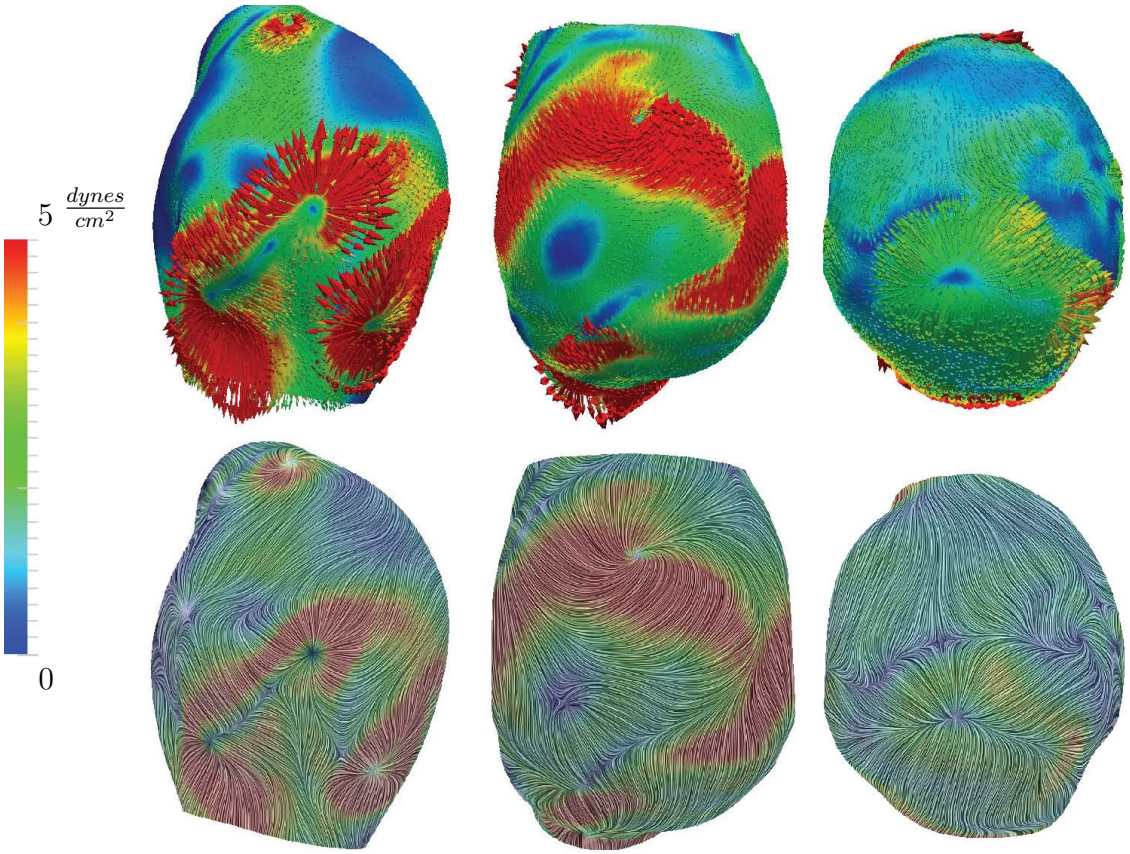

Figure 6.4: Instantaneous complex WSS vectors, and the corresponding WSS streamlines for three patients. To improve visualization, the WSS vectors are scaled differently in each patient, however the same color mapping was used among all cases.

2. WSS magnitude spatial gradient, and WSS vector spatial gradient are highly correlated with correlation coefficient close to one. Similar observation is made for WSS temporal gradients.

3. The high positive correlation of TAWSS with WSS magnitude/vector spatial and temporal gradient motivates the definition of relative WSS spatial gradient ($\frac{\|\nabla \boldsymbol{\tau}\|}{\|\boldsymbol{\tau}\|}$) and relative WSS temporal gradient ($\frac{\|\boldsymbol{\tau}'\|}{\|\boldsymbol{\tau}\|}$). These new measures are no longer correlated with TAWSS, and at the same time have relatively moderate correlation with WSS gradients.

4. Angle based measures (Δ_{90}, $\nabla\theta$, θ') are uncorrelated to TAWSS.

5. Comparison of $\overline{|\tau_t|}$ and $\overline{|\tau_b|}$ correlations shows that $\overline{|\tau_b|}$ is less correlated with spatial

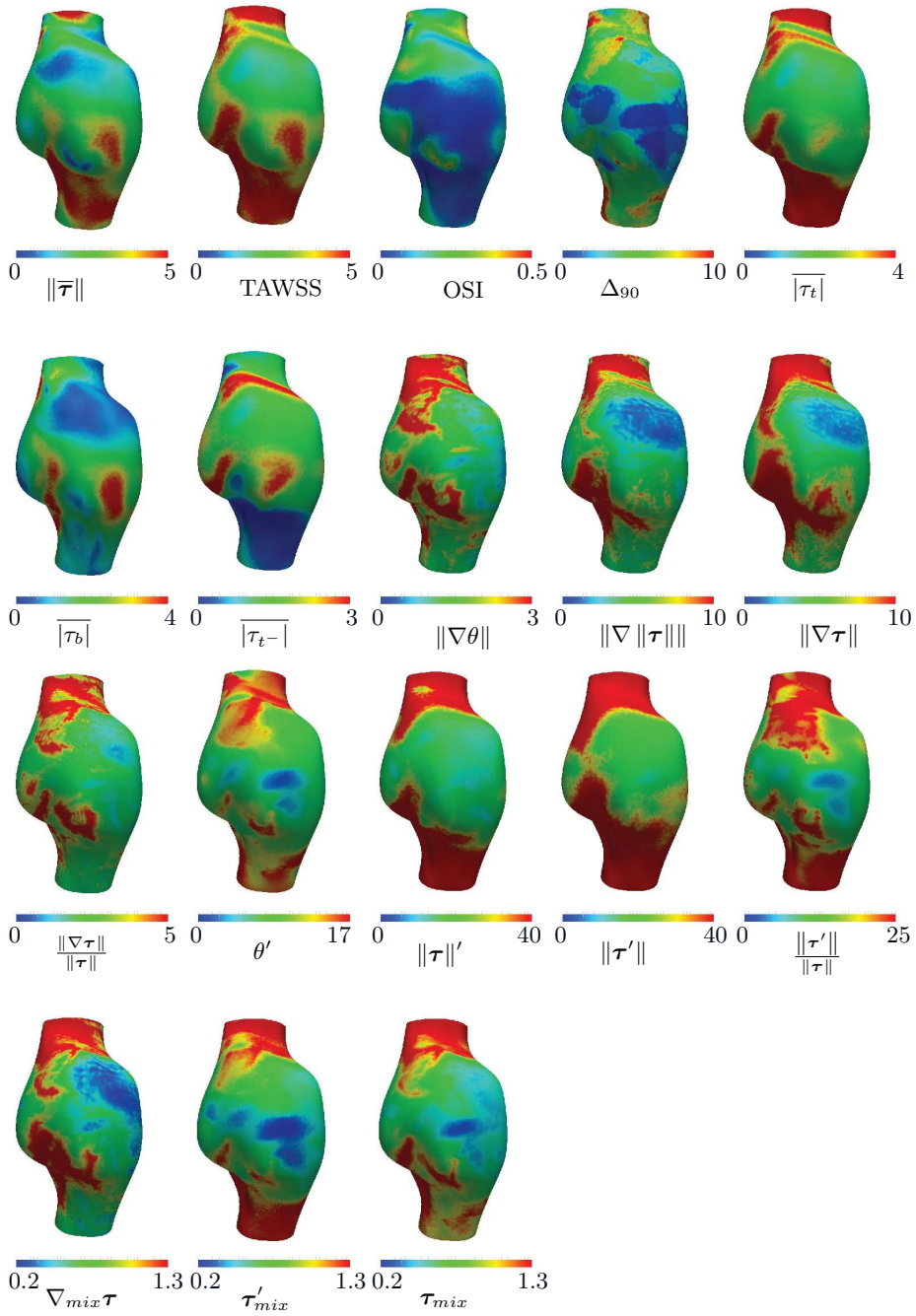

Figure 6.5: WSS parameters for a representative case (Patient 3). The anterior view is shown in this figure. All units are based on $\frac{dynes}{cm^2}$ for WSS magnitude, radians for WSS angle, cm for spatial gradients, and seconds for time. OSI, Δ_{90} and mix parameters are dimensionless.

and temporal changes of WSS.

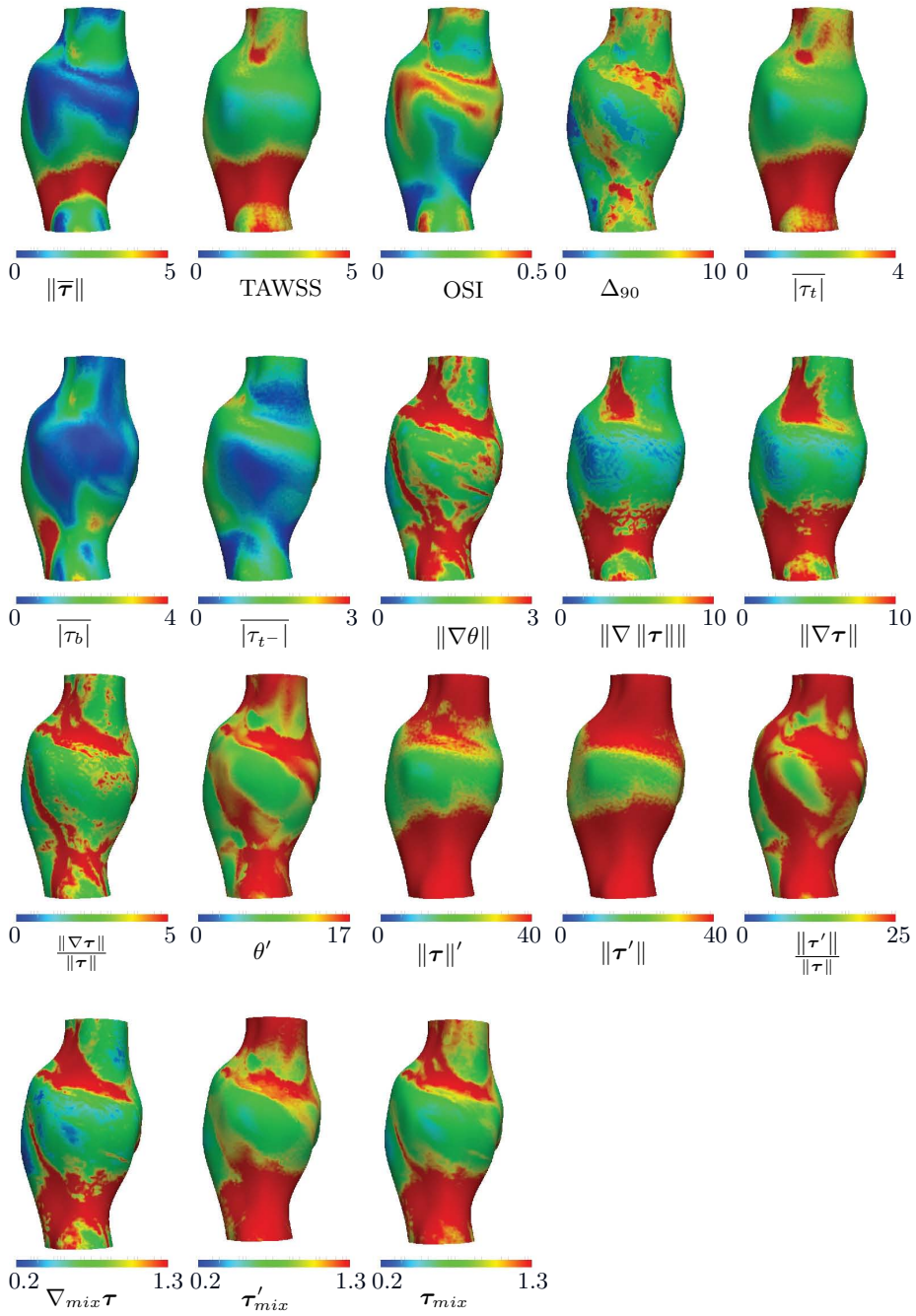

Figure 6.6: WSS parameters for a representative case (Patient 3). The posterior view is shown in this figure. All units are based on $\frac{dynes}{cm^2}$ for WSS magnitude, rad for WSS angle, cm for spatial gradients, and seconds for time. OSI, Δ_{90} and mix parameters are dimensionless.

6. $\boldsymbol{\tau}_{mix}$ is moderately to strongly correlated to all the parameters with high statistical significance, except to OSI, $\overline{|\tau_b|}$ and $\overline{|\tau_{t^-}|}$.

The weighting coefficients used for the mix WSS parameters in Eqs. (6.11)–(6.13), were found to be $w_s = 0.62 \pm 0.04$, $w_t = 0.63 \pm 0.05$, $w_{st} = 0.40 \pm 0.05$ for the present data. Removing the absolute value from the definition of $\overline{|\tau_t|}$ in Eq. (6.9) enables one to distinguish between regions of dominant forward and backward near wall flow, as shown in Fig. 6.7. The positive regions in the figure represent dominant forward WSS vectors, whereas the negative regions indicate dominant backward WSS vectors. Similarly, removing the absolute values in the $\overline{|\tau_b|}$ definition of Eq. (6.9) enables the distinction between dominant clockwise and counter-clockwise rotating near wall flow, as shown in Fig. 6.8. The positive regions show dominant counter-clockwise WSS vectors, whereas the negative regions show dominant clockwise WSS vectors. The ratio of $\overline{|\tau_b|}$ to TAWSS was found to be on average 0.38 ± 0.06 for each patient.

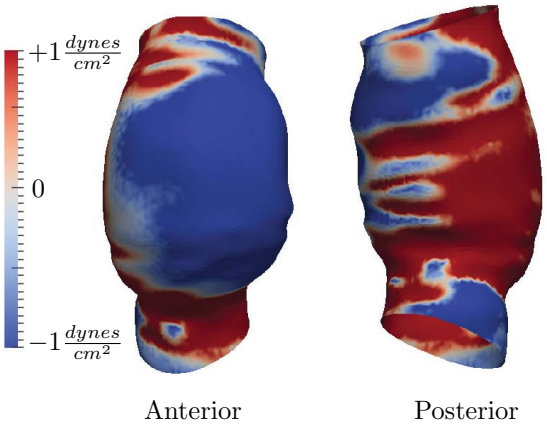

Figure 6.7: Sum of WSS vectors in the tangent direction ($\int_0^T \tau_t \ \mathrm{d}t$) for a representative case (Patient 4). Positive values (red) show regions with dominant forward near wall flow. Negative values (blue) show regions with dominant backward near wall flow. The colorbar range does not represent peak values.

The effects of surface curvature on the WSS vector gradient appears to have been mostly overlooked in the literature. These effects were investigated in this study (see Sec. 6.3 for the formulation) and it was found that including the curvature terms into the gradient changed the correlation coefficients less than 0.01 for our data, which provides justification for prior works that have neglected this effect.

6.5 Discussion

WSS is a vectorial quantity, with often complicated spatial and temporal variation. These factors can confound both the quantification and interpretation of WSS in cardiovascular flows. While the traditional TAWSS is treated as a scalar quantity, the vectorial nature of WSS and its gradients vastly increase the dimensionality of WSS data, and possibilities

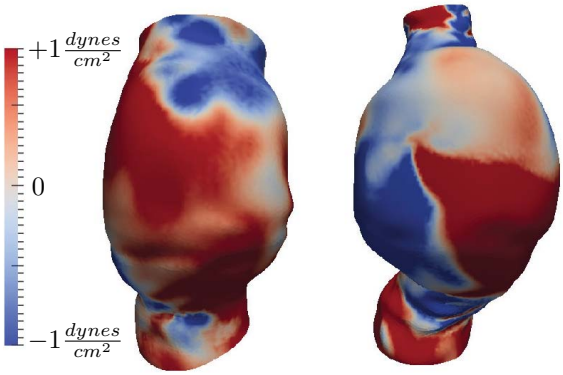

Figure 6.8: Sum of WSS vectors in the binormal direction ($\int_0^T \tau_b \, \mathrm{d}t$) for two representative cases (Patients 4 and 6). Anterior views are shown. Positive values (red) show regions with dominant counter-clockwise near wall rotating flow. Negative values (blue) show regions with dominant clockwise near wall rotating flow. The colorbar range does not represent peak values.

for how it can be quantified. Therefore, it is fruitful to consider how various quantifications correlate to reduce the possible parameters needed to effectively quantify or interpret hemodynamics data.

Various WSS parameters and their correlations in complex arterial flow have been investigated. Several WSS metrics were considered, and emphasis was placed on the temporal and spatial fluctuations of WSS angle, magnitude, and vector in space and time. The correlation results showed high positive correlation of vectorial spatial (temporal) gradient of WSS with its magnitude spatial (temporal) gradient. While fluctuations in WSS are affected by both changes in magnitude and direction (angle), the correlation results show there is a strong bias of WSS vectorial changes with magnitude changes. This motivated the definition of mix WSS spatial (temporal) gradient to incorporate spatial (temporal) changes of angle and magnitude into single measures. These measures were then combined to derive a mix WSS, $\boldsymbol{\tau}_{mix}$, parameter, which demonstrated statistically significant positive correlation (moderate to strong) with all of the WSS parameters except OSI, $\overline{|\tau_b|}$ and $\overline{|\tau_{t^-}|}$.

Relatively high positive correlation between TAWSS and WSS spatial/temporal gradient was observed, consistent with previous findings in carotid arteries [144]. This should not be surprising, since small relative changes of WSS in a high shear region can lead to a higher spatial/temporal gradient than large relative changes of WSS in a low shear region. Therefore, high shear regions are biased to produce higher gradients. This motivated the definition of relative gradients. These relative measures were uncorrelated to TAWSS, while they had relatively moderate correlation with WSS gradients. These differences should be contextualized from the perspective of the endothelial cells in contact with blood flow. Large relative spatial fluctuations among WSS vectors with small magnitude will likely lead to small measured gradients. However, these small gradients may be as significant to ECs as high

gradients resulting from relatively minor changes among large magnitude WSS. The same could be said for temporal gradients. For example, high gradients in WSS are observed in regions of flow dividers that are usually atherosclerosis free, while the likely smaller in magnitude WSS gradients in regions of recirculation promote atherosclerosis [20]. Hence, although relative gradient measures should not replace absolute gradient measures, they should serve as additional measures to guide the interpretation of WSS gradients.

In this study we observed a very weak positive correlation between TAWSS and WSS angle gradient. Lee *et al.* [144] have reported a relatively weak negative correlation between these measures in carotid arteries. Moreover, the correlations between WSS angle gradient and other measures considered in that study were also different than observed herein. The discrepancy may be due to the modified definition of WSS angle gradient in this study, or the different flow environments. Otherwise, the correlations in common between these two studies were in relative agreement.

In this paper we used a wall tangent direction aligned with the nominal direction of flow as the reference direction for quantifying directional variations in WSS. This approach is particularly suitable if one is interested in WSS as a measure characterizing near wall transport. The WSS vectors are indicators of flow topology next to the wall. Their role in transport of biochemicals near the wall becomes particularly significant if transport of biochemicals from the wall is confined to a thin boundary layer next to the wall [136, 109]. This happens in transport of biochemicals with high Schmidt number, which is typically the case in cardiovascular applications [86]. Most studies use the TAWSS direction in their characterizations, being motivated by the fact that the endothelial cells prefer to align to the time average direction of the WSS vector. However, in complex flows such as aneurysms the time average direction will yield a reference direction that is dependent on the complexities involved in flow behavior. Therefore, measures based on the TAWSS direction confound interpretation of WSS variations in complex flows. Moreover, the time average direction can become prone to numerical errors in regions of low WSS, typically seen in aneurysms.

It is noteworthy that the aneurysm formation indicator (AFI) measure [165, 52] defined as $\text{AFI} = \frac{\boldsymbol{\tau}\cdot\overline{\boldsymbol{\tau}}}{\|\boldsymbol{\tau}\|\|\overline{\boldsymbol{\tau}}\|}$ is similar to $\overline{|\tau_t|}$ used in this study, where the time average direction $\overline{\boldsymbol{\tau}}$ is replaced by $\mathbf{e}_t$ (Eq. 6.3) and magnitude is taken into account. The transWSS measure [197, 178] defined as the average magnitude of WSS perpendicular to the $\overline{\boldsymbol{\tau}}$ direction is similar to $\overline{|\tau_b|}$, where the the time average direction is replaced by $\mathbf{e}_t$. Recently, Morbiducci *et al.* [181] used a similar approach to what is used in this study to define axial and secondary WSS similar to $\overline{|\tau_t|}$ and $\overline{|\tau_b|}$, respectively. In their study axial and secondary WSS were directly projected to the centerline and perpendicular to centerline directions, producing WSS components that do not lie in the local tangent plane, whereas the approach herein used projections that lie in the local tangent plane.

The correlation results demonstrated a lower correlation of $\overline{|\tau_b|}$ with spatial/temporal changes of WSS angle and magnitude, compared to $\overline{|\tau_t|}$. The increase in $\overline{|\tau_b|}$ can be due to the helical nature of flow [240], suggesting that this type of flow can reduce the spatial and temporal changes in WSS. This finding is consistent with prior studies in carotid arteries

where helical flow has been shown to suppress disturbed flow, and contribute to uniformity in WSS [95]. Helical flow can reduce the accumulation of specific atherogenic chemicals on the vessel wall, and prevent platelet adhesion to the vessel wall, therefore protecting against atherosclerosis and thrombosis, respectively [157]. These protective mechanisms are due to the modification of near-wall transport topology, which is manifested in the WSS vector field.

In this study we only used one cardiac cycle of WSS data for our calculations. It has been shown that in transitional flows such as AAAs, time-averaged WSS measures might need several cardiac cycles to converge [203]. However, the purpose of our study was to compute correlations across parameters, therefore this issue is not expected to affect our results, significantly. Nevertheless, care must be taken when correlating time-averaged WSS parameters to different aspects of AAA disease.

The capability of endothelial cells to respond to the local flow patterns [129], along with the realization that the WSS vector field is important in determining near wall transport, brings the need for renewed perspectives in WSS characterizations. The prevailing theory of association of low and oscillatory WSS with atherosclerosis has been questioned [198], and conflicting results regarding the common belief about low WSS and high OSI have been reported [12, 178]. These findings encourage further attention in revisiting the traditional approaches used in WSS characterizations and their correlation with disease. The next Chapters demonstrate major steps towards this goal.

Table 6.2: Pearson correlation coefficients among all the WSS parameters studied. Significant correlations ($p < 0.05$) are shown in bold. Very significant correlations are marked with ** ($p < 0.01$). Total of 13592 ± 3956 surface points were analyzed for each of the six patients.

	TAWSS	OSI	Δ_{90}	$\overline{\lvert\tau_t\rvert}$	$\overline{\lvert\tau_b\rvert}$	$\overline{\lvert\tau_{t-}\rvert}$	$\lVert\nabla\theta\rVert$	$\lVert\nabla\lVert\boldsymbol{\tau}\rVert\rVert$	$\lVert\nabla\boldsymbol{\tau}\rVert$	$\frac{\lVert\nabla\boldsymbol{\tau}\rVert}{\lVert\boldsymbol{\tau}\rVert}$	θ'	$\lVert\boldsymbol{\tau}\rVert'$	$\lVert\boldsymbol{\tau}'\rVert$	$\frac{\lVert\boldsymbol{\tau}'\rVert}{\lVert\boldsymbol{\tau}\rVert}$	$\nabla_{mix}\boldsymbol{\tau}$	$\boldsymbol{\tau}'_{mix}$	$\boldsymbol{\tau}_{mix}$
$\lVert\overline{\boldsymbol{\tau}}\rVert$	**0.85****	**−0.70****	−0.02	**0.82****	**0.49****	0.05	0.00	**0.54****	**0.51****	0.02	−0.01	**0.64****	**0.61****	0.05	**0.32****	**0.38****	**0.39****
TAWSS		**−0.35****	0.09	**0.96****	**0.59****	0.22	**0.10**	**0.67****	**0.67****	**0.08**	0.09	**0.85****	**0.85****	0.11	**0.46****	**0.56****	**0.57****
OSI			**0.22**	**−0.29****	**−0.33**	0.06	**0.14**	**−0.18****	**−0.15**	0.08	0.19	−0.11	−0.09	**0.13**	−0.02	0.05	0.01
Δ_{90}				0.13	−0.10	−0.13	**0.55****	**0.19****	**0.23****	**0.42****	**0.92****	**0.36****	**0.39****	**0.52****	**0.44****	**0.77****	**0.68****
$\overline{\lvert\tau_t\rvert}$					**0.36****	0.21	**0.11**	**0.65****	**0.63****	**0.09**	0.12	**0.86****	**0.82****	0.16	**0.45****	**0.59****	**0.58****
$\overline{\lvert\tau_b\rvert}$						0.18	0.02	**0.39****	**0.43****	−0.01	−0.07	**0.37****	**0.48****	−0.10	**0.24****	0.18	**0.24**
$\overline{\lvert\tau_{t-}\rvert}$							−0.04	0.14	0.15	−0.03	**−0.19**	0.12	0.13	−0.06	0.06	−0.05	0.01
$\lVert\nabla\theta\rVert$								**0.41****	**0.49****	**0.75****	**0.58****	**0.30****	**0.32****	**0.38****	**0.84****	**0.52****	**0.76****
$\lVert\nabla\lVert\boldsymbol{\tau}\rVert\rVert$									**0.98****	**0.43****	**0.20****	**0.64****	**0.65****	**0.15**	**0.84****	**0.50****	**0.75****
$\lVert\nabla\boldsymbol{\tau}\rVert$										**0.48****	**0.25****	**0.65****	**0.68****	**0.16**	**0.87****	**0.54****	**0.79****
$\frac{\lVert\nabla\boldsymbol{\tau}\rVert}{\lVert\boldsymbol{\tau}\rVert}$											**0.44****	**0.22****	**0.22****	**0.52****	**0.70****	**0.40****	**0.62****
θ'												**0.39**	**0.43**	**0.54****	**0.46****	**0.83****	**0.73****
$\lVert\boldsymbol{\tau}\rVert'$													**0.97****	**0.30****	**0.56****	**0.83****	**0.77****
$\lVert\boldsymbol{\tau}'\rVert$														**0.28****	**0.58****	**0.84****	**0.78****
$\frac{\lVert\boldsymbol{\tau}'\rVert}{\lVert\boldsymbol{\tau}\rVert}$															**0.31****	**0.51**	**0.45**
$\nabla_{mix}\boldsymbol{\tau}$																**0.61****	**0.89****
$\boldsymbol{\tau}'_{mix}$																	**0.90****

Chapter 7

Lagrangian wall shear stress structures and near-wall transport

7.1 Introduction

Wall shear stress (WSS) is the tangential component of traction on the wall. WSS provides two types of information. First, it can be used to quantify the frictional drag force per unit area on the wall. Second, it provides a first order approximation for near wall convective transport. In the context of mass or heat transfer, the importance of near wall flow is emphasized in high Schmidt (Sc) or high Prandtl (Pr) open flows with a flux of species concentration or heat at the wall, and a convection dominated free stream carrying a specific species concentration or temperature over the no-slip boundary. In this paper, we focus on high Sc mass transfer, however, the ideas could be used in high Pr heat transfer applications as well.

Mass transfer in the cardiovascular system, including the transport of solutes (e.g. oxygen and nutrients) or that of proteins and cells (e.g. low density lipids and blood cells), represents an important application of high Sc flows [86]. The methods presented herein will be applied to pulsatile blood flow inside abdominal aortic aneurysm (AAA). AAA is a permanent widening of the aorta in the abdominal region. The sudden expansion of the aorta, complex vascular anatomy, presence of branch arteries, and pulsatility of blood flow together lead to complex flow inside AAAs [91, 73, 10], accompanied with complex WSS distributions [214] and particle residence times [246, 247].

It is known that in convection dominated flows, a flux of species concentration at the wall will lead to the formation of a thin concentration boundary layer. The common approach to obtain the species concentration distribution is to solve the advection diffusion equation in an Eulerian framework. However, this approach requires an extremely high resolution near the wall, often leading to numerical difficulties in complex 3D flows [86]. Alternatively, in the case of high Sc flows, the near wall region can be considered isolated from the rest of the flow, with the core flow having negligible *direct* effect on the concentration distribution. Because the

WSS vector field can be scaled to obtain a first order approximation for the velocity vector field next to the wall, it may be used to compute surface-bound trajectories representing the transport of a material species near the wall. In the case of high Sc numbers, the concentration boundary layer is very thin, making this first order approximation reasonable for understanding near wall transport.

Previous studies have shown that for a prescribed concentration (Dirichlet boundary condition) on the wall, the resulting flux of concentration from the wall is mostly independent of the chaotic flow away from the wall [99]. The observation that the boundary layer distribution of a concentration is largely unaffected by advection far from the wall motivates a reduced-order, near-wall approach, which can be based on the WSS vector field. It should be noted however that the large scale core flow features determine the WSS patterns [83], therefore the near wall transport depends on the flow topology away from the wall indirectly.

In prior work, critical points of the WSS vector field and their dynamics have been observed to play an important role in organizing near wall transport [201, 43]. Also, the structure of WSS lines have been used in developing theories for flow separation using dynamical system methods [248, 249]. Recently, WSS critical points associated with rare near wall backflow have been observed in turbulent channel flows [149, 39]. WSS patterns have been demonstrated to affect the heat transfer in impinging jets. As examples, the heat transfer coefficient has been shown to have similar distribution as WSS with a phase shift [105], and it has been shown that the secondary vortex resulting from flow impingement creates negative WSS regions that correspond to heat transfer augmentation [70].

The correlations observed in the above studies between WSS and transport processes motivates more mechanistic exploration of near wall flow topology induced by the WSS vector field. In steady flows the critical points of the vector field and their associated invariant manifolds largely determine the flow topology. In unsteady flows Lagrangian coherent structures (LCS) have been used to obtain a template for transport [226, 106], including cardiovascular applications [233, 227]. These structures represent prominent flow features that organize the flow from a Lagrangian perspective. This study demonstrates the relevancy of similar structures obtained from the WSS vector field for organizing near wall transport in the context of patient specific AAA models. Namely, species accumulation in the boundary layer in connection with these structures will be demonstrated. The influence of diffusion and flow normal to the wall, is also investigated and discussed.

7.2 Methods

Figure 7.1 shows one of the two AAA models used in this Chapter, to exemplify the anatomy of the model, morphology of volumetric flow waveform, and the nature of mesh. The results presented in this Chapter are mostly based on this model for demonstration purposes, although similar results were observed for other patient-specific geometries (see Chapter 8). The peak Reynolds number was $Re = 1750$ and the Womersley number was $\alpha = 12.8$. The

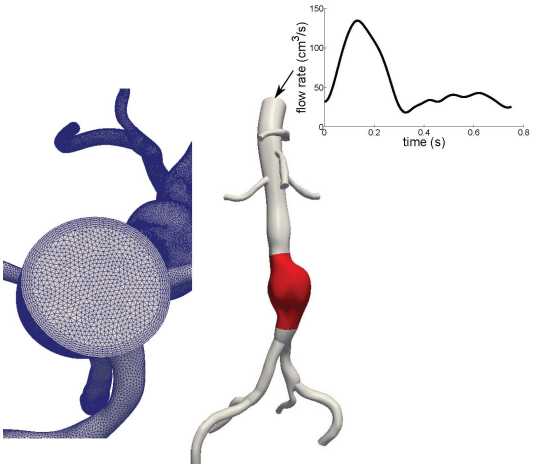

Figure 7.1: Example AAA model. The region of interest where trajectories are tracked is highlighted in red. The volumetric flow rate waveform at the inlet and the mesh are also shown. The first patient is shown in this figure.

convective near wall transport can be derived by Taylor expansion of the fluid velocity near the wall [96] as

$$\boldsymbol{u}_\pi = \frac{\boldsymbol{\tau}\delta n}{\mu} + O(\delta n^2) \,, \tag{7.1}$$

where $\boldsymbol{u}_\pi$ is the velocity vector in the local wall tangent plane, $\boldsymbol{\tau}$ is the WSS vector, μ is the dynamic viscosity, and the δn is the distance normal to the wall where the velocity is being evaluated. While this equation is derived for a planar surface, it can be shown that the leading terms are not changed when considering non-planar surfaces with curvature.

The vector field defined by the first term on the right hand side of Eq. (7.1) was used to study transport. This vector field is defined on the surface mesh, however it represents the near wall fluid velocity (per Eq. 7.1), as fluid velocity is zero on the vessel surface itself due to the no-slip, no-penetration condition. To study transport on this discrete surface manifold, the methods used in [296, 51] to obtain surface streamlines were extended to unsteady vector fields to obtain WSS surface pathlines. Trajectories are seeded on the entire surface of the region of interest uniformly and integrated based on the near-wall fluid velocity (Eq. 7.1) for 100 cardiac cycles, or until they left the domain. In order to obtain a uniform initial distribution of surface trajectories, OpenFlipper (www.openflipper.org) was used to remesh the triangular surface mesh to the desired number of vertices while enforcing a uniform distribution of vertices. These vertices were used as the initial location of the surface trajectories. Trajectories were computed using a forward Euler integration with sufficiently small time step. These WSS trajectories were computationally confined to stay on the surface, while they represent the trajectories in a small near-wall distance δn. To confine these trajectories on the curved surface, the computation is conducted within the

individual triangular (i.e., linear) elements of the surface, which are locally planar. The coordinate conversion between two neighboring triangles during the numerical integration is achieved via the transformation of the two corresponding local coordinate systems.

After several cardiac cycles of flow simulation, the WSS vector field was recorded and assumed periodic since the inflow boundary condition was periodic. This enabled velocity data to be reused for the purposes of trajectory integration over many cardiac cycles. The species concentration was assumed to be dilute and modeled by advection of non-interacting passive tracers.

In order to evaluate the regions of species accumulation in the boundary layer, we introduce a WSS exposure time measure, which is defined for each surface element (triangle) as the accumulated amount of time of all trajectories visiting that element

$$\mathrm{WSS}_{ET}(e) = \sqrt{\tfrac{A_m}{A_e}} \sum_{p=1}^{N_t} \int_0^{\mathcal{T}} H_e(p,t)\, \mathrm{d}t \tag{7.2}$$

$$H_e = \begin{cases} 1 \text{ if } \boldsymbol{x}_p(t) \in e \\ 0 \text{ if } \boldsymbol{x}_p(t) \notin e \end{cases} ,$$

where A_e is the area of the element, A_m is the average area of all the elements, $\mathbf{x}_p(t)$ is the position of the near wall trajectory, H_e is the indicator function for element e, N_t is the total number of trajectories released, and $\mathcal{T}$ is the integration time. For each trajectory, we define the WSS residence time as the amount of time that it takes to leave the near wall flow domain, mapped back to the initial condition

$$\mathrm{WSS}_{RT}(\mathbf{x}_0, t_0; \Gamma) = \min(t) \in (0, \mathcal{T}) \;\text{ s.t. }\; \mathbf{x}(\mathbf{x}_0, t_0 + t) \notin \Gamma \,, \tag{7.3}$$

where Γ is the near wall flow domain.

In order to characterize the near wall flow topology induced by the WSS vectors in complex geometries, one approach would be to compute the finite time Lyapunov exponent (FTLE) field on the lumen surface to identify LCS [147]. In this study, LCS were identified by simply advecting a large enough number of trajectories (≈ 42000) and identifying coherent structures formed. With sufficient forward time integration, the trajectories trace out prominent attracting LCS, and with backward time integration prominent repelling LCS are delineated. The motivation for this simple approach was to aid visualization; the temporal persistence of these near wall LCS made this possible. We refer to these as WSS LCS, which demonstrate organizing structures of near wall transport.

The above analysis ignores two effects that may be of importance. The reconstructed velocity in Eq. (7.1) ignores the normal near wall velocity. This velocity is second order, and is considered small close to the wall. However, over longer integrations in time this second order term might become important. The normal velocity can be written from the same series expansion used above [96] as

$$u_n = -\frac{1}{2\mu} \nabla \cdot \boldsymbol{\tau}\, \delta n^2 + O(\delta n^3) \,. \tag{7.4}$$

Thus, the divergence of WSS contributes to normal wall flux. Positive WSS divergence indicates flow towards the wall (e.g., impingement or reattachment), and negative WSS divergence indicates flow away from the wall (e.g., separation).

The effect of diffusion on near wall transport is also ignored. A simple dimensional analysis shows that the diffusion in the wall normal direction is more significant than the streamwise diffusion. The normal diffusion in a Lagrangian framework can be modeled with a random walk approach [99]

$$\begin{aligned} \delta n(t+\Delta t) &= \delta n(t) + \zeta \\ \zeta &\sim \mathcal{N}(0,\ 2D\Delta t)\ , \end{aligned} \tag{7.5}$$

where D is the mass diffusion coefficient, Δt is the integration time step, and ζ is a random variable determined from a Gaussian distribution, with zero mean and variance of $2D\Delta t$. In order to model the normal to the wall transport effects considered by Eq. (7.4) and Eq. (7.5), trajectories were confined to stay on the wall surface, however their normal-to-wall distance was tracked by these equations. Therefore, at each time step the trajectories experience a slightly different value of δn, which contributes to a different value for near wall velocity $\mathbf{u}_\pi$ (see Eq. 7.1) in addition to the inherent spatial and temporal change of the vector field. The normal to the wall transport was tracked until the trajectory left a near wall threshold ($\delta n_{\max}$), whereby the trajectory was assumed to be out of the near wall flow region where this model holds and the integration was terminated. Due to the stochastic nature of random walk, a large number of samples is needed to obtain a smooth field. To achieve this, the simulations involving diffusion were carried out 60 times, using independent series of random numbers. The 60 simulations were averaged to obtain the final result.

The near wall distance δn remains to be chosen. This distance needs to be chosen within the concentration boundary layer thickness δ_c. To approximate this, the order of magnitude of the momentum boundary layer thickness δ was evaluated from inspection of the thickness of the high vorticity region near the wall. The concentration boundary layer thickness was subsequently estimated using $\delta/\delta_c = Sc^{\frac{1}{3}}$ [266]. A mass diffusion coefficient of $D = 5 \times 10^{-6} \frac{cm^2}{s}$ was used, which is approximative of the diffusivity of chemicals and proteins in blood. The kinematic viscosity for blood was set to $\nu = 0.0377\ \frac{cm^2}{s}$, which gives a Sc number of $Sc = \frac{\nu}{D} \approx 7500$. Using the above estimates, the concentration boundary layer thickness was estimated as $\delta_c \approx 0.005$ cm. Since δn should be chosen within δ_c, a $\delta n = 0.0014\ cm$ was chosen. The sensitivity to this choice will be later discussed. The maximum near wall region thickness δn_{max} was chosen within the momentum boundary layer thickness δ in the region where the velocity profile was mostly linear ($\delta n_{max} \approx 0.05$ cm). A smaller δn_{max} was tested to ensure the results were not sensitive to this choice.

The full continuum 3D advection-diffusion problem was solved to validate the proposed Lagrangian surface transport approach. The advection-diffusion equation is written as

$$\frac{\partial c}{\partial t} + \boldsymbol{u} \cdot \nabla c = D\nabla^2 c\ , \tag{7.6}$$

where c is a non-dimensional concentration, $\boldsymbol{u}$ is the velocity and D is the mass diffusivity as above. A Neumann boundary condition of $\frac{\partial c}{\partial n} = 10\ cm^{-1}$ was prescribed at the no-slip wall representing a uniform flux of concentration. The inlet and outlet boundary conditions were set to $c = 0$. Zero Dirichlet outlet boundary condition was preferred to zero Neumann, due to the presence of reverse flow. The outlet boundary was extended to ensure minimal influence of the outlet boundary condition. A finite element method was used to solve the equation using streamline upwind/Petrov-Galerkin (SUPG) formulation [36, 24], implemented in the FEniCS package [158]. Second order tetrahedral elements were used with an edge size of 0.1 cm in the interior and a boundary layer mesh with next to wall edge size of 6.6 μm in order to resolve the concentration boundary layer. The simulation was run for 60 cardiac cycles until the surface concentration reached steady state with very small inta-cycle fluctuations.

7.3 Results

Figure 7.2 shows the WSS exposure time and WSS residence time fields in the first AAA model. Forward and backward time WSS trajectories are shown in the figure. In forward time (top row), WSS trajectories are seen to cluster towards distinct curves, which identify attracting WSS LCS. Trajectories remain in the vicinity of the attracting LCS for a long time, therefore the WSS exposure time is high in such regions. Moreover, the attracting LCS demonstrates little motion over time, which causes the region of high exposure time (red region in Fig. 7.2) to be confined to narrow bands. In backward time, WSS trajectories cluster to distinct curves, which identify a repelling WSS LCS. In this case the repelling LCS marks the boundary between the trajectories that eventually leave the domain, and those that remain in the near wall region for a long time (high residence time region). The trajectories starting from the high residence time regions will be attracted to one of the attracting LCS, and remain in its vicinity for a very long time, due to the temporal persistence of these structures.

Figure 7.3 further demonstrates the role of the WSS LCS in organizing near wall transport. The second patient is shown in this figure, due to interesting WSS LCS patterns. Three repelling WSS LCS, indicated by clustering of black tracers, divide the surface into four regions. Additional tracers are seeded and colored based on their initial position with respect to these regions. Upon advection of the colored sets of tracers it is seen that the trajectories starting in any of these four regions move collectively towards a different location in forward time. Namely, the repelling WSS LCS indicate boundaries between different basins of attraction for near wall species, and also form transport barriers.

The effect of diffusion and normal velocity on near wall transport was modeled as described above and the results are shown in Fig. 7.4. The region of high WSS exposure time formed by the attracting WSS LCS remains robust with respect to these effects (top row). Diffusion causes some of the trajectories to leave the near wall domain in long integration times, therefore the exposure time is generally reduced, although the same features persist.

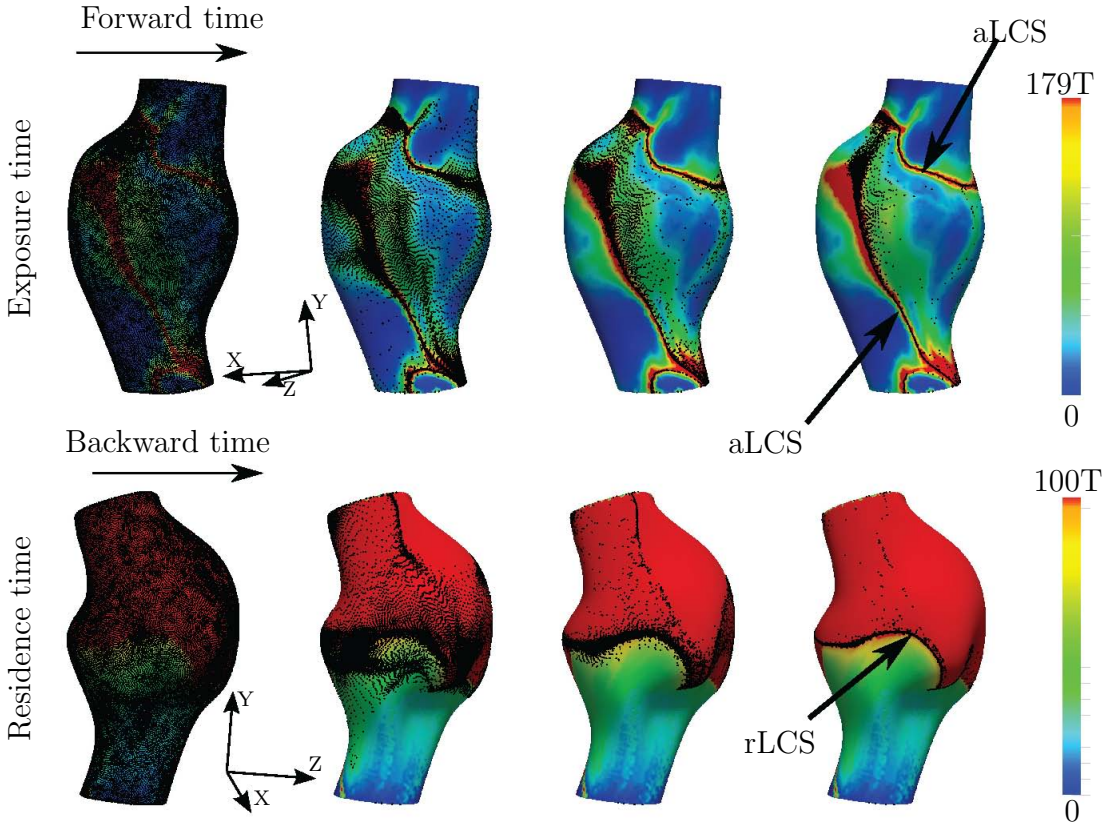

Figure 7.2: WSS exposure time and WSS residence time plots in first AAA model. Forward time trajectories are superimposed on the exposure time field, and backward time trajectories are superimposed on the residence time field. The forward and backward trajectories aggregate to attracting and repelling WSS LCS, respectively. $T = 0.75$ s is the cardiac cycle of the patient. The absolute time instances shown correspond to $t = 0$, $t = 27T$, $t = 61T$, and $t = 100T$ from left to right.

Residence time results (bottom row) are more sensitive to diffusion and normal velocity effects. Diffusion causes trajectories to randomly leave the region of high residence time, and in general more noisy and lower residence time values are observed. However, the boundary between the region of high residence time and low residence time persists. Introduction of normal velocity leads to more dramatic change in the spatial distribution of residence time. This is for two reasons. First, the effect of normal flow is spatially dependent; in regions with large negative WSS divergence tracers will more quickly escape from the near wall region. Second, residence time, by its definition, is more sensitive to individual tracers leaving the near wall region. Alternatively, exposure time depends on the collective behavior of trajectories and is therefore less sensitive to this influence.

Next we consider the effect of different choices for δn on the results, as shown in Fig. 7.5. We note that the dynamic variation of δn is tacitly considered in the results of Fig. 7.4,

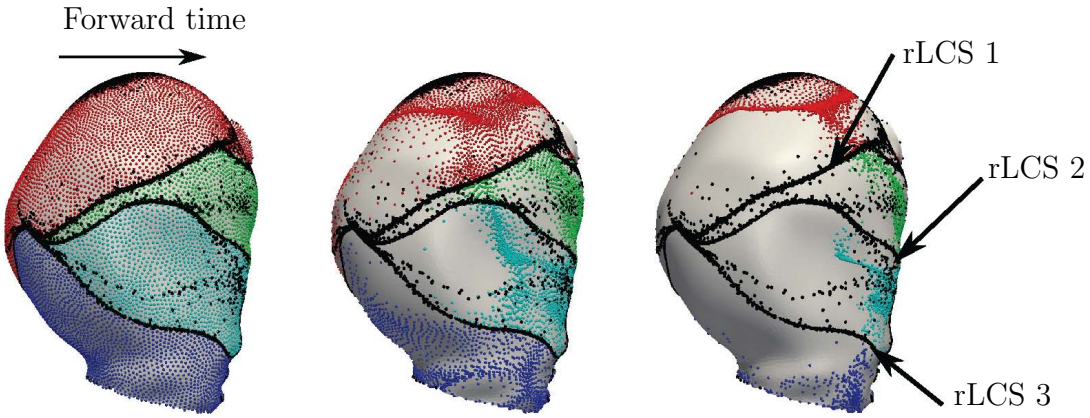

Figure 7.3: Three repelling WSS LCS are formed from backward time integration of WSS trajectories (black spheres). These LCS mark the boundary of four different near wall regions. Trajectories starting in each of these regions are colored differently, and are shown to have different fates. The second patient is shown in this figure. The time instances shown correspond to $t = 0$, $t = 34T$, and $t = 100T$ from left to right. $T = 0.95$ s is the cardiac cycle of this patient.

however our goal here is to demonstrate more directly the underlying relationship of the flow behavior to near-wall distance. For small values of δn (top left) the WSS LCS is almost stationary, fluctuating in a very narrow region of high WSS exposure time. The reason for this quasi-steady behavior is that very close to the wall the WSS trajectories have a small velocity, thus have small displacements during one cardiac cycle, which is the time scale of flow unsteadiness. Subsequently, the near wall transport becomes quasi-steady with the time-average WSS vector governing transport. Indeed, upon inspection of the limiting streamlines computed from the TAWSS vector field (bottom right), it can be observed that the attracting WSS LCS coincide with unstable manifolds of fixed points in the TAWSS vector field for small values of δn. For larger values of δn (top right and bottom left) it can be seen that the WSS LCS demonstrate increasing fluctuation with an increase in δn, as near wall convective transport becomes less stationary. However, for large Sc numbers, as long as δn is within δ_c the WSS LCS change modestly, and the WSS exposure time and residence time features are persistent.

In the presented WSS exposure time results the tracers are only released once during the start of the cardiac cycle. In a separate simulation, tracers were released at a few time points during the first cardiac cycle and then subsequently integrated. Identical qualitative results were obtained, due to the quasi-steady behavior. In the diffusion simulations, the initial value of δn was chosen within the concentration boundary layer. An additional simulation was carried out where the initial value of δn was set to zero and the tracers were subsequently allowed to diffuse normal to the wall and advect along the wall. The resulting WSS exposure time field was verified to be similar.

To test the validity of using the first-order near-wall velocity approximation to integrate

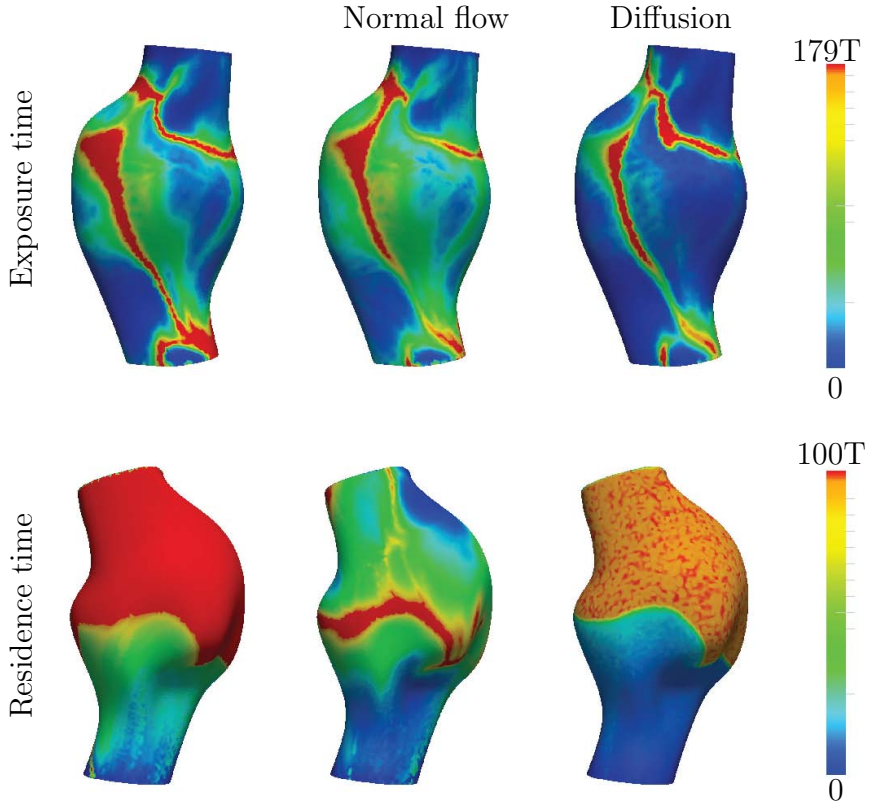

Figure 7.4: The effect of diffusion and normal flow on WSS exposure time and WSS residence time. $T = 0.75$ s is the cardiac cycle of the patient. Different views of the first patient is shown in this figure.

near-wall particle transport, Figure 7.6 compares the WSS exposure time derived from the surface transport model, and the surface concentration obtained from the full 3D advection-diffusion solution. The spatially averaged Sherwood number $Sh = \frac{\partial c}{\partial n} d \;/\; (C_s - C_i)$, where d is the maximum aneurysm diameter, C_s is the (spatially averaged) surface concentration, and $C_i = 0$ is the inlet concentration, was found to be 387. Relative agreement can be observed between the main features (identified hot spots) using the two approaches, validating the surface-based Lagrangian approach. To establish convergence of the numerical results, Figure 7.7 shows a comparison of the baseline TAWSS streamlines and WSS LCS to those derived from a Navier-Stokes solution using a finer mesh with next to wall edge size of 100 μm. Relatively minor change in the structures are observed, indicating adequate near-wall resolution of the flow field solution.

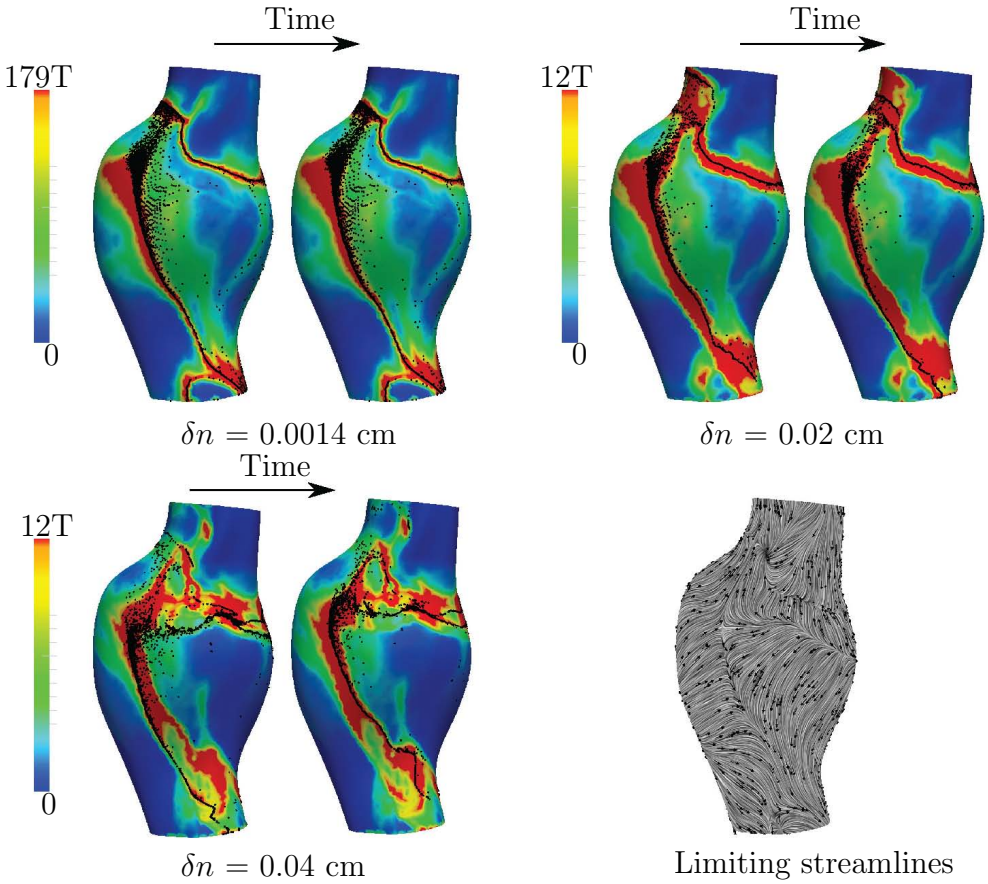

Figure 7.5: WSS exposure time contours with the attracting WSS LCS (indicated by particle clustering) for different values of δn in the first patient. Two different time instances are shown to visualize the extremes in temporal displacement of the LCS. The limiting streamlines of the TAWSS vector field are also shown, with normalized arrows showing the direction of WSS vectors. For smaller δn, the attracting LCS demonstrate less movement and are well-approximated by the unstable manifolds of the TAWSS vector field. For larger δn, near wall transport, and hence WSS LCS, become more unsteady. $T = 0.75$ s is the cardiac cycle for the patient. The two time instances shown differ by 2T.

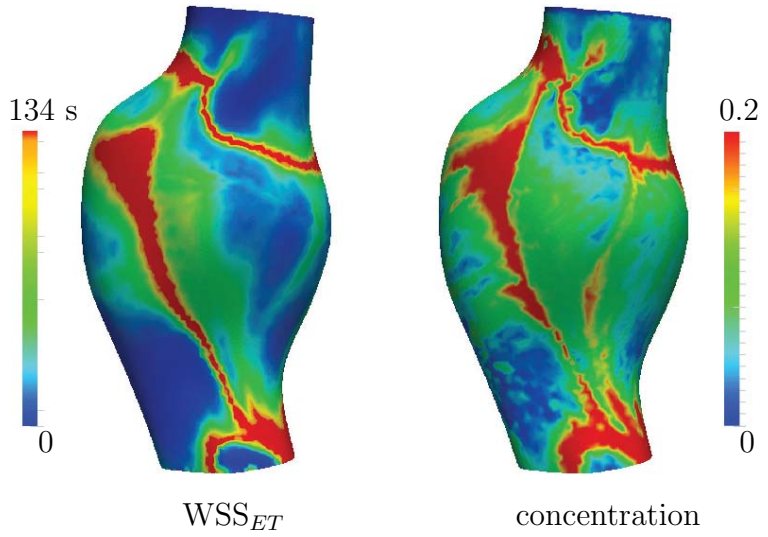

Figure 7.6: Comparison of WSS exposure time (WSS$_{ET}$) with the non-dimensional surface concentration obtained from the corresponding 3D continuum advection-diffusion equation.

7.4 Discussion

In this study the role of Lagrangian wall shear stress structures on organizing the near wall transport of high Sc flows was investigated in the context of blood flow in abdominal aortic aneurysm. It was shown that the attracting and repelling WSS LCS act as templates of near wall transport. The applicability of this approach relies on the existence of a thin concentration/thermal boundary layer. Using δ to scale the normal to wall distance, the relative error in neglecting the higher order terms in Eq. (7.1) is $O(\frac{\delta n}{\delta})$. δn is chosen as the same order as δ_c, therefore the relative error in the linear approximation is $O(\frac{\delta_c}{\delta})$. A relative error of 10% gives $Sc \approx 1000$. Therefore, the current approach may give reasonable results for Sc or Pr number $O(10^3)$ or higher (in the examples shown $Sc \approx 7500$). Interestingly, preliminary investigations demonstrated that the prominent attracting WSS LCS can still lead to high surface concentration in their vicinity for Sc numbers as low as $O(1)$. We note however that the second order term scales with WSS divergence, thus the near wall transport model can break down in locations of high WSS divergence (cf. Fig. 7.4).

It has been shown that for $Sc \gtrsim O(10^3)$ mass transfer resulting from unsteady blood flow was similar to that obtained from the time-averaged components [162]. Our result are consistent and provide further explanation. Two different time scales govern the near wall transport. The time scale for variations in the base flow (one cardiac cycle) is much smaller than the time scale for effective transport of near wall species (several cardiac cycles), implying that near wall transport is quasi-steady. It is important to keep in mind that in complex flows a time-dependent flow solve is still needed, as the time-averaged WSS field obtained from the time-dependent flow can be different from the WSS field obtained from

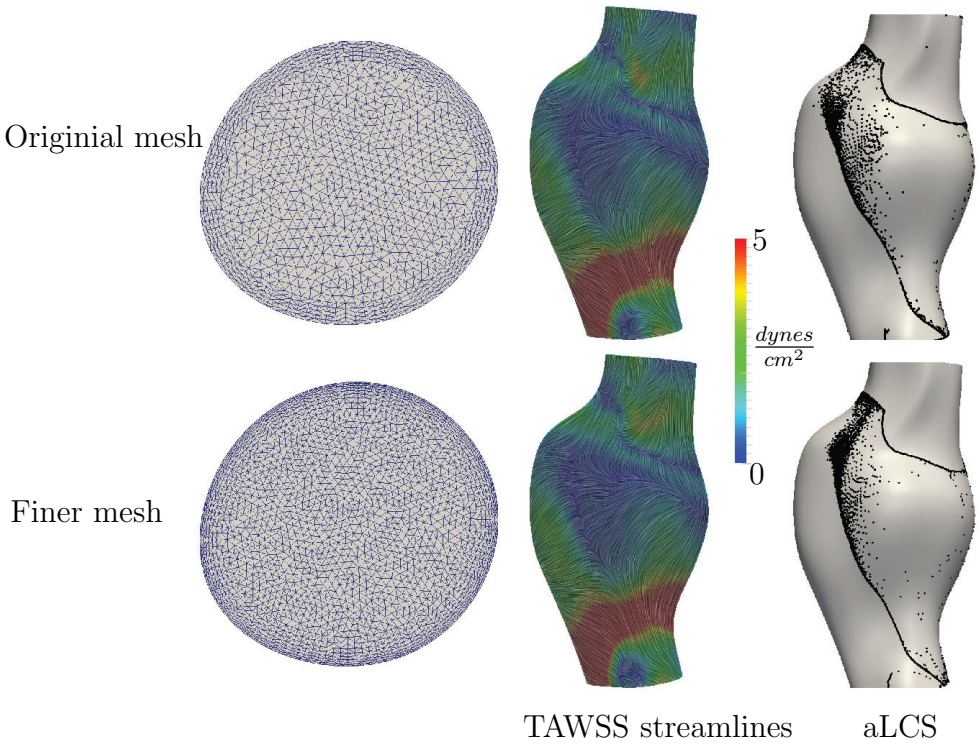

Figure 7.7: Comparison of the TAWSS streamlines and attracting LCS (aLCS) obtained from the original mesh (next to wall edge size 200 μm) to a finer mesh (next to wall edge size 100 μm) in the first patient. The TAWSS streamlines are colored based on the TAWSS vector magnitude.

a steady simulation with a time-averaged inflow. For the flow conditions considered in this study, we verified that using the TAWSS vector as a steady vector produced nearly identical WSS_{ET} results to the corresponding unsteady WSS vector field. Our results also demonstrated that the quasi-steady behavior of near wall transport led to the conforming of the WSS LCS with the stable/unstable manifolds of the TAWSS vector field. Moreover, it has been shown that stable/unstable manifolds in the velocity field emerge from critical points of the time-averaged WSS field in periodic two-dimensional flows [234]. Therefore, the relation between WSS critical points and their invariant manifolds with the core flow features can provide insight into the basis of near wall transport.

For high Sc, as long as δn was chosen within the concentration boundary layer, the exact choice did not significantly affect the qualitative behavior of the WSS LCS, WSS exposure time and residence time fields. We note that a decrease in Sc number yields a larger concentration boundary layer thickness, and subsequently more unsteadiness in near wall transport manifested in the temporal variations of WSS LCS. In the case of smaller Sc number flows, a higher order representation of the near wall flow by means of a series expansion [200] may be employed to accurately model the near wall transport with a larger

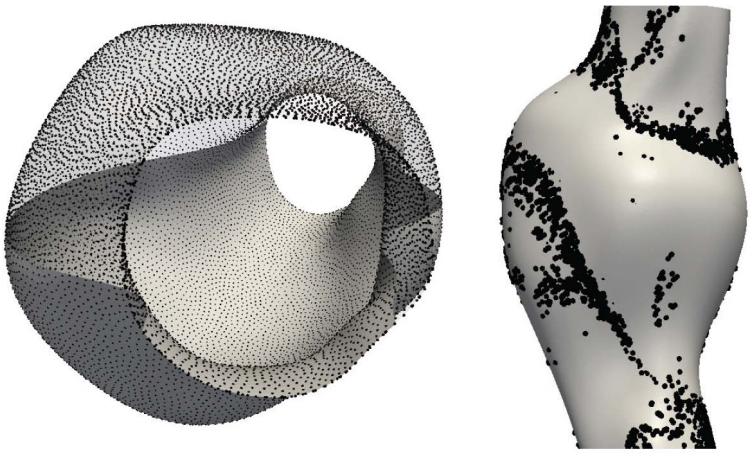

Initial tracer seed 3D particle tracking

Figure 7.8: Tracers are seeded near the wall ($\delta n = 7\mu m$) and integrated in forward time using the first patient model. The left panel shows tracer seed locations. The right panel shows the emerging near wall structures after sufficient forward 3D integration. Particles on right are enlarged to become visual through the surface.

δn. In this case, depending on the Sc number it is likely that the trajectories closer to the wall will be controlled by the time-averaged WSS vector field manifolds, and trajectories further away from the wall will be subject to unsteadiness around these manifolds (cf. Fig.7.5).

While one may use the full 3D velocity field to track near wall tracers, this can be difficult to implement. For validation, we seeded tracers $\delta n = 7\mu m$ from the wall and integrated them forward in time using the full 3D flow field until coherent structures were formed near the wall as shown in Fig. 7.8. It can be observed that tracers accumulate near the same attracting WSS LCS as shown in Fig. 7.2. However, in using the 3D velocity field for integrating near wall tracers, small errors in numerical integration are more easily amplified. Namely, such errors result in (1) increases in δn causing higher normal velocities and tracers leaving the near-wall region prematurely, or (2) decreases in δn causes tracers to stick to, or penetrate, the wall. Over long integration times needed to understand near wall transport, the accuracy of near wall integration can become significantly impaired due to these effects. Alternatively, the surface integration method provides a more efficient approach, while maintaining accuracy as for example demonstrated by the agreement between WSS_{ET} and the surface concentration obtained from solving the 3D continuum advection-diffusion equation (cf. Fig.7.6).

For most vascular applications, the emergent WSS LCS patterns will be largely dependent on the vascular geometry and Reynolds and Womersley numbers as these factor most influence flow topology. Indeed, it has been shown that small changes in the AAA geometry can significantly affect the WSS distribution [102], and changes in the curvature of the vessel wall have also been shown to affect WSS [238]. In the next Chapter, we will demonstrate

emergence of similar WSS LCS structures that influence surface concentration fields in other vascular examples.

The inlet flow waveforms used in this study were patient specific resting waveforms obtained from phase contrast magnetic resonance measurements. Pulsatile blood flow may have some cycle to cycle variations due to transient effects from the fluid mechanics or physiology. In this study we assumed a periodic WSS vector field to generate WSS trajectories. Depending on the Reynolds and Womersley numbers, the intercycle variations in the flow field can break down the quasi-steady behavior of the WSS LCS, leading to greater unsteadiness in the near wall transport. Under such conditions the WSS LCS may demonstrate time dependent behavior and deviate from the stable/unstable manifolds of the TAWSS field. Additional considerations that remain to be studied are that higher WSS divergence magnitudes typically observed under exercise conditions, as well as physiologic deformation of the vessel wall due to wall compliance, may increase transport normal to the vessel wall in the boundary layer. To visualize the WSS LCS in this study we relied on a simple advection of tracers. Alternatively, one could compute the finite-time Lyapunov exponents (FTLE) on a non-Euclidean manifold to visualize the LCS [147]. The simple approach employed here is nonetheless able to identify the more prominent LCS, which affect the concentration pattern on the vessel surface.

The current study provides a framework for understanding the mechanisms underlying mass/heat flux at a no-slip wall in disturbed high Sc/Pr flows. In particular, attracting WSS LCS determine patterns of high species concentration, and repelling WSS LCS mark the boundaries of different basins of attraction. Therefore, the WSS LCS provide a template for the distribution and evolution of wall generated species. Recently, the separation between near wall species with different Sc numbers has been demonstrated [185]. This separation could also happen due to the partitioning effect of the repelling WSS LCS as demonstrated in Fig 7.3. From a design perspective, it would be interesting to manipulate these structures to obtain a WSS pattern with a desired outcome of wall concentration/temperature distribution, in similar fashion to [118], who investigated the effect of vortical structures near the boundary layer on heat transfer augmentation. Finally, the bearing of these structures on near wall transport of turbulent flows remains to be investigated.

Chapter 8

Near-wall stagnation in large arteries

8.1 Introduction

Biomechanical interactions between blood flow and the vessel wall are central to the initiation and progression of most cardiovascular diseases. Indeed, the majority of computational and experimental investigations into blood flow seek to understand how local flow mechanics relates to disease progression in or on the vessel wall. Blood flow conditions in diseased vessels are usually spatially and temporally complex and are challenging to characterize alone [233, 227], without reference to the coupled biochemical or biophysical processes driving disease progression. Nonetheless, the role of blood flow mechanics in the "near-wall" region is of utmost importance since this is where such couplings are most profound. In the near-wall region, blood flow serves to impart mechanical stresses on the vessel wall, as well as regulate the local transport of reactive material between the tissue and fluid domains. It is this latter mechanism that motivates the work presented herein.

A compelling scenario involving the interaction between blood flow and the vessel wall is atherosclerosis, which is a leading cause of death worldwide. Atherosclerosis occurs mainly in locations of disturbed blood flow patterns [44, 219]. The local transport of several substances near and at the vessel wall are known to influence atherosclerosis progression [272]. For example, previous studies have looked into transport of low density lipoproteins (LDL) [69, 88, 140, 64], high density lipoproteins (HDL) [175, 110], oxygen [68, 120], nitric oxide (NO) [202, 156], monocytes [58, 64], and adenine triphosphate ATP and adenine diphosphate ADP [61, 65, 33] as important mass transport processes involved in atherosclerosis.

The intravascular thrombosis is another compelling pathology associated with most cardiovascular diseases where near-wall transport becomes important [23, 115]. For example, the role of intraluminal thrombus in abdominal aortic aneurysm (AAA) [282, 264] is an important application. The chaotic flow field in AAAs [10] leads to complex WSS distributions [11] and interesting near-wall flow structures [8]. Thrombosis in the left ventricle [223], aortic dissection [176], stented arteries [124], and flow diverter treated cerebral aneurysms [195]

represent other applications.

Most computational investigations of intravascular transport have relied on continuum models that solve the advection-diffusion equations in the blood flow domain. However, due to the high Schmidt numbers (Sc) in most arterial flows, thin concentration boundary layers are typically formed next to the wall where most interesting biological processes occur [86]. The thin concentration boundary layer thickness causes numerical difficulties in resolving the near-wall dynamics [109], which is precisely the region of greatest interest. Hansen and Shadden [109] recently proposed a continuum surface transport model to study mass transport in the thin concentration boundary layer next to the wall. This model is based on the idea that the core flow minimally influences the mass transport in the concentration boundary layer in high Sc flows, and thus surface transport PDEs can be derived in terms of the WSS vector field. Similarly, a surface-based Lagrangian method has been proposed to study the near-wall transport of high Sc species by using Lagrangian particle tracking based on the WSS vector field [8].

Transport often depends on emergent, multidimensional, nonlinear and transient processes that cannot be completely quantified through a single measure. On the other hand, to report, compare and evaluate hemodynamic processes it is important to develop simple measures that effectively quantify physiologically-relevant aspects of near-wall transport. Flow stagnation is one important aspect of transport, which has been widely regarded as an event promoting atherogenic and thrombogenic processes. In order to quantify near-wall stagnation, particle tracking techniques have been used to define near-wall residence time [159]. While the Lagrangian nature of this measure is desirable for capturing emergent behavior of the flow, a very high resolution of particles is often needed to accurately sample the near-wall region. A more readily obtained measure is relative residence time (RRT), which is defined as the inverse of time average WSS (TAWSS) vector magnitude [116, 144]. The relevance of this measure could be explained as follows. As discussed in [109, 8], the WSS vector can be scaled to obtain the near-wall fluid velocity, and because displacements of fluid in the concentration boundary layer are small over each cardiac cycle, the time-averaged WSS vector field dominates transport. Therefore, in regions of low TAWSS vector magnitude (high RRT) the near-wall species are displaced to smaller extent, implying higher near-wall stagnation. However, because RRT is an instantaneous Eulerian measure, it cannot as effectively provide information about the concentration or origin of near-wall species when compared to a Lagrangian measure. This is valuable information, since high near-wall stagnation and concentration are both essential for effective atherogenic or thrombogenic processes to occur.

In this study, we present a WSS exposure time (WSSET) measure that is computed from Lagrangian tracking of surface-bound tracers, which can account for stagnation (low flow) and species redistribution. It has the advantage of being a Lagrangian-based measure, but has significantly less computational cost compared to Eulerian advection-diffusion solvers. We compare WSSET with RRT in different vascular pathologies. To this end, image-based models of aortic aneurysm, carotid bifurcation, cerebral aneurysm, and coronary aneurysm are used. WSS divergence is also computed and its relevance to near-wall transport is discussed. These measures are compared with surface concentration fields obtained from the

solution of the complete 3D advection-diffusion transport equation. We demonstrate that WSSET is able to better approximate the locations of near-wall stagnation and concentration build-up of chemical species. This improvement comes at an increased computational cost when compared to RRT, however this cost is far below that needed to quantify the 3D transport problem. To further demonstrate the relevance of the WSSET measure and to characterize the near-wall flow topology, stable and unstable manifolds of the TAWSS vector field are computed and related to WSSET fields.

8.2 Methods

8.2.1 Computational fluid dynamics (CFD)

Six patient-specific AAA models were used in this study and WSS data was obtained from computational fluid dynamics (CFD) simulations described in Chapter 2. Using SimVascular, two carotid artery models were constructed from computed tomography angiography. Linear tetrahedral elements were used with a global edge size of 400 μm and a boundary layer meshing with next to wall edge size of 50 μm. The mean common carotid volumetric flow rate used in a previous study [143] was assigned as inlet boundary condition for both patients. Resistance boundary conditions were used at the outlets to divide 70% of the flow rate to the internal carotid artery and 30% to the external carotid artery. The time step was chosen to divide the cardiac cycle (T = 0.88 s) into 5000 time steps. A cerebral aneurysm model used in a previous study [97] was remeshed with a higher mesh resolution (next to wall edge size of 100 μm). The same boundary conditions and parameters used in [97] were specified. A typical volumetric waveform was used at the inlet with the flow rate scaled according to the inlet cross section area. Zero pressure gradient was applied at the outlet. The time step divided the cardiac (T = 0.85 s) cycle to 100 time steps. Similarly, a coronary aneurysm model (Kawasaki disease) used in a previous study [222] was remeshed with a higher resolution (next to wall edge size of 60 μm in the aneurysm branch). The same boundary conditions and parameters were used for the flow solution (this model and simulation parameters were obtained from vascularmodel.com). A typical aortic waveform was prescribed at the inlet, and a circuit analogy lumped parameter network was coupled to the outlets to model coronary pressure and flow. The simulation time step was 1 ms. Rigid wall and Newtonian blood rheology were assumed in all simulations. The cerebral aneurysm simulation was done in OpenFOAM (finite volume method), and all the other simulations were carried out in SimVascular (finite element method). Figure 8.1 shows the full computational models, and the highlighted region shows the region of interest where flow conditions were analyzed using the WSSET, RRT and WSS divergence measures.

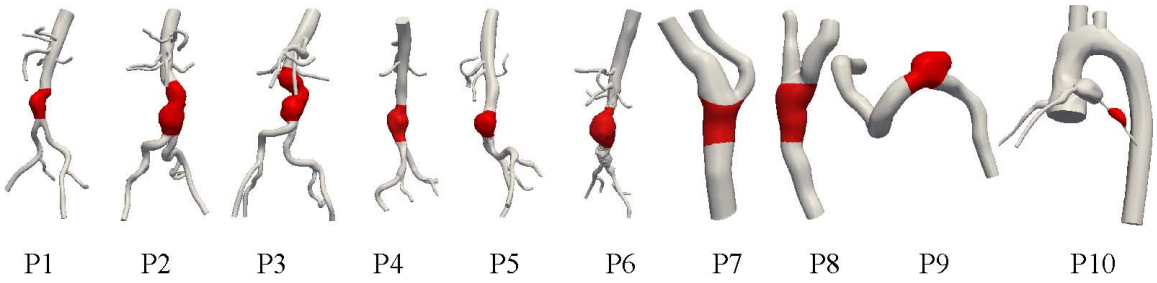

Figure 8.1: The full computational models where image-based CFD was performed. The highlighted region shows the region of interest where post-processing was performed. P1–P6 are the abdominal aortic aneurysm (AAA) models, P7–P8 are carotid artery models, P9 is a cerebral aneurysm model, and P10 is a coronary aneurysm model.

8.2.2 Near-wall stagnation

In this section, the WSS measures used to quantify near-wall stagnation are defined. The WSS vector field ($\boldsymbol{\tau}$) is computed as the tangential component of traction on the wall. Relative residence time (RRT), a traditional measure used in characterization of near-wall stagnation, is defined as

$$\mathrm{RRT} = \frac{1}{\|\frac{1}{T}\int_0^T \boldsymbol{\tau} dt\|} = \frac{1}{\|\overline{\boldsymbol{\tau}}\|} , \tag{8.1}$$

where T is the cardiac cycle duration, and $\overline{\boldsymbol{\tau}} = \frac{1}{T}\int_0^T \boldsymbol{\tau} dt$ is the TAWSS vector. Note that this definition is the same as the more common form written in terms of oscillatory shear index (OSI)

$$\begin{aligned} \mathrm{RRT} &= \frac{1}{(1-2\cdot\mathrm{OSI})\int_0^T \|\boldsymbol{\tau}\| dt} , \\ \mathrm{OSI} &= \frac{1}{2}\left(1 - \frac{\|\overline{\boldsymbol{\tau}}\|}{\int_0^T \|\boldsymbol{\tau}\| dt}\right) . \end{aligned} \tag{8.2}$$

The form in Eq. (8.1) provides a clearer correspondence to TAWSS vectors and near-wall transport. We also compute time averaged WSS divergence (WSSdiv)

$$\mathrm{WSSdiv} = \frac{1}{T}\int_0^T \nabla \cdot \boldsymbol{\tau} dt . \tag{8.3}$$

Positive WSSdiv represents expansion of WSS vectors, and negative WSSdiv shows contraction, which could exemplify flow impingement and separation, respectively. The relevance of this measure to near-wall flow will be demonstrated.

WSSET was computed as explained in Chapter 7. In this Chapter WSSET was also normalized by the total integration time $\mathcal{T}$ to enable comparison between patients. Namely,

$$\text{WSSET}(e) = \frac{1}{\mathcal{T}}\sqrt{\frac{A_m}{A_e}}\sum_{p=1}^{N_t}\int_0^{\mathcal{T}} H_e(p,t)\,\mathrm{d}t \tag{8.4}$$

$$H_e = \begin{cases} 1 \text{ if } \boldsymbol{x}_p(t) \in e \\ 0 \text{ if } \boldsymbol{x}_p(t) \notin e \end{cases},$$

where A_e is the area of the surface element, A_m is the average area of all the surface elements, $\mathbf{x}_p(t)$ is the position of the WSS trajectory, H_e is the indicator function for element e, N_t is the total number of trajectories released, and $\mathcal{T}$ is the integration time. An integration time of 100 cardiac cycles ($\mathcal{T} = 100T$) was used for each patient, and the WSS data was assumed periodic to enable trajectory integration for such time scale. A mass diffusion coefficient of $D = 1 \times 10^{-5}\frac{cm^2}{s}$ [68] is assumed to estimate the species concentration boundary layer thickness $\delta_c = \delta Sc^{\frac{-1}{3}}$, where δ is the momentum boundary layer thickness, and $Sc = \frac{\nu}{D}$ where ν is blood's kinematic viscosity. A normal to wall distances of $\delta n = 15\mu m$, $0.7\mu m$, $1\mu m$, and $1\mu m$ are chosen in this study, which are within δ_c in the AAA, carotid artery, cerebral aneurysm, and coronary aneurysm models, respectively. The significance of this choice is discussed in the previous Chapter.

8.2.3 Advection-diffusion transport

Simulations of chemical concentration fields on surface of each model were computed by solving the 3D advection-diffusion equation to provide a comparison of the wall-bounded WSS measures with the full 3D transport. The advection-diffusion equation can be written as

$$\frac{\partial c}{\partial t} + \boldsymbol{u}\cdot\nabla c = D\nabla^2 c\,, \tag{8.5}$$

where c is a non-dimensional concentration, $\boldsymbol{u}$ is the velocity, and D is the same mass diffusivity as above. A Neumann boundary condition of $\frac{\partial c}{\partial n} = 5\ cm^{-1}$ was prescribed at the no-slip wall representing a uniform flux of concentration into the lumen. Zero Dirichlet boundary conditions were used at the inlet and outlets. Homogenous Dirichlet outlet boundary conditions were preferred to homogenous Neumann, due to backflow at the outlets. The outlet boundary was extended based on the available CFD data (between 1 to 3 times the diameter) to ensure minimal influence of the outlet boundary condition and improve convergence. The advection-diffusion equation was solved using the finite element method implemented in the FEniCS package [158]. No stabilization was used in the weak form. Time integration was done using the generalized-alpha method [123]. *Second order* tetrahedral elements were used with an edge size of 0.1 cm , 400 μm, 400 μm, and 200 μm in the interior for the AAA, carotid artery, cerebral aneurysm, and coronary aneurysm models, respectively. A boundary layer mesh was generated with next to wall edge size of 6.6 μm, 1.5 μm, 1.6 μm, and 1.6 μm for the AAA, carotid artery, cerebral aneurysm, and coronary aneurysm models, respectively. The velocity field obtained from the CFD simulation was linearly interpolated to the (more

highly resolved in the near-wall region) advection-diffusion mesh. The simulations were run for at least 25 cardiac cycles until the surface concentration reached steady state, with very small intra-cycle fluctuations.

Outlet boundary condition

Treatment of the outlet boundary condition is an important issue in cardiovascular mass transport problems. Backflow can be present at the outlet due to the inherent flow topology and the truncated nature of the domain. The presence of backflow at the outlet prevents the use of a homogenous Neumann boundary condition, which is the ideal choice for the outlet boundary condition. To overcome this issue a homogenous Dirichlet boundary condition can be imposed. However, this can lead to sharp internal boundary layers near the outlet, which can lead to numerical divergence. To overcome this issue different methods were tested:

1. The velocity direction at the outlet can be checked at each time step, and the homogenous Dirichlet boundary condition can be only applied whenever the velocity direction is backward at a computational node.

2. The method of weak Dirichlet boundary condition developed by Bazilevs and Hughes can be used [25], where the Dirichlet boundary condition is weakly imposed on the outlet, by adding a term to the weak form.

3. A damping boundary condition can be implemented to diminish the structures approaching the outlet boundary, thereby preventing emergence of a sharp interface at the outlet. The domain of interest can be extended in both upstream and downstream directions (see Figure 8.2). The Neumann flux boundary condition is applied on the walls at the domain of interest (Ω) , whereas homogenous Neumann boundary condition is applied to the wall on the extended domains. The diffusion coefficient D in the extended domain is increased sufficiently to prevent formation of any sharp interface at the outlet. The success of this method relies on a few factors. First, the extension domain should be sufficiently extended. Second, the diffusion coefficient in the extension domain should be sufficiently large. However, increase in the diffusion condition leads to ill-conditioning of the system, which increases the computational cost of the linear solver. Therefore, care must be taken in choosing this value. This method was eventually used to obtain the results in this study.

8.2.4 WSS stable/unstable manifolds

In the previous Chapter we demonstrated emergence of Lagrangian coherent structures (LCS) computed from WSS (WSS LCS) and how they relate to the near-wall transport in AAAs. These structures match the stable and unstable manifolds of the TAWSS vector in high Schmidt numbers, where $\delta n \sim \delta_c$ is small. Therefore, the TAWSS vector field alone could be used in characterization of near-wall flow topology in such flows, as opposed to the

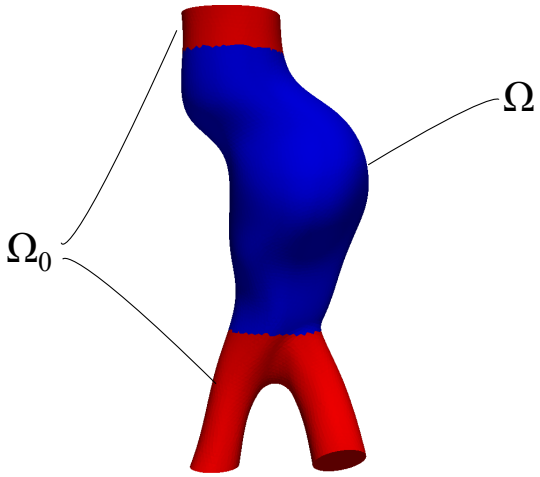

Figure 8.2: The computational domain (Ω) is extended to include an extension region (Ω_0) where the diffusion is increased to create a damping boundary condition.

time-dependent WSS vector field (assuming periodicity of the flow field for TAWSS to be sensible). Employing this observation, we use a different method to directly compute WSS LCS by computing stable and unstable manifolds of the (steady) TAWSS vector field. A stable and unstable manifold corresponding to a saddle-type fixed point of a vector field are the set of all the trajectories that asymptote to the fixed point in forward and backward time integrations, respectively. The unstable manifold tends to attract nearby trajectories, and the stable manifold tends to repel nearby trajectories in time and therefore these structures are often identified as attracting and repelling LCS, particularly in the context of unsteady vector fields.

Stable and unstable manifolds of TAWSS fixed points are computed to identify WSS LCS, a template for near-wall transport. The first step in this approach is the detection of the fixed points of the TAWSS vector field, which can be achieved by locating the triangles whose Poincaré indices are non-trivial (i.e., 1 or -1) [265]. Next, the vector field is linearized around the fixed points $\mathbf{x}_0$, i.e., $\overline{\boldsymbol{\tau}}(\mathbf{x}) = \overline{\boldsymbol{\tau}}(\mathbf{x}_0) + J_{\mathbf{x}_0}(\mathbf{x} - \mathbf{x}_0)$, where $J_{\mathbf{x}_0} = \nabla\overline{\boldsymbol{\tau}}(\mathbf{x}_0)$ is the Jacobian of $\overline{\boldsymbol{\tau}}$, from which the two eigenvalues/eigenvectors are computed. The fixed points that are of saddle-type (i.e their two eigenvalues are real and have different signs, and the eigenvectors are real) are identified. These fixed points are perturbed along the positive eigenvector (i.e., corresponding to the positive eigenvalue) in two opposite directions to obtain two initial conditions [97]. The WSS trajectories constructed from these initial conditions in forward time will trace out the unstable manifold. Similarly, perturbation along the negative eigenvector (i.e., corresponding to the negative eigenvalue) direction with backward time integration delineates the stable manifold. The trajectory integration is continued until the trajectory reaches another fixed point (typically a source or sink) or leaves the domain. Figure 8.3 depicts the procedure for computation of TAWSS manifolds and WSSET.

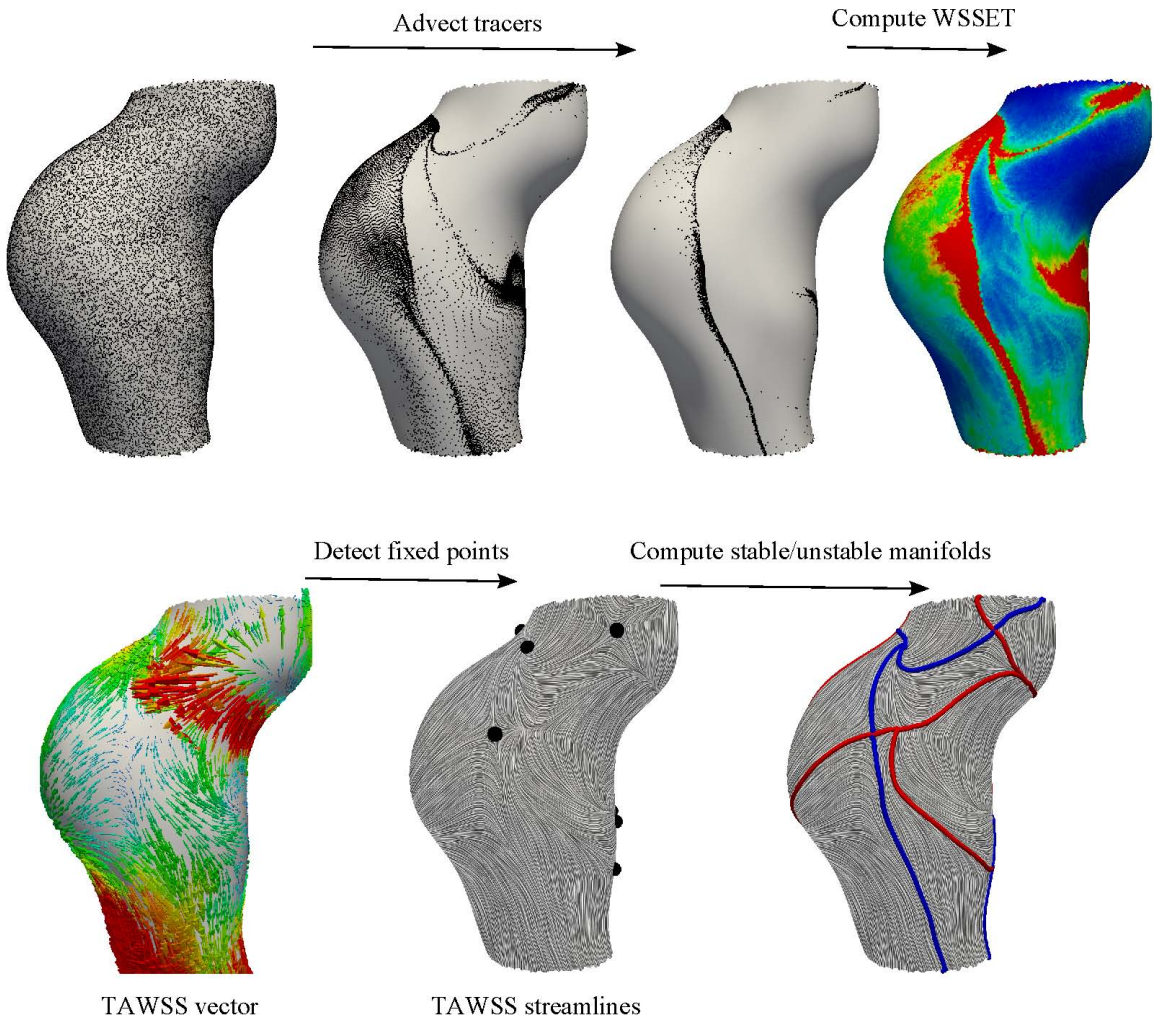

Figure 8.3: The procedure used in computation of WSS exposure time (WSSET) and TAWSS stable (red lines) and unstable (blue lines) manifolds. Trajectories are seeded on the aneurysm surface and advected in forward time to compute WSSET. Stable and unstable manifolds of the TAWSS vector field corresponding to saddle-type fixed points are computed with backward and forward time integration, respectively. These manifolds usually terminate in fixed points of other types (e.g., source or sink).

8.2.5 Transport to and from the wall

In this section, an analogy between transport into the wall versus transport from the wall is established. In Section 8.2.3 we considered the problem of continuum transport from the wall into the lumen. However, certain chemicals such as oxygen are transported from the lumen into the wall. Assuming a homogenous concentration at the inlet, such problems can

be written as

$$\frac{\partial c}{\partial t} + \boldsymbol{u} \cdot \nabla c = D\nabla^2 c \,, \tag{8.6a}$$

$$c = c_0 \quad \text{Inlet} \,, \tag{8.6b}$$

$$\frac{\partial c}{\partial n} = -A \quad \text{Wall.} \tag{8.6c}$$

In order to observe the analogy between this problem and the considerations of Section 8.2.3, let us introduce a new variable $\widetilde{c} = c_0 - c$. Substituting this into Eq 8.6 for c and simplifying gives:

$$\frac{\partial \widetilde{c}}{\partial t} + \boldsymbol{u} \cdot \nabla \widetilde{c} = D\nabla^2 \widetilde{c} \,, \tag{8.7a}$$

$$\widetilde{c} = 0 \quad \text{Inlet} \,, \tag{8.7b}$$

$$\frac{\partial \widetilde{c}}{\partial n} = A \quad \text{Wall.} \tag{8.7c}$$

Note that this is the same problem that is solved in Section 8.2.3. Therefore, referring to the change of the variable introduced, an increase (decrease) in c corresponds to a decrease (increase) in $\widetilde{c}$. Therefore, in the regions where WSSET predicts high concentration, a low concentration is actually obtained if the transport is originated from the lumen and travels into the wall. This implies that if high WSSET happens in regions of low WSS (which is usually but not always the case), then high WSS is likely to occur in regions where concentration of lumen-originated species is high. However, this is not an issue as a direct analogy can be established between the two cases. A few remarks follow.

Remark 1. The value of A will have different physical meanings in the two problems, and therefore its value will be different. However, this difference simply shifts the concentration values uniformly.

Remark 2. The above analogy is physically correct as long as $\widetilde{c} \leq c_0$. The issue arises in the negative flux boundary condition introduced in Eq 8.6. The negative flux boundary condition $\frac{\partial c}{\partial n} = -A$ will be physically wrong if c becomes zero near the wall, and this will lead to erroneous negative values for c at the wall. The requirement for c to be positive leads to $\widetilde{c} \leq c_0$.

Remark 3. The above issue does not occur if one considers a physically more realistic Robin type boundary condition $\frac{\partial c}{\partial n} = -kc$, where k is a constant. It should be mentioned that the incorporation of a Robin type boundary condition breaks the analogy, although the analogy is expected to hold in some qualitative extent. Future work should investigate this claim.

8.3 Results

Figure 8.4 and 8.5 show contour plots of WSSET, RRT, WSSdiv, and surface concentration for the AAA (P1–P6) and the other (P7–P10) models, respectively. It is observed that some of the features in regions of high WSSET and RRT match. However, a comparison of WSSET and RRT to surface concentration reveals that WSSET features are in better agreement with surface concentration. The agreement between RRT and surface concentration is improved for the simpler geometries, due to the simpler flow topology. In general, regions of high WSSET have high RRT and negative WSSdiv. However, this trend does not occur in all regions. The motivation behind the WSSdiv measure shown in the figures is that regions of negative WSSdiv correspond to converging WSS vectors, which can indicate accumulation of near-wall trajectories in these regions.

Scatter plots of the data are shown for a better comparison of the WSS measures. Figure 8.6 shows scatter plots of WSSdiv vs. RRT colored based on the WSSET value. This figure shows that high WSSET largely occurs where WSSdiv is negative and RRT is higher than a certain threshold. No apparent correlation was observed between RRT and WSSdiv. The reason for this is that RRT is based on the wall shear stress, which is proportional to the tangential velocity component, while WSSdiv is proportional to near-wall normal velocity [96, 8], thus these measures represent orthogonal velocity components. Figures 8.7 and 8.8 show scatter plots of the data comparing RRT and WSSET measures to surface concentration. The rank of the data are plotted in these figures instead of the values. This was chosen due to the nonlinear nature of the WSSET measure, which produces a wide range of values, thereby restricting any linear correlation between the data. Namely, as the integration time becomes higher, more WSS trajectories accumulate near certain fixed points of the TAWSS vector field, contributing to very high WSSET values in the vicinity of these fixed points. These figures demonstrate that WSSET has a strong correlation with surface concentration. Table 8.1 shows the Spearman's rank correlation coefficient between the WSS measures and surface concentration. WSSET and RRT are both correlated with surface concentration, however the WSSET correlation is stronger. The improvement in the WSSET correlation over RRT is more pronounced in the AAA and cerebral aneurysm models, which have more complex flows. WSSdiv is inversely correlated with surface concentration; however, the correlation is not as strong as the other measures. No correlation is obtained for WSSdiv in the coronary aneurysm case, although as Fig. 8.5 and 8.6 demonstrate regions of high surface concentration and WSSET still mostly coincides with negative WSSdiv.

Figures 8.9 and 8.10 show the stable and unstable manifolds of the TAWSS vector field colored by red and blue lines, respectively. The vector lengths are normalized for visualization and colored based on their magnitude. Comparison of these figures with Fig. 8.4 and 8.5 shows that unstable manifolds of TAWSS lead to high WSSET and high surface concentration in their surroundings. Near-wall trajectories are attracted to unstable manifolds of TAWSS and accumulate around these manifolds producing high WSSET and high surface concentration.

Figure 8.11 shows an example of how the intersections of stable and unstable manifolds

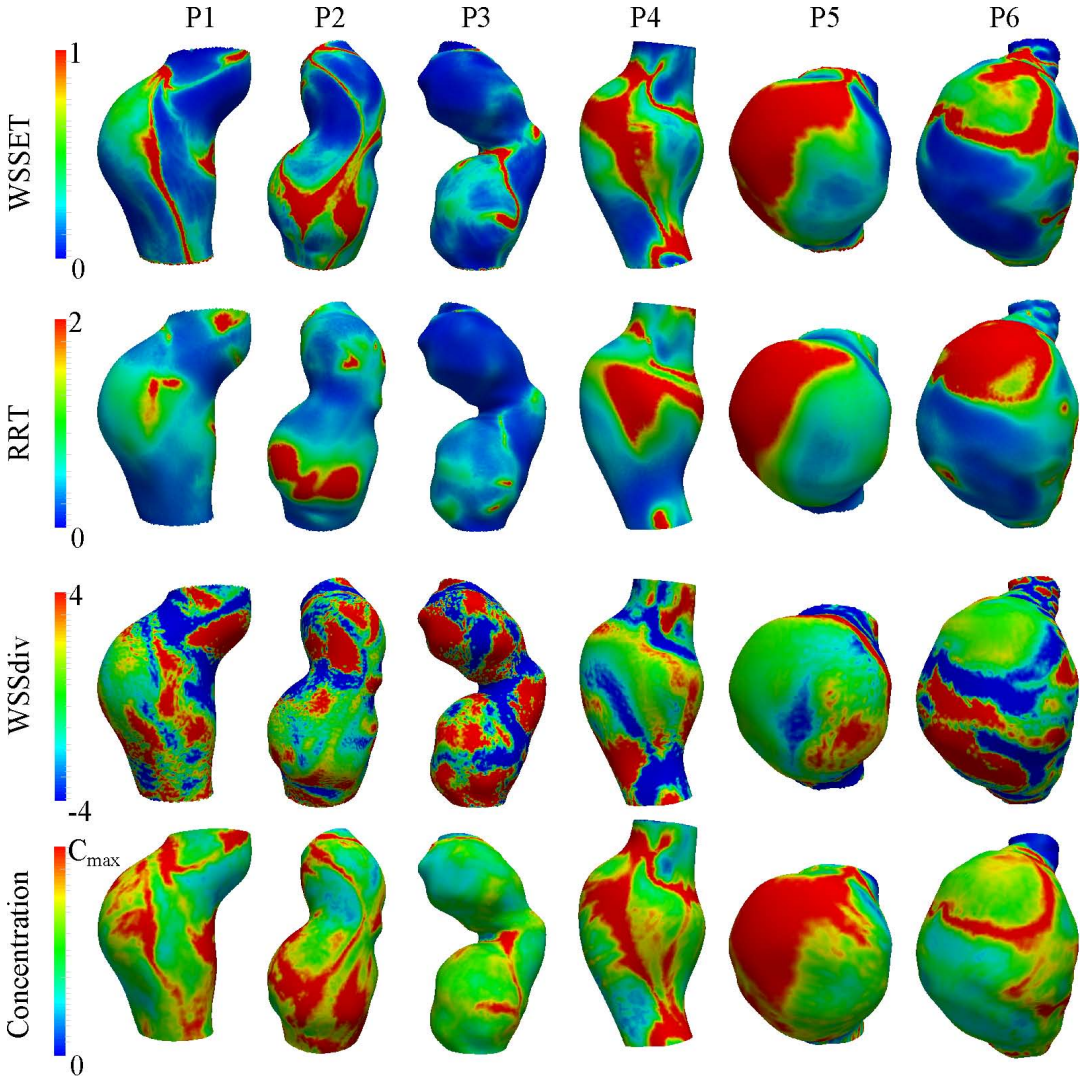

Figure 8.4: Contour plots of WSS exposure time (WSSET), relative residence time (RRT), WSS divergence (WSSdiv), and surface concentration for the six abdominal aortic aneurysm patients. RRT and WSSdiv units are $\frac{cm^2}{dynes}$ and $\frac{dynes}{cm^3}$, respectively. WSSET and concentration are defined dimensionless. Th C_{max} value in the colorbar is equal to 0.08 for Patient 1, 2, 4, and 5. It is equal to 0.03 and 0.04 for Patient 3 and 6, respectively.

of TAWSS vector divide the surface into different regions. Region I and II are the basins of attraction for the first fixed point (F1). WSS trajectories starting in these regions are attracted to this fixed point. Similarly, region III and IV are the basins of attraction for the second fixed point (F2). WSS trajectories starting in region V leave the aneurysm region, therefore region V could be regarded as the basin of attraction for a fixed point in infinity.

To evaluate the accuracy of the surface concentration results, a mesh independence study

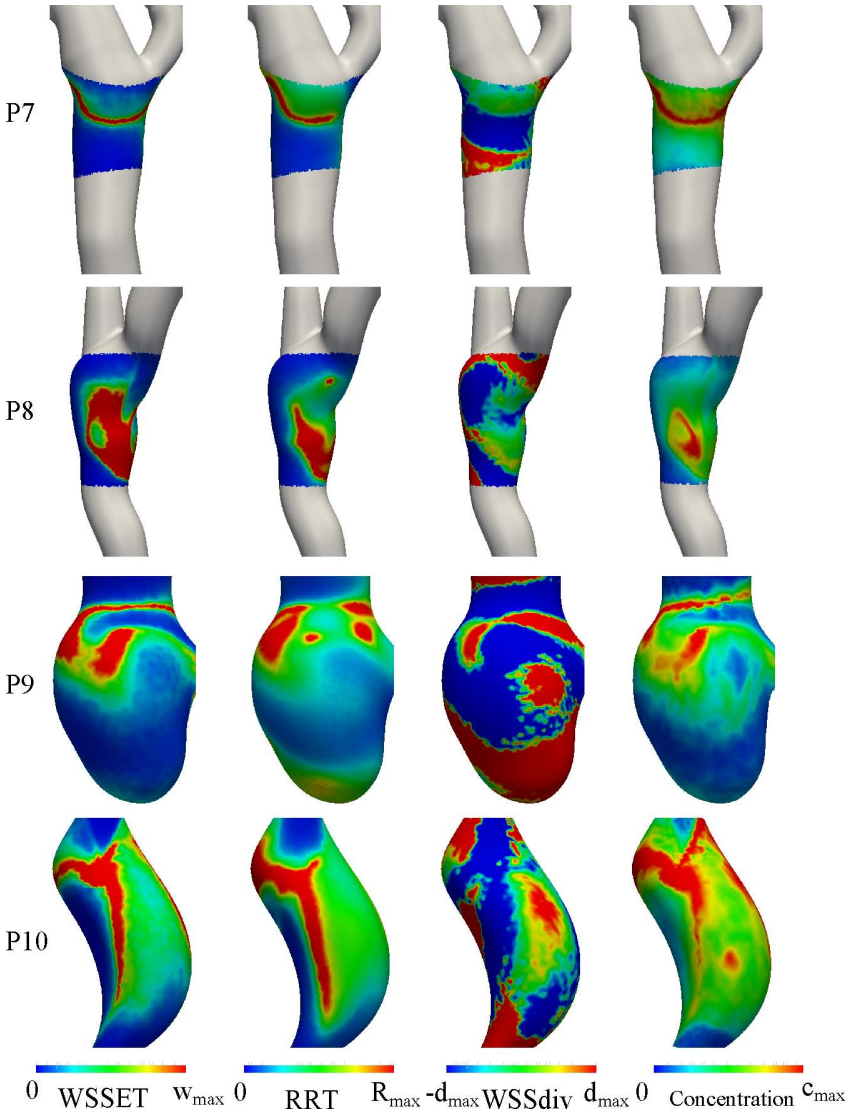

Figure 8.5: Contour plots of WSS exposure time (WSSET), relative residence time (RRT), WSS divergence (WSSdiv), and surface concentration for the carotid (P7–P8), cerebral aneurysm (P9), and coronary aneurysm (P10) patients. RRT and WSSdiv units are $\frac{cm^2}{dynes}$ and $\frac{dynes}{cm^3}$, respectively. WSSET and concentration are defined dimensionless. Th w_{max} value in the colorbar is equal to 2 for Patient 10 and 1 for the rest of the patients. R_{max} is equal to 1.5 for P7–P8, 0.3 for P9, and 0.5 for P10. d_{max} is equal to 10 for P7–P8 and 20 for P9–P10. c_{max} is equal to 0.04 for P10 and 0.05 for the other patients.

was done. Figure 8.12 shows the comparison of the original surface concentration to the surface concentration obtained with a next to wall edge size of 3.3 μm (half the original mesh) for P1. Good agreement can be seen between the two solutions.

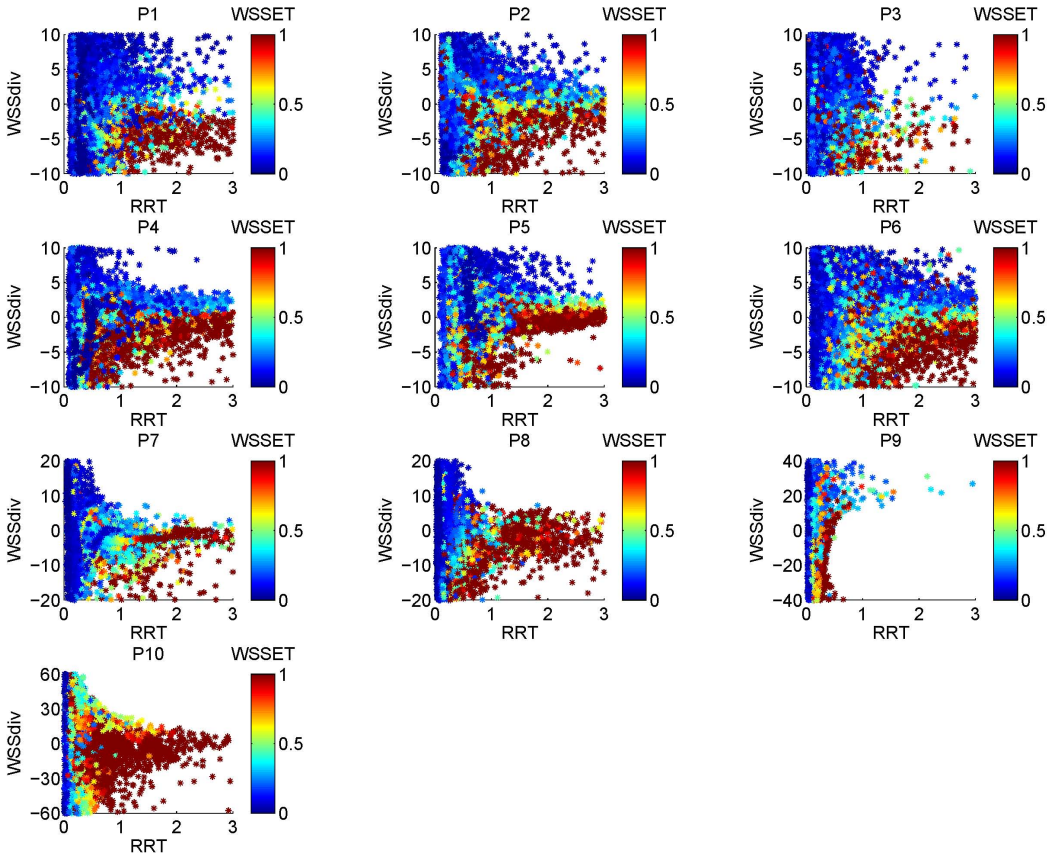

Figure 8.6: Scatter plots of WSS divergence (WSSdiv) vs. relative residence time (RRT), colored with the WSS exposure time (WSSET) value for all the patients. High WSSET occurs mostly in regions of high RRT and negative WSSdiv. RRT and WSSdiv units are $\frac{cm^2}{dynes}$ and $\frac{dynes}{cm^3}$, respectively. WSSET is defined dimensionless.

8.4 Discussion

Near-wall transport is of paramount importance in cardiovascular mass transport problems. The reasons for this are two-fold. First, coupling of hemodynamics with biological processes, such as intimal hyperplasia, atherosclerosis or thrombosis mostly involve interactions at or near the luminal surface and are therefore highly influenced by the near-wall flow conditions. Second, the high Sc numbers encountered in arterial flows leads to the formation of thin concentration boundary layers next to the wall, which marginalizes the *direct* effect of the core flow on near-wall transport.

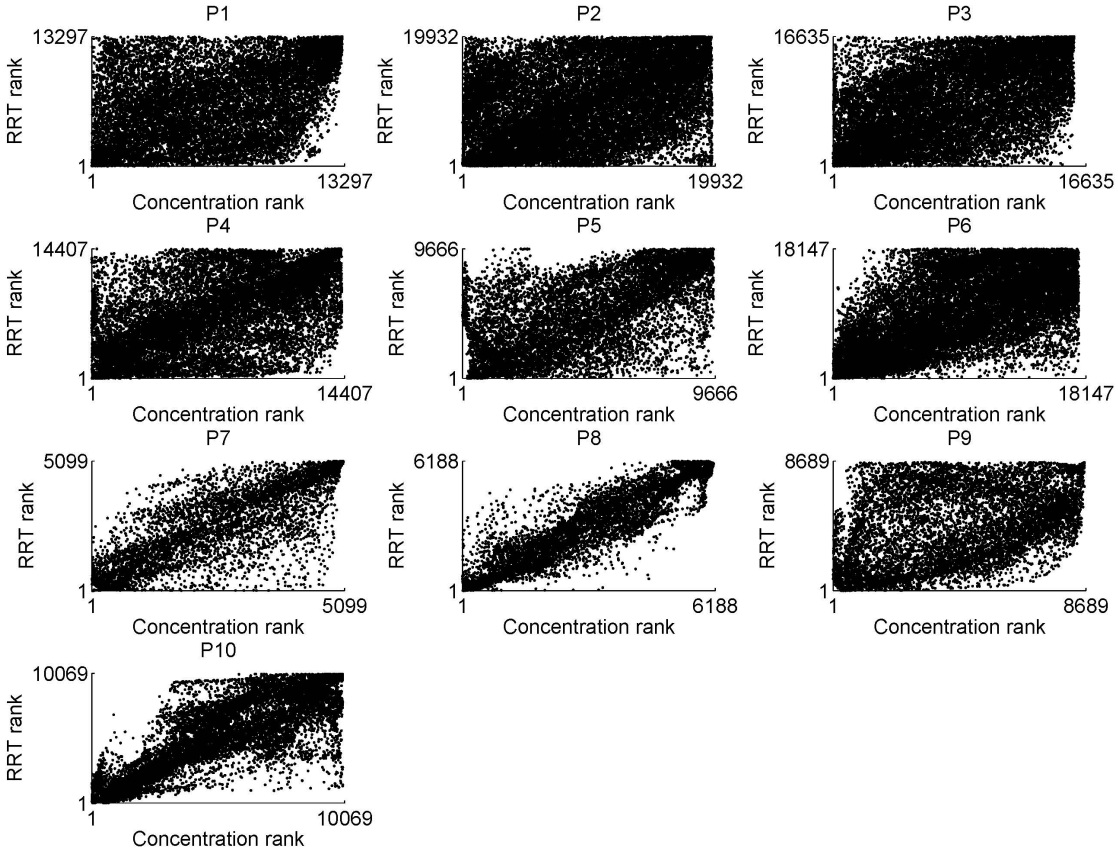

Figure 8.7: Scatter plots of relative residence time (RRT) rank vs. surface concentration rank for all the patients.

In this study we have proposed WSSET as a novel measure for quantification of near-wall stagnation and concentration. WSSET quantifies the concentration and amount of time that wall-generated species spend near the wall. Consequently, regions of high WSSET typically exhibit negative WSSdiv and elevated RRT. A comparison of WSS measures to surface concentration shows that WSSET has the best correlation with surface concentration. Namely, WSSET measures concentration residence time, and hence quantifies what is expected to be a driving mechanism for atherogenic or thrombogenic processes. WSS LCS, computed from stable and unstable manifolds of TAWSS vector field saddle points, provide insight on the near-wall flow topology and help explain WSSET distributions. Unstable manifolds of TAWSS attract the trajectories in their basin of attraction, thus trajectories accumulate near these manifolds contributing to high WSSET. Stable manifolds of TAWSS repel their

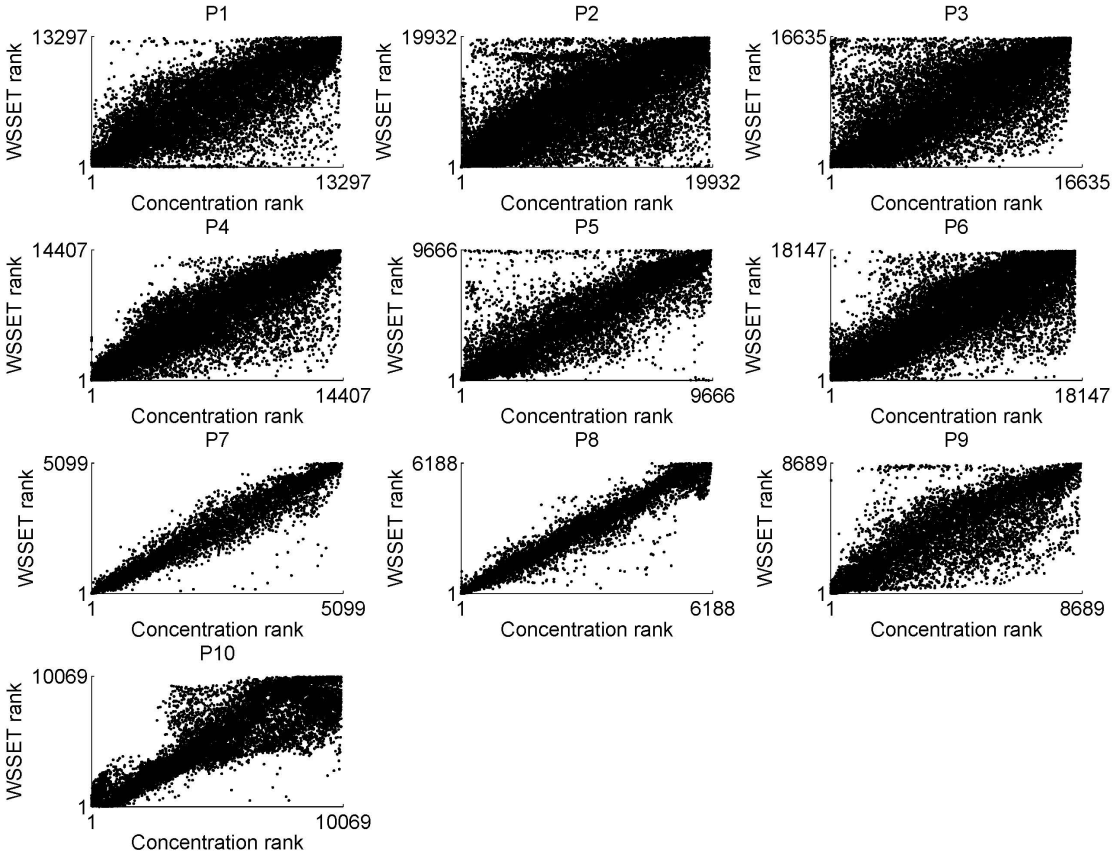

Figure 8.8: Scatter plots of WSS exposure time (WSSET) rank vs. surface concentration rank for all the patients.

nearby trajectories and mark the boundaries of different basins of attraction.

In the context of the endothelial cells (ECs) lining the vessel wall, such cells are known to sense and respond to their environment by *direct* and *indirect* mechanisms [19]. In the direct mechanism, ECs sense and respond to mechanical forces by converting forces to chemical signals (mechanotransduction) and reorganizing their cytoskeleton to affect gene expression or cell functionality [57]. In the indirect mechanism, agonists in the blood flow interact with ECs to activate various responses [72]. WSS provides a means to quantify both near-wall mechanisms. For the direct mechanism, WSS measures the frictional force per unit area exerted on the ECs. For the indirect mechanism, WSS is a surrogate for the near-wall transport velocity, and WSSET can be used to quantify the potential for indirect mechanisms on EC response. Of course, the role of WSS on the local transport of molecules, enzymes, or

Table 8.1: Point-wise Spearman's rank correlation coefficient between surface concentration and the different WSS parameters, relative residence time (RRT), WSS exposure time (WSSET), and WSS divergence (WSSdiv). The δn value used in WSSET calculations are different in each case. The correlation coefficient shown is the mean correlation coefficient between the different patients for the abdominal aortic aneurysm (AAA) and carotid patients.

	RRT	WSSET	WSSdiv
AAA patients	0.51 ± 0.09	0.79 ± 0.07	-0.47 ± 0.09
Carotid patients	0.84 ± 0.09	0.96 ± 0.01	-0.24 ± 0.04
Cerebral aneurysm	0.43	0.83	-0.57
Coronary aneurysm	0.82	0.87	0.02

cells in the near-wall region is important beyond the affect to ECs–in particular for locations where the lumen has a compromised or absent endothelial layer.

While solving the 3D advection-diffusion equation directly quantifies the complete transport of any continuum species, the high computational cost and numerical difficulties involved in accurately resolving the concentration boundary layer makes this approach prohibitively expensive in routine image-based hemodynamics applications. Computation of WSSET is far less computationally expensive, but still able to accurately convey and characterize near-wall transport. We note, however, that RRT can be computed from WSS with trivial computational effort and provides good agreement with WSSET and surface concentration in relatively simple flow environments–making it a preferred measure in such applications. WSS LCS can be computed with minimal computational time and can provide mechanistic insight not conveyed by WSSET or RRT fields.

While flow stagnation affects intravascular biological processes, it is more broadly the concentration of near-wall species, and perhaps their origin, that is more directly important. For example, Chiu *et al.* [58] have shown that monocyte adhesion to ECs occurs in regions of high near-wall concentration and long residence time. Near-wall species spend more time in regions of low TAWSS due to the smaller near-wall fluid velocity. This near-wall stagnation is captured by both RRT and WSSET measures. However, the WSSET measure is influenced not only by the amount of time that trajectories spend near the wall, but also the concentration of near-wall trajectories and their origin. In relation, the fixed points of TAWSS that have larger basins of attraction will generate higher WSSET in their vicinity (cf. Fig. 8.11). The stable manifolds of TAWSS show the boundary of these basins of attraction and could be used to estimate how much an attracting fixed point contributes to high WSSET.

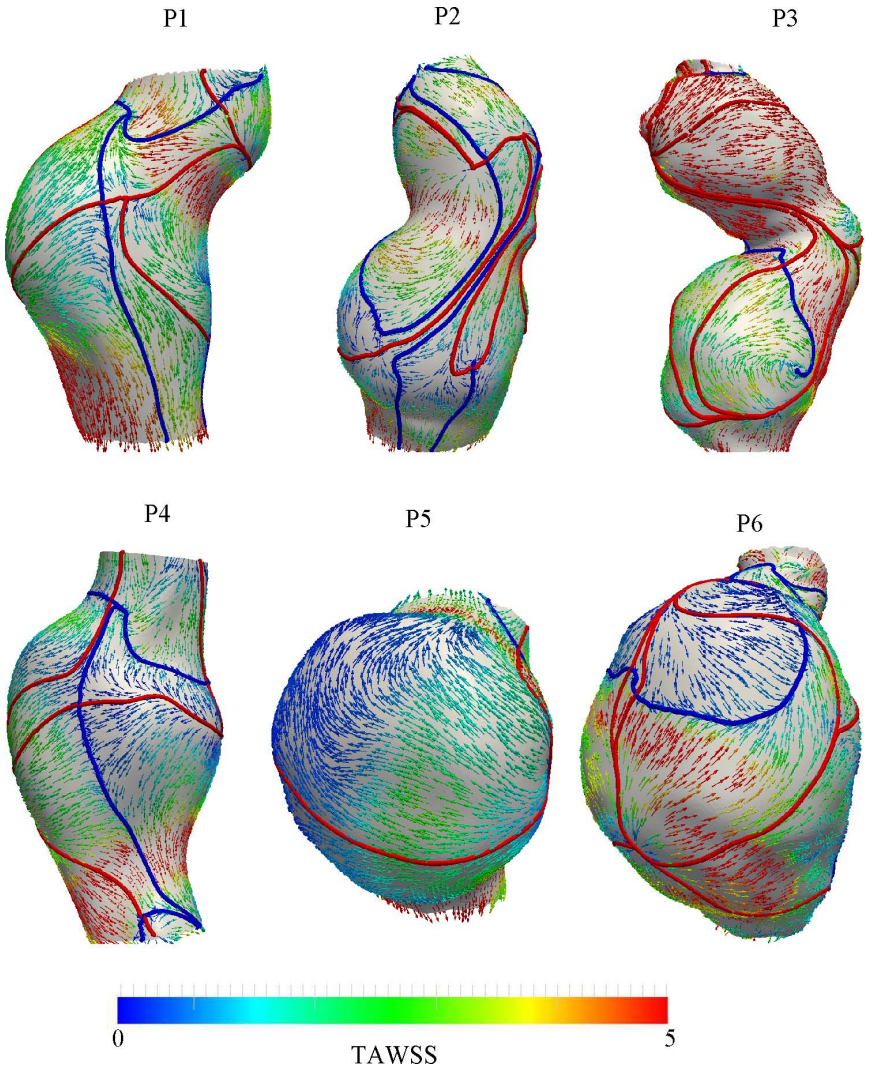

Figure 8.9: Stable (red line) and unstable (blue line) manifolds of TAWSS vector field for the six abdominal aortic aneurysm patients. The TAWSS vector length is normalized for visualization, and colored based on its magnitude. The unit for TAWSS is $\frac{dynes}{cm^2}$.

OSI [135] is a leading WSS measure that has been widely used to characterize oscillations in the WSS vector field. The main motivation behind this measure is the observation that ECs prefer to align in regions with a well defined TAWSS vector direction and demonstrate inflammatory response in regions with oscillatory WSS. From a transport perspective, the peak value of OSI = 0.5 corresponds to a TAWSS vector with zero magnitude (infinite RRT). Therefore, in these regions no net tangential convective displacement occurs contributing to high near-wall stagnation. On the other hand, in a region with zero OSI the WSS vector does not change its direction, therefore contributing to a potentially larger TAWSS vector

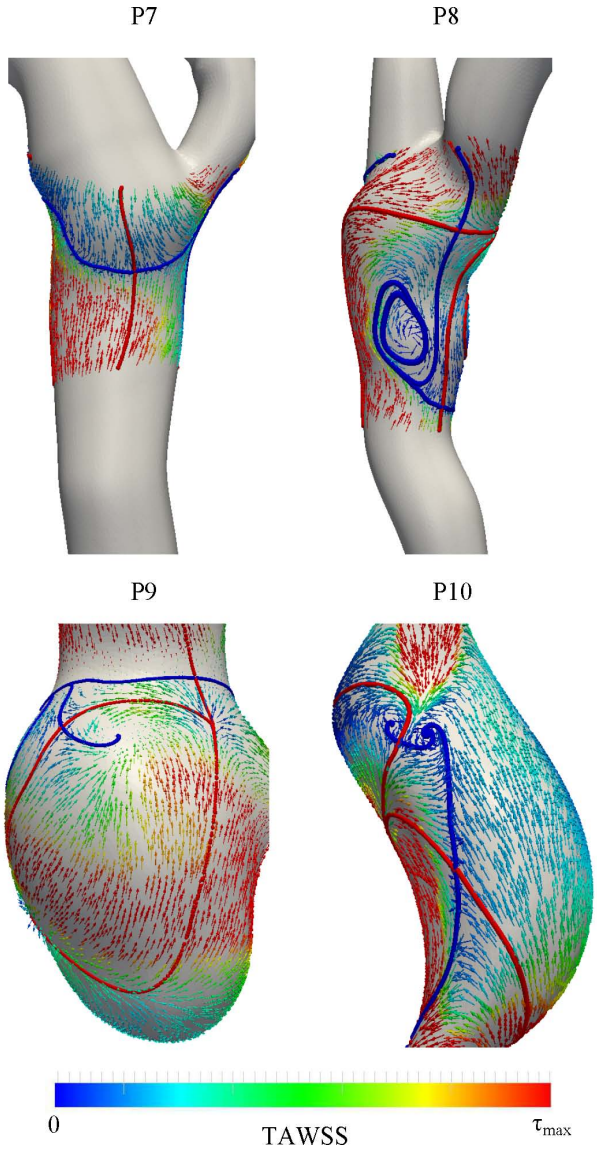

Figure 8.10: Stable (red line) and unstable (blue line) manifolds of TAWSS vector field for the carotid (P7–P8), cerebral aneurysm (P9), and coronary aneurysm (P10) patients. The TAWSS vector length is normalized for visualization, and colored based on its magnitude. The unit for TAWSS is $\frac{dynes}{cm^2}$. The τ_{max} value is equal to 10 for P7–P8 and 20 for P9–P10.

magnitude with a typically well defined direction. However, the OSI measure by itself does not explain transport. OSI only explains amplification or reduction in effective near-wall transport. This observation is similar to concepts of mobility discussed by [172] in a broader context of Eulerian vector field characterization. Regions of low OSI contribute to a more effective near-wall convective tangential transport, whereas high OSI reduces effective trans-

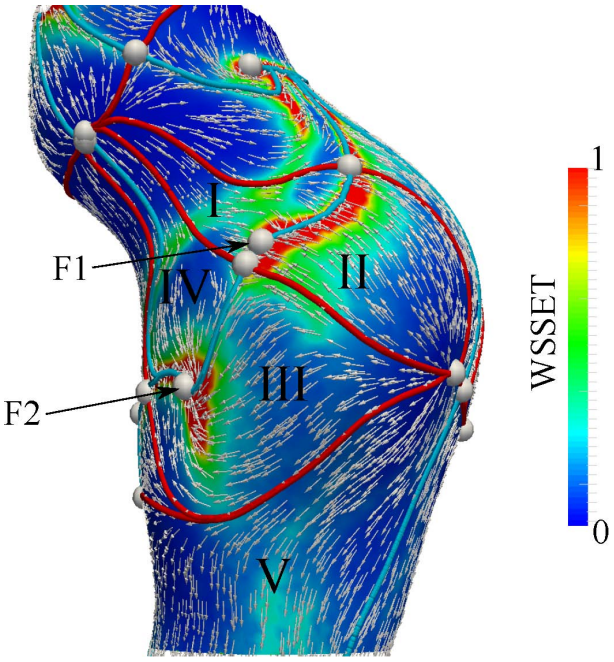

Figure 8.11: Intersection of stable (red line) and unstable (blue line) manifolds of the TAWSS vector divide the aneurysm surface into different regions. WSS trajectories in regions I and II are attracted to one TAWSS vector fixed point (F1), while trajectories in regions III and IV are attracted to another fixed point (F2). The TAWSS manifolds largely influence the WSS exposure time (WSSET). TAWSS vectors are normalized for visualization. Fixed points of TAWSS are marked with grey spheres. Patient 1 is shown in this figure.

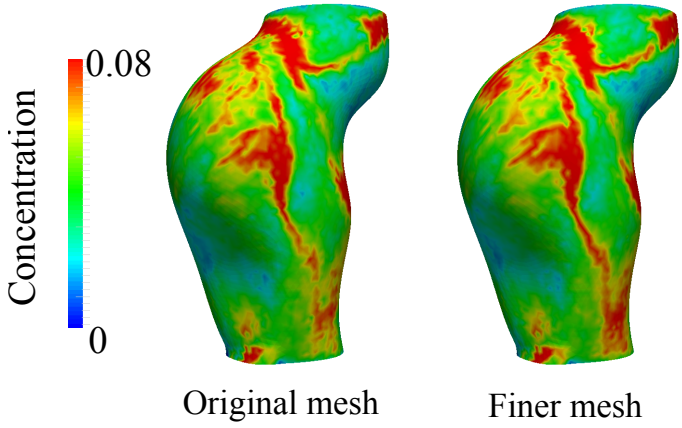

Figure 8.12: Comparison of surface concentration obtained from the original mesh (next to wall edge size 6.6 μm) to a finer mesh (next to wall edge size 3.3 μm) for the first AAA Patient (P1).

port due to the rapid temporal change in WSS vector. It should be emphasized though that the WSS vector magnitude needs to be considered to quantify near-wall transport. Recently, the prevailing theory that atherosclerosis is positively correlated with OSI has been challenged [198]. A possible explanation for these inconsistencies may be that many experimental studies impose uniform oscillatory flow in simple settings. This can lead to exaggeratedly high near-wall stagnation, promoting atherogenic processes. However, in vivo values of OSI are typically more moderate, and in such contexts the correspondence between locations of higher OSI and the accumulation of near-wall species is less direct. Due to the spatially uniform or less complex flows in experimental studies, this phenomena can be overlooked.

In order to compute WSSET, we seeded trajectories uniformly on the surface. These trajectories represent surface-generated near-wall species. Therefore, regions of high WSSET will represent high near-wall concentration of species if the effective flux of species is coming from the wall into the lumen. In correspondence with the Eulerian advection-diffusion equation, this implies that the flux boundary condition at the wall needs to be inward (into the lumen). In cases where the flux boundary condition at the wall is outward (into the vessel wall) and uniform concentration of species exists at the inlet of the domain (e.g. oxygen or platelet), opposite relations woud be obtained (see Section 8.2.5). For instance, at a reattachment or impingement point, a source type fixed point in the WSS vector field can be generated. This source will push wall-generated trajectories away, therefore causing low WSSET in its vicinity. However, if the species are coming from the core flow, high concentration will occur in this region. Therefore, it is important to keep the nature of the transport process in mind when measures such as WSSET or RRT are being studied.

Another important consideration is that WSS and the flux boundary condition at the wall can be interconnected. For example, WSS can affect the permeability of the ECs to certain species, therefore creating a shear-stress-dependent mechanism for the resistance of the surface to mass transfer [254]. WSS can also influence the flux of wall-generated species. For example, high WSS can lead to a higher flux of NO at the vessel wall [202]. These effects could be accounted for in the WSSET approach by releasing tracers at each location proportional to the non-uniform flux. However, such modifications can not be integrated in the RRT measure.

We have ignored the effect of diffusion and normal velocity on the WSSET measure. In the previous Chapter we showed that the qualitative behavior of WSSET is minimally changed . Diffusion causes random near-wall trajectories to escape the near-wall region in long integration times, therefore the WSSET is generally reduced. Normal velocity is second order in δn and generally small near the wall; however, it is proportional to WSS divergence. Significant negative WSS divergence can cause near-wall trajectories to escape the near-wall region. The effect of WSS divergence on WSSET can become important in higher Reynolds numbers where the WSS divergence can become very high. In the present study, we only used one cardiac cycle of WSS data and assumed periodicity to generate WSS trajectories, although cycle-to-cycle variations in WSS exist in some cardiovascular flows such as AAAs [203]. However, our aim in this study was to demonstrate the applicability of our

approach and comparison to existing methods.

In this study, to characterize the near-wall flow topology we computed the stable/unstable manifolds of TAWSS vector. This is based on the observation that the near-wall transport is quasi-steady and the WSS LCS match the TAWSS stable/unstable manfiolds. However, this quasi-steady behavior can break down if the Reynolds and Womersley numbers are sufficiently increased. For example, exercise in AAA patients creates a more complex flow field [9], with higher WSS values [151]. If the intensity of exercise is strong, the WSS LCS can slightly deviate from the stable/unstable manifolds of TAWSS and demonstrate some time dependence behavior. Figure 8.13 shows the surface concentration obtained from exercise during two time points in a cardiac cycle. Small intra-cycle variations are observed. Complex patterns in surface concentration are observed where some of the features do not match the attracting WSS LCS obtained from the unstable manifolds.

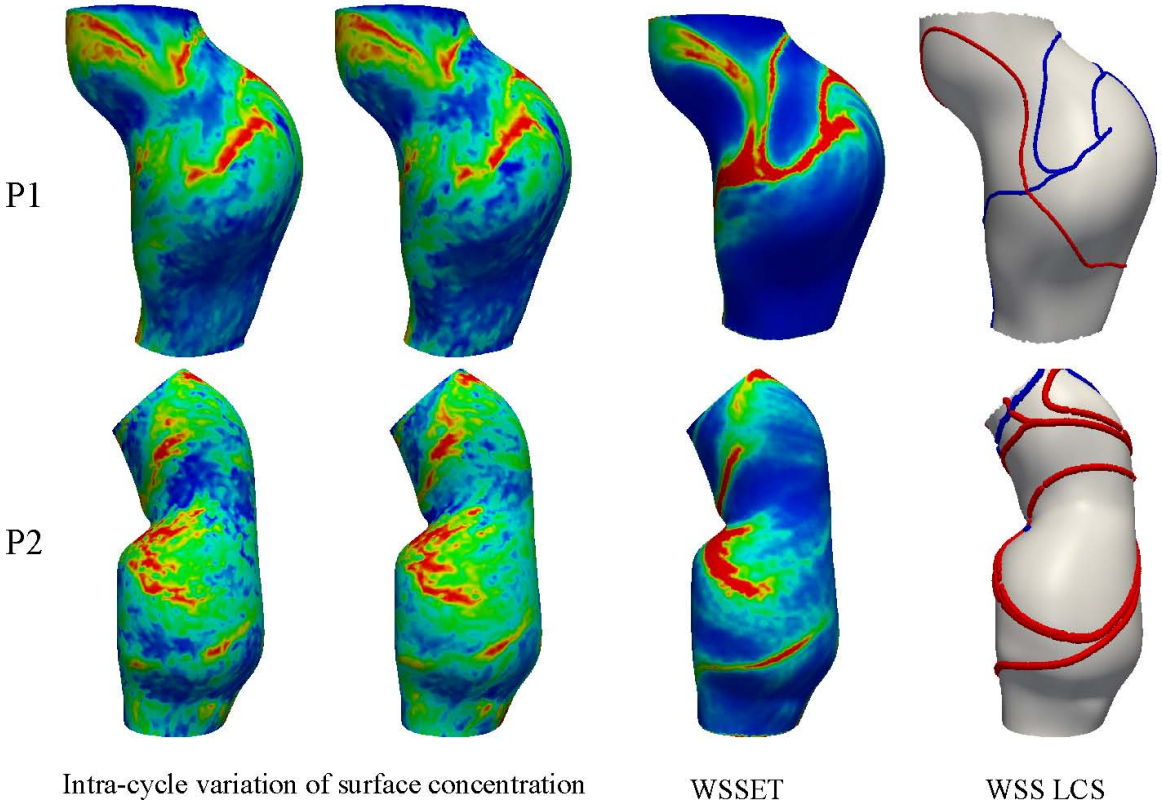

Figure 8.13: Surface concentration, WSS exposure time (WSSET), and WSS LCS (blue line is unstable manifold, and red line is stable manifold) during exercise. Slight intra-cycle variation in the surface concentration is observed. The first two patients are shown in this figure.

Fortunately, in order to characterize the near-wall stagnation, the WSSET measure can still be applied under these flow conditions, since it is a Lagrangian approach. However, the

relevance of RRT as an Eulerian measure becomes questionable, since the TAWSS vector no longer indicates effective near-wall transport. Time-averaged measures like RRT always have the risk of being inaccurate if their averaging time does not capture the flow transients. Finally, the Newtonian blood rheology assumption might be questionable. This can potentially affect our results in two different ways. First, the WSS vector field obtained from a Newtonian and non-Newtonian assumption can be different, although these differences have been shown to be small in patient-specific AAAs [166]. Second, variations in viscosity affect the near-wall fluid velocity in Eq. 7.1. However, these variations only scale the near-wall fluid velocity and will not change the near-wall velocity direction. Therefore, as long as these changes in the magnitude of the near-wall fluid velocity do not violate the quasi-steady transport behavior, WSS LCS will still be identified from stable/unstable manifolds of the TAWSS vector. Consequently, the same near-wall flow topology will persist and the qualitative aspect of WSSET will not be affected.

Chapter 9

On the importance of wall shear stress fixed points in cardiovascular flow

9.1 Introduction

While different measures have been developed to study different WSS patterns (see Chapter 6), the full vectorial nature of WSS has received less attention. In this Chapter the fixed points of the WSS vector field are visited. A fixed point (equilibrium point or critical point) of a vector field is a point where the vector field takes a zero value. It should be mentioned that instantaneous critical points are not truly fixed in unsteady flows, as they could appear, move and disappear with the flow [146]. However, we will adapt this terminology for both steady and unsteady flows.

Consider a vector field given by

$$\dot{\mathbf{x}} = \mathbf{f}(x, t) \ . \tag{9.1}$$

Assume a fixed point exists at $\mathbf{x} = \mathbf{0}$. The vector field can be linearized around this fixed point:

$$\dot{\mathbf{x}} = \mathcal{A}\mathbf{x} \ , \tag{9.2}$$

where $\mathcal{A}$ is an $n \times n$ matrix, and n is the spatial dimension of the vector field. Note that the linearized form $\mathcal{A}$ depends on the fixed point being considered. The fixed point can be classified based on the eigenvalues of $\mathcal{A}$. Table 9.1 shows the different classifications. The node type fixed points could also be further classified as star and degenerate fixed points. Figure 9.1 depicts the different types of fixed points

A few studies have identified the WSS fixed points in the context of blood flow. WSS fixed points have been identified in cerebral aneurysms and have been linked to wall thinning [262, 250]. Saddle type WSS fixed points were observed on the aortic side of the aortic valve, and the complex WSS vector field that this induces has been hypothesized to be related to calcific aortic valve disease, which often occurs on the aortic side of the valve [98].

Table 9.1: Classification of fixed points based on the eigenvalues (λ) of the linearized vector field.

λ	fixed point
$\lambda_1, \lambda_2 < 0$	stable node (sink)
$\lambda_1, \lambda_2 > 0$	unstable node (source)
$\lambda_1 < 0 < \lambda_2$	saddle point (hyperbolic)
$\lambda_{1,2} = -\alpha \pm i\beta$	stable spiral (sink)
$\lambda_{1,2} = \alpha \pm i\beta$	unstable spiral (source)
$\lambda_{1,2} = \pm i\beta$	center (elliptic)

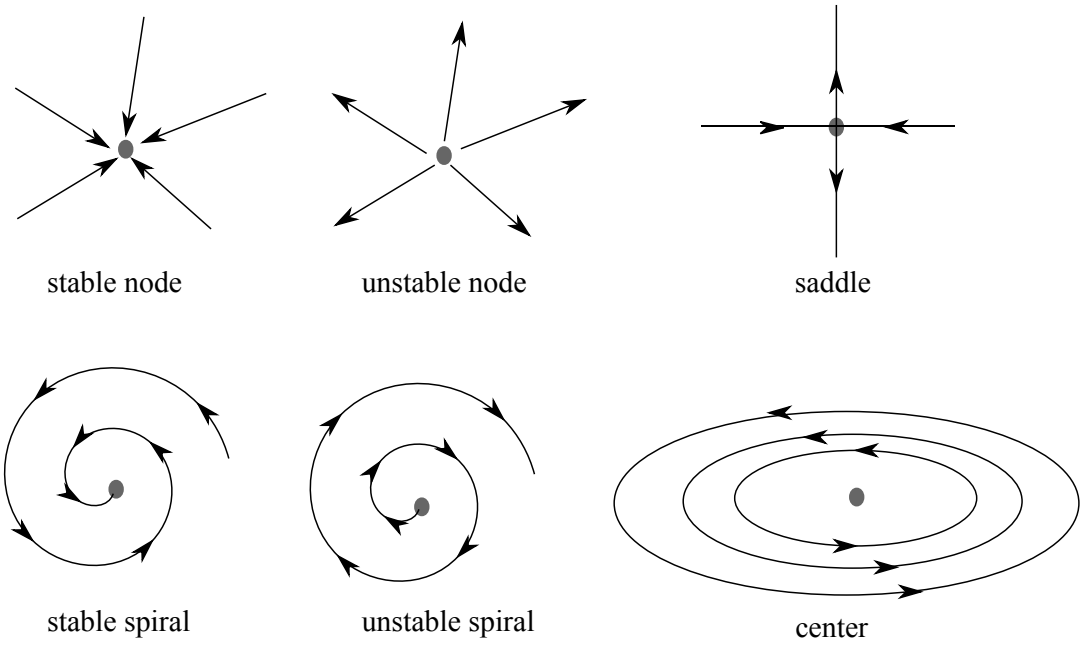

Figure 9.1: The different classifications of fixed points.

The importance of WSS fixed points can be viewed in three different ways. First, the WSS fixed points are closely related to the flow topology, and flow features like flow separation and impingement affect these fixed points. Second, the fixed points of the time-average WSS vector field and their associated manifolds govern the near-wall transport in cardiovascular mass transport problems. Finally, the instantaneous WSS fixed points can potentially influ-

ence the endothelial cells (ECs) as these points have no preferred direction (zero magnitude) and the WSS vector direction changes dramatically around them. These three mechanisms are discussed in the next sections.

9.2 WSS fixed points and flow topology

WSS streamlines (also called skin-friction lines and limiting streamlines) have been used extensively as wall signatures of flow separation, in the fluid dynamics and aerospace literature. Loosely speaking, the approaching of the WSS magnitude to zero and convergence of WSS vectors is an indicator of upwelling motion and possibly flow separation [285]. While WSS streamlines and fixed points have been used for a long time to study flow separation [42, 261, 201], a rigorous theory of flow separation based on WSS and dynamical systems theory has been proposed for steady flows more recently [249]. According to this theory, four different robust closed separation patterns are possible. The separation point corresponds to a saddle type fixed point of WSS and the reattachment point can be either a stable node, a stable spiraling node, or a limit cycle. The separation pattern can also be simply just an attracting limit cycle. Figure 9.2 depicts these scenarios. The authors have also extended this theory to a special type of unsteady flows [249]. Alternatively, one could also use the vorticity lines on the surface instead of the wall shear stress, as they are orthogonal to each other:

$$\boldsymbol{\tau} = \mu \hat{\mathbf{n}} \times \omega_{wall} \ , \tag{9.3}$$

where ω_{wall} is the vorticity at the wall, and $\hat{\mathbf{n}}$ is the normal vector.

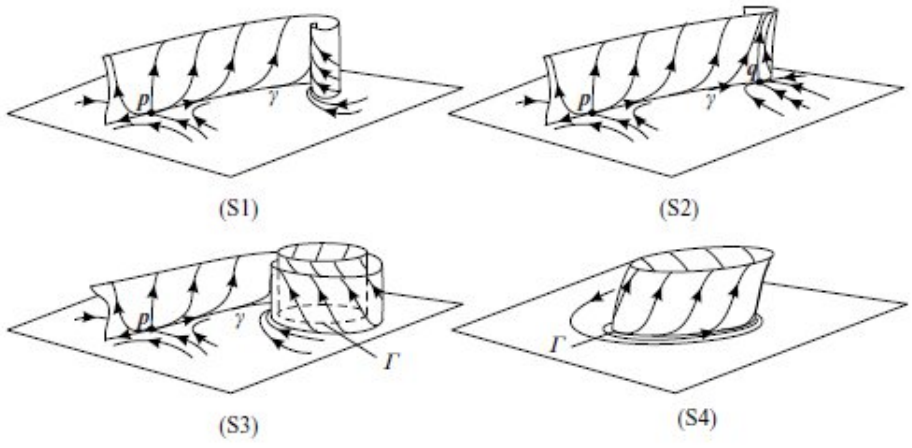

Figure 9.2: Four different separation patterns. In the first three cases the separation point is a saddle type fixed point and the reattachment point is a stable spiralling node (S1), a stable node (S2), or a limit cycle (S3). S4 is a stable limit cycle. Figure adapted from [249].

Flow separation can also occur at an ordinary point of the WSS vector field where the WSS vectors are converging. This has been termed open separation [277, 285]. It should be pointed out that emergence of WSS fixed points in attached flows are rare, however recently they have been observed in turbulent channel flows and have been associated with the transport of a vortex at the tail of a large scale structure towards the wall [149, 39]. WSS fixed points have also been closely related to chaotic advection in porous media [152], which could perhaps impact the mixing of solutes in thrombus clots. Finally, experimental techniques such as oil-film visualization have been used to visualize the WSS topology and fixed points associated with flow separation [155, 300].

In unsteady flows, the instantaneous fixed points of the WSS vector field can have less obvious relevance to the actual transport, due to the inherent unsteadiness in the flow. However, in most cardiovascular applications the instantaneous WSS fixed points persist for some time while being modestly advected, therefore these structures could still be relevant to flow topology. For instance, the saddle type fixed points can be signatures of possible flow separation, and stable node type fixed points can be indicators of possible upwelling motion. The temporal persistence of these fixed points can become reduced in complex turbulent flows and therefore their relevance less obvious, although their topology has been studied for wall-bounded turbulent flows [62].

A local Taylor series expansion can be performed around a no slip wall to obtain a reduced-order estimate of flow topology near the wall [201, 114, 297]. This leads to expression of velocity near the wall in terms of WSS, WSS gradient, and pressure gradient, reducing the Navier-Stokes to a set of ODEs. It would be interesting to extend these methods to include pulsatile flows with Womersley solution.

A source type fixed point in WSS vector field can be associated with flow impingement. Flow impingement often occurs in aneurysms (see Chapter 3). Flow impingement causes local elevation in the pressure on the vessel wall. Although these local elevations are fairly small compared to blood pressure, it can cause greater wall motion [290]. This greater wall deformation can be translated to the smooth muscle cells and fibroblast, potentially inducing response. In cerebral aneurysms, small and narrow impingement jets have been correlated to rupture [47]. Source type fixed points in WSS have been related to wall thinning in cerebral aneurysms [262, 250]. Furthermore, hyperplasia has been observed in the sites of flow impingement [174].

Figure 9.3 shows examples of different types of WSS fixed points emerging in the abdominal aortic aneurysms.

9.3 WSS fixed points and near-wall transport

In the previous Chapter, the role of saddle type fixed points of the time-average WSS vector field on near-wall transport was discussed. These fixed points and their associated stable and unstable manifold govern the near-wall transport in cardiovascular mass transports. The unstable manifold of these fixed points correspond to the attracting WSS LCS, which attract

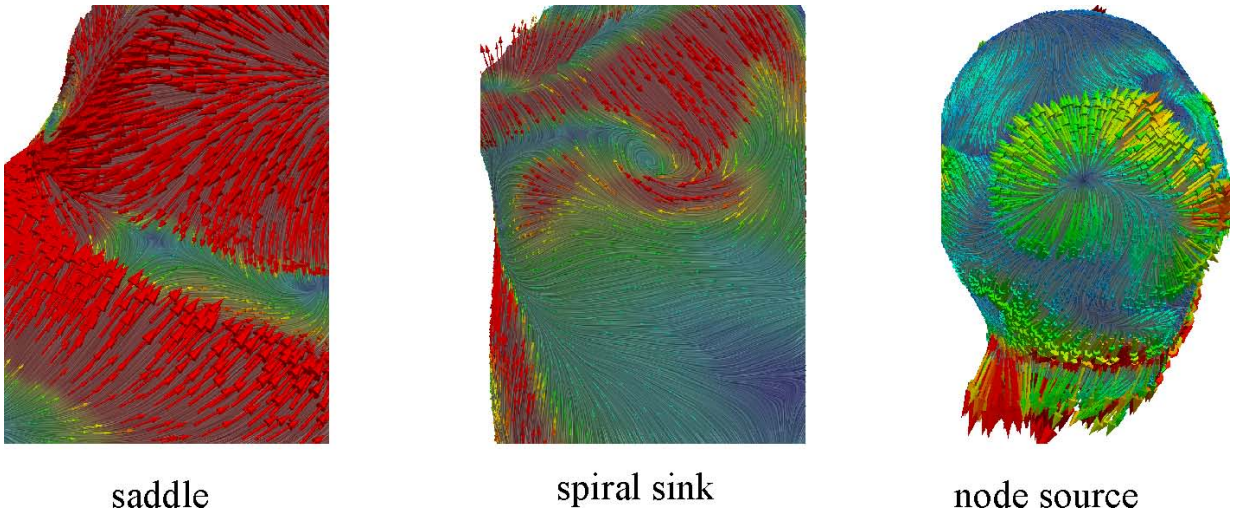

Figure 9.3: Example of different types of WSS fixed points in abdominal aortic aneurysms.

the biochemicals in their vicinity and lead to high surface concentration. The exact location of the saddle type fixed point will be the location with the highest surface concentration along the unstable manifold, as this fixed point acts as an attractor.

The source and sink type fixed points of the time-average WSS vector also play an important role in near-wall transport. The stable and unstable manifolds originating from the saddle type fixed points terminate in the source/sink fixed points. Therefore, these fixed points determine the extent of the manifolds. Furthermore, the sink type fixed points also attract biochemicals in their surrounding, leading to high concentration at these locations. Figure 8.11 in the previous Chapter shows an example of how time-average WSS fixed points and their associated manifolds govern near-wall transport.

Some studies have depicted WSS streamlines as signatures of near-wall transport in blood flow [128, 56]. For instance, the changes in WSS streamlines in cerebral aneurysms after coiling has been studied [103]. Complex vectorial WSS patterns have been shown in aneurysms using phase-contrast magnetic resonance imaging [187]. Different types of WSS fixed points have been identified in cerebral aneurysms [56, 16]. However, the relation of WSS fixed points and WSS LCS to near-wall transport had not been investigated prior to our study [8]. Recently, the role of attracting WSS LCS in heat transfer in Rayleigh-Benard convection has been established [18]. Interestingly, the Prandtl number in that study was 0.7, well below the 1000 threshold proposed in Chapter 7. Our preliminary investigations of lower Schmidt numbers in abdominal aortic aneurysm mass transport also revealed that the prominent attracting LCS can still be relevant in determining the qualitative high surface concentration patterns in much lower Schmidt numbers, although some changes in the patterns do appear. This suggests that these structures can be useful in studying heat/mass transfer at even much lower Prandtl/Schmidt number. This is anticipated to open up a new venue for studying these structures in various applications.

9.4 WSS fixed points and endothelial cells

The instantaneous fixed points in the WSS vector field can have potential impact on the ECs. It is well known that the ECs exhibit inflammatory response in regions of low WSS. Moreover, high spatial gradients in WSS vector field (particularly direction) can potentially impact EC functionality, as ECs respond to flow in a collective manner and high spatial variations in WSS direction can impair their response. The fixed points in the WSS vector field have zero WSS magnitude and large variations in WSS direction occurs around them. We propose to track WSS fixed points and define a WSS fixed point exposure time measure that for each surface element measures the accumulated amount of time that all the WSS fixed points spend inside that element

$$\text{WSSfET}(e) = \sum_{p=1}^{N_t} \int_0^{\mathcal{T}} H_e(p,t)\ \mathrm{d}t \tag{9.4}$$
$$H_e = \begin{cases} 1 \text{ if } \boldsymbol{x}_p(t) \in e \\ 0 \text{ if } \boldsymbol{x}_p(t) \notin e \end{cases},$$

where, $\mathbf{x}_p(t)$ is the position of the WSS fixed point, H_e is the indicator function for element e, N_t is the total number of WSS fixed points. To compute WSSfET the location of all the fixed points at each time step needs to be identified.

The eigenvalue of the linearization of the WSS vector field around the fixed point can also be incorporated into the above definition as a measure of how strong the fixed point is. Namely,

$$\text{WSSfET}(e) = \sum_{p=1}^{N_t} \int_0^{\mathcal{T}} H_e(p,t)\lambda(p,t)\ \mathrm{d}t \tag{9.5}$$
$$H_e = \begin{cases} 1 \text{ if } \boldsymbol{x}_p(t) \in e \\ 0 \text{ if } \boldsymbol{x}_p(t) \notin e \end{cases},$$

where $\lambda(p,t)$ is the sum of the magnitude of the two eigenvalues of $\mathbf{x}_p(t)$.

Figure 9.4 shows an example of the WSSfET measure. The relevance of this measure should be validated with cell culturing experiments. It may be perceived that the ECs might also be sensitive to the type of WSS fixed point, which can easily be incorporated in the above measures. Future experiments should investigate these mechanisms.

9.5 Discussion

WSS is the most studied parameter in cardiovascular flows. Various measures have been proposed to study different aspects of WSS relevant to cardiovascular disease (see Chapter 6). In this study we propose new perspectives on WSS vector fields. Particularly, the WSS fixed

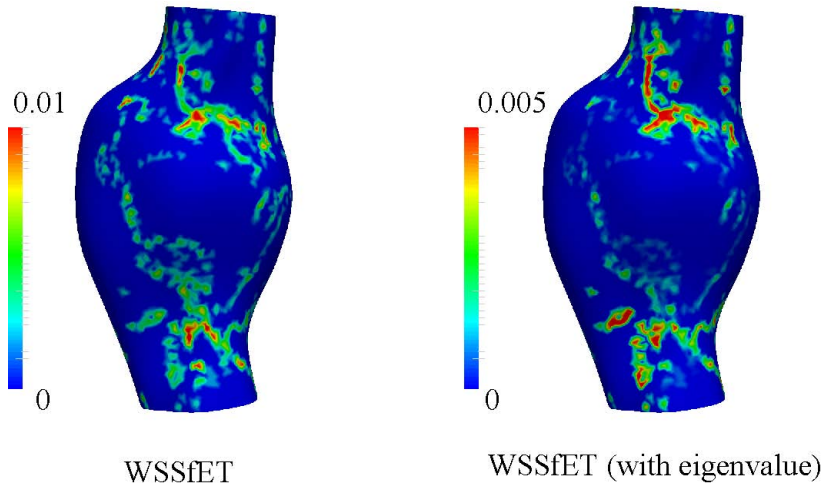

Figure 9.4: WSS fixed point exposure time (WSSfET) for an abdominal aortic aneurysm. The right pannel accounts for the eigenvalue magnitudes.

points are an important aspect of WSS vector field that has received very little attention. In this Chapter we have outline three different aspects where WSS fixed points can be useful in studying blood flow. The first aspect deals with relevance of these fixed points to the flow topology away from the wall. This area is well studied in the fluid dynamics literature. Although, unsteady flows represent a major challenge. Next, the fixed points of the time-average WSS vector field play a vital role in cardiovascular mass transport problems. These points and their associated manifolds organize mass transport near the vessel wall. Finally, the instantaneous WSS fixed points are likely to be important on EC mechanotransduction. This unexplored area remains to be studied in future experiments.

Chapter 10

Conclusion

In this thesis, the flow topology, complex wall shear stress patterns, and progression of abdominal aortic aneurysms (AAA) has been investigated. We have used Lagrangian coherent structures to study the flow topology during rest and exercise. We have quantified mixing using Lagrangian particle tracking. The expansion of the lumen, and deposition of intraluminal thrombus between baseline and followup images have been compared with hemodynamics. Complex spatial and temporal variations in wall shear stress (WSS) vector have been characterized. The concept of Lagrangian WSS structures and their utility in studying near-wall transport has been introduced. We have defined WSS exposure time (WSSET) as a novel measure of near-wall stagnation and concentration. Finally, the different important roles that WSS fixed points can play in blood flow have been discussed.

10.1 Future directions

There are several areas that this research can be extended in future work:

1. Positron emission tomography-computed tomography (PETCT) has recently gained attention in quantifying inflammatory cellular activity inside AAA wall. Figure 10.1 shows an example in one of the AAA patients used in this study. Correlation of the metabolic activity quantified by PETCT to hemodynamics would be an interesting study. Particularly, we hypothesize that near-wall transport quantified by WSSET plays an important role.

2. A preliminary investigation on the effect of exercise on mass transport in AAAs was done in Chapter 8. It appears that exercise can create very complex near-wall transport patterns, without necessarily eliminating regions of high surface concentration. Future work should investigate this observation.

3. Very good correlation between surface concentration obtained from continuum transport and WSSET was observed in this thesis. The continuum transport models utilized

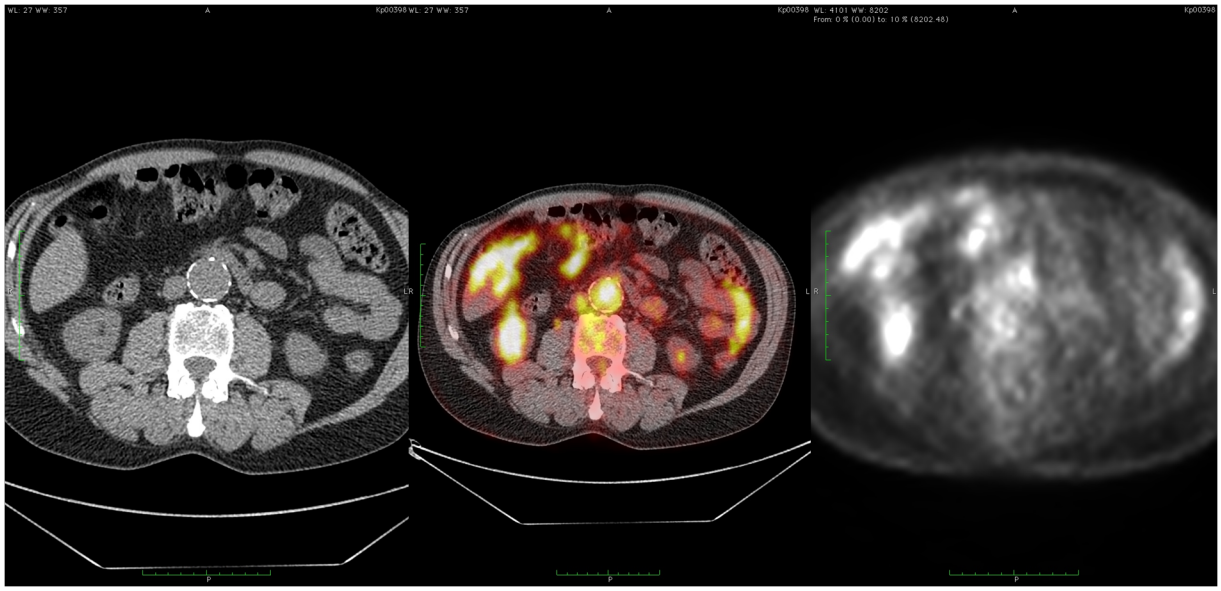

Figure 10.1: Positron emission tomography-computed tomography (PETCT) scan of a AAA patient.

Neumann boundary conditions, while many cardiovascular applications involve Robyn boundary conditions. Future work will investigate the role of Lagrangian WSS structures in those problems. Moreover, extension of the Lagrangian surface transport model to include reaction between different species is an interesting topic. Lagrangian methods have been used to model advection-diffusion-reaction using Lagrangian particle tracking [206]. We carried out a preliminary investigation on this topic. We extended the methods in [206] to system of advection-diffusion-reaction in several species for 2D flows. While using these methods for homogeneous flows reproduced the correct analytical results, we observed difficulty and serious limitations in extension to spatially heterogenous flows.

4. Lagrangian WSS structures and WSSET tools have been developed for rigid arteries. Future work should investigate the effect of wall deformation on these structures and investigate whether their relevance to mass transport is reduced with wall deformation.

5. The concept of Lagrangian WSS structures and WSSET are a promising tool for many cardiovascular applications where near-wall transport is important. Drug eluting stents represent an important application where the near-wall transport of the drugs can cause damage to the endothelial cells and lead to tissue regrowth [224]. A collaboration is currently underway with Dr. John LaDisa's group to study this problem using WSSET and clinical data.

6. The application of Lagrangian WSS structures to turbulent mass transport remains to be investigated. Moreover, the connection between these structures and the coherent structures in turbulent boundary layers is interesting.

7. A preliminary investigation of WSS LCS to low Schmidt number continuum mass transport showed promising results, where the prominent WSS LCS still influenced surface concentration patterns. This can open up a new venue for the application of these structures to a range of applications in heat and mass transfer.

8. Transport of leukocytes (white blood cells) within aneurysms and their subsequent uptake by the vessel wall plays an important role in the inflammation pathways. Leukocytes are inertial particles and deviate from fluid flow trajectories. Therefore, a dissipative dynamical system with persistence chaos might be created. This can be investigated using dynamical systems techniques. Moreover, the extension of WSS LCS to near-wall transport of inertial particles is an interesting topic.

9. We have used mix-norm and mix-variance with Lagrangian particle tracking to quantify mixing. It is known that existence of chaotic flow in all scales of a system is an indicator of efficient mixing [191]. This suggest the use of finite-time Lyapunov exponent (FTLE) in a mix-norm measure to quantify mixing. A preliminary investigation on this was done with our data, however more rigorous theoretical justifications are needed.

10. Vortex wall interaction is a beautiful classical fluid dynamics problem. This phenomenon greatly determines the WSS patterns, which will in turn affect disease pathology. A careful examination of vortex wall interaction in the complex flow setting of aneurysms and the effect of a non-zero diastolic background flow on this phenomenon is a topic of future work. Moreover, the impingement of the flow jet into the aneurysm wall and its relation to wall histology and thickness is an important topic. While some work has been done in this area for cerebral aneurysms, future research should also study AAAs.

11. The concept of Eulerian indicators in studying unsteady transport has been introduced recently [172]. It would be interesting to apply these methods to pulsatile blood flow in aneurysms and compare with Lagrangian transport to see if these simplified tools can be useful in studying transport.

10.2 Resultant journal publications

The material in this research has been published in different journal publications. Chapter 3 is published in [10]:

Arzani, A., and S. C. Shadden. "Characterization of the transport topology in patient-specific abdominal aortic aneurysm models" Physics of Fluids (1994-present) 24.8 (2012): 081901.

Chapter 4 is published in [9]:

Arzani, A., Les, A. S., Dalman, R. L., and Shadden, S. C "Effect of exercise on patient specific abdominal aortic aneurysm flow topology and mixing." International journal for Numerical Methods in Biomedical Engineering 30.2 (2014): 280-295.

Chapter 5 is published in [12]:

Arzani, A., Suh, G. Y., Dalman, R. L., and Shadden, S. C "A longitudinal comparison of hemodynamics and intraluminal thrombus deposition in abdominal aortic aneurysms." American Journal of Physiology-Heart and Circulatory Physiology 307.12 (2014): H1786-H1795.

Chapter 6 is published in [11]:

Arzani, A., and S. C. Shadden. "Characterizations and correlations of wall shear stress in aneurysmal flow." Journal of Biomechanical Engineering 138.1 (2016): 014503.

Chapter 7 is published in [8]:

Arzani, A., Gambaruto, A. M., Chen, G., and Shadden, S. C. "Lagrangian wall shear stress structures and near-wall transport in high-Schmidt-number aneurysmal flows." Journal of Fluid Mechanics 790 (2016): 158-172.

Chapter 8 is currently under consideration for publication:

Arzani, A., Gambaruto, A. M., Chen, G., and Shadden, S. C. "Wall shear stress exposure time: A Lagrangian measure of near-wall stagnation and concentration in cardiovascular flows." Submitted.

Bibliography

[1] G. Ailawadi, J. L. Eliason, and G. R. Upchurch. Current concepts in the pathogenesis of abdominal aortic aneurysm. *Journal of Vascular Surgery*, 38(3):584–588, 2003.

[2] B. R. Alevriadou, J. L. Moake, N. A. Turner, Z. M. Ruggeri, B. J. Folie, M. D. Phillips, A. B. Schreiber, M. E. Hrinda, and L. V. McIntire. Real-time analysis of shear-dependent thrombus formation and its blockade by inhibitors of von Willebrand factor binding to platelets. *Blood*, 81(5):1263–1276, 1993.

[3] M. Alimohammadi, O. Agu, S. Balabani, and V. Díaz-Zuccarini. Development of a patient-specific simulation tool to analyse aortic dissections: assessment of mixed patient-specific flow and pressure boundary conditions. *Medical Engineering & Physics*, 36(3):275–284, 2014.

[4] L. Antiga, M. Piccinelli, L. Botti, B. Ene-Iordache, A. Remuzzi, and D. A. Steinman. An image-based modeling framework for patient-specific computational hemodynamics. *Medical & biological engineering & computing*, 46(11):1097–1112, 2008.

[5] P. Aparício, M. S. Thompson, and P. N. Watton. A novel chemo-mechano-biological model of arterial tissue growth and remodelling. *Journal of Biomechanics*, 2016.

[6] J. P. Archie Jr, S. Hyun, C. Kleinstreuer, P. W. Longest, G. A. Truskey, and J. R. Buchanan. Hemodynamic parameters and early intimal thickening in branching blood vessels. *Critical Reviews in Biomedical Engineering*, 29(1):1–64, 2001.

[7] A. Arzani, P. Dyverfeldt, T. Ebbers, and S. C. Shadden. In vivo validation of numerical prediction for turbulence intensity in an aortic coarctation. *Annals of Biomedical Engineering*, 40(4):860–870, 2011.

[8] A. Arzani, A. M. Gambaruto, G. Chen, and S. C. Shadden. Lagrangian wall shear stress structures and near-wall transport in high-Schmidt-number aneurysmal flows. *Journal of Fluid Mechanics*, 790:158–172, 2016.

[9] A. Arzani, A. S. Les, R. L. Dalman, and S. C. Shadden. Effect of exercise on patient specific abdominal aortic aneurysm flow topology and mixing. *International Journal for Numerical Methods in Biomedical Engineering*, 30(2):280–295, 2014.

[10] A. Arzani and S. C. Shadden. Characterization of the transport topology in patient-specific abdominal aortic aneurysm models. *Physics of Fluids*, 24(8):1901, 2012.

[11] A. Arzani and S. C. Shadden. Characterizations and correlations of wall shear stress in aneurysmal flow. *Journal of Biomechanical Engineering*, 138(1):014503, 2016.

[12] A. Arzani, G. Y. Suh, R. L. Dalman, and S. C. Shadden. A longitudinal comparison of hemodynamics and intraluminal thrombus deposition in abdominal aortic aneurysms. *American Journal of Physiology-Heart and Circulatory Physiology*, 307(12):H1786–H1795, 2014.

[13] M. Astorino, J. Hammers, S. C. Shadden, and J. F. Gerbeau. A robust and efficient valve model based on resistive immersed surfaces. *International Journal for Numerical Methods in Biomedical Engineering*, 28(9):937–959, 2012.

[14] U. Ayachit. The paraview guide: a parallel visualization application. 2015.

[15] L. Badimon, J. J. Badimon, A. Galvez, J. H. Chesebro, and V. Fuster. Influence of arterial damage and wall shear rate on platelet deposition. ex vivo study in a swine model. *Arteriosclerosis, Thrombosis, and Vascular Biology*, 6(3):312–320, 1986.

[16] H. Baek, M. V. Jayaraman, P. D. Richardson, and G. E. Karniadakis. Flow instability and wall shear stress variation in intracranial aneurysms. *Journal of the Royal Society Interface*, page rsif20090476, 2009.

[17] H. G. Bahraseman, K. Hassani, M. Navidbakhsh, D. M. Espino, Z. A. Sani, and N. Fatouraee. Effect of exercise on blood flow through the aortic valve: a combined clinical and numerical study. *Computer Methods in Biomechanics and Biomedical Engineering*, 17(16):1821–1834, 2014.

[18] V. Bandaru, A. Kolchinskaya, K. Padberg-Gehle, and J. Schumacher. Role of critical points of the skin friction field in formation of plumes in thermal convection. *Physical Review E*, 92(4):043006, 2015.

[19] A. I. Barakat and D. K. Lieu. Differential responsiveness of vascular endothelial cells to different types of fluid mechanical shear stress. *Cell Biochemistry and Biophysics*, 38(3):323–343, 2003.

[20] K. A. Barbee. Role of subcellular shear–stress distributions in endothelial cell mechanotransduction. *Annals of Biomedical Engineering*, 30(4):472–482, 2002.

[21] T. D. Barwick, O. T. A. Lyons, N. G. Mikhaeel, M. Waltham, and M. J. ODoherty. 18F-FDG PET-CT uptake is a feature of both normal diameter and aneurysmal aortic wall and is not related to aneurysm size. *Eur J Nucl Med Mol imaging*, 41(12):2310–2318, 2014.

[22] C. Basciano, C. Kleinstreuer, S. Hyun, and E. A. Finol. A relation between near-wall particle-hemodynamics and onset of thrombus formation in abdominal aortic aneurysms. *Annals of Biomedical Engineering*, 39:2010–2026, 2011.

[23] D. Basmadjian. The effect of flow and mass transport in thrombogenesis. *Annals of Biomedical Engineering*, 18(6):685–709, 1990.

[24] Y. Bazilevs, V. M. Calo, T. E. Tezduyar, and T. J. R. Hughes. Yzβ discontinuity capturing for advection-dominated processes with application to arterial drug delivery. *Int J Numer Methods Fluids*, 54:593–608, 2007.

[25] Y. Bazilevs and T. J. R. Hughes. Weak imposition of Dirichlet boundary conditions in fluid mechanics. *Computers & Fluids*, 36(1):12–26, 2007.

[26] P. Berg, D. Stucht, G. Janiga, O. Beuing, O. Speck, and D. Thévenin. Cerebral blood flow in a healthy circle of willis and two intracranial aneurysms: computational fluid dynamics versus four-dimensional phase-contrast magnetic resonance imaging. *Journal of Biomechanical Engineering*, 136(4):041003, 2014.

[27] J. Biasetti, T. C. Gasser, M. Auer, U. Hedin, and F. Labruto. Hemodynamics of the normal aorta compared to fusiform and saccular abdominal aortic aneurysms with emphasis on a potential thrombus formation mechanism. *Annals of Biomedical Engineering*, 38:380–390, 2010.

[28] J. Biasetti, F. Hussain, and T. C. Gasser. Blood flow and coherent vortices in the normal and aneurysmatic aortas: A fluid dynamical approach to intra-luminal thrombus formation. *Journal of The Royal Society Interface*, 8(63):1449–1461, 2011.

[29] J. Biasetti, P. G. Spazzini, J. Swedenborg, and T. C. Gasser. An integrated fluid-chemical model toward modeling the formation of intra–luminal thrombus in abdominal aortic aneurysms. *Frontiers in physiology*, 3(266), 2012.

[30] J. F. Blanchard. Epidemiology of abdominal aortic aneurysms. *Epidemiologic Reviews*, 21(2):207–221, 1999.

[31] D. Bluestein, K. Dumont, M. De Beule, J. Ricotta, P. Impellizzeri, Be. Verhegghe, and P. Verdonck. Intraluminal thrombus and risk of rupture in patient specific abdominal aortic aneurysm – FSI modelling. *Computer Methods in Biomechanics and Biomedical Engineering*, 12(1):73–81, 2009.

[32] D. Bluestein, L. Niu, R. T. Schoephoerster, and M. K. Dewanjee. Steady flow in an aneurysm model: Correlation between fluid dynamics and blood platelet deposition. *Journal of Biomechanical Engineering*, 118(3):280–286, 1996.

[33] E. Boileau, R. L. T. Bevan, I. Sazonov, M. I. Rees, and P. Nithiarasu. Flow-induced ATP release in patient-specific arterial geometries–a comparative study of computational models. *International Journal for Numerical Methods in Biomedical Engineering*, 29(10):1038–1056, 2013.

[34] I. Borazjani. Fluid–structure interaction, immersed boundary-finite element method simulations of bio-prosthetic heart valves. *Computer Methods in Applied Mechanics and Engineering*, 257:103–116, 2013.

[35] L. Boussel, V. Rayz, A. Martin, G. Acevedo-Bolton, M. T. Lawton, R. Higashida, W. S. Smith, W. L. Young, and D. Saloner. Phase-contrast magnetic resonance imaging measurements in intracranial aneurysms in vivo of flow patterns, velocity fields, and wall shear stress: comparison with computational fluid dynamics. *Magnetic Resonance in Medicine*, 61(2):409–417, 2009.

[36] A. N. Brooks and T. J. R. Hughes. Streamline upwind/Petrov-Galerkin formulations for convection dominated flows with particular emphasis on the incompressible Navier-Stokes equations. *Computer Methods in Applied Mechanics and Engineering*, 32(1-3):199–259, 1982.

[37] R. Brown and L. O. Chua. Clarifying chaos: Examples and counterexamples. *International Journal of Bifurcation and Chaos*, 6(2):219–249, 1996.

[38] L. D. Browne, S. O'Callaghan, D. A. Hoey, P. Griffin, T. M. McGloughlin, and M. T. Walsh. Correlation of hemodynamic parameters to endothelial cell proliferation in an end to side anastomosis. *Cardiovascular Engineering and Technology*, 5(1):110–118, 2014.

[39] C. Brücker. Evidence of rare backflow and skin-friction critical points in near-wall turbulence using micropillar imaging. *Physics of Fluids (1994-present)*, 27(3):031705, 2015.

[40] J. R. Buchanan, C. Kleinstreuer, S. Hyun, and G. A. Truskey. Hemodynamics simulation and identification of susceptible sites of atherosclerotic lesion formation in a model abdominal aorta. *Journal of Biomechanics*, 36(8):1185–1196, 2003.

[41] J. R. Buchanan Jr, C. Kleinstreuer, G. A. Truskey, and M. Lei. Relation between non-uniform hemodynamics and sites of altered permeability and lesion growth at the rabbit aorto-celiac junction. *Atherosclerosis*, 143(1):27–40, 1999.

[42] J. Buckmaster. Perturbation technique for the study of three-dimensional separation. *Physics of Fluids (1958-1988)*, 15(12):2106–2113, 1972.

[43] J. I. Cardesa, J. P. Monty, J. Soria, and M. S. Chong. Skin-friction critical points in wall-bounded flows. In *Journal of Physics: Conference Series*, volume 506, page 012009, 2014.

[44] C. G. Caro, J. M. Fitz-Gerald, and R. C. Schroter. Arterial wall shear and distribution of early atheroma in man. *Nature*, 223:1159–1161, 1969.

[45] T. W. G. Carrell, K. G. Burnand, N. A. Booth, J. Humphries, and A. Smith. Intraluminal thrombus enhances proteolysis in abdominal aortic aneurysms. *Vascular*, 14(1):9–16, 2006.

[46] J. L. G. Cavalcanti Filho, R. S. L. Lima, L. S. M. Neto, L. K. Bittencourt, R. C. Domingues, and L. M. B. da Fonseca. PET/CT and vascular disease: current concepts. *European Journal of Radiology*, 80(1):60–67, 2011.

[47] J. R. Cebral, M. A. Castro, J. E. Burgess, R. S. Pergolizzi, M. J. Sheridan, and C. M. Putman. Characterization of cerebral aneurysms for assessing risk of rupture by using patient-specific computational hemodynamics models. *American Journal of Neuroradiology*, 26(10):2550–2559, 2005.

[48] J. R. Cebral, F. Mut, D. Sforza, R. Löhner, E. Scrivano, P. Lylyk, and C. Putman. Clinical application of image-based CFD for cerebral aneurysms. *International Journal for Numerical Methods in Biomedical Engineering*, 27(7):977–992, 2011.

[49] A. Chakraborty, S. Chakraborty, V. R. Jala, B. Haribabu, M. K. Sharp, and R. E. Berson. Effects of biaxial oscillatory shear stress on endothelial cell proliferation and morphology. *Biotechnology and Bioengineering*, 109(3):695–707, 2012.

[50] A. Chakraborty, S. Chakraborty, V. R. Jala, J. M. Thomas, M. K. Sharp, R. E. Berson, and B. Haribabu. Impact of bi-axial shear on atherogenic gene expression by endothelial cells. *Annals of Biomedical Engineering*, pages 1–14, 2016.

[51] G. Chen, K. Mischaikow, R. S. Laramee, P. Pilarczyk, and E. Zhang. Vector field editing and periodic orbit extraction using morse decomposition. *Visualization and Computer Graphics, IEEE Transactions on*, 13(4):769–785, 2007.

[52] H. Chen, A. Selimovic, H. Thompson, A. Chiarini, J. Penrose, Y. Ventikos, and P. N. Watton. Investigating the influence of haemodynamic stimuli on intracranial aneurysm inception. *Annals of Biomedical Engineering*, 41(7):1492–1504, 2013.

[53] C. P. Cheng, R. J. Herfkens, and C. A. Taylor. Abdominal aortic hemodynamic conditions in healthy subjects aged 50–70 at rest and during lower limb exercise: in vivo quantification using MRI. *Atherosclerosis*, 168(2):323–331, 2003.

[54] Z. Cheng, N. B. Wood, R. G. J. Gibbs, and X. Y. Xu. Geometric and flow features of type b aortic dissection: initial findings and comparison of medically treated and stented cases. *Annals of Biomedical Engineering*, 43(1):177–189, 2015.

[55] C. Cherubini, S. Filippi, A. Gizzi, and M. G. C. Nestola. On the wall shear stress gradient in fluid dynamics. *Communications in Computational Physics*, 17(03):808–821, 2015.

[56] A. Chien, S. Tateshima, M. Castro, J. Sayre, J. Cebral, and F. Vinuela. Patient-specific flow analysis of brain aneurysms at a single location: comparison of hemodynamic characteristics in small aneurysms. *Medical & Biological Engineering & Computing*, 46(11):1113–1120, 2008.

[57] S. Chien. Mechanotransduction and endothelial cell homeostasis: the wisdom of the cell. *American Journal of Physiology-Heart and Circulatory Physiology*, 292(3):H1209–H1224, 2007.

[58] J. J. Chiu, C. N. Chen, P. L. Lee, C. T. Yang, H. S. Chuang, S. Chien, and S. Usami. Analysis of the effect of disturbed flow on monocytic adhesion to endothelial cells. *Journal of Bbiomechanics*, 36(12):1883–1895, 2003.

[59] J. J. Chiu and S. Chien. Effects of disturbed flow on vascular endothelium: pathophysiological basis and clinical perspectives. *Physiological Reviews*, 91(1):327–387, 2011.

[60] Y. I. Cho, M. P. Mooney, and D. J. Cho. Hemorheological disorders in diabetes mellitus. *Journal of Diabetes Science and Rechnology*, 2(6):1130–1138, 2008.

[61] H. W. Choi, K. W. Ferrara, and A. I. Barakat. Modulation of ATP/ADP concentration at the endothelial surface by shear stress: effect of flow recirculation. *Annals of Biomedical Engineering*, 35(4):505–516, 2007.

[62] M. S. Chong, J. P. Monty, C. Chin, and I. Marusic. The topology of skin friction and surface vorticity fields in wall-bounded flows. *Journal of Turbulence*, (13):N6, 2012.

[63] B. Chung and J. R. Cebral. CFD for evaluation and treatment planning of aneurysms: review of proposed clinical uses and their challenges. *Annals of Biomedical Engineering*, 43(1):122–138, 2015.

[64] M. Cilla, E. Peña, and M. A. Martínez. Mathematical modelling of atheroma plaque formation and development in coronary arteries. *Journal of The Royal Society Interface*, 11(90):20130866, 2013.

[65] A. Comerford, M. J. Plank, and T. David. Endothelial nitric oxide synthase and calcium production in arterial geometries: an integrated fluid mechanics/cell model. *Journal of Biomechanical Engineering*, 130(1):011010, 2008.

[66] D. E. Conway and M. A. Schwartz. Flow-dependent cellular mechanotransduction in atherosclerosis. *Journal of Cell Science*, 126(22):5101–5109, 2013.

[67] D. E. Conway, M. R. Williams, S. G. Eskin, and L. V. McIntire. Endothelial cell responses to atheroprone flow are driven by two separate flow components: low time-average shear stress and fluid flow reversal. *American Journal of Physiology-Heart and Circulatory Physiology*, 298(2):H367–H374, 2010.

[68] G. Coppola and C. Caro. Oxygen mass transfer in a model three-dimensional artery. *Journal of The Royal Society Interface*, 5(26):1067–1075, 2008.

[69] M. Dabagh, P. Jalali, and J. M. Tarbell. The transport of LDL across the deformable arterial wall: the effect of endothelial cell turnover and intimal deformation under hypertension. *American Journal of Physiology-Heart and Circulatory Physiology*, 297(3):H983–H996, 2009.

[70] T Dairay, V Fortuné, E Lamballais, and L. E. Brizzi. Direct numerical simulation of a turbulent jet impinging on a heated wall. *Journal of Fluid Mechanics*, 764:362–394, 2015.

[71] R. L. Dalman, M. M. Tedesco, J. Myers, and C. A. Taylor. AAA disease. *Annals of the New York Academy of Sciences*, 1085(1):92–109, 2006.

[72] P. F. Davies. Flow-mediated endothelial mechanotransduction. *Physiological Reviews*, 75(3):519–560, 1995.

[73] V. Deplano, Y. Knapp, E. Bertrand, and E. Gaillard. Flow behaviour in an asymmetric compliant experimental model for abdominal aortic aneurysm. *Journal of Biomechanics*, 40:2406–2413, 2007.

[74] P. Di Achille, G. Tellides, C. A. Figueroa, and J. D. Humphrey. A haemodynamic predictor of intraluminal thrombus formation in abdominal aortic aneurysms. In *Proc. R. Soc. A*, volume 470, page 20140163, 2014.

[75] E. Di Martino, S. Mantero, F. Inzoli, G. Melissano, D. Astore, R. Chiesa, and R. Fumero. Biomechanics of abdominal aortic aneurysm in the presence of endoluminal thrombus: experimental characterisation and structural static computational analysis. *European Journal of Vascular and Endovascular Surgery*, 15(4):290–299, 1998.

[76] E. S. Di Martino and D. A. Vorp. Effect of variation in intraluminal thrombus constitutive properties on abdominal aortic aneurysm wall stress. *Annals of Biomedical Engineering*, 31(7):804–809, 2003.

[77] J. M. Dolan, J. Kolega, and H. Meng. High wall shear stress and spatial gradients in vascular pathology: A review. *Annals of Biomedical Engineering*, 41(7):1411–1427, 2013.

[78] J. M. Dolan, H. Meng, S. Singh, R. Paluch, and J. Kolega. High fluid shear stress and spatial shear stress gradients affect endothelial proliferation, survival, and alignment. *Annals of Biomedical Engineering*, 39(6):1620–1631, 2011.

[79] M. M. Dua and R. L. Dalman. Hemodynamic influences on abdominal aortic aneurysm disease: application of biomechanics to aneurysm pathophysiology. *Vascular pharmacology*, 53(1):11–21, 2010.

[80] V. Duvernois, A. L. Marsden, and S. C. Shadden. Lagrangian analysis of hemodynamics data from FSI simulation. *International Journal for Numerical Methods in Biomedical Engineering*, 29(4):445–461, 2013.

[81] V. G. Eck, W. P. Donders, J. Sturdy, J. Feinberg, T. Delhaas, L. R. Hellevik, and W. Huberts. A guide to uncertainty quantification and sensitivity analysis for cardiovascular applications. *International Journal for Numerical Methods in Biomedical Engineering*, 2015.

[82] C. J. Egelhoff, R. S. Budwig, D. F. Elger, T. A. Khraishi, and K. H. Johansen. Model studies of the flow in abdominal aortic aneurysms during resting and exercise conditions. *Journal of Biomechanics*, 32(12):1319–1329, 1999.

[83] M. El Hassan, H. H. Assoum, R. Martinuzzi, V. Sobolik, K. Abed-Meraim, and A. Sakout. Experimental investigation of the wall shear stress in a circular impinging jet. *Physics of Fluids (1994-present)*, 25(7):077101, 2013.

[84] F. Ene, C. Gachon, P. Delassus, R. Carroll, F. Stefanov, P. O'Flynn, and L. Morris. In vitro evaluation of the effects of intraluminal thrombus on abdominal aortic aneurysm wall dynamics. *Medical Engineering and Physics*, 33(8):957–966, 2011.

[85] M. Esmaily-Moghadam, Y. Bazilevs, and A. L. Marsden. A new preconditioning technique for implicitly coupled multidomain simulations with applications to hemodynamics. *Computational Mechanics*, 52(5):1141–1152, 2013.

[86] C. R. Ethier. Computational modeling of mass transfer and links to atherosclerosis. *Annals of Biomedical Engineering*, 30(4):461–471, 2002.

[87] H. M. Ezzeldin, M. D. de Tullio, M. Vanella, S. D. Solares, and E. Balaras. A strain-based model for mechanical hemolysis based on a coarse-grained red blood cell model. *Annals of Biomedical Engineering*, 43(6):1398–1409, 2015.

[88] S. Fazli, E. Shirani, and M. R. Sadeghi. Numerical simulation of LDL mass transfer in a common carotid artery under pulsatile flows. *Journal of Biomechanics*, 44(1):68–76, 2011.

[89] C. A. Figueroa. *A Coupled-momentum Method to Model Blood Flow and Vessel Deformation in Human Arteries: Applications in Disease Research and Simulation-based Medical Planning*. PhD thesis, Stanford University, 2006.

[90] C. A. Figueroa, S. Baek, C. A. Taylor, and J. D. Humphrey. A computational framework for fluid–solid-growth modeling in cardiovascular simulations. *Computer Methods in Applied Mechanics and Engineering*, 198(45):3583–3602, 2009.

[91] E. A. Finol and C. H. Amon. Blood flow in abdominal aortic aneurysms: pulsatile flow hemodynamics. *Journal of Biomechanical Engineering*, 123(5):474–484, 2001.

[92] E. A. Finol and C. H. Amon. Flow dynamics in anatomical models of abdominal aortic aneurysms: Computational analysis of pulsatile flow. *Acta Científica Venezolana*, 54(1):43–49, 2003.

[93] E. A. Finol, K. Keyhani, and C. H. Amon. The effect of asymmetry in abdominal aortic aneurysms under physiologically realistic pulsatile flow conditions. *Journal of Biomechanical Engineering*, 125(2):207–217, 2003.

[94] D. Gallo, G. Isu, D. Massai, F Pennella, M. A. Deriu, R. Ponzini, C. Bignardi, A. Audenino, G. Rizzo, and U. Morbiducci. A survey of quantitative descriptors of arterial flows. In *Visualization and Simulation of Complex Flows in Biomedical Engineering*, pages 1–24. Springer, Dordrecht, 2014.

[95] D. Gallo, D. A. Steinman, P. B. Bijari, and U. Morbiducci. Helical flow in carotid bifurcation as surrogate marker of exposure to disturbed shear. *Journal of Biomechanics*, 45(14):2398–2404, 2012.

[96] A. M. Gambaruto, D. J. Doorly, and T. Yamaguchi. Wall shear stress and near-wall convective transport: Comparisons with vascular remodelling in a peripheral graft anastomosis. *Journal of Computational Physics*, 229(14):5339–5356, 2010.

[97] A. M. Gambaruto and A. J. João. Flow structures in cerebral aneurysms. *Computers & Fluids*, 65:56–65, 2012.

[98] L. Ge and F. Sotiropoulos. Direction and magnitude of blood flow shear stresses on the leaflets of aortic valves: is there a link with valve calcification? *Journal of Biomechanical Engineering*, 132(1):014505, 2010.

[99] S. Ghosh, A. Leonard, and S. Wiggins. Diffusion of a passive scalar from a no-slip boundary into a two-dimensional chaotic advection field. *Journal of Fluid Mechanics*, 372:119–163, 1998.

[100] J. Golledge, P. S. Tsao, R. L. Dalman, and P. E. Norman. Circulating markers of abdominal aortic aneurysm presence and progression. *Circulation*, 118(23):2382–2392, 2008.

[101] S. S. Gopalakrishnan, B. Pier, and A. Biesheuvel. Dynamics of pulsatile flow through model abdominal aortic aneurysms. *Journal of Fluid Mechanics*, 758:150–179, 2014.

[102] S. S. Gopalakrishnan, B. Pier, and A. Biesheuvel. Global stability analysis of flow through a fusiform aneurysm: steady flows. *Journal of Fluid Mechanics*, 752:90, 2014.

[103] L. Goubergrits, B. Thamsen, A. Berthe, J. Poethke, U. Kertzscher, K. Affeld, C. Petz, H. C. Hege, H. Hoch, and A. Spuler. In vitro study of near-wall flow in a cerebral aneurysm model with and without coils. *American Journal of Neuroradiology*, 31(8):1521–1528, 2010.

[104] A. Grytsan, P. N. Watton, and G. A. Holzapfel. A thick-walled fluid–solid-growth model of abdominal aortic aneurysm evolution: Application to a patient-specific geometry. *Journal of Biomechanical Engineering*, 137(3):031008, 2015.

[105] M Hadžiabdić and K Hanjalić. Vortical structures and heat transfer in a round impinging jet. *Journal of Fluid Mechanics*, 596:221–260, 2008.

[106] G. Haller. Lagrangian coherent structures. *Annual Review of Fluid Mechanics*, 47:137–162, 2015.

[107] G. Haller and G. Yuan. Lagrangian coherent structures and mixing in two-dimensional turbulence. *Physica D: Nonlinear Phenomena*, 147(3-4):352–370, 2000.

[108] K. B. Hansen, A. Arzani, and S. C. Shadden. Mechanical platelet activation potential in abdominal aortic aneurysms. *Journal of Biomechanical Engineering*, 137(4):041005, 2015.

[109] K. B. Hansen and S. C. Shadden. A reduced-dimensional model for near-wall transport in cardiovascular flows. *Biomechanics and Modeling in Mechanobiology*, 15(3):713–722, 2016.

[110] W. Hao and A. Friedman. The LDL-HDL profile determines the risk of atherosclerosis: a mathematical model. *PloS One*, 9(3):e90497, 2014.

[111] D. Hardman, B. J. Doyle, S. I. K. Semple, J. M. J. Richards, D. E. Newby, W. J. Easson, and P. R. Hoskins. On the prediction of monocyte deposition in abdominal aortic aneurysms using computational fluid dynamics. *Proceedings of the Institution of Mechanical Engineers, Part H: Journal of Engineering in Medicine*, 227(10):1114–1124, 2013.

[112] D. Hardman, S. I. Semple, J. M. Richards, and P. R. Hoskins. Comparison of patient-specific inlet boundary conditions in the numerical modelling of blood flow in abdominal aortic aneurysm disease. *International Journal for Numerical Methods in Biomedical Engineering*, 29(2):165–178, 2013.

[113] L. P. Harter, B. H. Gross, P. W. Callen, and R. A. Barth. Ultrasonic evaluation of abdominal aortic thrombus. *Journal of Ultrasound in Medicine*, 1(8):315–318, 1982.

[114] J. N. Hartnack. Streamline topologies near a fixed wall using normal forms. *Acta Mechanica*, 136(1-2):55–75, 1999.

[115] J. J. Hathcock. Flow effects on coagulation and thrombosis. *Arteriosclerosis, Thrombosis, and Vascular Biology*, 26(8):1729–1737, 2006.

[116] H. A. Himburg, D. M. Grzybowski, A. L. Hazel, J. A. LaMack, X. M. Li, and M. H. Friedman. Spatial comparison between wall shear stress measures and porcine arterial endothelial permeability. *American Journal of Physiology-Heart and Circulatory Physiology*, 286(5):H1916–H1922, 2004.

[117] Y. Hoi, S. H. Woodward, M. Kim, D. B. Taulbee, and H. Meng. Validation of CFD simulations of cerebral aneurysms with implication of geometric variations. *Journal of Biomechanical Engineering*, 128(6):844–851, 2006.

[118] D. O. Hubble, P. P. Vlachos, and T. E. Diller. The role of large–scale vortical structures in transient convective heat transfer augmentation. *Journal of Fluid Mechanics*, 718:89–115, 2013.

[119] J. D. Humphrey and C. A. Taylor. Intracranial and abdominal aortic aneurysms: similarities, differences, and need for a new class of computational models. *Annual Review of Biomedical Engineering*, 10:221, 2008.

[120] F. Iori, L. Grechy, R. W. Corbett, W. Gedroyc, N Duncan, C. G. Caro, and P. E. Vincent. The effect of in–plane arterial curvature on blood flow and oxygen transport in arterio–venous fistulae. *Physics of Fluids (1994-present)*, 27(3):031903, 2015.

[121] L. Itu, P. Sharma, K. Ralovich, V. Mihalef, R. Ionasec, A. Everett, R. Ringel, A. Kamen, and D Comaniciu. Non-invasive hemodynamic assessment of aortic coarctation: validation with in vivo measurements. *Annals of Biomedical Engineering*, 41(4):669–681, 2013.

[122] H. Jalalzadeh, R. Indrakusuma, R. N. Planken, D. A. Legemate, M. J. W. Koelemay, and R. Balm. Inflammation as a predictor of abdominal aortic aneurysm growth and rupture: A systematic review of imaging biomarkers. *European Journal of Vascular and Endovascular Surgery*, 2016.

[123] K. E. Jansen, C. H. Whiting, and G. M. Hulbert. A generalized-alpha method for integrating the filtered Navier-Stokes equations with a stabilized finite element method. *Computer methods in applied mechanics and engineering*, 190(3-4):305–319, 2000.

[124] J. M. Jiménez, V. Prasad, M. D. Yu, C. P. Kampmeyer, A. H. Kaakour, P. J. Wang, S. F. Maloney, N. Wright, I. Johnston, Y. Z. Jiang, and P. F. Davies. Macro- and microscale variables regulate stent haemodynamics, fibrin deposition and thrombomodulin expression. *Journal of The Royal Society Interface*, 11(94):20131079, 2014.

[125] K. John and A. I. Barakat. Modulation of ATP/ADP concentration at the endothelial surface by shear stress: effect of flow-induced ATP release. *Annals of Biomedical Engineering*, 29(9):740–751, 2001.

[126] L. D. Jou and M. E. Mawad. Timing and size of flow impingement in a giant intracranial aneurysm at the internal carotid artery. *Medical & Biological Engineering & Computing*, 49(8):891–899, 2011.

[127] M. Ju, S. S. Ye, B. Namgung, S. Cho, H. T. Low, H. L. Leo, and S. Kim. A review of numerical methods for red blood cell flow simulation. *Computer Methods in Biomechanics and Biomedical Engineering*, 18(2):130–140, 2015.

[128] M. R. Kaazempur-Mofrad, S. Wada, J. G. Myers, and C. R. Ethier. Mass transport and fluid flow in stenotic arteries: axisymmetric and asymmetric models. *International Journal of Heat and Mass Transfer*, 48(21):4510–4517, 2005.

[129] N. Kataoka, S. Ujita, and M. Sato. Effect of flow direction on the morphological responses of cultured bovine aortic endothelial cells. *Medical and Biological Engineering and Computing*, 36(1):122–128, 1998.

[130] K. M. Khanafer, J. L. Bull, G. R. Upchurch, and R. Berguer. Turbulence significantly increases pressure and fluid shear stress in an aortic aneurysm model under resting and exercise flow conditions. *Annals of Vascular Surgery*, 21(1):67–74, 2007.

[131] K. M. Khanafer, P. Gadhoke, R. Berguer, and J. L. Bull. Modeling pulsatile flow in aortic aneurysms: Effect of non-Newtonian properties of blood. *Biorheology*, 43(5):661–679, 2006.

[132] H. J. Kim, C. A. Figueroa, T. J. R. Hughes, K. E. Jansen, and C. A. Taylor. Augmented Lagrangian method for constraining the shape of velocity profiles at outlet boundaries for three-dimensional finite element simulations of blood flow. *Computer Methods in Applied Mechanics and Engineering*, 198(45):3551–3566, 2009.

[133] J. Knight, S. C. Olgac, U.and Saur, D. Poulikakos, W. Marshall Jr, P. C. Cattin, H. Alkadhi, and V. Kurtcuoglu. Choosing the optimal wall shear parameter for the prediction of plaque location—a patient-specific computational study in human right coronary arteries. *Atherosclerosis*, 211(2):445–450, 2010.

[134] C. W. Kotze, A. M. Groves, L. J. Menezes, R. Harvey, R. Endozo, I. A. Kayani, P. J. Ell, and S. W. Yusuf. What is the relationship between 18F-FDG aortic aneurysm

uptake on PET/CT and future growth rate? *Eur J Nucl Med Mol imaging*, 38(8):1493–1499, 2011.

[135] D. N. Ku, D. P. Giddens, C. K. Zarins, and S. Glagov. Pulsatile flow and atherosclerosis in the human carotid bifurcation. positive correlation between plaque location and low oscillating shear stress. *Arteriosclerosis, Thrombosis, and Vascular Biology*, 5(3):293–302, 1985.

[136] A. L. Kuharsky and A. L Fogelson. Surface-mediated control of blood coagulation: the role of binding site densities and platelet deposition. *Biophysical Journal*, 80(3):1050–1074, 2001.

[137] E. Kung, A. M. Kahn, J. C. Burns, and A. Marsden. In vitro validation of patient-specific hemodynamic simulations in coronary aneurysms caused by kawasaki disease. *Cardiovascular Engineering and Technology*, 5(2):189–201, 2014.

[138] E. O. Kung, A. S. Les, F. Medina, R. B. Wicker, M. V. McConnell, and C. A. Taylor. In vitro validation of finite-element model of AAA hemodynamics incorporating realistic outlet boundary conditions. *Journal of Biomechanical Engineering*, 133(4):041003, 2011.

[139] J. F. LaDisa, C. A. Figueroa, I. E. Vignon-Clementel, H. J. Kim, N. Xiao, L. M. Ellwein, F. P. Chan, J. A. Feinstein, and C. A. Taylor. Computational simulations for aortic coarctation: representative results from a sampling of patients. *Journal of Biomechanical Engineering*, 133(9):091008, 2011.

[140] J. Lantz and M. Karlsson. Large eddy simulation of LDL surface concentration in a subject specific human aorta. *Journal of Biomechanics*, 45(3):537–542, 2012.

[141] J. C. Lasheras. The biomechanics of arterial aneurysms. *Annual Review of Fluid Mechanics*, 39:293–319, 2007.

[142] T. B. Le, I. Borazjani, and F. Sotiropoulos. Pulsatile flow effects on the hemodynamics of intracranial aneurysms. *Journal of Biomechanical Engineering*, 132(11):111009, 2010.

[143] S. E. Lee, S. W. Lee, P. F. Fischer, H. S. Bassiouny, and F. Loth. Direct numerical simulation of transitional flow in a stenosed carotid bifurcation. *Journal of Biomechanics*, 41(11):2551–2561, 2008.

[144] S. W. Lee, L. Antiga, and D. A. Steinman. Correlations among indicators of disturbed flow at the normal carotid bifurcation. *Journal of Biomechanical Engineering*, 131(6):061013, 2009.

[145] K. Leiderman and A. L. Fogelson. Grow with the flow: a spatial–temporal model of platelet deposition and blood coagulation under flow. *Mathematical Medicine and Biology*, 28(1):47–84, 2011.

[146] F. Lekien and C. Coulliette. Chaotic stirring in quasi-turbulent flows. *Philosophical Transactions of the Royal Society of London A: Mathematical, Physical and Engineering Sciences*, 365(1861):3061–3084, 2007.

[147] F. Lekien and S. D Ross. The computation of finite-time Lyapunov exponents on unstructured meshes and for non-Euclidean manifolds. *Chaos: An Interdisciplinary Journal of Nonlinear Science*, 20(1):017505, 2010.

[148] F. Lekien, S.C. Shadden, and J.E. Marsden. Lagrangian coherent structures in n-dimensional systems. *Journal of Mathematical Physics*, 48:065404, 2007.

[149] P. Lenaers, Q. Li, G. Brethouwer, P. Schlatter, and R. Örlü. Rare backflow and extreme wall-normal velocity fluctuations in near-wall turbulence. *Physics of Fluids (1994-present)*, 24(3):035110, 2012.

[150] A. S. Les. *Quantification of Hemodynamics and Luminal Wall Motion in Human Abdominal Aortic Aneurysms Using Magnetic Resonance Imaging and Computational Fluid Dynamics*. PhD thesis, Stanford University, 2010.

[151] A. S. Les, S. C. Shadden, C. A. Figueroa, J. M. Park, M. M. Tedesco, R. J. Herfkens, R. L. Dalman, and C. A. Taylor. Quantification of hemodynamics in abdominal aortic aneurysms during rest and exercise using magnetic resonance imaging and computational fluid dynamics. *Annals of Biomedical Engineering*, 38:1288–1313, 2010.

[152] D. R. Lester, G. Metcalfe, and M. G. Trefry. Is chaotic advection inherent to porous media flow? *Physical Review Letters*, 111(17):174101, 2013.

[153] J. H. Leung, A. R. Wright, N. Cheshire, J. Crane, S. A. Thom, A. D. Hughes, and Y. Xu. Fluid structure interaction of patient specific abdominal aortic aneurysms: a comparison with solid stress models. *Biomedical Engineering Online*, 5(1):1, 2006.

[154] X. Li, Z. Peng, H. Lei, M. Dao, and G. E. Karniadakis. Probing red blood cell mechanics, rheology and dynamics with a two-component multi-scale model. *Phil. Trans. R. Soc. A*, 372(2021):20130389, 2014.

[155] T. Liu, S. Woodiga, and T Ma. Skin friction topology in a region enclosed by penetrable boundary. *Experiments in Fluids*, 51(6):1549–1562, 2011.

[156] X. Liu, Y. Fan, X. Y. Xu, and X. Deng. Nitric oxide transport in an axisymmetric stenosis. *Journal of The Royal Society Interface*, 9(75):2468–2478, 2012.

[157] X. Liu, A. Sun, Y. Fan, and X. Deng. Physiological significance of helical flow in the arterial system and its potential clinical applications. *Annals of Biomedical Engineering*, 43(1):3–15, 2015.

[158] A. Logg, K. A. Mardal, and G. Wells. *Automated solution of differential equations by the finite element method*, volume 84. Springer, Berlin, Heidelberg, 2012.

[159] P. W. Longest and C. Kleinstreuer. Numerical simulation of wall shear stress conditions and platelet localization in realistic end-to-side arterial anastomoses. *Journal of Biomechanical Engineering*, 125(5):671–681, 2003.

[160] A. Lonyai, A. M. Dubin, J. A. Feinstein, C. A. Taylor, and S. C. Shadden. New insights into pacemaker lead-induced venous occlusion: simulation-based investigation of alterations in venous biomechanics. *Cardiovascular Engineering*, 10(2):84–90, 2010.

[161] D. Lu and G. S. Kassab. Role of shear stress and stretch in vascular mechanobiology. *Journal of The Royal Society Interface*, page rsif20110177, 2011.

[162] P. Ma, X. Li, and D. N. Ku. Heat and mass transfer in a separated flow region for high prandtl and schmidt numbers under pulsatile conditions. *International journal of heat and mass transfer*, 37(17):2723–2736, 1994.

[163] A. Maier, M. Essler, M. W. Gee, H. H. Eckstein, W. A. Wall, and C. Reeps. Correlation of biomechanics to tissue reaction in aortic aneurysms assessed by finite elements and [18F]–fluorodeoxyglucose–PET/CT. *International Journal for Numerical Methods in Biomedical Engineering*, 28(4):456–471, 2012.

[164] A. Maier, M. W. Gee, C. Reeps, J. Pongratz, H. H. Eckstein, and W. A. Wall. A comparison of diameter, wall stress, and rupture potential index for abdominal aortic aneurysm rupture risk prediction. *Annals of Biomedical Engineering*, 38(10):3124–3134, 2010.

[165] A. Mantha, C. Karmonik, G. Benndorf, C. Strother, and R. Metcalfe. Hemodynamics in a cerebral artery before and after the formation of an aneurysm. *American Journal of Neuroradiology*, 27(5):1113–1118, 2006.

[166] V. L. Marrero, J. A. Tichy, O. Sahni, and K. E. Jansen. Numerical study of purely viscous non-Newtonian flow in an abdominal aortic aneurysm. *Journal of Biomechanical Engineering*, 136(10):101001, 2014.

[167] A. L. Marsden, I. E. Vignon-Clementel, F. P. Chan, J. A. Feinstein, and C. A. Taylor. Effects of exercise and respiration on hemodynamic efficiency in CFD simulations of the total cavopulmonary connection. *Annals of Biomedical Engineering*, 35(2):250–263, 2007.

[168] J. Martorell, P. Santomá, K. Kolandaivelu, V. B. Kolachalama, P. Melgar-Lesmes, J. J. Molins, L. Garcia, E. R. Edelman, and M. Balcells. Extent of flow recirculation governs expression of atherosclerotic and thrombotic biomarkers in arterial bifurcations. *Cardiovascular Research*, 103(1):37–46, 2014.

[169] G. Martufi and T. C. Gasser. Review: The role of biomechanical modeling in the rupture risk assessment for abdominal aortic aneurysms. *Journal of Biomechanical Engineering*, 135(2):021010, 2013.

[170] G. Mathew, I. Mezić, and L. Petzold. A multiscale measure for mixing. *Physica D: Nonlinear Phenomena*, 211(1):23–46, 2005.

[171] M. Mathur, G. Haller, T. Peacock, J. E. Ruppert-Felsot, and H. L. Swinney. Uncovering the Lagrangian skeleton of turbulence. *Physical Review Letters*, 98(14):144502, 2007.

[172] K. L. McIlhany and S. Wiggins. Eulerian indicators under continuously varying conditions. *Physics of Fluids (1994-present)*, 24(7):073601, 2012.

[173] H. Meng, V. M. Tutino, J. Xiang, and A. Siddiqui. High WSS or low WSS? complex interactions of hemodynamics with intracranial aneurysm initiation, growth, and rupture: toward a unifying hypothesis. *American Journal of Neuroradiology*, 35(7):1254–1262, 2014.

[174] H. Meng, Z. Wang, Y. Hoi, L. Gao, E. Metaxa, D. D. Swartz, and J. Kolega. Complex hemodynamics at the apex of an arterial bifurcation induces vascular remodeling resembling cerebral aneurysm initiation. *Stroke*, 38(6):1924–1931, 2007.

[175] W. Meng, F. Yu, H. Chen, J. Zhang, E. Zhang, K. Dian, and Y. Shi. Concentration polarization of high-density lipoprotein and its relation with shear stress in an in vitro model. *BioMed Research International*, 2009:695838–695838, 2009.

[176] C. Menichini and X. Y. Xu. Mathematical modeling of thrombus formation in idealized models of aortic dissection: initial findings and potential applications. *Journal of Mathematical Biology*, pages 1–22, 2016.

[177] M. E. Moghadam, Y. Bazilevs, T. Y. Hsia, I. E. Vignon-Clementel, and A. L. Marsden. A comparison of outlet boundary treatments for prevention of backflow divergence with relevance to blood flow simulations. *Computational Mechanics*, 48(3):277–291, 2011.

[178] Y. Mohamied, E. M. Rowland, E. L. Bailey, S. J. Sherwin, M. A. Schwartz, and P. D. Weinberg. Change of direction in the biomechanics of atherosclerosis. *Annals of Biomedical Engineering*, 43(1):16–25, 2015.

[179] S. J. Montain, S. M. Jilka, A. A. Ehsani, and J. M. Hagberg. Altered hemodynamics during exercise in older essential hypertensive subjects. *Hypertension*, 12(5):479–484, 1988.

[180] J. E. Moore Jr and D. N. Ku. Pulsatile velocity measurements in a model of the human abdominal aorta under resting conditions. *Journal of biomechanical engineering*, 116(3):337, 1994.

[181] U. Morbiducci, D. Gallo, S. Cristofanelli, R. Ponzini, M. A. Deriu, G. Rizzo, and D. A. Steinman. A rational approach to defining principal axes of multidirectional wall shear stress in realistic vascular geometries, with application to the study of the influence of helical flow on wall shear stress directionality in aorta. *Journal of Biomechanics*, 48(6):899–906, 2015.

[182] J. N. Myers, J. J. White, B. Narasimhan, and R. L. Dalman. Effects of exercise training in patients with abdominal aortic aneurysm: preliminary results from a randomized trial. *Journal of Cardiopulmonary Rehabilitation and Prevention*, 30(6):374–383, 2010.

[183] A. Nchimi, A. Courtois, M. El Hachemi, Z. Touat, P. Drion, N. Withofs, and G. et al. Warnock. Multimodality imaging assessment of the deleterious role of the intraluminal thrombus on the growth of abdominal aortic aneurysm in a rat model. *European Radiology*, 26(7):2378–2386, 2016.

[184] R. M. Nerem, J. A. Runberger, D. R. Gross, W. W. Muir, and G. L. Geiger. Hot film coronary artery velocity measurements in horses. *Cardiovascular Research*, 10(3):301, 1976.

[185] Q. Nguyen, C. Srinivasan, and D. V. Papavassiliou. Flow-induced separation in wall turbulence. *Physical Review E*, 91(3):033019, 2015.

[186] C. O'Farrell and J. O. Dabiri. A Lagrangian approach to identifying vortex pinch-off. *Chaos*, 20(1), 2010.

[187] P. Ooij, W. V. Potters, A. Guédon, J. J. Schneiders, H. A. Marquering, C. B. Majoie, E. vanBavel, and A. J. Nederveen. Wall shear stress estimated with phase contrast mri in an in vitro and in vivo intracranial aneurysm. *Journal of Magnetic Resonance Imaging*, 38(4):876–884, 2013.

[188] M. J. O'Rourke, J. P. McCullough, and S. Kelly. An investigation of the relationship between hemodynamics and thrombus deposition within patient-specific models of abdominal aortic aneurysm. *Proceedings of the Institution of Mechanical Engineers, Part H: Journal of Engineering in Medicine*, 226(7):548–564, 2012.

[189] M. A. Ostrowski, N. F. Huang, T. W. Walker, T. Verwijlen, C. Poplawski, A. S. Khoo, J. P. Cooke, G. G. Fuller, and A. R. Dunn. Microvascular endothelial cells migrate upstream and align against the shear stress field created by impinging flow. *Biophysical Journal*, 106(2):366–374, 2014.

[190] J. M. Ottino. *The kinematics of mixing: stretching, chaos, and transport*. Cambridge University Press, 1989.

[191] J. M. Ottino. Mixing, chaotic advection, and turbulence. *Annual Review of Fluid Mechanics*, 22(1):207–254, 1990.

[192] C. Ou, W. Huang, and M. M. F. Yuen. A computational model based on fibrin accumulation for the prediction of stasis thrombosis following flow-diverting treatment in cerebral aneurysms. *Medical & Biological Engineering & Computing*, pages 1–11, 2016.

[193] D. Palombo, S. Morbelli, G. Spinella, B. Pane, C. Marini, N. Rousas, M. Massollo, G. Cittadini, D.o Camellino, and G. Sambuceti. A positron emission tomography/computed tomography (PET/CT) evaluation of asymptomatic abdominal aortic aneurysms: another point of view. *Annals of Vascular Surgery*, 26(4):491–499, 2012.

[194] Y. Papaharilaou, J. A. Ekaterinaris, E. Manousaki, and A. N. Katsamouris. A decoupled fluid structure approach for estimating wall stress in abdominal aortic aneurysms. *Journal of Biomechanics*, 40(2):367–377, 2007.

[195] T. W. Peach, M. Ngoepe, K. Spranger, D. Zajarias-Fainsod, and Y. Ventikos. Personalizing flow-diverter intervention for cerebral aneurysms: from computational hemodynamics to biochemical modeling. *International Journal for Numerical Methods in Biomedical Engineering*, 30(11):1387–1407, 2014.

[196] R. A. Peattie, T. J. Riehle, and E. I. Bluth. Pulsatile flow in fusiform models of abdominal aortic aneurysms: Flow fields, velocity patterns and flow-induced wall stresses. *Journal of Biomechanical Engineering*, 126(4):438–446, 2004.

[197] V. Peiffer, S. J. Sherwin, and P. D. Weinberg. Computation in the rabbit aorta of a new metric–the transverse wall shear stress–to quantify the multidirectional character of disturbed blood flow. *Journal of Biomechanics*, 46(15):2651–2658, 2013.

[198] V. Peiffer, S. J. Sherwin, and P. D. Weinberg. Does low and oscillatory wall shear stress correlate spatially with early atherosclerosis? a systematic review. *Cardiovascular Research*, page cvt044, 2013.

[199] P. Perdikaris, L. Grinberg, and G. E. Karniadakis. Multiscale modeling and simulation of brain blood flow. *Physics of Fluids (1994-present)*, 28(2):021304, 2016.

[200] A. E. Perry and M. S. Chong. A series-expansion study of the navier–stokes equations with applications to three-dimensional separation patterns. *Journal of fluid mechanics*, 173:207–223, 1986.

[201] A. E. Perry and M. S. Chong. A description of eddying motions and flow patterns using critical-point concepts. *Annual Review of Fluid Mechanics*, 19(1):125–155, 1987.

[202] A. M. Plata, S. J. Sherwin, and R. Krams. Endothelial nitric oxide production and transport in flow chambers: the importance of convection. *Annals of Biomedical Engineering*, 38(9):2805–2816, 2010.

[203] C. Poelma, P. N. Watton, and Y. Ventikos. Transitional flow in aneurysms and the computation of haemodynamic parameters. *Journal of The Royal Society Interface*, 12(105):20141394, 2015.

[204] S. Pothapragada, P. Zhang, J. Sheriff, M. Livelli, M. J. Slepian, Y. Deng, and D. Bluestein. A phenomenological particle-based platelet model for simulating filopodia formation during early activation. *International Journal for Numerical Methods in Biomedical Engineering*, 31(3), 2015.

[205] M. L. Raghavan, M. M. Hanaoka, J. A. Kratzberg, M. L. Higuchi, and E. S. da Silva. Biomechanical failure properties and microstructural content of ruptured and unruptured abdominal aortic aneurysms. *Journal of Biomechanics*, 44(13):2501–2507, 2011.

[206] M. Rahbaralam, D. Fernàndez-Garcia, and X. Sanchez-Vila. Do we really need a large number of particles to simulate bimolecular reactive transport with random walk methods? a kernel density estimation approach. *Journal of Computational Physics*, 303:95–104, 2015.

[207] A. Raptis, M. Xenos, S. Dimas, A. Giannoukas, N. Labropoulos, D. Bluestein, and M. I. Matsagkas. Effect of macroscale formation of intraluminal thrombus on blood flow in abdominal aortic aneurysms. *Computer Methods in Biomechanics and Biomedical Engineering*, 19(1):84–92, 2016.

[208] M. Raschi, F. Mut, G. Byrne, C. M. Putman, S. Tateshima, F. Viñuela, T. Tanoue, K. Tanishita, and J. R. Cebral. CFD and PIV analysis of hemodynamics in a growing intracranial aneurysm. *International Journal for Numerical Methods in Biomedical Engineering*, 28(2):214–228, 2012.

[209] S. S. Raut, S. Chandra, J. Shum, and E. A. Finol. The role of geometric and biomechanical factors in abdominal aortic aneurysm rupture risk assessment. *Annals of Biomedical Engineering*, 41(7):1459–1477, 2013.

[210] V. L. Rayz, L. Boussel, L. Ge, J. R. Leach, A. J. Martin, M. T. Lawton, C. McCulloch, and D. Saloner. Flow residence time and regions of intraluminal thrombus deposition in intracranial aneurysms. *Annals of Biomedical Engineering*, 38(10):3058–3069, 2010.

[211] V. L. Rayz, L. Boussel, M. T. Lawton, G. Acevedo-Bolton, L. Ge, W. L. Young, R. T. Higashida, and D. Saloner. Numerical modeling of the flow in intracranial aneurysms: prediction of regions prone to thrombus formation. *Annals of Biomedical Engineering*, 36(11):1793–1804, 2008.

[212] C. Reeps, M. Essler, J. Pelisek, S. Seidl, H. H. Eckstein, and B. J. Krause. Increased 18F-fluorodeoxyglucose uptake in abdominal aortic aneurysms in positron emission/computed tomography is associated with inflammation, aortic wall instability, and acute symptoms. *Journal of Vascular Surgery*, 48(2):417–423, 2008.

[213] C. Reeps, A. Maier, J. Pelisek, F. Härtl, V. Grabher-Meier, W. A. Wall, M. Essler, H. H. Eckstein, and M. W. Gee. Measuring and modeling patient-specific distributions of material properties in abdominal aortic aneurysm wall. *Biomechanics and Modeling in Mechanobiology*, 12(4):717–733, 2013.

[214] A. V. Salsac, S. R. Sparks, J. M. Chomaz, and J. C. Lasheras. Evolution of the wall shear stresses during the progressive enlargement of symmetric abdominal aortic aneurysms. *Journal of Fluid Mechanics*, 560:19–52, 2006.

[215] A. V. Salsac, S. R. Sparks, and J. C. Lasheras. Hemodynamic changes occurring during the progressive enlargement of abdominal aortic aneurysms. *Annals of Vascular Surgery*, 18(1):14–21, 2004.

[216] S. Sankaran, L. Grady, and C. A. Taylor. Impact of geometric uncertainty on hemodynamic simulations using machine learning. *Computer Methods in Applied Mechanics and Engineering*, 297:167–190, 2015.

[217] S. Sankaran and A. L. Marsden. A stochastic collocation method for uncertainty quantification and propagation in cardiovascular simulations. *Journal of Biomechanical Engineering*, 133(3):031001, 2011.

[218] J. T. C. Schrauwen, D. J. Koeze, J. J. Wentzel, F. N. van de Vosse, A. F. W. van der Steen, and F. J. H. Gijsen. Fast and accurate pressure-drop prediction in straightened atherosclerotic coronary arteries. *Annals of Biomedical Engineering*, 43(1):59–67, 2015.

[219] C. J. Schwartz, A. J. Valente, E. A. Sprague, J. L. Kelley, and R. M. Nerem. The pathogenesis of atherosclerosis: an overview. *Clinical Cardiology*, 14(S1):1–16, 1991.

[220] C. M. Scotti, A. D. Shkolnik, S. C. Muluk, and E. A. Finol. Fluid-structure interaction in abdominal aortic aneurysms: effects of asymmetry and wall thickness. *Biomedical Engineering Online*, 4(1):1, 2005.

[221] P. A. Segalova, G. Xiong, K. T. V. Rao, C. K. Zarins, and C. A. Taylor. Evaluating design of abdominal aortic aneurysm endografts in a patient-specific model using computational fluid dynamics. *Journal of Medical Devices*, 5(4):041005, 2011.

[222] D. Sengupta, A. M. Kahn, J. C. Burns, S. Sankaran, S. C. Shadden, and A. L. Marsden. Image-based modeling of hemodynamics in coronary artery aneurysms caused by kawasaki disease. *Biomechanics and Modeling in Mechanobiology*, 11(6):915–932, 2012.

[223] J. H. Seo, T. Abd, R. T. George, and R. Mittal. A coupled chemo-fluidic computational model for thrombogenesis in infarcted left ventricles. *American Journal of Physiology-Heart and Circulatory Physiology*, page 00855, 2016.

[224] T. Seo, A. Lafont, S. Y. Choi, and A. I. Barakat. Drug-eluting stent design is a determinant of drug concentration at the endothelial cell surface. *Annals of Biomedical Engineering*, 44(2):302–314, 2016.

[225] S. C. Shadden. FlowVC. `http://shaddenlab.berkeley.edu/software/`, 2010.

[226] S. C. Shadden. Lagrangian coherent structures. In *Transport and Mixing in Laminar Flows: From Microfluidics to Oceanic Currents*. Wiley-VCH Verlag GmbH & Co. KGaA, 2011.

[227] S. C. Shadden and A. Arzani. Lagrangian postprocessing of computational hemodynamics. *Annals of Biomedical Engineering*, 43(1):41–58, 2015.

[228] S. C. Shadden, M. Astorino, and J. F. Gerbeau. Computational analysis of an aortic valve jet with Lagrangian coherent structures. *Chaos*, 20(1):017512–1, 2010.

[229] S. C. Shadden, J. O. Dabiri, and J. E. Marsden. Lagrangian analysis of fluid transport in empirical vortex ring flows. *Physics of Fluids*, 18(4):047105, 2006.

[230] S. C. Shadden and S. Hendabadi. Potential fluid mechanic pathways of platelet activation. *Biomechanics and Modeling in Mechanobiology*, 12(3):467–474, 2013.

[231] S. C. Shadden, K. Katija, M. Rosenfeld, J. E. Marsden, and J. O. Dabiri. Transport and stirring induced by vortex formation. *Journal of Fluid Mechanics*, 593:315–332, 2007.

[232] S. C. Shadden, F. Lekien, and J. E. Marsden. Definition and properties of Lagrangian coherent structures from finite-time Lyapunov exponents in two-dimensional aperiodic flows. *Physica D: Nonlinear Phenomena*, 212(3-4):271–304, 2005.

[233] S. C. Shadden and C. A. Taylor. Characterization of coherent structures in the cardiovascular system. *Annals of Biomedical Engineering*, 36:1152–1162, 2008.

[234] K. Shariff, T. H. Pulliam, and J. M. Ottino. A dynamical systems analysis of kinematics in the time-periodic wake of a circular cylinder. *Lect. Appl. Math*, 28:613–646, 1991.

[235] A. Sheidaei, S. C. Hunley, S. Zeinali-Davarani, L. G. Raguin, and S. Baek. Simulation of abdominal aortic aneurysm growth with updating hemodynamic loads using a realistic geometry. *Medical Engineering & Physics*, 33(1):80–88, 2011.

[236] Y. Shimogonya, T. Ishikawa, Y. Imai, N. Matsuki, and T. Yamaguchi. Can temporal fluctuation in spatial wall shear stress gradient initiate a cerebral aneurysm? a proposed novel hemodynamic index, the gradient oscillatory number (GON). *Journal of Biomechanics*, 42(4):550–554, 2009.

[237] J. Shum, G. Martufi, E. Di Martino, C. B. Washington, J. Grisafi, S. C. Muluk, and E. A. Finol. Quantitative assessment of abdominal aortic aneurysm geometry. *Annals of Biomedical Engineering*, 39(1):277–286, 2011.

[238] J. H. Siggers and S. L. Waters. Unsteady flows in pipes with finite curvature. *Journal of Fluid Mechanics*, 600:133–165, 2008.

[239] J. S. Soares, C. Gao, Y. Alemu, M. Slepian, and D. Bluestein. Simulation of platelets suspension flowing through a stenosis model using a dissipative particle dynamics approach. *Annals of Biomedical Engineering*, 41(11):2318–2333, 2013.

[240] A. F. Stalder, M. F. Russe, A. Frydrychowicz, J. Bock, J. Hennig, and M. Markl. Quantitative 2d and 3d phase contrast MRI: optimized analysis of blood flow and vessel wall parameters. *Magnetic Resonance in Medicine*, 60(5):1218–1231, 2008.

[241] C. Stamatopoulos, D. S. Mathioulakis, Y. Papaharilaou, and A. Katsamouris. Experimental unsteady flow study in a patient-specific abdominal aortic aneurysm model. *Experiments in Fluids*, 50:1695–1709, 2011.

[242] D. A. Steinman. Assumptions in modelling of large artery hemodynamics. In *Modeling of Physiological Flows*. Springer Milan, 2012.

[243] D. A. Steinman and C. A. Taylor. Flow imaging and computing: large artery hemodynamics. *Annals of Biomedical Engineering*, 33(12):1704–1709, 2005.

[244] J. Stenbaek, B. Kalin, and J. Swedenborg. Growth of thrombus may be a better predictor of rupture than diameter in patients with abdominal aortic aneurysms. *European Journal of Vascular and Endovascular Surgery*, 20(5):466–469, 2000.

[245] N. Stergiopulos, J. J. Meister, and N. Westerhof. Simple and accurate way for estimating total and segmental arterial compliance: the pulse pressure method. *Annals of Biomedical Engineering*, 22(4):392–397, 1994.

[246] G. Y. Suh, A. S. Les, A. S. Tenforde, S. C. Shadden, R. L. Spilker, J. J. Yeung, C. P. Cheng, R. J. Herfkens, R. L. Dalman, and C. A. Taylor. Quantification of particle residence time in abdominal aortic aneurysms using magnetic resonance imaging and computational fluid dynamics. *Annals of Biomedical Engineering*, 39:864–883, 2011.

[247] G. Y. Suh, A. S. Tenforde, S. C. Shadden, R. L. Spilker, C. P. Cheng, R. J. Herfkens, R. L. Dalman, and C. A. Taylor. Hemodynamic changes in abdominal aortic aneurysms

with increasing exercise intensity using MR exercise imaging and image-based computational fluid dynamics. *Annals of Biomedical Engineering*, 39:2186–2202, 2011.

[248] A. Surana, O. Grunberg, and G. Haller. Exact theory of three-dimensional flow separation. part 1. steady separation. *Journal of fluid mechanics*, 564:57–103, 2006.

[249] A. Surana, G. B. Jacobs, O. Grunberg, and G. Haller. An exact theory of three-dimensional fixed separation in unsteady flows. *Physics of Fluids (1994-present)*, 20(10):107101, 2008.

[250] D. Suzuki, K. Funamoto, S. Sugiyama, T. Nakayama, T. Hayase, and T. Tominaga. Investigation of characteristic hemodynamic parameters indicating thinning and thickening sites of cerebral aneurysms. *Journal of Biomechanical Science and Engineering*, 2015.

[251] F. P. P. Tan, A. Borghi, R. H. Mohiaddin, N. B. Wood, S. Thom, and X. Y. Xu. Analysis of flow patterns in a patient-specific thoracic aortic aneurysm model. *Computers & Structures*, 87(11):680–690, 2009.

[252] B. T. Tang, C. P. Cheng, M. T. Draney, N. M. Wilson, P. S. Tsao, R. J. Herfkens, and C. A. Taylor. Abdominal aortic hemodynamics in young healthy adults at rest and during lower limb exercise: quantification using image-based computer modeling. *American Journal of Physiology-Heart and Circulatory Physiology*, 291(2):668–676, 2006.

[253] B. T. Tang, T. A. Fonte, F. P. Chan, P. S. Tsao, J. A. Feinstein, and C. A. Taylor. Three-dimensional hemodynamics in the human pulmonary arteries under resting and exercise conditions. *Annals of Biomedical Engineering*, 39(1):347–358, 2011.

[254] J. M. Tarbell. Mass transport in arteries and the localization of atherosclerosis. *Annual Review of Biomedical Engineering*, 5(1):79–118, 2003.

[255] C. A. Taylor, C. P. Cheng, L. A. Espinosa, B. T. Tang, D. Parker, and R. J. Herfkens. In vivo quantification of blood flow and wall shear stress in the human abdominal aorta during lower limb exercise. *Annals of Biomedical Engineering*, 30(3):402–408, 2002.

[256] C. A. Taylor and C. A. Figueroa. Patient-specific modeling of cardiovascular mechanics. *Annual Review of Biomedical Engineering*, 11:109–134, 2009.

[257] C. A. Taylor, T. J. R. Hughes, and C. K. Zarins. Finite element modeling of blood flow in arteries. *Computer Methods in Applied Mechanics and Engineering*, 158(1):155–196, 1998.

[258] C. A. Taylor, T. J. R. Hughes, and C. K. Zarins. Finite element modeling of three-dimensional pulsatile flow in the abdominal aorta: relevance to atherosclerosis. *Annals of Biomedical Engineering*, 26(6):975–987, 1998.

[259] C. A. Taylor, T. J. R. Hughes, and C. K. Zarins. Effect of exercise on hemodynamic conditions in the abdominal aorta. *Journal of Vascular Surgery*, 29(6):1077–1089, 1999.

[260] T. W. Taylor and T. Yamaguchi. Three-dimensional simulation of blood flow in an abdominal aortic aneurysm—steady and unsteady flow cases. *Journal of Biomechanical Engineering*, 116(1):89–97, 1994.

[261] M. Tobak and D. J. Peake. Topology of three-dimensional separated flows. *Annual Review of Fluid Mechanics*, 14(1):61–85, 1982.

[262] Y. Tobe, T. Yagi, Y. Iwabuchi, M. Yamanashi, K. Takamura, T. Sugiura, M. Umezu, Y. Hayashi, H. Yoshida, and A. et al. Nakajima. Relationship between pathology and hemodynamics of human unruptured cerebral aneurysms. In *The 15th International Conference on Biomedical Engineering*, pages 44–47, 2014.

[263] J. Tong, T. Cohnert, P. Regitnig, J. Kohlbacher, R. Birner-Gruenberger, A. J. Schriefl, G. Sommer, and G. A. Holzapfel. Variations of dissection properties and mass fractions with thrombus age in human abdominal aortic aneurysms. *Journal of Biomechanics*, 47(1):14–23, 2014.

[264] J. Tong and G. A Holzapfel. Structure, mechanics, and histology of intraluminal thrombi in abdominal aortic aneurysms. *Annals of Biomedical Engineering*, 43(7):1488–1501, 2015.

[265] X. Tricoche, G. Scheuermann, and H. Hagen. Continuous topology simplification of planar vector fields. In *Proceedings of the conference on Visualization'01*, pages 159–166, 2001.

[266] G. A. Truskey, F. Yuan, and D. F. Katz. *Transport phenomena in biological systems*. Pearson/Prentice Hall Upper Saddle River NJ:, 2004.

[267] V. T. Turitto and H. R Baumgartner. Platelet interaction with subendothelium in flowing rabbit blood: effect of blood shear rate. *Microvascular Research*, 17(1):38–54, 1979.

[268] S. Van Wyk, L. P. Wittberg, and L. Fuchs. Atherosclerotic indicators for blood-like fluids in 90-degree arterial-like bifurcations. *Computers in Biology and Medicine*, 50:56–69, 2014.

[269] J. J. Vaquero and P. Kinahan. Positron emission tomography: current challenges and opportunities for technological advances in clinical and preclinical imaging systems. *Annual Review of Biomedical Rngineering*, 17:385–414, 2015.

[270] J. Vétel, A. Garon, and D. Pelletier. Lagrangian coherent structures in the human carotid artery bifurcation. *Experiments in Fluids*, 46:1067–1079, 2009.

[271] I. E. Vignon-Clementel, C. A. Figueroa, K. E. Jansen, and C. A. Taylor. Outflow boundary conditions for three-dimensional finite element modeling of blood flow and pressure in arteries. *Computer Methods in Applied Mechanics and Engineering*, 195(29-32):3776–3796, 2006.

[272] P. E. Vincent and P. D. Weinberg. Flow-dependent concentration polarization and the endothelial glycocalyx layer: multi-scale aspects of arterial mass transport and their implications for atherosclerosis. *Biomechanics and Modeling in Mechanobiology*, 13(2):313–326, 2014.

[273] J. F. Vollmar, P. Pauschinger, E. Paes, E. Henze, and A. Friesch. Aortic aneurysms as late sequelae of above-knee amputation. *The Lancet*, 334(8667):834–835, 1989.

[274] D. A. Vorp. Biomechanics of abdominal aortic aneurysm. *Journal of Biomechanics*, 40(9):1887–1902, 2007.

[275] D. A. Vorp, P. C. Lee, D. H. J. Wang, M. S. Makaroun, E. M. Nemoto, S. Ogawa, and M. W. Webster. Association of intraluminal thrombus in abdominal aortic aneurysm with local hypoxia and wall weakening. *Journal of Vascular Surgery*, 34(2):291–299, 2001.

[276] D. H. J. Wang, M. S. Makaroun, M. W. Webster, and D. A. Vorp. Effect of intraluminal thrombus on wall stress in patient-specific models of abdominal aortic aneurysm. *Journal of Vascular Surgery*, 36(3):598–604, 2002.

[277] K. C. Wang. Three-dimensional boundary layer near the plane of symmetry of a spheroid at incidence. *Journal of Fluid Mechanics*, 43(01):187–209, 1970.

[278] P. N. Watton, A. Selimovic, N. B. Raberger, P. Huang, G. A. Holzapfel, and Y. Ventikos. Modelling evolution and the evolving mechanical environment of saccular cerebral aneurysms. *Biomechanics and Modeling in Mechanobiology*, 10(1):109–132, 2011.

[279] J. S. Weiss and B. E. Sumpio. Review of prevalence and outcome of vascular disease in patients with diabetes mellitus. *European Journal of Vascular and Endovascular Surgery*, 31(2):143–150, 2006.

[280] C. R. White, M. Haidekker, X. Bao, and J. A. Frangos. Temporal gradients in shear, but not spatial gradients, stimulate endothelial cell proliferation. *Circulation*, 103(20):2508–2513, 2001.

[281] C. H. Whiting and K. E. Jansen. A stabilized finite element method for the incompressible Navier-Stokes equations using a hierarchical basis. *International Journal for Numerical Methods in Fluids*, 35(1):93–116, 2001.

[282] J. S. Wilson, L. Virag, P. Di Achille, I. Karšaj, and J. D. Humphrey. Biochemomechanics of intraluminal thrombus in abdominal aortic aneurysms. *Journal of Biomechanical Engineering*, 135(2):021011–021011, 2013.

[283] N. Wilson, F. R. Arko, and C. A. Taylor. Patient-specific operative planning for aortofemoral reconstruction procedures. *Lecture Notes in Computer Science*, 3217:422–429, 2004.

[284] J. Wu and S. C. Shadden. Coupled simulation of hemodynamics and vascular growth and remodeling in a subject-specific geometry. *Annals of Biomedical Engineering*, 43(7):1543–1554, 2015.

[285] J. Z. Wu, H. Y. Ma, and M. D. Zhou. *Vorticity and vortex dynamics*. Springer Science & Business Media, 2007.

[286] Z. Wu, Z. Xu, O. Kim, and M. Alber. Three-dimensional multi-scale model of deformable platelets adhesion to vessel wall in blood flow. *Phil. Trans. R. Soc. A*, 372(2021):20130380, 2014.

[287] M. Xenos, S. H. Rambhia, Y. Alemu, S. Einav, N. Labropoulos, A. Tassiopoulos, J. J. Ricotta, and D. Bluestein. Patient-based abdominal aortic aneurysm rupture risk prediction with fluid structure interaction modeling. *Annals of Biomedical Engineering*, 38:3323–3337, 2010.

[288] X. Xie, Y. Wang, and H Zhou. Impact of coronary tortuosity on the coronary blood flow: a 3D computational study. *Journal of Biomechanics*, 46(11):1833–1841, 2013.

[289] Z. Xu, N. Chen, S.C. Shadden, J.E. Marsden, M.M. Kamocka, E.D. Rosen, and M. Alber. Study of blood flow impact on growth of thrombi using a multiscale model. *Soft Matter*, 5:769–779, 2009.

[290] T. Yagi, A. Sato, M. Shinke, S. Takahashi, Y. Tobe, H. Takao, Y. Murayama, and M. Umezu. Experimental insights into flow impingement in cerebral aneurysm by stereoscopic particle image velocimetry: transition from a laminar regime. *Journal of The Royal Society Interface*, 10(82):20121031, 2013.

[291] T. Yamaguchi, Y. Yamamoto, and H. Liu. Computational mechanical model studies on the spontaneous emergent morphogenesis of the cultured endothelial cells. *Journal of Biomechanics*, 33(1):115–126, 2000.

[292] J. J. Yeung, H. J. Kim, T. A. Abbruzzese, I. E. Vignon-Clementel, M. T. Draney-Blomme, K. K. Yeung, I. Perkash, R. J. Herfkens, C. A. Taylor, and R. L. Dalman. Aortoiliac hemodynamic and morphologic adaptation to chronic spinal cord injury. *Journal of Vascular Surgery*, 44(6):1254–1265, 2006.

[293] H. F. Younis, M. R. Kaazempur-Mofrad, C. Chung, R. C. Chan, and R. D. Kamm. Computational analysis of the effects of exercise on hemodynamics in the carotid bifurcation. *Annals of Biomedical Engineering*, 31(8):995–1006, 2003.

[294] P. A. Yushkevich, J. Piven, H. C. Hazlett, R. G. Smith, S. Ho, J. C. Gee, and G. Gerig. User-guided 3D active contour segmentation of anatomical structures: significantly improved efficiency and reliability. *Neuroimage*, 31(3):1116–1128, 2006.

[295] B. A. Zambrano, H. Gharahi, C. Lim, F. A. Jaberi, J. Choi, W. Lee, and S. Baek. Association of intraluminal thrombus, hemodynamic forces, and abdominal aortic aneurysm expansion using longitudinal CT images. *Annals of biomedical engineering*, 44(5):1502–1514, 2016.

[296] E. Zhang, K. Mischaikow, and G. Turk. Vector field design on surfaces. *ACM Transactions on Graphics (TOG)*, 25(4):1294–1326, 2006.

[297] J. Zhang and Y. Liu. Some singularities in fluid dynamics and their bifurcation analysis. In *Complex Motions and Chaos in Nonlinear Systems*, pages 39–73. Springer, 2016.

[298] J. M. Zhang, L. Zhong, B. Su, M. Wan, J. S. Yap, J. P. L. Tham, L. P. Chua, D. N. Ghista, and R. S. Tan. Perspective on CFD studies of coronary artery disease lesions and hemodynamics: A review. *International Journal for Numerical Methods in Biomedical Engineering*, 30(6):659–680, 2014.

[299] Y. Zhang, V. H. Barocas, S. A. Berceli, C. E. Clancy, D. M. Eckmann, M. Garbey, G. S. Kassab, D. R. Lochner, and R. et al. McCulloch, A. D .and Tran-Son-Tay. Multi-scale modeling of the cardiovascular system: Disease development, progression, and clinical intervention. *Annals of Biomedical Engineering*, pages 1–19, 2016.

[300] H. Zhong, S. Woodiga, P. Wang, J. Shang, X. Cui, J. Wang, and T. Liu. Skin-friction topology of wing–body junction flows. *European Journal of Mechanics-B/Fluids*, 53:55–67, 2015.